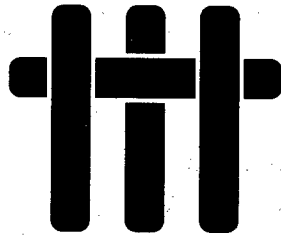


FINAL REPORT

University Research Initiative

Contract No.: N00014-92-J-1808

May 1996 - September 1997



Mechanism-Based Design for High-Temperature, High-Performance Composites

by

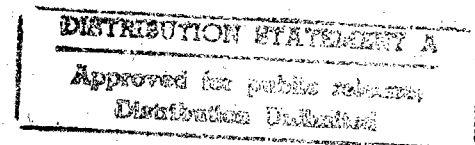
A.G. Evans & F.A. Leckie
University of California,
Santa Barbara, CA

and

J.W. Hutchinson
Harvard University,
Cambridge, MA

Cambridge University
Harvard University
Washington State University
University of Pennsylvania
University of Virginia

19980721 083



DTIC QUALITY INSPECTED 6

**SUMMARY
OF
TABLE OF CONTENTS**

EXECUTIVE SUMMARY

BOOK 1: CONSTITUENT PROPERTIES AND MACROSCOPIC PERFORMANCE OF CMC - I

BOOK 2: CONSTITUENT PROPERTIES AND MACROSCOPIC PERFORMANCE OF CMC - II

BOOK 3:

Section A: CONSTITUENT PROPERTIES AND MACROSCOPIC PERFORMANCE OF MMC

Section B: CONSTITUTIVE LAWS AND DESIGN

BOOK 4: MEASUREMENT AND MICRO-MECHANISMS

BOOK 2

CONSTITUENT PROPERTIES AND MACROSCOPIC PERFORMANCE OF CMC - II

Mechanical Performance of Ceramic Matrix Composite I-Beams	F.E. Heredia M.Y. He A.G. Evans	1
In-Plane Mechanical Properties of an All-Oxide Ceramic Composite	J.A. Heathcote X.-Y. Gong J. Yang U. Ramamurty F.W. Zok	13
The Processing and Performance of an All-Oxide Ceramic Composite	C.G. Levi J.Y. Yang B.J. Dalgleish F.W. Zok A.G. Evans	59
Notched Strength of Ceramic-Matrix Composites	W.P. Keith K.T. Kedward	93
Shear Damage Mechanisms in a Woven, Nicalon-Reinforced Ceramic-Matrix Composite	W.P. Keith K.T. Kedward	99
Effect of Matrix Grain Growth Kinetics on Composite Densification	O. Sudre F.F. Lange	107
Anisotropic Damage Evolution in Unidirectional Fiber Reinforced Ceramics	Y.M. Liu T.E. Mitchell H.N.G. Wadley	111
Elastic Properties of Laminated Calcium Aluminosilicate/Silicon Carbide Composites Determined by Resonant Ultrasound Spectroscopy	Y. Liu Y. He F. Chu T.E. Mitchell H.N.G. Wadley	151
The Influence of Fiber/Matrix Interface on the Mechanical Behavior of Nicalon SiC Fiber Reinforced Glass-Ceramic Composites	Y.M. Liu T.E. Mitchell H.N.G. Wadley	159
Effects of Off-Axis Loading on the Tensile Behavior of a Ceramic-Matrix Composite	C.S. Lynch A.G. Evans	165
Rupture Simulations for Unidirectional Ceramic Matrix Fiber Composites	R.M. McMeeking M.A. McGlockton B.N. Cox	177

Application of Weakest-Link Fracture Statistics to Fiber-Reinforced Ceramic-Matrix Composites	J.C. McNulty F.W. Zok	185
Notch-Sensitivity of Fiber-Reinforced Ceramic Matrix Composites: Effects of Inelastic Straining and Volume-Dependent Strength	J.C. McNulty F.W. Zok G.M. Genin A.G. Evans	195
Failure of a Porous Solid from a Deep Notch	P. Redanz N.A. Fleck R.M. McMeeking	239
Effect of Notch Root Radius on the Initiation Toughness of a C-Fiber/SiC-Matrix Composite	J.Y. Shen J.P. Hirth F.W. Zok J.A. Heathcote	265
Stress Rupture of an Enhanced Nicalon TM /SiC Composite at Intermediate Temperatures	T.E. Steyer F.W. Zok D.P. Walls	271

Mechanical performance of ceramic matrix composite I-beams

F. E. Heredia, M. Y. He and A. G. Evans*

Materials Department, University of California – Santa Barbara, Santa Barbara,
CA 93106-5050, USA

(Received 15 August 1995; revised 15 March 1996)

Experimental studies have been performed on ceramic matrix composite (CMC) I-sections, which typify joint designs for CMC components. Axial loads and moments have been applied to activate delamination mechanisms. The maximum load bearing capacity has large variability, governed by the severity of manufacturing flaws located in the transition region of the I-section. This variability leads to an unsatisfactory design situation. Delaminations that form from these flaws arrest and behave in a stable manner, subject to a remanent load bearing capacity. This remanent capacity has minimal variability. Hence, design based on the remanent load would be robust. An expression for this design criterion is presented. Copyright © 1996 Elsevier Science Limited

(Keywords: mechanical performance; ceramic matrix composite; I-beams)

INTRODUCTION

Many designs of thermostructural components made from composites include junctions, such as T-intersections, I-sections and C-segments^{1–5} (Figure 1). The responses of these junctions to applied loads and moments¹, as well as thermal gradients², are often performance limiting. Yet, there are no published experimental results on the mechanical performance of such junctions in ceramic matrix composites (CMCs). This article addresses the deficiency by presenting initial experimental findings on I-junctions made from a SiC/C composite⁶. Associated stress analyses, as well as related mechanics considerations, are presented and used to interpret the experiments and to propose design criteria.

The mechanical performance of composite joints and sections is typically dominated by the formation of delaminations^{1–5}. These are activated by interlaminar tensile stresses and interlaminar shear stresses. In turn, these stresses are induced by applied moments and temperature gradients. The stresses interact with manufacturing flaws to initiate the delaminations, resulting in appreciable variability in the load bearing capacity, with adverse effects on the design allowables. This variability and its association with the flaws typically found in CMCs are explored in this study.

Most CMC components are subject to negligible

pressure loads. The predominant loads are thermal and are associated with temperature gradients along the length, as well as through the thickness. For a component with multiple I-sections, there are temperature differences between these sections. Those at the lower temperatures experience axial tension, plus bending. Those at the higher temperatures are in axial compression. The former are most susceptible to degradation by delamination. This scenario motivates the present study.

MATERIALS AND TESTING

The CMC material used in this study is a SiC/C manufactured by HITCO^{6,7}. The fibres are Nicalon SiC and the matrix comprises C containing carbide particulates. The fibres were incorporated as a cloth, with eight-harness satin weave, and configured into a preform using graphite dies. The matrix was introduced through a sequence of liquid and vapour phase infiltrations, followed by pyrolysis and heat treatment steps. The material contains manufacturing defects. The principal defects found in plane sections comprise translaminar shrinkage flaws and interlaminar porosity⁷. Most of the in-plane properties are not sensitive to these defects, because of the existence of inelastic shear strain mechanisms that enable stress redistribution and provide notch insensitivity^{8,9}. However, the I-sections include additional manufacturing flaws. An assessment of their

*To whom correspondence should be addressed. Present address: Division of Applied Science, Harvard University, Pierce Hall, Cambridge, MA 02138, USA

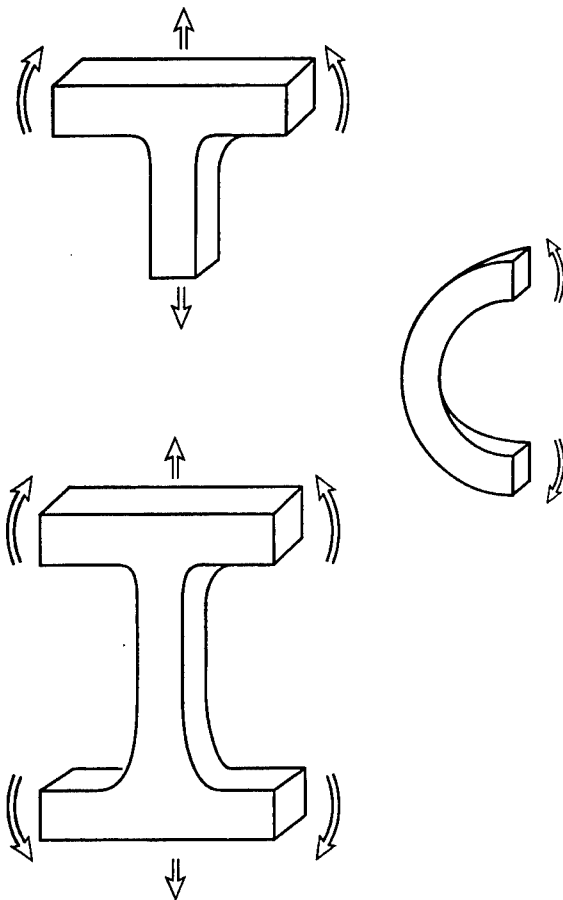


Figure 1 Schematic of some of the junction configurations used in designing components with CMCs

effect on the mechanical performance constitutes one theme of this investigation.

The as-manufactured configurations were in the form of long I-beams having cross-sectional dimensions $20\text{ mm} \times 20\text{ mm}$. These were cut into sections $\sim 3\text{ mm}$ thick, using a diamond saw. These sections were used to assess the mechanical performance. The testing configuration was designed to enable a combination of axial loads and bending moments to be imposed in order to simulate the typical design problem noted above (Figure 2a). It comprises a steel frame with loading points that contact the I-section at four locations. The contact locations are adjustable, enabling changes to be made in the ratio of the axial load to the moment. The frame was attached to the cross-head of a servohydraulic testing machine.

Strain gauges were attached to the specimen at the locations indicated on Figure 2a. These were used to assess the inelastic strains that accompany deformation. Two different loading spans were used for most tests: the wider span was 19 mm and the narrower span 8 mm . The tests were monitored using an optical telescope in order to identify and monitor the damage mechanisms and their sequence. Pre-test and post-test characterizations performed by scanning electron microscopy

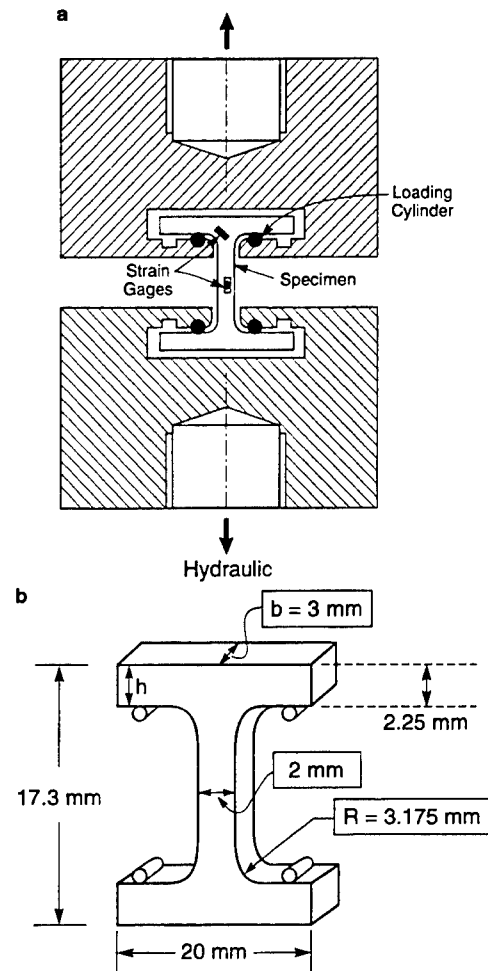


Figure 2 Schematic of the loading fixture used to test the I-sections. (a) Overview of the loading train and the specimen, indicating the locations of the strain gauges; (b) CMC specimen dimensions

(SEM) were used to identify the manufacturing flaws at the failure origins.

MEASUREMENTS AND OBSERVATIONS

Microstructural characterization and manufacturing flaws

Polished cross-sections (Figures 3–5) reveal the orientations of the weave and the manufacturing defects, particularly those in the triangular regions located at the transitions, designated the 'T' interstices. The weave in the 'T' comprises the fibre preform, infiltrated with the matrix, with one set of fibres oriented normal to the section and the others contoured around the 'T' (Figure 3). Manufacturing flaws in the interstice comprise regions of interconnected porosity between the plies, ranging in size up to $300\text{ }\mu\text{m}$ in length and $30\text{ }\mu\text{m}$ wide (Figure 3). There are also flaws around the perimeter of the interstice (Figure 4). Translaminar shrinkage flaws are apparent throughout (Figure 5).

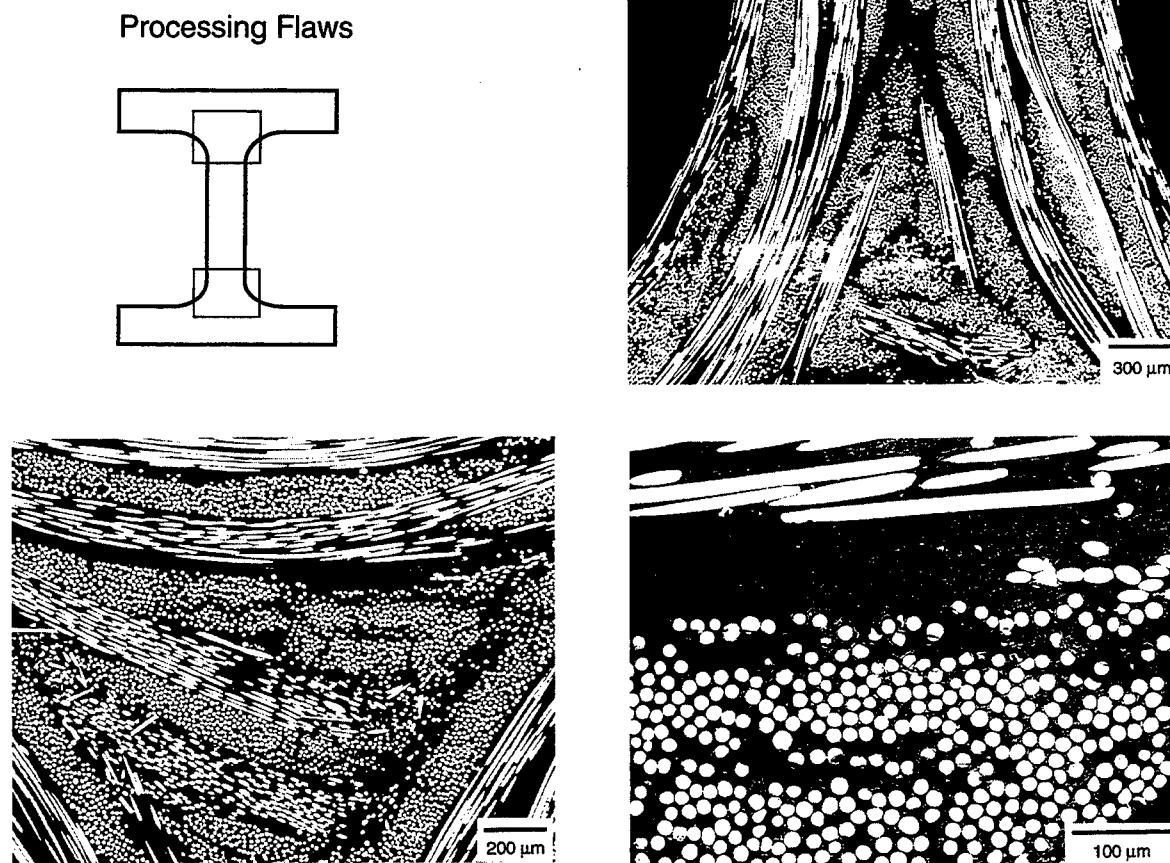


Figure 3 Sections that reveal the weave architecture and the manufacturing flaws in the vicinity of the 'T' interstice

Load/deflection response

Typical load/deflection responses obtained upon loading at a constant displacement rate ($10 \mu\text{m s}^{-1}$) are summarized in Figure 6. In most instances, the load increased linearly up to a maximum, followed by a load drop. A load bearing capacity was retained after the drop, with the load gradually decreasing as the deformation continued. In some instances, a slight non-linearity developed prior to the peak load.

Test results obtained with the narrower (8 mm) loading span are summarized on Figure 6a. In all cases, the stresses refer to the axial stresses σ^A on the centre section of the I. Two of the specimens (1 and 2) had similar compliance, but differing ultimate 'strengths' S_u : 60 and 90 MPa, respectively. The peak was followed by a load drop, with the retained strength $S_R \sim 20$ MPa, being essentially the same. The corresponding retained moment (relative to the symmetry plane of the I) is $M_R \sim 0.8 \text{ Nm}$. A third specimen (3) had a much larger compliance and a considerably reduced strength: only 30 MPa. It also exhibited appreciable non-linear deformation prior to the peak load. The subsequent load drop was small. The strength and moment retained after the drop slightly exceeded that found for the other

specimens. Prior to testing, there were no obvious differences in the flaws present in these three specimens.

Corresponding results obtained for two other specimens (4 and 5) using the wider loading span (19 mm) are presented on Figure 6b. In all cases, the compliances were about twice those obtained with the narrower span. The peak loads were also much lower, with S_u being in the range 20–30 MPa. But the load drops were smaller, such that the retained strengths after the drop, $S_R \sim 15$ MPa, and the retained moments, $M_R \sim 1 \text{ Nm}$, were essentially the same as those for the narrower span.

Stress induced damage

Following the load drop, each of the specimens exhibited one or more delamination cracks. Typical morphologies are depicted on Figures 7a and b. The cracks extended along the axis and partially penetrated the opposing arms of the I, apparently along the periphery of the 'T' interstice. Higher resolution images (Figure 8) confirm that the delamination progresses around this periphery, through the transverse ply. Specimens tested with the wider span exhibited additional cracks on the upper periphery of the 'T' (Figure 7b). In some regions, the delaminations cross

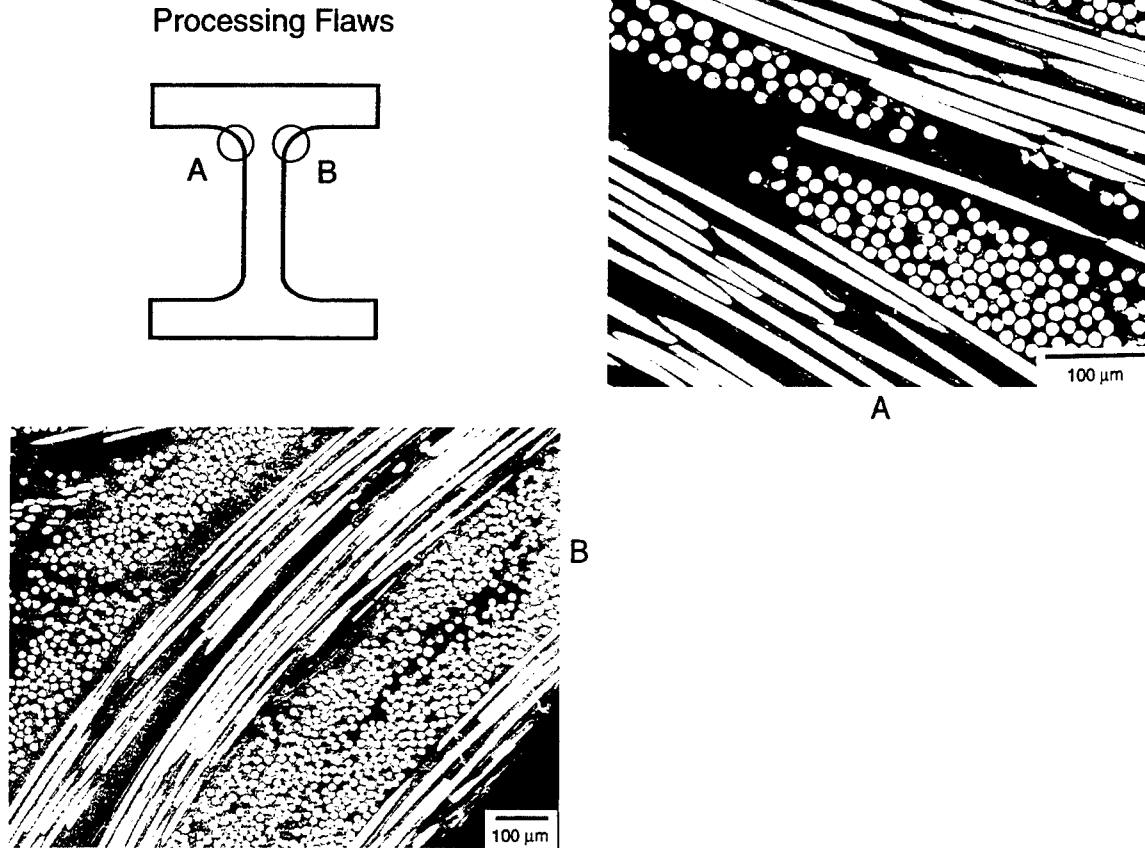


Figure 4 Manufacturing flaw near the perimeter of the 'I'

over fibre bundles (Figure 9a), causing these bundles to act as crack bridging ligaments. The cracks also deflect at shrinkage flaws (Figure 9b), resulting in irregular crack morphologies. Subsequent deformation caused the delaminations to further penetrate the arms, accompanied by additional fibre bundle bridging (Figure 10). But, some integrity was always retained: that is *penetration of the arms by the delaminations occurred in a stable manner*.

Post-test inspections by SEM revealed that each of the delaminations originated at manufacturing defects, with porous zones constituting the predominant 'flaw' (Figures 3 and 4). However, there are no obvious associations between the dimensions of those flaws observed prior to the testing and the peak load bearing capacity.

BASIC MECHANICS

Two basis analyses are performed in order to interpret the results and to provide a robust design criterion. (a) The first is performed for the sections without cracks, in the elastic range. The results are used to evaluate the stresses that act at the manufacturing flaws, and thereby establish flaw sensitivity rules governing the peak load

bearing capacity. (b) The second analysis is performed in the presence of delamination cracks. Energy release rates G are calculated as a function of the crack length a , with emphasis on the range where the cracks are stable: that is, where G decreases as a increases.

Initial insight is provided by some analytical results for curved beams (Figure 11) and corners, with emphasis on the stresses along the curved interface AC (Figure 12). The curved beam solutions indicate that the radial stresses σ_{rr} governing delamination are dominated by the applied moment M and the radius of curvature R (Figure 11), in the non-dimensional form¹ (see Figure 14):

$$\sigma_{rr} h^2 b / M = f_{rr}(h/R, E_L/E_T) \quad (1)$$

where $2h$ is the width of the beam, b its thickness (as defined on Figure 2b), E_L is the longitudinal modulus and E_T the transverse modulus: an analytical form of the function f_{rr} has been identified in work by Lu *et al.*¹

When a delamination initiates along the centre of the beam and propagates around the mid-section, the energy release rate G has the non-dimensional form¹:

$$E_L G h^3 b^2 / M^2 = F(a/R) \quad (2)$$

where $2a$ is the length of the delamination and F is the function plotted on Figure 11. Note that G reaches a peak

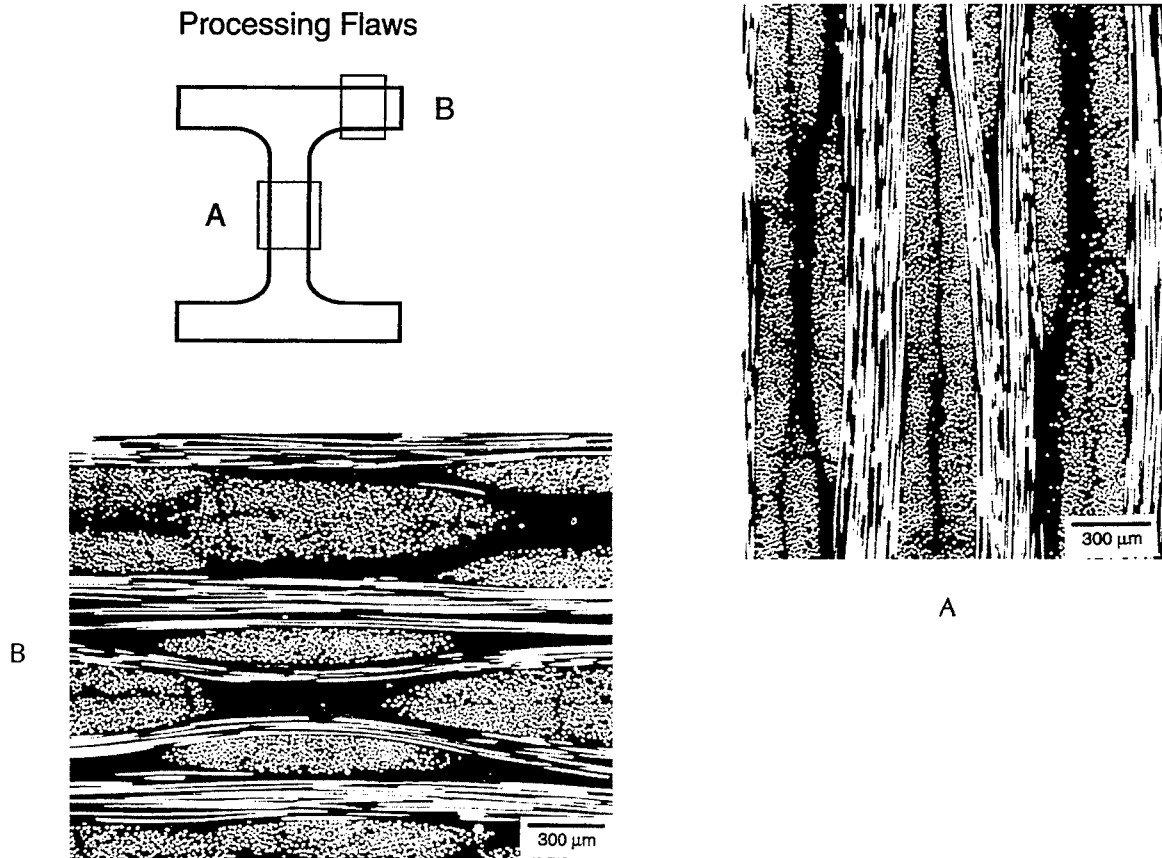


Figure 5 Interlaminar shrinkage flaws in plane sections

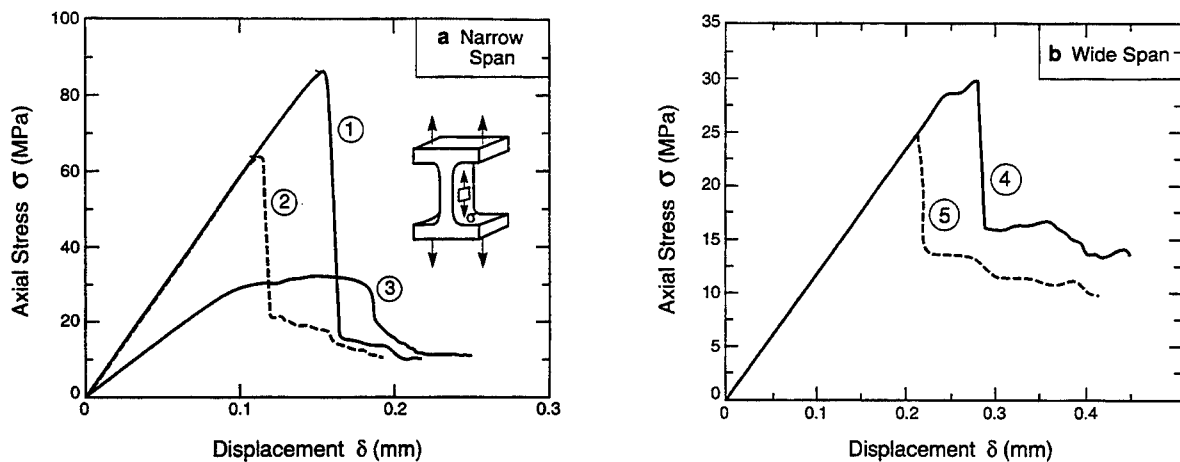


Figure 6 Stress/deflection responses of I-sections. (a) Narrow span; (b) wide span

and then diminishes as the delamination length a increases. Beyond the peak, the delamination is stable. This is the behaviour emphasized in the present analysis.

Solutions for corners¹⁰ indicate that stress concentrations may arise at B and C (Figure 12), weakly dependent on the elastic modulus orthotropy and on the ply

configuration. These are largely negated in the present junction design because the moduli are continuous. Hence, the stresses at these locations have less importance to junction performance than the stresses along AC, which interact with the manufacturing flaws within the 'T'.

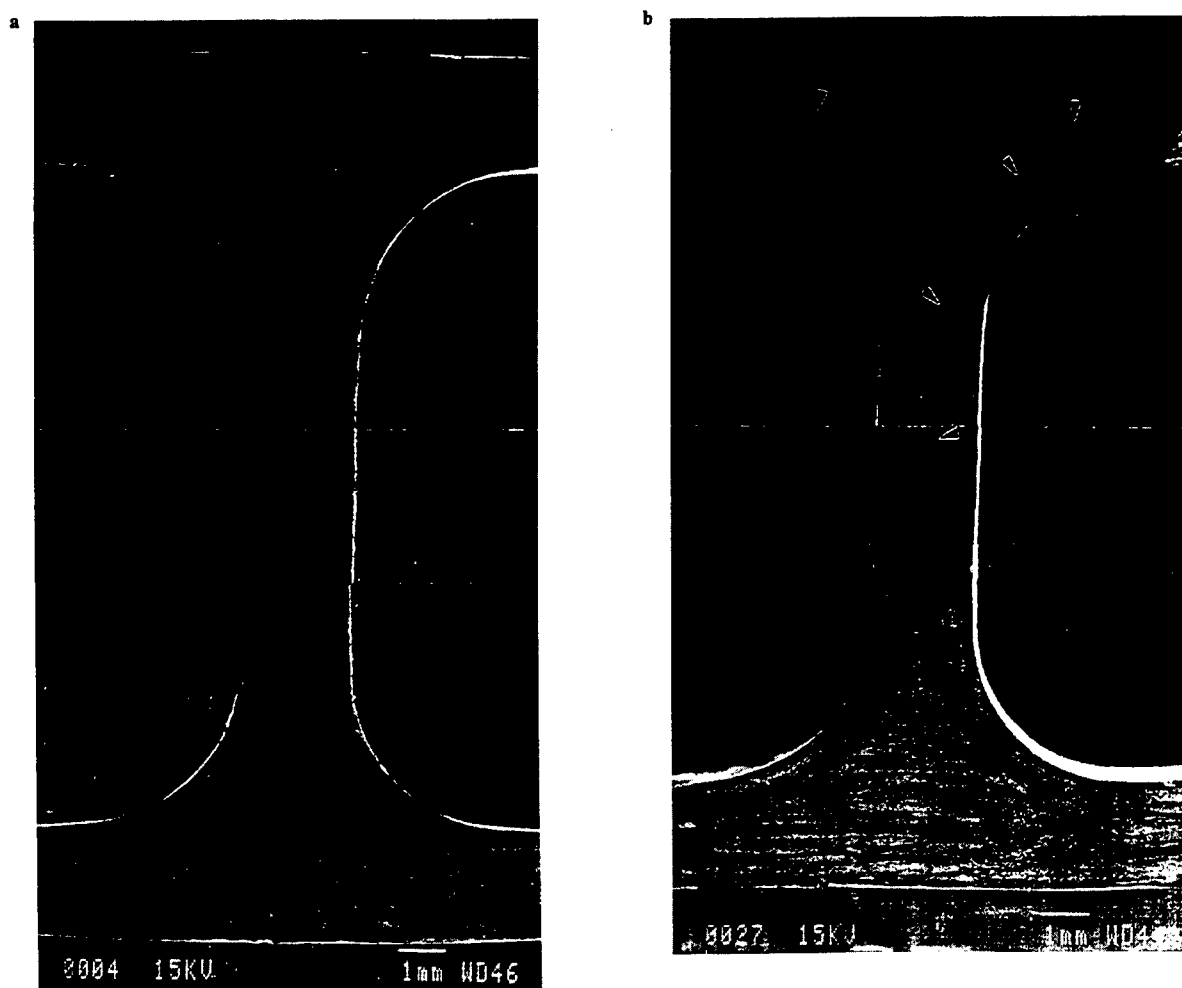


Figure 7 Delamination cracks that develop at the load drop. (a) Narrow span: (b) wide span

Table 1 Constituent properties

Longitudinal modulus, E_L (GPa)	60
Transverse modulus, E_T (GPa)	10
Longitudinal thermal expansion coefficient, α_L (K^{-1})	5×10^{-6}
Transverse thermal expansion coefficient, α_T (K^{-1})	10×10^{-6}
Cooling range, ΔT (K)	1000
Transverse fracture toughness, K_{Ic} (MPa \sqrt{m})	3
Ultimate tensile strength (MPa)	350
Compressive strength (MPa)	320

Stress distributions

The finite element method and the ABAQUS code have been used to perform the stress analysis. The meshes are shown on Figure 12. The elastic properties used in the calculations and the associated regions of the junction are indicated on Table 1. For comparative purposes, calculations are also performed for an elastically isotropic junction. To facilitate presentation, the stresses are normalized in accordance with equation (1). For this purpose, the moment arm is considered to originate at the symmetry plane of the I.

As expected, there are relatively large bending induced in-plane tensile and compressive stresses along the arms of the I (Figure 13). These stresses do not appear to activate deformation or damage modes in the present tests and they are not involved in the delamination. For the larger span, these stresses are similar to magnitudes estimated using simple beam theory¹¹, upon assuming that the beam is supported along the edge of the interstice, OO' (Figure 12). Moreover, the delaminations have not been found to originate near the loading points, where localized shear stresses exist. Consequently, shear effects have also been disregarded.

Of more pertinence to delamination are the normal and tangential stresses along the curved interface ABC, summarized on Figure 14. These are both predominantly tensile. These stresses induce an energy release rate at delaminations, which motivates their growth, as elaborated later. The elementary normalization for curved sections [equation (1)] rationalizes the influence of the loading and the span on the *radial* stresses, at least for orientations up to about 50° . The non-dimensional magnitude, $\sigma_{rr} h / 2b / M$, ranges between about 0.3 and 1.2

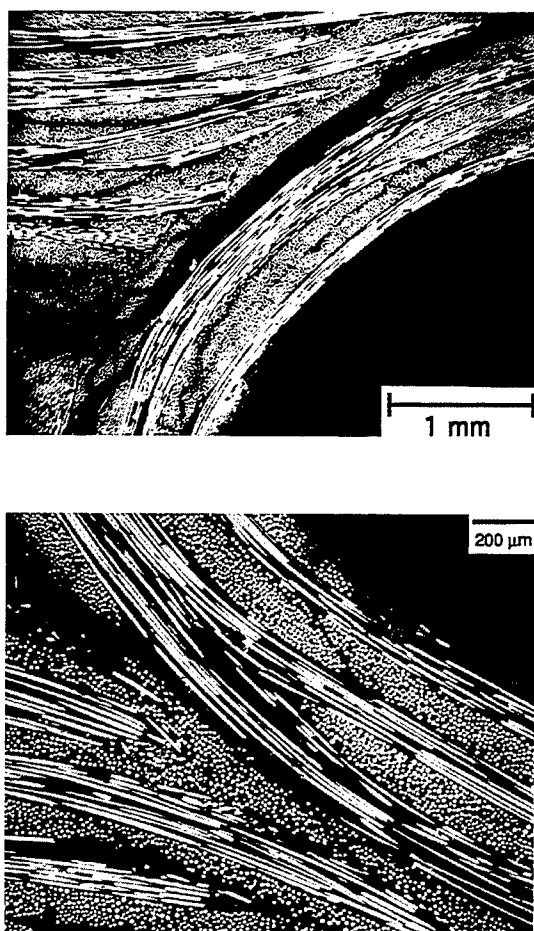


Figure 8 SEM of the delamination trajectory around the periphery of the 'T'

in this angular regime. The tangential stresses do not appear to normalize in the same manner; a fact which remains to be rationalized.

Residual stresses

The mismatch in thermal expansion between the fibres and the matrix induces residual stresses within the junction. The 'T' interstice has *tangential* expansion mismatch with the surrounding composite. Calculations performed subject to this mismatch yield the stress contours within the interstice summarized on Figure 15. All stresses are presented in accordance with the non-dimensional parameter, $\chi_{ij} = \sigma_{ij} / E_L \Delta\alpha \Delta T$, where $\Delta\alpha$ is the tangential thermal expansion mismatch between the 'T' interstice and the composite ($\alpha_T - \alpha_L$) (Table I), ΔT is the difference between the ambient temperature and the processing temperature, and χ_{ij} is dependent on the elastic properties and the interstice geometry. The largest stresses along BC are predominantly *tensile*, with $\chi_{yy} \sim 0.2$. These stresses exist in regions of the junction containing manufacturing flaws (Figure 3). They superpose on those from the applied loads, thereby diminishing the load bearing capacity of the junction. In some

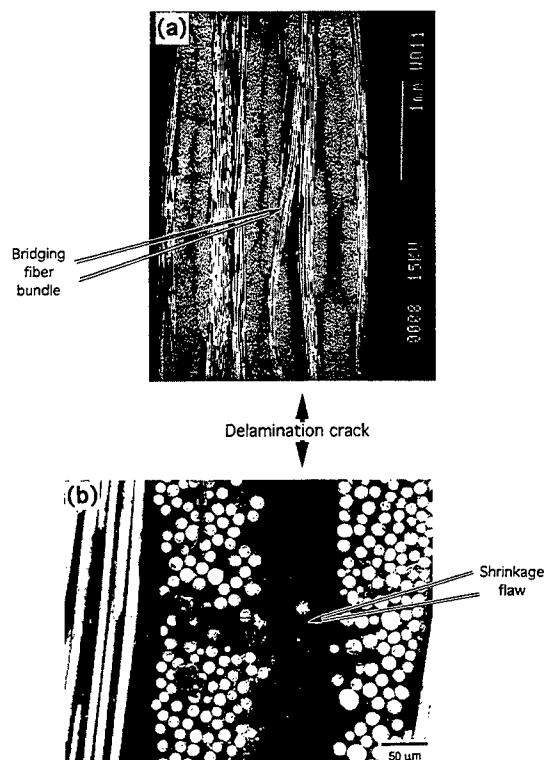


Figure 9 Interactions of the delaminations with the microstructure. (a) Bridging fibre bundle; (b) deflection at translaminar shrinkage flaw



Figure 10 Propagation of the delamination into the I accompanied by fibre bundle bridging

cases, these stresses may be large enough to cause delamination upon cooling from the consolidation temperature. This may be the reason for the inferior load bearing capacity of specimen 3 (Figure 6a).

Energy release rates

Beyond the peak load, after the delamination has formed, the energy release rate relative to the delamination fracture toughness governs the load capacity.

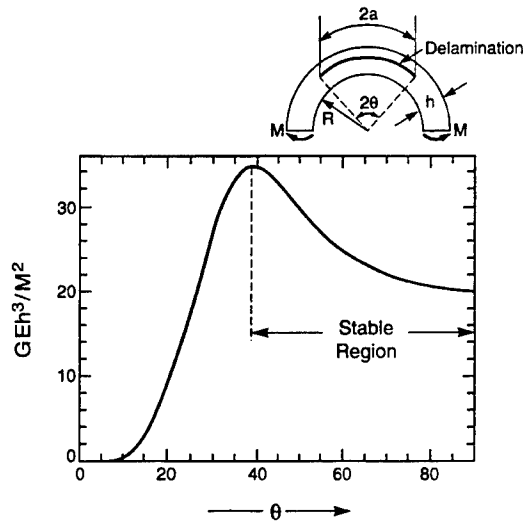


Figure 11 Energy release rate characteristics for delaminations in a curved beam, width h , subject to an applied moment M per unit thickness

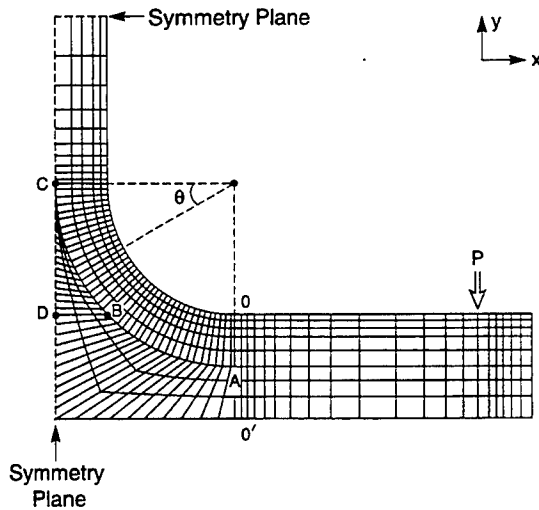


Figure 12 Finite element mesh used for elastic stress analysis

The energy release rates G , normalized in accordance with equation (2), have been calculated for a range of crack sizes by using the J-integral method (Figure 16) with the mesh shown in Figure 17. Emphasis has been placed on the regime in which the delaminations are stable, that is, where G decreases as a increases. The stable region commences at $a/R \sim 1.6$. Furthermore, the results for the narrow and wide spans appear to be rationalized by the curved beam normalization [equation (2)]. The compliance of the delaminated system has also been calculated. An example for the wider span is presented on Figure 17.

ANALYSIS AND INTERPRETATION

Delamination at peak load

The trends in the delamination-limited load bearing

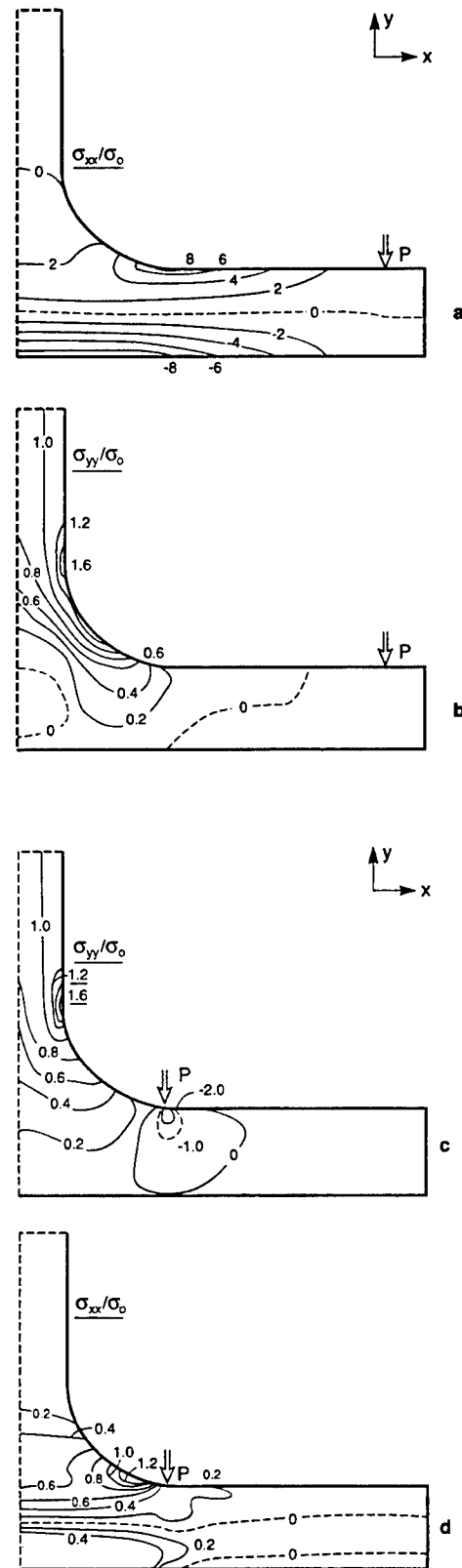


Figure 13 Contours of the σ_{xx} and σ_{yy} stresses throughout the beam: (a), (b) wide span; (c), (d) narrow span. All stresses are normalized by the tensile stress induced at the central axis of the I

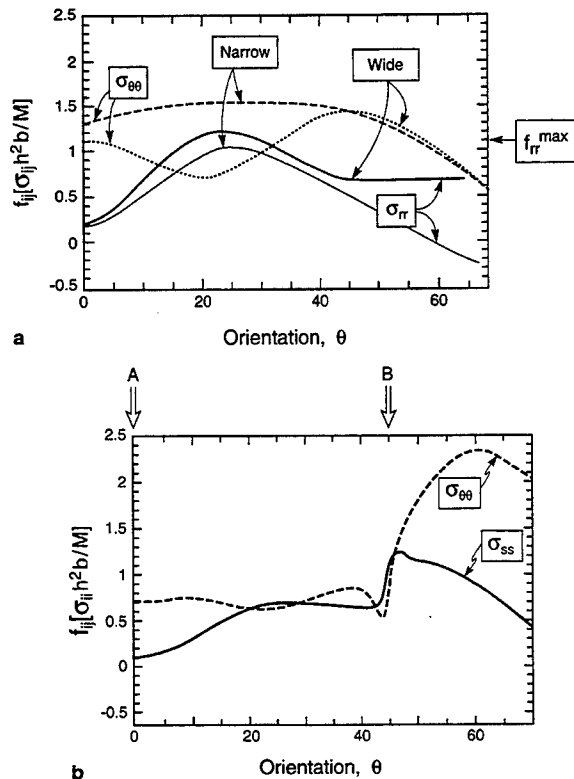


Figure 14 Distributions of radial and tangential stresses along the curved plane ABC normalized by the moment relative to the symmetry plane: (a) isotropic; (b) anisotropic

capacity of the junction between the narrow and wide spans are in accordance with the effect of the moment on the radial stresses along the ABC plane (Figure 14). That is, relative to the narrow span, the loads applied at the wider span exert about *twice* the moment and yield about *half* the load capacity.

More quantitatively, the *measured peak loads* may be used with the *stress analysis* to determine the magnitudes of the stresses that activate the manufacturing flaws. In the absence of residual strains, the largest stresses along ABC at the load peak would be in the range 70–130 MPa, for both the narrow and wide loading arrangement (although in the anomalous specimen 3 the stress at the peak is only 40 MPa). The residual stresses are ~60 MPa, obtained using the material properties from Table 1, with $\Delta T \sim 1000^\circ\text{C}$. The magnitude of the manufacturing flaws, $2a_o$, that could be activated by these combined stresses may be estimated by assuming that the penny-crack solution applies to the manufacturing flaws¹², with the flaw plane normal to the radial stresses. This solution has the form:

$$a_o = \pi(K_T/2\sigma)^2 = \pi K_T^2 / 4(Mf/bh^2 + E_L \Delta\alpha\Delta T \chi_{IT})^2 \quad (3)$$

where K_T is the transverse fracture toughness of the composite and σ is the sum of the stresses induced by the applied loads and the residual field. If it is

assumed that $K_T \approx 3 \text{ MPa}\sqrt{\text{m}}$ (typical for graphitic C¹³) then $a_o \sim 400 \mu\text{m}$. Manufacturing flaws of this size are prevalent within the 'T' regions of the junctions (Figure 3).

More quantitative assessments would require additional knowledge about the transverse toughness of the composite and the manufacturing flaw sensitivity relative to cracks having the same dimensions. For this purpose, a systematic evaluation of the effect of controlled flaws on the load capacity would be needed¹⁴.

Tensile and compressive failure

Since the in-plane tensile and compressive stresses (Figure 13) can be appreciably larger than the inter-laminar stresses, especially at the larger applied moments, there is potential for either tensile or compressive failure. Evaluations of the largest in-plane tensile and compressive stresses at the peak loads borne by the beams tested with the wider span (~260 MPa) indicate that they are somewhat lower than the in-plane ultimate tensile and compressive strengths of this composite (Table 1). The occurrence of the delamination, rather than either tensile or compressive failure, is consistent with the in-plane stresses being lower than these strengths. The implication, however, is that tensile or compressive failure modes would become prevalent if the beams were subjected to moments larger than that induced by the wider span. In this situation, the stresses that cause failure could be predicted from beam theory calculations.

Remanent strength

After delamination, there is a remanent strength. This strength might be contemplated as a basis for a fail-safe design criterion. The moment that can be sustained

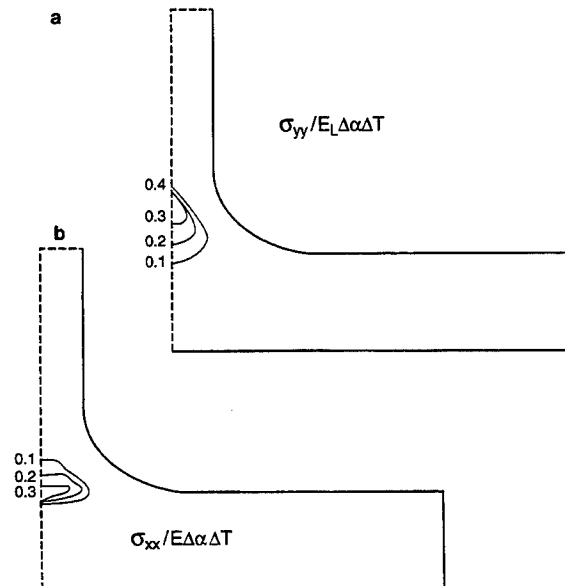


Figure 15 Contours of residual stress associated with the junction: (a) σ_{yy} stresses; (b) σ_{xx} stresses

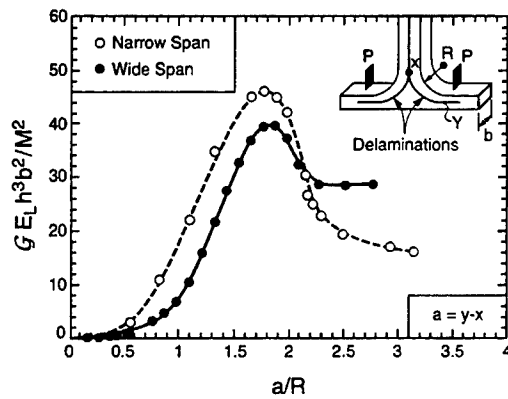


Figure 16 Non-dimensional strain energy release rate as a function of the relative delamination length in the stable region

in this condition M_c is obtained from equation (2), with G equated to the transverse fracture toughness, $\Gamma_T = K_T^2/E_T$. This is given by:

$$M_c/bh^{3/2}K_T = (E_L/E_T F)^{1/2} \quad (4)$$

M_c can be estimated by using the results for F from Figure 16. In the stable range, $a/R \gtrsim 2$, and with $K_T \sim 13 \text{ MPa}\sqrt{\text{m}}$, $b = 3 \text{ mm}$ and $h = 2.5 \text{ mm}$, M_c is of the order 0.6 Nm , comparable to the measured values (see section on Load-deflection response). The basic effects thus seem to be captured by this simple approach. Moreover, the importance of the transverse (matrix) fracture toughness K_T in determining the allowable moment M_c is evident. It remains to be determined whether M_c is large enough to ensure satisfactory design loads using this criterion.

IMPLICATIONS

The measurements and calculations provide some preliminary guidelines for design, which may also be used to assess the effects of scaling. The load bearing capacity can be expressed through the moment M_D . This is feasible because the radial stresses that activate the delamination have a magnitude controlled primarily by the moment (Figure 14). The maximum stress is related to the moment by [equation (1)]:

$$\sigma_{\pi}^{\max} = M f_{\pi}^{\max} / b h^2 \quad (5)$$

with $f_{\pi}^{\max} \sim 1.0$ (Figure 14). Combining this stress with the residual stress (Figure 15), the delamination criterion becomes:

$$M_D = (b h^2 / f_{\pi}^{\max}) (\sqrt{\pi} K_T / 2 a_o^{1/2} - \chi_{\pi} E_L \Delta \alpha \Delta T) \quad (6)$$

with $\chi_{\pi} \sim 0.2$. The sensitivity of the mechanical performance of the I-section to the size of the manufacturing flaws a_o and to the residual stress poses problems for the design. An approach based on weakest link statistics would be needed, such as that used to design monolithic ceramics¹⁵. The limitation would be the ability to characterize the manufacturing

flaws through non-destructive methods, augmented by statistical data¹⁴.

The problems associated with design based on weakest link statistics suggest that an alternative, fail-safe approach based on the assumption that delaminations already exist may be preferable. Then, the design condition is given by equation (4) as:

$$M_D = b h^{3/2} K_T \sqrt{E_L/E_T F} \quad (7)$$

The practical utility of this approach remains to be determined.

CONCLUDING REMARKS

CMC I-sections subject to bending moments are susceptible to delamination. Similar effects may be inferred for T-junctions and C-sections. The delaminations are activated by radial stresses, which interact with manufacturing flaws located within the interstices of the intersection. These flaws typically comprise extended pores that arise from a combination of incomplete matrix infiltration and constrained shrinkage. In the SiC/C composite explored here, these pores approach $300 \mu\text{m}$ in diameter.

The delamination propagates primarily through the matrix, which has a relatively low toughness. The consequence is that the peak load bearing capacity

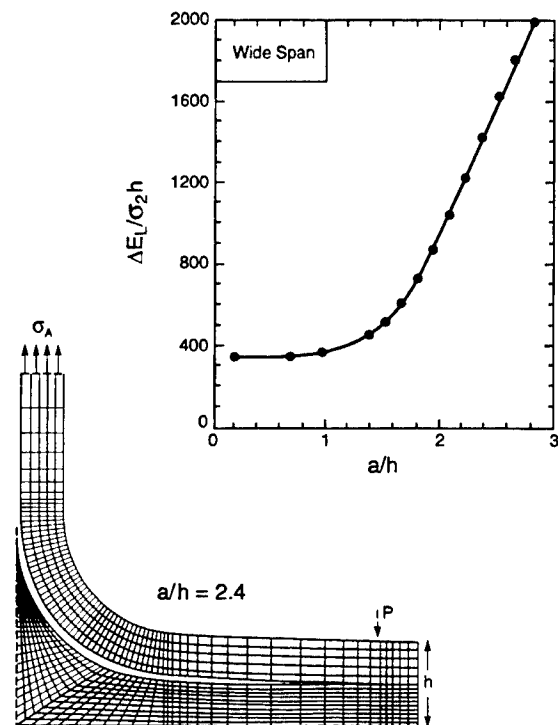


Figure 17 Compliance of the delaminated beam for the wide loading span. The finite element representation is also shown for one of the crack lengths: $a/h \sim 2.4$. A finer mesh is used for crack calculations than for stress analysis (Figure 12)

exhibits considerable variability, governed by the size distribution of manufacturing flaws. Weakest link behaviour is inferred, with implications for statistical variability and size scaling effects analogous to those applicable to monolithic ceramics^{15,16}.

Subsequent to the initiation of delamination at the peak load, the cracks enter a stable regime and *arrest*. This enables the section to retain some load bearing capability, even when the delaminations are present. This *remnant strength* S_R has minimal variability and is subject to an explicitly lower bound. Consequently, S_R provides a robust design criterion, provided that the associated low load capacity and high compliance can be accommodated in the structural design.

REFERENCES

- 1 Lu, T.J., Xia, Z.C. and Hutchinson, J.W. *Mater. Sci. Eng.* 1994, **A188**, 107
- 2 Lu, T.J. and Hutchinson, J.W. *J. Am. Ceram. Soc.* 1995, **78**, 261
- 3 Carlsson, L.A., Gillespie, J.W. and Pipes, R.B. *J. Compos. Mater.* 1988, **22**, 469
- 4 Wang, Y. and Williams, J.G. *Compos. Sci. Technol.* 1992, **43**, 251
- 5 Hutchinson, J.W. and Suo, Z. *Adv. Appl. Mech.* 1992, **29**, 1
- 6 Heredia, F.E., Spearing, S.M. and Evans, A.G. *J. Am. Ceram. Soc.* 1992, **75**, 3017
- 7 Turner, K., Speck, J.S. and Evans, A.G. *J. Am. Ceram. Soc.* 1995, **78**, 1841
- 8 Brøndsted, P.A., Heredia, F.E. and Evans, A.G. *J. Am. Ceram. Soc.* 1994, **77**, 2569
- 9 Mackin, T.J., He, M.Y., Evans, A.G., Mosher, P. and Brøndsted, P.A. *J. Am. Ceram. Soc.* 1994, **77**, 2817
- 10 Williams, M.L. *J. Appl. Mech.* 1956, **23**, 477
- 11 Timoshenko, S. and Goodier, J.N. 'Theory of Elasticity', McGraw-Hill, 1950
- 12 Tada, H., Paris, P. and Irwin, G. 'Handbook of Stress Intensity Factors', Del, 1985
- 13 Zhao, J.X., Bradt, R.C. and Walker, P.L. *Carbon* 1985, **23**, 15-18
- 14 Evans, A.G. *J. Am. Ceram. Soc.* 1982, **65**, 127
- 15 Johnson, C.A. and Tucker, W.T. *ASTM STP 1201* (Eds C.R. Brinkman and S.F. Duffy), 1993, pp. 250-264
- 16 Evans, A.G. *Trans. Proc. Roy. Soc.* 1995, **351**, 511

NOMENCLATURE

a	crack (delamination) length
a_0	length of manufacturing flaw
b	beam thickness (<i>Figure 2b</i>)
E	Young's modulus
E_L	longitudinal modulus
E_T	transverse modulus
f	radial stress function
F	energy release rate function (<i>Figure 11</i>)
G	energy release rate
h	beam width (<i>Figure 2b</i>)
K_T	transverse fracture toughness of composite
M	bending moment
R	radius of curvature
T	temperature
ΔT	cooling range from processing to ambient
α	thermal expansion coefficient
α_L	longitudinal thermal expansion coefficient
α_T	transverse thermal expansion coefficient
$\Delta\alpha$	thermal expansion mismatch, $\alpha_T - \alpha_L$
σ_{ij}	stress
σ_{rr}	radial stress
χ_{ij}	non-dimensional stress



IN-PLANE MECHANICAL PROPERTIES OF AN ALL-OXIDE CERAMIC COMPOSITE

J.A. Heathcote, X.-Y. Gong, J. Yang, U. Ramamurty* and F.W. Zok

Materials Department
University of California
Santa Barbara, California 93106

*Presently with
School of Mechanical & Production Engineering
Nanyang Technological University
Singapore 639798

Submitted to the *Journal of the American Ceramic Society*

April, 1998

ABSTRACT

The present article examines the in-plane tensile properties of a 2D all-oxide ceramic composite. The distinguishing characteristics of the material include the fine-scale porosity within the matrix and the absence of a fiber coating. The anisotropy in the elastic-plastic properties is studied through tension tests in the axial (fiber) direction and at 45° to the fiber axes, both in the presence and the absence of holes or notches. The notch sensitivity in the axial direction is found to be comparable to that of conventional dense-matrix, weak-interface composites. These results serve as a demonstration of the effectiveness of the porous matrix in enabling damage tolerance. Furthermore, the trends in notch sensitivity are rationalized using models that account for the effects of inelastic straining on stress distributions around notches and holes, coupled with a scale-dependent failure criterion. In the off-axis orientation, failure occurs by a plastic instability, analogous to necking in metals. Following instability, deformation continues within a diffuse localized deformation band, with a length that scales with the specimen width. Similar deformation and fracture characteristics are obtained both with and without holes, and independent of hole size. The role of the matrix porosity in enabling crack deflection and inelastic straining is discussed.

1. INTRODUCTION

There is growing interest in all-oxide fiber-reinforced ceramic-matrix composites (CMCs) [1-6] for use in advanced gas turbine engines. Historically, the SiC-based CMCs have been deemed to be superior to the oxides, because of their high creep resistance and high thermal conductivity. However, it has become increasingly evident that the SiC CMCs are strongly susceptible to oxidative embrittlement at stresses exceeding the matrix cracking limit [7-18]. Clearly the oxide systems are inherently more resistant to oxidation effects and thus have better potential for long-term durability. Recognizing the relative merits and shortcomings of the two classes of composites, it is anticipated that the all-oxide systems will find application in long-life components under moderately high operating temperatures (to ~ 1100 - 1200°C), whereas the SiC-based materials will be the choice for components requiring shorter lives but higher temperatures.

The present article examines the mechanical performance of a relatively new all-oxide CMC, building upon the work recently reported by Levi et al. [6]. The distinguishing characteristics of the material include fine-scale porosity within the matrix and the absence of a fiber coating. The porosity is the key microstructural feature that enables crack deflection and damage tolerance. The article focuses specifically on the in-plane tensile properties of a 2D woven composite, both in the absence and in the presence of notches or holes. The degree of anisotropy is probed through tests performed both parallel and at 45° to the fiber axes. Models are used to elucidate the relevant composite and constituent properties and to rationalize the notch effects.

2. PROCEDURES

2.1 Materials

The composite material comprised Nextel 610 Al_2O_3 fiber cloth in an 8-harness satin weave and a porous matrix of 80% mullite and 20% alumina. Details of the microstructural design and the processing route are described in [6]. Briefly, the material was made by vacuum infiltration of an aqueous slurry containing the matrix powders into a preform of the fiber cloths. The matrix powders were $\sim 1\ \mu\text{m}$ diameter MU-107 mullite (Showa Denko K.K.) and $\sim 0.2\ \mu\text{m}$ diameter AKP-50 alumina (Sumitomo Chemical). The packing density of the matrix powder was $\approx 55\%$. Following infiltration, the green panels were dried and sintered at 900°C for 2h, to promote the development of alumina bridges between the mullite particles. The panels subsequently were impregnated with an alumina precursor solution (aluminum hydroxychloride) and pyrolyzed at 900°C for 2h. This impregnation and pyrolysis sequence was performed four times. The panels were given a final heat treatment at 1200°C for 2h in order to stabilize the precursor-derived alumina and to enhance the integrity of the alumina bridges. Examinations of polished cross-sections of the consolidation panels indicated uniform infiltration of the powder slurry both within and between the fiber tows.

Panels were made with fibers oriented either parallel or at 45° to the panel edges, thus facilitating preparation of tensile specimens in both the longitudinal ($0^\circ/90^\circ$) and off-axis ($\pm 45^\circ$) orientations. A summary of the panels and their fiber content and porosity are summarized in Table I. The fiber content, f , was determined from knowledge of the cloth volume and the final plate dimensions. The porosity, p , was measured in accordance with ASTM Standard C20-92. These properties were relatively uniform between panels, with values $f \approx 0.37\text{-}0.42$ and $p \approx 22\%\text{-}25\%$.

2.2 Testing Procedures

A series of mechanical tests was performed to elucidate the tensile properties of the composite in both the $0^\circ/90^\circ$ and the $\pm 45^\circ$ orientations. The $0^\circ/90^\circ$ properties were measured using standard dog-bone tensile specimens, with a gauge length of 115 mm and gauge width of 8.5 mm. The properties in the $\pm 45^\circ$ orientation were obtained from either dog-bone specimens or straight-sided specimens with end-tabs. Both geometries resulted in gauge failures. The widths in the $\pm 45^\circ$ specimens were varied from 4.9 to 19.5 mm. The longitudinal strains were measured using a non-contacting laser extensometer over a 70 mm gauge length. In addition, some of the specimens were instrumented with longitudinal and transverse strain gauges. The longitudinal gauges were typically 6-12 mm long, whereas the transverse gauges were selected to cover approximately one half of the specimen width. In comparing the results from different panels, the strengths were "corrected" to an average fiber volume fraction of 40%, assuming the strength to be proportional to the fiber volume fraction. The magnitude of these corrections did not exceed 5%.

Notch-sensitivity of strength was investigated through a series of tensile tests on $\pm 45^\circ$ and $0^\circ/90^\circ$ specimens with center-holes (Fig. 1). The ratio of hole diameter, $2a$, to specimen width, $2w$, was fixed at $1/3$. Scale effects were probed by varying the absolute hole diameter, from 3 to 10 mm. In some instances, small strain gauges (1.6×1.6 mm) were placed at the hole edge in order to determine the local tensile strain at failure. Tests were performed also on $\pm 45^\circ$ specimens with semi-circular "edge holes", as illustrated in Fig. 1(b). The ratio a/w was fixed at $1/3$ and the hole diameter was varied from 3 to 6.6 mm.

Complementary measurements of the $0^\circ/90^\circ$ tensile strength and notch-sensitivity were obtained from four-point flexure tests. Such tests were

performed on straight, 6 mm-wide specimens, oriented to produce in-plane stresses only. The inner and outer loading spans were 25 mm and 127 mm, respectively. The strains on both the tensile and compressive faces were measured using strain gauges. In addition, three-point flexure tests were performed on 12 mm wide specimens, each with a 6 mm-long edge-notch located at the specimen center. The notch width was ~ 0.4 mm. The loading span was 190 mm.

2.3 Modeling of Stress Distributions and Notched Strength

The stress and strain distributions around the notches and holes in the $0^\circ/90^\circ$ specimens were calculated using two different models. The first was based on a continuum description of deformation, with no provision for localization phenomena such as macroscopic cracks or shear bands. The material response was assumed to follow the nonlinear constitutive law developed by Genin and Hutchinson [19]. The law was calibrated using the uniaxial stress-strain measurements in the $\pm 45^\circ$ and $0^\circ/90^\circ$ orientations. Details of the calibration and implementation procedures are presented elsewhere [19, 20].

The second model assumed that the nonlinear deformation was confined to shear bands, emanating from the holes or notch tips and propagating parallel to the loading direction. The shear bands were assumed to form and propagate at a critical value of shear stress, τ_0 [21], taken to be one-half of the ultimate tensile strength in the $\pm 45^\circ$ orientation. Outside of the shear bands, the material was taken to be linear-elastic, with the appropriate elastic constants. The use of this model was motivated by the low "hardening rate" in the $\pm 45^\circ$ tensile response at strains exceeding $\approx 0.2\%$ along with the large shear strains along the plane of the incipient shear band that were predicted by the nonlinear continuum model.

Both models were implemented in the ABAQUS finite element code. The computed stress distributions coupled with the notched strength measurements

were used to infer the local conditions at the onset of failure. A simple engineering approach that has found utility in predicting failure in notched specimens of both ceramic [20] and polymer matrix composites (PMC) [22-26] involves the use of the point stress failure criterion. Here failure is postulated to occur when a critical stress is attained over a characteristic distance, d , ahead of the notch or hole. In the present study, the critical stress was taken to be the unnotched tensile strength of the composite and the characteristic distance was inferred from comparisons between the measured and predicted strengths. A similar approach was used to rationalize the difference in strengths measured in tension and in flexure.

3. UNNOTCHED PROPERTIES

3.1 0°/90° Orientation

The results of the unnotched tensile and flexure tests are plotted in Fig. 2. The tensile response exhibited only very slight nonlinearity, developing progressively with increasing stress. The initial modulus was $E_0 \approx 95\text{-}100$ GPa and the Poisson's ratio, $\nu_0 = 0.05$. The modulus decreased with increasing stress, and reached $E'_0 \approx 75\text{-}78$ GPa at failure. The latter value is about the same as the contribution expected from the longitudinal fibers: $f E_f/2 \approx 74$ GPa, where E_f is the Young's modulus of the fibers (380 GPa). The progressive nonlinearity is believed to be associated with microcracking within the matrix, causing the effective matrix modulus to be negligible at the point of composite fracture. An additional inference is that matrix microcracking is initiated at strains that are much lower than the ultimate failure strain. Similar nonlinearity was obtained in flexure (Fig. 2(b)). The latter results also indicated very slight asymmetry in the material response, as manifest by the differences in the tensile and compressive strains.

The measured elastic constants were used to infer the Young's modulus of the porous matrix through classical lamination theory. For this purpose, the composite was treated as a balanced cross-ply laminate. The longitudinal and transverse moduli of the unidirectional lamina were estimated using the standard upper and lower bound solutions, respectively, and the Poisson's ratios of the fibers and matrix were taken to be 0.2. In doing this, the inferred (initial) matrix modulus is $E_m \approx 20$ to 25 GPa. With this modulus, the Poisson's ratio ν_0 of the laminate was predicted to be 0.066-0.078, which is comparable to the measured value of 0.05.

The inferred matrix modulus is about an order of magnitude lower than that expected for the fully-dense matrix: $E_d \approx 240$ -250 GPa (depending on whether the upper or lower bound solution is used for averaging the properties of the mullite and the alumina). The difference is attributable to the high matrix porosity. Measurements of the elastic moduli of monolithic ceramics with comparable levels of porosity suggest a scaling of the form [27, 28]

$$E_m/E_d = 1 - p_m/p_o \quad (1)$$

where p_o is the initial porosity, prior to densification. In the present composite, $p_m \approx 0.39$ and $p_o \approx 0.45$, yielding a predicted modulus ratio, $E_m/E_d = 0.13$. This is similar to the value inferred from the $0^\circ/90^\circ$ modulus: $E_m/E_d \approx 0.1$.

The tensile strengths, σ_o , and failure strains, ϵ_o , measured in tension were 195-235 MPa and 0.22-0.24%, respectively. The corresponding properties obtained from the flexure tests were higher: 250-260 MPa and 0.29-0.31%. The differences suggest a scale-dependence in the tensile strength, as found in other fiber-reinforced CMCs [29], and can be rationalized in terms of the point stress failure criterion. Upon comparing the strengths measured in tension and flexure, and assuming a linear distribution of stress across the flexure specimens, the characteristic distance is

inferred to be 0.4 ± 0.2 mm. This range is slightly lower than that reported for other fiber-reinforced CMCs (0.5-0.75 mm) [20] as well as for polymer matrix composites (0.5-1.3 mm) [22-26].

3.2 $\pm 45^\circ$ Orientation

Representative stress-strain curves obtained from the $\pm 45^\circ$ tension tests are plotted in Fig. 3. In this orientation, the Young's modulus, $E_{45} = 50$ GPa, and the Poisson's ratio, $\nu_{45} = 0.55$. Following lamination theory and using the matrix modulus inferred from the $0^\circ/90^\circ$ tests ($E_m = 20$ -25 GPa), the composite properties are predicted to be $E_{45} = 42$ -51 GPa and $\nu_{45} = 0.54$ -0.59. These values agree well with the measured ones.

Recognizing that only three of the four elastic constants obtained from the $\pm 45^\circ$ and $0^\circ/90^\circ$ tests are independent, an additional check was made on the consistency of the measured elastic constants. For orthotropic materials with equivalent elastic properties in two orthogonal directions, the constants are related through

$$\frac{E_{45}}{E_0} = \frac{1 - \nu_{45}}{1 - \nu_0} \quad (2)$$

Using the measured Poisson's ratios, the predicted modulus ratio is $E_{45}/E_0 = 0.47$, which is similar to the measured ratio, $E_{45}/E_0 = 0.50$.

Nonlinearity was initiated at $\approx 0.05\%$ strain and ≈ 20 MPa stress. At higher stress levels (≥ 20 MPa), both the longitudinal and transverse strains exhibited similar amounts of nonlinearity, although the two were of opposite sense. Interestingly, the inelastic in-plane dilation, characterized by the sum of the inelastic strains, $\epsilon_L^{\text{in}} + \epsilon_L^{\text{in}}$, was essentially zero up to the stress maximum (Fig. 3(a)). In

contrast, significant dilation occurs prior to failure in dense-matrix CMCs [30], because of the development of long, bridged matrix cracks. It is surmised that the inelastic deformation in the porous-matrix composites is accommodated by microcracking of the necks between matrix particles and subsequent particle rearrangement. Evidently this mode of deformation can occur with minimal dilation (at least at small strains). Attempts to image this damage in the scanning electron microscope were unsuccessful, presumably because of the extremely fine scale of the damage as well as the small residual strains ($\approx 0.05\%$) upon unloading from the load maximum.

Tensile failure in the $\pm 45^\circ$ orientation occurred by the formation of a diffuse localized deformation band, initiating at strains of $\approx 0.25\text{-}0.4\%$. Substantial additional strains were obtained within the localized band. Final fracture occurred along a plane at $\sim 45^\circ$ to the loading direction, with minimal fiber fracture. In contrast, in dense-matrix CMCs, fracture occurs catastrophically at the load maximum, with the majority of fibers breaking in the process [30].

Strain localization was manifested in the mechanical measurements in three ways. (i) The stress-strain response exhibited progressive softening with increased strain, with a tangent modulus, $d\sigma/d\varepsilon \approx 0$, at the onset of localization. (ii) Following localization, substantial displacement was obtained without fracture, because of the additional inelastic strains within the localized band. (iii) Because of the diffuse nature of the localization, the strain measurements exhibited wide variability near the stress maximum, depending upon the location of the measurement with respect to the localized band. That is, in instances where the strain gauge was located away from the localized band, the strain reached a peak and diminished as the load dropped (e.g. open circular symbols in Fig. 3(a)). Conversely, when the gauge was located near the localized band, the strain continued to increase following localization (e.g. triangular symbols in Fig. 3(a)). The post-localization response of

the laser extensometer exhibited similar trends. That is, large additional strain was obtained when the localized band was located within the gauge length (Fig. 3(b)); otherwise, the strain diminished with increasing remote displacement (Fig. 3(a)).

The measurements demonstrate that failure occurs by a *plastic instability*, analogous to necking in metals, and not by a catastrophic fracture event. In metals, instability occurs when the rate of geometric softening associated with area reduction overcomes the intrinsic hardening due to dislocation generation and interaction. Evidently the strain required for instability in the composites is much smaller than those in metals, implying that the intrinsic "hardening" of the composite is small. Nevertheless, the fact that failure occurs through a plastic instability has important implications in the degree of notch-sensitivity, as described in Section 4.2.

Comparisons of measurements on specimens of varying width indicate that the length of the localized band scales with the specimen width. This inference was drawn from the observation that the post-localization displacement was proportional to the width (Fig. 4(a)). A similar trend was observed in the total energy dissipated following localization (Fig. 4(b)). These results differ from those obtained in thin metal sheets, wherein the length of the localized band is proportional to the thickness and failure ultimately occurs by localization in the thickness direction. Because of the fiber architecture in the composite, inelastic straining is restricted to the plane containing the fiber cloths, precluding through-thickness localization. This anisotropy in the inelastic response is responsible for the unique localization characteristics of the CMCs and the large post-localization displacement and fracture energy. Optical examinations of the fractured specimens confirmed the effects of width on the size of the localized band (Fig. 5).

Following localization, the additional strain was accommodated by rotation of the fiber tows towards the loading direction and extensive comminution of the matrix (Fig. 5(a)). In this regime, the damage was highly dilational, as evidenced by the pronounced swelling in the thickness direction (Fig. 5(b)). The swelling is attributable to the rearrangement of the matrix particles at high strain levels.

The energy absorbed by this process can be partitioned into two components: (i) energy associated with surface area, created through fracture of the particle necks, and (ii) friction arising from subsequent particle rearrangement. A rough estimate of the former contribution can be made readily by calculating the area of broken particle necks within the localized region. The result is

$$\Gamma \approx (n_p \gamma_b \alpha^2) (w/d) (1-f) \Gamma_n \quad (3)$$

where n_p is the number of necks per particle (≈ 3 , assuming a particle coordination number of 6); γ_b is the fractional number of necks that break within the localized volume (the volume being taken as $w^2 t$); d is the particle diameter ($\approx 1 \mu\text{m}$); α is the ratio of the neck diameter to the particle diameter (roughly 0.1); and Γ_n is the fracture energy of the necks ($\approx 1 \text{ J/m}^2$). An upper bound estimate of this contribution is obtained by assuming that *all* of the necks break ($\gamma_b = 1$), yielding the result, $\Gamma/w \approx 2 \times 10^4 \text{ J/m}^3$. By comparison, the measurements give a value which is more than two orders of magnitude greater: $\Gamma/w \approx 4 \times 10^6 \text{ J/m}^3$. The inference is that the majority of the energy is dissipated through *friction following fracture of the necks*, not through the fracture process itself. Though a suitable model for the frictional contribution is not available, it is expected that this contribution would also scale inversely with particle size (analogous to Eqn. 3), because the relevant energy dissipation mechanism operates at the scale of the matrix particles. Thus, the large fracture energy can be attributed to the fine scale of both the matrix porosity

and the matrix damage, coupled with the diffuse nature of the localized deformation band.

The two panels of $\pm 45^\circ$ material yielded slightly different failure properties: one with a slightly higher strength and a lower failure strain than the other (60 MPa vs. 50 MPa, and 0.25% vs. 0.35%). Given the similarities in the matrix porosity and fiber content in these panels, the origin of the differences is not known.

4. NOTCHED PROPERTIES

4.1 $0^\circ/90^\circ$ Orientation

The trends in the net-section tensile strength, σ_N , with hole radius, a , are plotted in Fig. 6. Also shown are the expected results for two limiting cases: (i) completely notch-insensitive ($\sigma_N/\sigma_o = 1$, with σ_o being the unnotched strength), and (ii) strongly notch-sensitive ($\sigma_N/\sigma_o = 1/k_\sigma \approx 0.35$, where k_σ is the elastic stress concentration factor). The measured strengths were between these limits. Moreover, the strength decreased gradually with increasing hole diameter, indicating a scale-dependent strength. Essentially identical results have been obtained for SiC-based CMCs with weak interfaces [20]. That is, the relative reductions in strength are the same at a given hole diameter.

The development of the local tensile strain ahead of the hole edge is shown in Fig. 7. The strain initially increased linearly with stress. Beyond 0.2% strain, large inelastic strains were obtained, reaching values of ~ 0.7 -1.2% at the stress maximum. It is surmised that a portion of the apparent strains may be associated with the formation of a macroscopic crack through failure of the fibers and the local opening of this crack prior to fracture, rather than uniform straining of the composite. Regardless of whether such cracks form, the measurements clearly indicate that

failure is not precipitated when the local strain reaches the unnotched failure strain ($\approx 0.2\%$), further supporting the idea of a scale-dependent strength.

The effects of nonlinear deformation on the local stress distribution in the open hole specimens have been calculated from both the nonlinear continuum model and the shear band model. The predicted distributions of the normal stress on the incipient fracture plane are shown in Fig. 8(a). The corresponding distribution of the effective plastic strain obtained from the continuum model is shown in Fig. 8(b). (Here the effective plastic strain is defined in the same manner as in metal plasticity.) The plastic strains are concentrated within long, narrow bands, oriented parallel to the loading direction. Indeed, the shape of this plastic zone was the motivation for also using the shear band model for calculating the stresses. The elongated shape is due to the strong anisotropy in the inelastic straining behavior, as seen in Figs. 2 and 3. At stresses near the measured strength, the plasticity causes a reduction in the normal stress along the incipient fracture plane over a distance of $\sim a/2$ (Fig. 8(a)). This reduction is $\sim 15\%$ near the hole edge. The results obtained from the shear band model show reductions that are somewhat smaller ($\sim 10\%$ at the hole edge) and diminish to zero at a distance of $\sim a/4$. The differences are due to the absence of hardening in the shear band model and hence the reduced effectiveness of the band in spreading plasticity and reducing stress concentrations.

The predicted stress distribution coupled with the point stress failure criterion have been used to rationalize the effects of hole size on strength. The results are plotted on Fig. 6. Upon comparison of the calculations with the measurements, the characteristic distance inferred from the continuum model is $\approx 0.5\text{-}0.75\text{ mm}$, whereas the one from the shear band model is $\approx 0.75\text{-}1.0\text{ mm}$. These values are comparable to those inferred from similar notch-sensitivity studies on dense-matrix weak-interface CMCs [20].

Figure 9 shows a photograph of a typical fractured test specimen. The specimens exhibited a fibrous appearance, a consequence of fiber failure occurring over a wide range of axial locations. The inference is that the porous matrix is effective in deflecting cracks, thus allowing fiber failure to occur in a more or less random manner. The unnotched specimens exhibited the same features.

Complementary information about the notch-sensitivity in the $0^\circ/90^\circ$ orientation was obtained from the edge-notched flexure tests. The results are plotted in Fig. 10. In this configuration, the degree of notch sensitivity in the ultimate strength was lower than that in the open-hole tensile specimen, despite the higher notch acuity and the correspondingly higher elastic stress concentration.

The predicted distributions of the normal stress along the incipient failure plane within the flexure specimens are plotted in Fig. 11. Inelastic straining causes a reduction in the stress concentration very near the notch tip, over a distance comparable to the notch root radius (0.2 mm). Additionally, the stress decays more rapidly than in the center-hole specimens, because the loads are applied through bending. The combination of the bending and the notch acuity results in only a very small volume of material being subjected to elevated stress. In the present geometry, the size of the zone in which the normal stress exceeds the maximum nominal net-section stress is only ~ 0.4 mm. This distance represents less than half of the width of a fiber tow. Despite the persistence of a high stress level very near the notch tip, the strength exhibits minimal notch sensitivity: a direct consequence of the volume-dependence of strength. Clearly, if the tensile strength was deterministic, the degree of notch sensitivity in the edge-notched flexure specimens would be significantly higher than that of the center-hole tensile specimens because of the differences in stress concentration. Upon application of the point stress criterion, the inferred characteristic distance is found to be $d \approx 0.5$ mm.

A characteristic feature of the notched-flexure test is the "tail" in the stress-displacement curve beyond the load maximum (Fig. 10). The deformation in this regime occurs stably, with no precipitous load drops. The work of fracture, W_f , measured by the area under the curve, is $\approx 6000 \text{ J/m}^2$, with an equivalent steady-state fracture toughness, $K_s = \sqrt{E W_f} \approx 25 \text{ MPa } \sqrt{\text{m}}$. The latter value is about an order of magnitude higher than that of comparable monolithic ceramics (either alumina or mullite). The inferred toughness is expected to dictate the notch-sensitivity in the regime of long cracks or notches, defined by $a > a_c \equiv \alpha \sqrt{E W_f / \sigma_o^2}$, with a_c being a critical crack length and α a numerical coefficient of order 2. Using the measured values of the relevant parameters yields $a_c \approx 30 \text{ mm}$.

Figure 10 also shows the predicted response of a sharply-notched specimen subject to small-scale yielding, with an initiation toughness $K_o = 12 \text{ MPa } \sqrt{\text{m}}$ (selected to give the same stress maximum as the measured value). Details of the calculation are in the Appendix. Beyond the stress maximum, the predicted curve strongly underestimates the measured response, indicating an increasing fracture resistance with crack growth. This result is qualitatively consistent with the high steady-state fracture toughness ($25 \text{ MPa } \sqrt{\text{m}}$), obtained from the work of fracture. Models based on large-scale yielding would be required to simulate the full response. The latter conclusion is further supported by the observation that the notch length (6 mm) is considerably smaller than that required for small scale yielding models to be applicable ($a > a_c \approx 30 \text{ mm}$).

4.2 $\pm 45^\circ$ Orientation

The notched behavior in the $\pm 45^\circ$ orientation was dramatically different. The key results are plotted in Figs. 12 and 13 and the fractured test specimens are shown in Fig. 14. In the presence of center-holes, the strength was essentially notch-independent; indeed, there was some indication of notch *strengthening* (by

~ 10-15%) at larger hole sizes (Fig. 12). As in the unnotched geometry, failure occurred by the formation of a diffuse localized deformation band. Final fracture was along a plane passing through the hole and inclined at ~ 45° to the loading direction (Fig. 14). Failure was accommodated by extensive matrix fragmentation and fiber rotation but minimal fiber fracture.

Measurements of the local strains at the edges of the center holes revealed substantial elevations in the extent of inelastic straining prior to failure (Fig. 13). That is, the local strains reached values of ~0.7-0.8% at the stress maximum: ~2-3 times the values obtained in the unnotched tests. Evidently the constraint associated with the hole suppresses the onset of localization within the most heavily stressed regions (immediately ahead of the hole), resulting in the observed notch-insensitivity. This constraint also appears to elevate slightly the average net-section stress at failure, above that of the unnotched geometry.

Failure of the $\pm 45^\circ$ specimens containing edge-holes occurred in a similar manner, with two notable differences. (i) Because of the tendency of failure to occur at ~45° to the loading direction, the fracture plane passed through only one of the two holes (Fig. 14(b)). Consequently, the relevant net-section is dictated by the dimension $2w-a$ (rather than $2w-2a$). (ii) The increase in the effective net-section resulted in an elevation in notched strength above that of the center-hole geometry. Assuming failure occurs at a critical value of the net-section stress, the strength of the edge-hole geometry is predicted to be

$$\frac{\sigma_N}{\sigma_o} = \frac{1 - a/2w}{1 - a/w} \quad (4)$$

In the present case, $a/w = 1/3$ and thus $\sigma_N/\sigma_o = 1.25$ (Fig. 12). As in the case of the center-hole geometry, the measured strengths exceeded the net-section prediction (by ~10%), because of the constraints associated with the holes.

For both the center-hole and edge-hole geometries, the post-localization behavior was essentially the same as that of the unnotched specimens. Notably, the localized zone was diffuse and of a length dictated by the specimen width. In addition, the inelastic displacements and fracture energy scaled with specimen width, as shown in Fig. 4. These trends further illustrate the absence of notch-sensitivity in the $\pm 45^\circ$ in-plane properties.

5. DISCUSSION

The results clearly show that inelastic straining and damage tolerance in CMCs can be enabled through fine-scale matrix porosity, without a fiber coating to promote crack deflection and fiber-matrix sliding. The following discussion focuses primarily on the role of this porosity in both the axial and the off-axis properties.

Broadly, damage tolerance in CMCs is effected by the arrest or deflection of cracks, emanating from either the matrix or the fibers. The conditions for deflection can be determined by comparing the energy release rates associated with penetration across the interphase boundary, G_p , and deflection along the boundary, G_d , with the appropriate toughnesses. The relevant solutions for plane cracks have been developed by He and Hutchinson [31]. The key material property dictating the ratio G_d/G_p is the elastic mismatch parameter: $\alpha \equiv (\bar{E}_1 - \bar{E}_2)/(\bar{E}_1 + \bar{E}_2)$ where \bar{E} is the plane strain modulus, and the subscripts 1 and 2 refer to the uncracked and cracked materials, respectively. Using the elastic moduli of the fibers and the porous matrix, the mismatch parameter relevant to cracks emanating from the matrix and impinging on the fibers is $\alpha \approx 0.85$. The corresponding energy release rate ratio, obtained from Fig. 3 of [31], is $G_d/G_p \approx 1.4$. Crack deflection is thus predicted to occur when $\Gamma_i/\Gamma_f \leq 1.4$, where Γ_i and Γ_f are the toughnesses of the fiber-matrix interface and the fibers, respectively. In the absence of a fiber coating, the interface toughness

is expected to be similar to that of the porous matrix, Γ_m . Moreover, measurements on porous monolithic ceramics indicate that the latter toughness follows a scaling similar to the one in Eqn. (1); that is [28]

$$\Gamma_m / \Gamma_m^0 = 1 - p_m / p_o \quad (5)$$

where Γ_m^0 is the toughness of the fully-dense matrix. For the matrix in the present composite, $p_m / p_o \approx 0.87$, and thus $\Gamma_m / \Gamma_m^0 \approx 0.13$. Assuming that the fiber toughness is comparable to that of the fully-dense matrix, the relevant toughness ratio becomes $\Gamma_i / \Gamma_f \approx 0.13$: about an order of magnitude lower than the critical value for penetration. The conclusion is that matrix cracks should deflect along the fiber-matrix interfaces rather than penetrate into the fibers.

A similar approach has been used to establish the minimum porosity level needed to enable crack deflection; below this level, matrix cracks will penetrate into the fibers and the damage tolerance will be lost. For this purpose, the energy release rate ratio in the regime $\alpha \geq 0$ ratio has been fit by the function

$$G_d / G_p = 0.24 (1 - \alpha)^{-0.91} \quad (6)$$

Then, combining Eqns. (1), (5) and (6), and taking the moduli of the fibers and the fully-dense matrix to be equal, the critical matrix porosity is found to be

$$0.24(1 - p_m / p_o)^{-1.91} (1 - p_m / 2p_o)^{0.91} = 1 \quad (7)$$

which has the solution $p_m = 0.27$. Below this level, fiber coatings would be needed to enable crack deflection.

In principle, a similar approach might be used to assess the fate of cracks emanating from the fibers and impinging on the matrix. However, the analysis is complicated by the inelastic deformation of the matrix at the strains at which fiber fracture begins. The tension results indicate that this inelastic straining begins at strains as low as 0.05%; at strains of 0.2-0.3%, the effective matrix modulus is largely reduced, as manifest by the reduction in the $0^\circ/90^\circ$ tangent modulus (to the level associated with the fibers alone), and the onset of macroscopic localization in the $\pm 45^\circ$ tests. At the higher strains, it would appear that the matrix more closely resembles a granular medium than a real solid. Consequently, the existing analysis for determining the crack trajectory is not valid.

It is expected that in the absence of a contiguous "solid" matrix, the stress associated with a fiber break cannot be readily transmitted to neighboring fibers and thus the sequence of fiber damage events should occur in a spatially random fashion. Indeed, this is consistent with the observations on the fractured test specimens. A tentative conclusion is that the damage tolerance is enabled in part by the fragmentation of the matrix *prior* to fiber fracture, thus decoupling the fibers from one another once they begin to break. Moreover, sliding of the broken fibers past the matrix is still expected to be resisted by friction, allowing load to be transferred to the broken fiber. As a result, the strength of the fiber bundle will be elevated, above that of the dry bundle. Nonlinear constitutive laws for brittle, porous materials are needed to model the load transfer behavior and its effect on both the development of fiber breakage and the fiber bundle strength.

The distributed nature of the matrix damage also has implications in the mechanical behavior in the $\pm 45^\circ$ orientation. That is, moderate amounts of global inelastic strain (~ 0.2 - 0.3%) can be obtained after the onset of matrix damage. This strain is accommodated by comminution of the matrix and rearrangement of the resulting matrix particles. The observation that the first damage event (taken at the

onset of nonlinearity) does not lead to catastrophic fracture also suggests an important role of the fibers in distributing the damage and preventing localization of the deformation. Such constraints would not occur in unidirectionally-reinforced composites in off-axis loadings, since matrix damage could spread readily along narrow bands parallel to the fibers. Evidently the woven fiber architecture delays the onset of localization and promotes the development of long, diffuse deformation bands. Similar constraint effects have been observed in fiber-reinforced metal- and polymer-matrix composites, with angle-ply laminates exhibiting higher failure strains and stresses than the corresponding unidirectional off-axis laminates [32]. In each of the latter cases, however, the load bearing capacity is dictated by a fracture event rather than a plastic instability.

The effects of the fiber architecture on the flow response in the $\pm 45^\circ$ orientation can be further rationalized using an analogy based on constrained deformation in metal bicrystals (Fig. 15). At the simplest level, the composite can be treated as a laminate comprising anisotropic elastic-plastic laminae, with the plastic deformation within each lamina being confined to a state of simple shear parallel to the fiber direction. If compatibility is to be maintained at the inter-laminae interface, shear straining within each lamina will be heavily constrained by the neighboring laminae. Similar constraints would be obtained in anisotropic metal bicrystals, oriented to produce slip on only one system in each of the two crystals, as illustrated in Fig. 15. Clearly, the constraints of the two grains would elevate the yield stress and promote work hardening. Without these constraints, and in the absence of intrinsic work hardening, a single crystal with one of these two orientations would undergo strain localization immediately upon yielding. It is surmised that the porous matrix within the composites has negligible intrinsic work hardening capacity and that the development of stable plasticity in the 2D architectures is a manifestation of analogous constrained deformation.

The absence of notch sensitivity in the $\pm 45^\circ$ orientation is also attributable to the inelastic deformation and the eventual plastic instability that dictates the ultimate strength. A key related feature that enables this notch insensitivity is the absence of an easy deformation path in the through-thickness direction. As a consequence, the length of the localized deformation band scales with the specimen width, rather than the thickness. The diffuse nature of this band allows for more effective redistribution in stress around the holes prior to localization. If the inelastic response was isotropic (as in metals), localization would occur by deformation in the thickness direction, at lower levels of applied stress. The spreading of the subsequent localized deformation would then dictate the notch-sensitivity, analogous to that of thin metal sheets [33, 34], and the strength would exhibit some notch sensitivity.

6. CONCLUDING REMARKS

Damage tolerance in CMCs can be enabled by matrix porosity, without the use of fiber coatings. The porosity serves to lower the matrix modulus and hence reduce the driving force for the penetration of matrix cracks into the fibers. Limits on the acceptable porosity level to effect this behavior can be established through the use of existing crack deflection criteria. Additionally, the pores act as sites for microcracking and comminution of the matrix during straining, with substantial energy dissipation occurring upon rearrangement of the resultant matrix particles. This damage also mitigates the stress concentration associated with fiber breaks. In off-axis orientations, the fibers play a central role in spreading the inelastic deformation and inhibiting strain localization. Further understanding of the deformation and fracture properties of these composites and the design of optimal matrix microstructures require the development of models for the inelastic

response of porous ceramic materials, with the porosity level being a key variable. This is the focus of ongoing research activities.

ACKNOWLEDGMENTS

Funding for this work was provided by the ARPA University Research Initiative Program at UCSB under ONR contract No. N00014-92-J-1808. The authors gratefully acknowledge many helpful discussions with C.G. Levi and F.A. Leckie, and the technical assistance of B.D. Dalglish and K.A. Fields.

REFERENCES

1. F.F. Lange, W.C. Tu and A.G. Evans, "Processing of Damage-Tolerant, Oxidation-Resistant Ceramic Matrix Composites by a Precursor Infiltration and Pyrolysis Method," *Mater. Sci. Eng.*, **A195**, 145-150 (1995).
2. R. Lundberg and L. Eckerbom, "Design and Processing of All-Oxide Composites," *Ceramic Transactions*, **58**, 95-104 (1995).
3. E. Mouchon and Ph. Colomban, "Oxide Ceramic Matrix/Oxide Fiber Woven Fabric Composites Exhibiting Dissipative Fracture Behavior," *Composites*, **26**, 175-82 (1995).
4. P.E.D. Morgan and D.B. Marshall, "Ceramic Composites of Monazite and Alumina," *J. Am. Ceram. Soc.*, **78** [6] 1553-63 (1995), also **78** [9] 2574 (1995).
5. W.C. Tu, F.F. Lange and A.G. Evans, "Concept for a Damage-Tolerant Ceramic Composite with Strong Interfaces," *J. Am. Ceram. Soc.*, **79**, 417-424 (1996).
6. C.G. Levi, J.Y. Yang, B.J. Dalglish, F.W. Zok and A.G. Evans, "The Processing and Performance of an All-Oxide Ceramic Composite," *J. Am. Ceram. Soc.*, in press.

7. J.J. Brennan, "Interfacial Chemistry and Bonding in Fiber Reinforced Glass-Ceramic Matrix Composites", pp. in Ceramic Microstructures: The Role of Interfaces, J.A. Pask and A.G. Evans, Editors. Plenum Press, New York, 1988.
8. E. Bischoff, M. Rühle, O. Sbaizero and A.G. Evans, "Microstructural Studies of the Interfacial Zone of a SiC-Fiber-Reinforced Lithium Aluminum Silicate Glass-Ceramic," *J. Am. Ceram. Soc.*, **72** [5] 741-45 (1989).
9. K.M. Prewo, B. Johnson and S. Starrett, "Silicon Carbide Fiber Reinforced Glass Ceramic Composite Tensile Behavior at Elevated Temperature," *J. Mater. Sci.*, **24** [4] 1373-79 (1989).
10. M. Huger, D. Fargeot, and C. Gault, "Ultrasonic Characterization of Oxidation Mechanism in Nicalon/C/SiC Composites," *J. Am. Ceram. Soc.*, **77**[10] 2554-60 (1994).
11. L. Filipuzzi, G. Camus, R. Naslain, and J. Thebault, "Oxidation Mechanisms and Kinetics of 1D-SiC/C/SiC Composite Materials I, An Experimental Approach," *J. Am. Ceram. Soc.*, **77**[2] 549-66 (1994).
12. F.E. Heredia, J.C. McNulty, F.W. Zok, and A.G. Evans, "An Oxidation Embrittlement Probe for Ceramic Matrix Composites," *J. Am. Ceram. Soc.*, **78**[8] 2097-100 (1995).
13. K.P. Plucknett, R.L. Cain, and M.H. Lewis, "Interface Degradation in CAS/Nicalon During Elevated Temperature Aging", pp. in Vol. 365 Ceramic Matrix Composites-Advanced High-Temperature Structural Materials, R.A. Lowden, *et al.*, Editors. Materials Research Society, Pittsburgh, 1995.
14. S.R. Nutt, "Environmental Effects on High Temperature Mechanical Behavior of Ceramic Matrix Composites," in *High Temperature Mechanical Behavior of Ceramic Composites*, eds. S.V. Nair and K. Jakus, (Boston, MA, Butterworth-Heinemann, 1995) 365-406.
15. F.E. Heredia, J.C. McNulty, F.W. Zok and A.G. Evans, "Oxidation Embrittlement Probe for Ceramic-Matrix Composites," *J. Am. Ceram. Soc.*, **78** [8] 2097-100 (1995).

16. A.G. Evans, F.W. Zok, R.M. McMeeking and Z.-Z. Du, "Models of High-Temperature Environmentally-Assisted Embrittlement in Ceramic Matrix Composites," *J. Am. Ceram. Soc.*, **79**, 2345-52 (1996).
17. G.N. Morscher, "Tensile Stress-Rupture of SiCf/SiCm Minicomposites with C and BN Interphases at Elevated Temperatures in Air," *J. Am. Ceram. Soc.*, **80** [8] 2029-42 (1997).
18. T.E. Steyer, F.W. Zok and D.P. Walls, "Stress Rupture of an Enhanced Nicalon/SiC Composite at Intermediate Temperatures," *J. Am. Ceram. Soc.*, in press.
19. G.M. Genin and J.W. Hutchinson, "Composite laminates in plane stress: constitutive modeling and stress redistribution due to matrix cracking," *J. Am. Ceram. Soc.*, **80** [5] 1245-55 (1997).
20. J.C. McNulty, F.W. Zok, G.M. Genin and A.G. Evans, "Notch-Sensitivity of Fiber-Reinforced Ceramic Composites: Effects of Inelastic Straining and Volume-Dependent Strength," submitted to *J. Am. Ceram. Soc.*,
21. F.E. Heredia, S.M. Spearing, T.J. Mackin, M.Y. He, A.G. Evans, P. Mosher and P. Bronsted, "Notch Effects in Carbon Matrix Composites," *J. Am. Ceram. Soc.*, **77** [11] 2817-27 (1994).
22. J.M. Whitney and R.J. Nuismer, "Stress fracture criteria for laminated composites containing stress concentrations," *J. Comp. Mat.*, **8**, 252-65 (1974).
23. J. Auerbuch and M.S. Madhukar, "Notched strength of composite laminates: predictions and experiments - A Review," *J. Rein. Plas. and Comp.*, **4**, 3-159 (1985).
24. S.C. Tan, "Effective stress fracture models for unnotched and notched multidirectional laminates," *J. Comp. Mat.*, **22**, 322-40 (1988).
25. H.G. Kim, W. Hwang, and K.S. Han, "Notched strength of woven laminate composites containing circular holes," *Key Engineering Materials*, **51-52**, 125-30 (1990).

26. J-K. Kim, D-S. Kim, and N. Takeda, "Notched strength and fracture criterion in fabric composite plates containing a circular hole," *J. Comp. Mat.*, **29** [7] 982-998 (1995).
27. D.C. Lam, F.F. Lange and A.G. Evans, "Mechanical Properties of Partially Dense Alumina Produced from Powder Compacts," *J. Am. Ceram. Soc.*, **77** (1994) 2113-17.
28. D.J. Green, C. Nader and R. Brezny, "The Elastic Behavior of Partially-Sintered Alumina," pp. 345-56 in *Ceramic Transactions*, vol. 7. Sintering of Advanced Ceramics, Eds. C.A. Handwerker, J.E. Bendell and W.A. Kaysser, American Ceramic Society, Westerville, OH, 1990.
29. J.C. McNulty and F.W. Zok, "Application of weakest-link fracture statistics to fiber-reinforced ceramic matrix composites," *J. Am. Ceram. Soc.*, **80** [6] 1327-32 (1997).
30. C. Lynch and A.G. Evans, "Effects of Off-axis Loading on the Tensile Behavior of a Ceramic-matrix Composite," *J. Am. Ceram. Soc.*, **79** [12] 3113-3123 (1996).
31. M.Y. He and J.W. Hutchinson, "Crack Deflection at an Interface Between Dissimilar Elastic Materials," *Int. J. Solids Struct.*, **25**, 1053-1067 (1989).
32. C.T. Herakovich, Mechanics of Fibrous Composites, John Wiley and Sons, Inc., New York (1998), Chap. 7.
33. D.S. Dugdale, "Yielding of Steel Sheets Containing Slits," *J. Mech. Phys. Solids*, **8**, 100-104 (1960).
34. B.A. Bilby, A.H. Cottrell and K.H. Swinden, "The Spread of Plastic Yield from a Notch," *Proc. Roy. Soc. London*, **A272**, 304-314 (1963).
35. H. Tada, The Stress Analysis of Cracks Handbook, Second Edition, Paris Production Inc., St. Louis, MO (1985).

APPENDIX

The predicted load-deflection response for an edge-notched 3-point flexure specimen subject to small scale yielding was obtained from well-established fracture mechanics solutions. The load, P , required for crack growth at a crack length, a , is [35]

$$P(a) = \frac{2K_c w^2 t}{3s\sqrt{\pi a} F(a/w)} \quad (A1)$$

where w and t are the width and thickness of the specimen, respectively, s is the span between loading points and $F(a/w)$ is

$$F(a/w) = \left\{ \frac{1.99 - a/w(1 - a/w) \left[2.15 - 3.93(a/w) + 2.7(a/w)^2 \right]}{\sqrt{\pi} (1 + 2a/w) (1 - a/w)^{3/2}} \right\} (1.1 - 0.1a/w) \quad (A2)$$

The deflection, $\Delta(a)$, is the sum of the deflection of an uncracked specimen and that due to the crack:

$$\Delta(a) = \frac{Ps^3}{4Ew^3t} + \frac{3Ps^2}{2w^2Et} V_2(a/w) \quad (A3)$$

where E is the elastic modulus (~ 100 GPa for the oxide composite) and $V_2(a/w)$ is

$$V_2(a/w) = \left(\frac{a/w}{1 - a/w} \right)^2 \left\{ 5.58 - 19.57(a/w) + 36.82(a/w)^2 - 34.94(a/w)^3 + 12.77(a/w)^4 \right\} \quad (A4)$$

Table I Summary of Composite Panels

Panel Designation	Fiber volume fraction, f (%)	Composite porosity, p_c (%)	Matrix porosity, p_m (%)
$0^\circ/90^\circ - 1$	41	24.9	42.2
$0^\circ/90^\circ - 2$	42	22.3	38.4
$0^\circ/90^\circ - 3$	38	24.7	39.8
$0^\circ/90^\circ - 4$	39	23.7	38.9
$\pm 45^\circ - 1$	37	24.5	38.9
$\pm 45^\circ - 2$	38	24.6	39.7

FIGURES

- Figure 1 Schematics showing (a) the center-hole, and (b) edge-hole geometries
- Figure 2 Properties in the $0^\circ/90^\circ$ orientation, measured in tension and in flexure.
- Figure 3 Tensile stress-strain behavior in the $\pm 45^\circ$ orientation: (a) panel $\pm 45^\circ - 2$, and (b) panel $\pm 45^\circ - 1$. The strain gauge measurements were obtained from one specimen at various locations along the gauge length.
- Figure 4 Effects of specimen width on the post-localization tensile response in the $\pm 45^\circ$ orientations, as characterized by (a) the stress-displacement behavior and (b) the energy dissipation. For the center-hole specimens, the relevant stress in (a) is the net-section stress, σ_N , and the net-section width is $2w-2a$; for the edge hole specimens, the corresponding quantities are $\sigma_N(1-a/2w)/(1-a/w)$ and $2w-a$.
- Figure 5 Macrophotographs of a fractured $\pm 45^\circ$ tensile specimen, viewed in two orthogonal directions.
- Figure 6 Notch-sensitivity of strength in the center-hole tensile specimens in $0/90^\circ$ orientation.
- Figure 7 Development of local tensile strain immediately ahead of the holes in the $0^\circ/90^\circ$ orientation. The two curves correspond to gauges located at opposite locations within the same specimen.
- Figure 8 Distributions of (a) the normal axial stress and (b) the effective plastic strain in the center-hole specimens.
- Figure 9 Macrophotograph of a fractured $0^\circ/90^\circ$ specimen.
- Figure 10 Stress-displacement response of an edge-notched flexure specimen ($a = 6$ mm, $w = 12$ mm). The dotted line is the predicted response for a material subject to small scale yielding. The horizontal dashed line is the predicted strength based on the shear band model and the point stress failure criterion.

- Figure 11 Distribution of normal stress in the edge-notched flexure specimen along plane of minimum cross-section (net width, $w - a = 6$ mm).
- Figure 12 Notch-sensitivity of strength in $\pm 45^\circ$ orientation.
- Figure 13 Development of local strain at hole edge in the center-hole specimens in the $\pm 45^\circ$ orientation. Arrows indicate strains at the stress maxima.
- Figure 14 Macrophotographs of $\pm 45^\circ$ specimens, with (a) a center-hole, and (b) edge-holes.
- Figure 15 Schematic of an anisotropic metal bicrystal, oriented for slip parallel to the two Burgers vectors \bar{b}_1 and \bar{b}_2 .

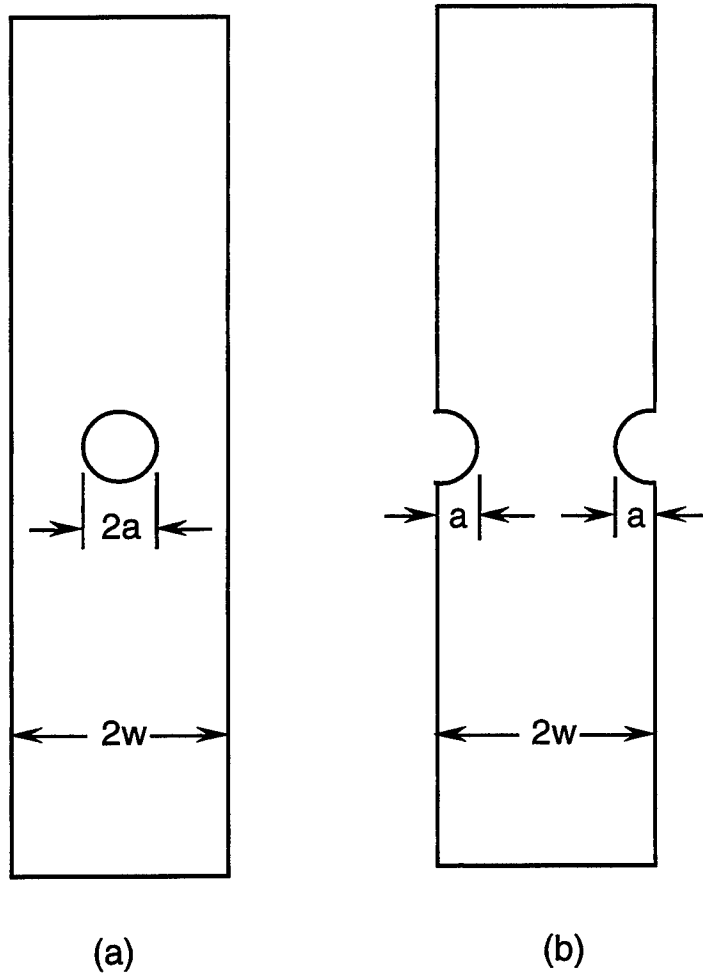


Figure 1. Schematics showing (a) the center-hole and (b) the edge-hole geometries.

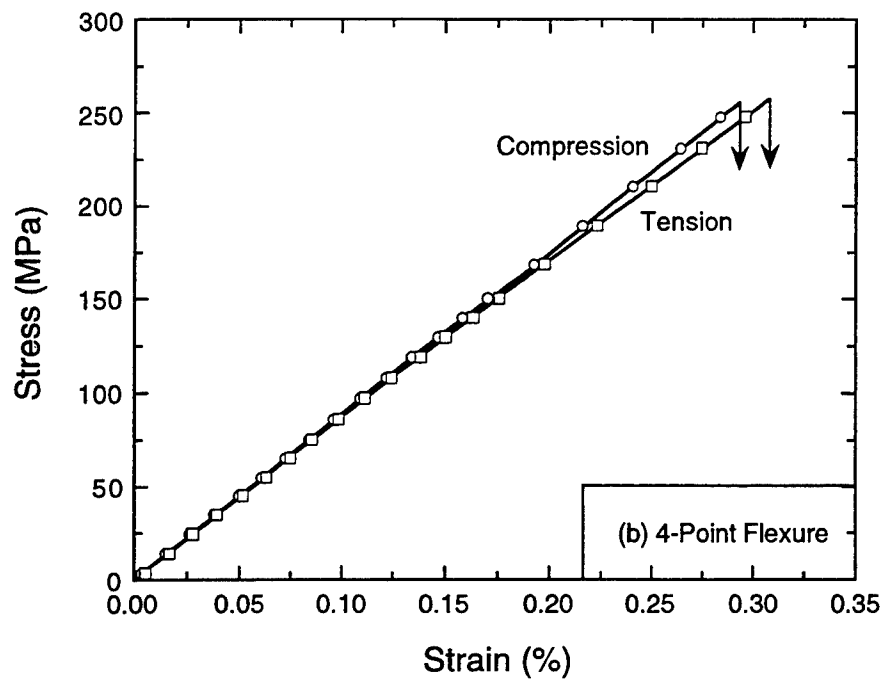
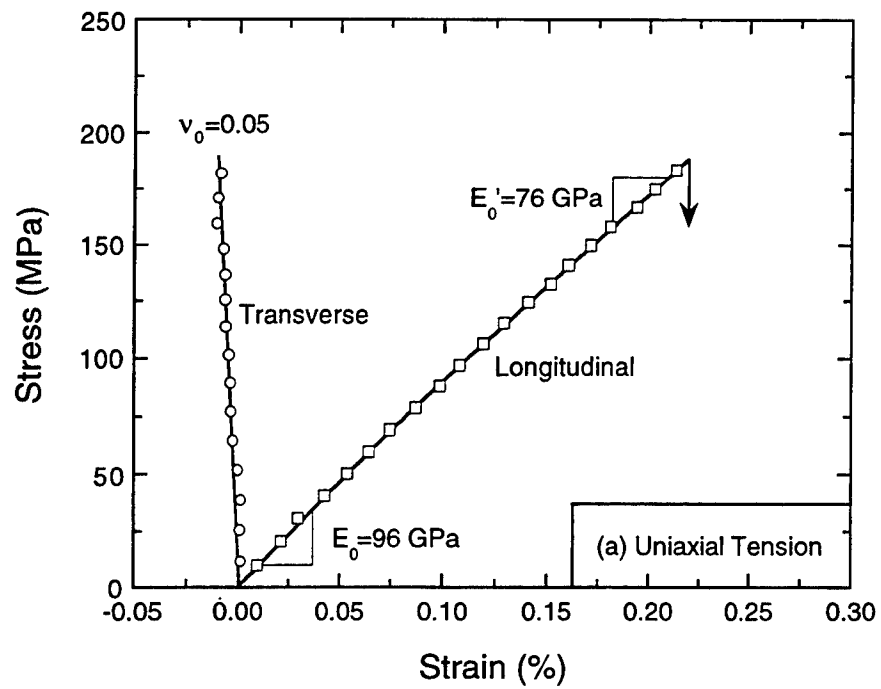


Figure 2. Properties in the $0^\circ/90^\circ$ orientation, measured in tension and in flexure.

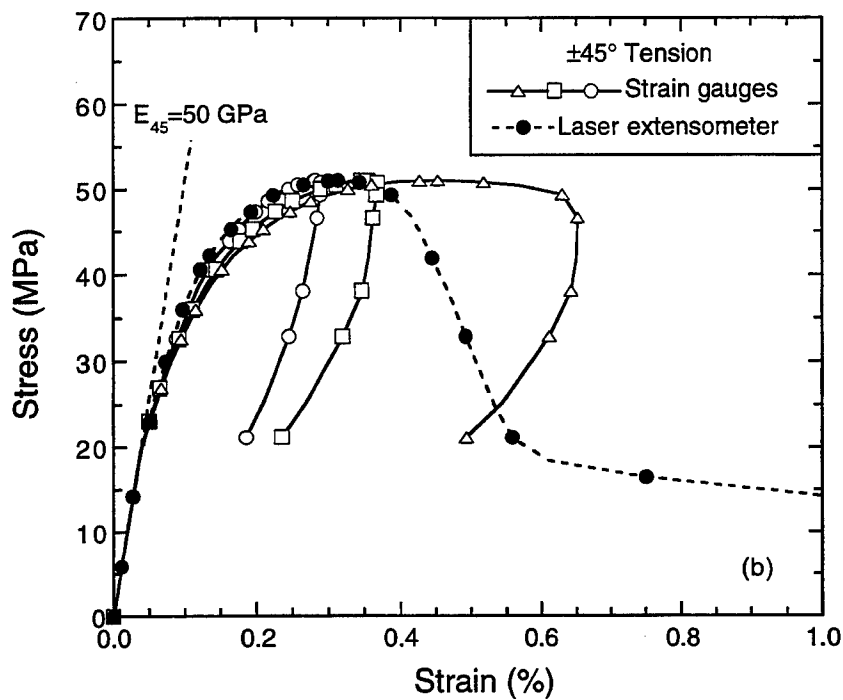
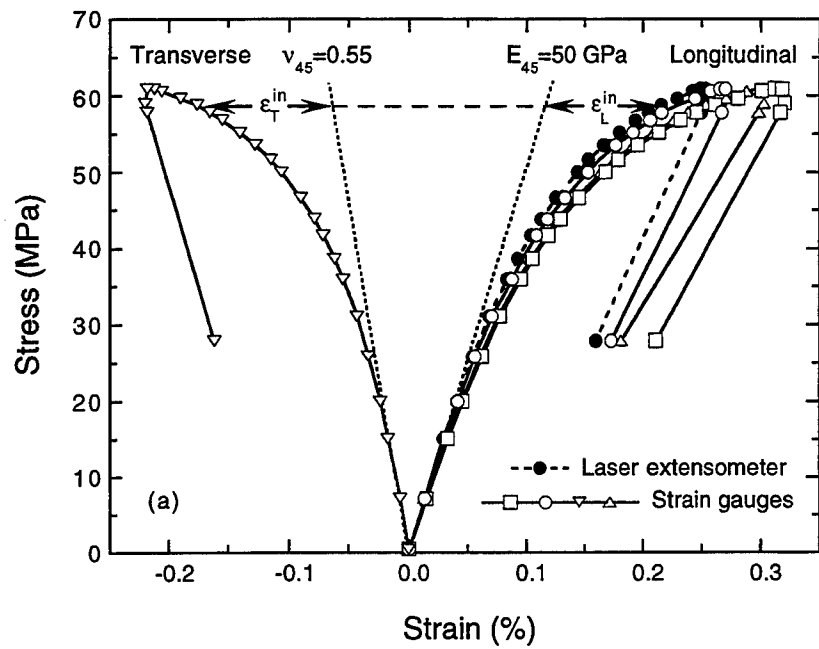


Figure 3. Tensile stress-strain behavior in the $\pm 45^\circ$ orientation: (a) panel $\pm 45^\circ$ -2, and (b) panel $\pm 45^\circ$ -1. The strain gauge measurements were obtained from one specimen at various locations along the gauge length.

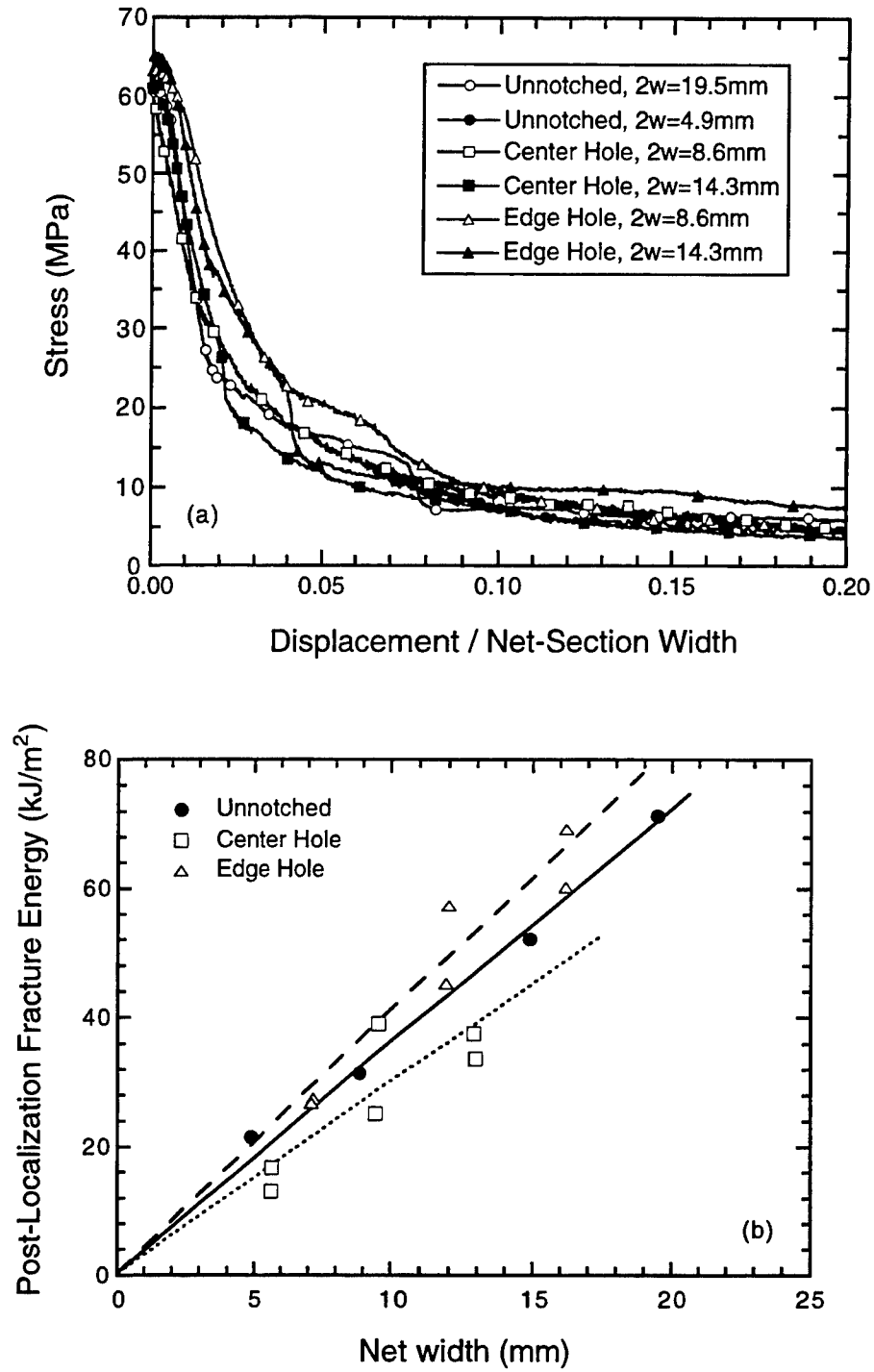


Figure 4. Effects of specimen width on the post-localization tensile response in the $\pm 45^\circ$ orientations, as characterized by (a) the stress-displacement behavior and (b) the energy dissipation. For the center-hole specimens, the relevant stress in (a) is the net-section stress, σ_N , and the net-section width is $2w-2a$; for the edge hole specimens, the corresponding quantities are $\sigma_N (1-a/2w) / (1-a/w)$ and $2w-a$.

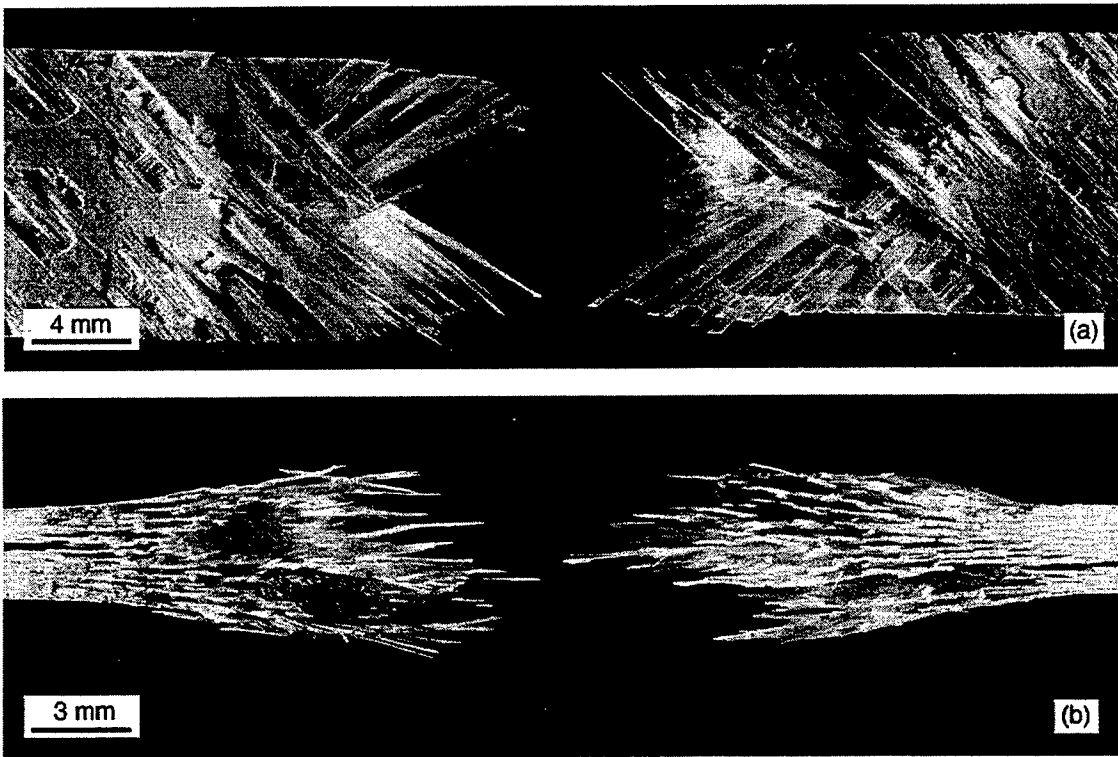


Figure 5. Macrophotographs of a fractured $\pm 45^\circ$ tensile specimen, viewed in two orthogonal directions.

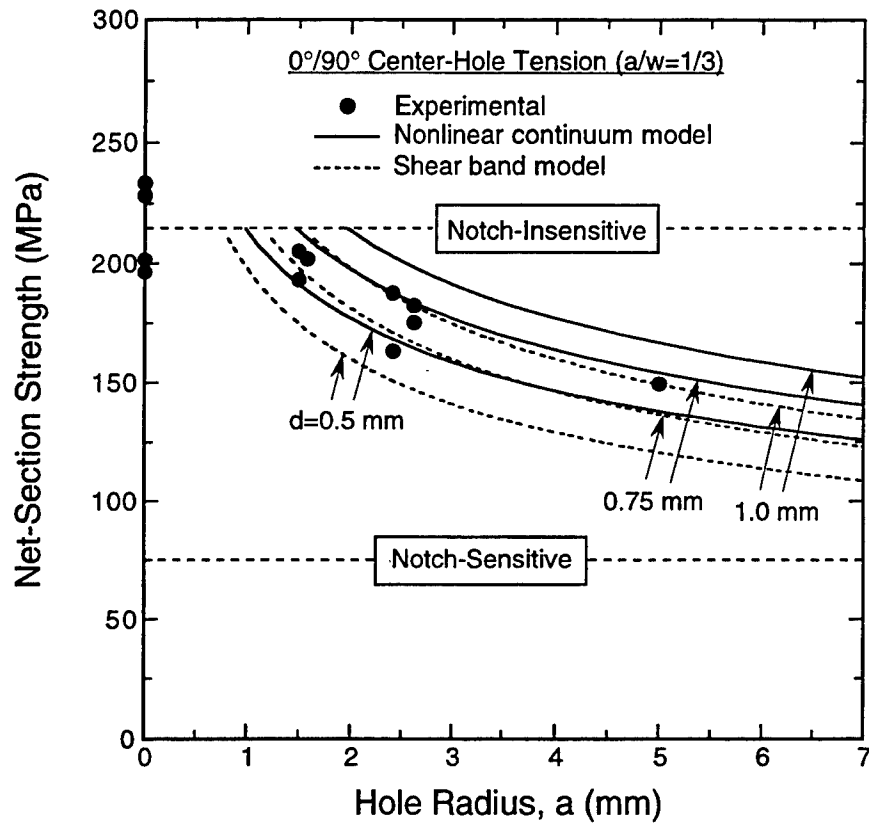


Figure 6. Notch sensitivity of strength in the center-hole tensile specimens.

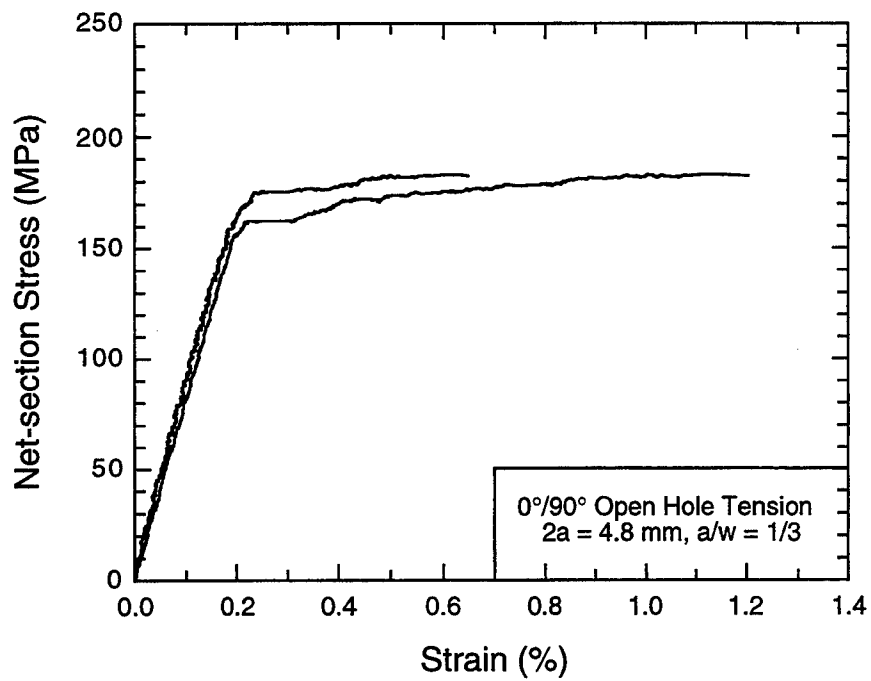


Figure 7. Development of local tensile strain immediately ahead of the holes in the 0°/90° orientation. The two curves correspond to gauges located at opposite hole edges within the same specimen.

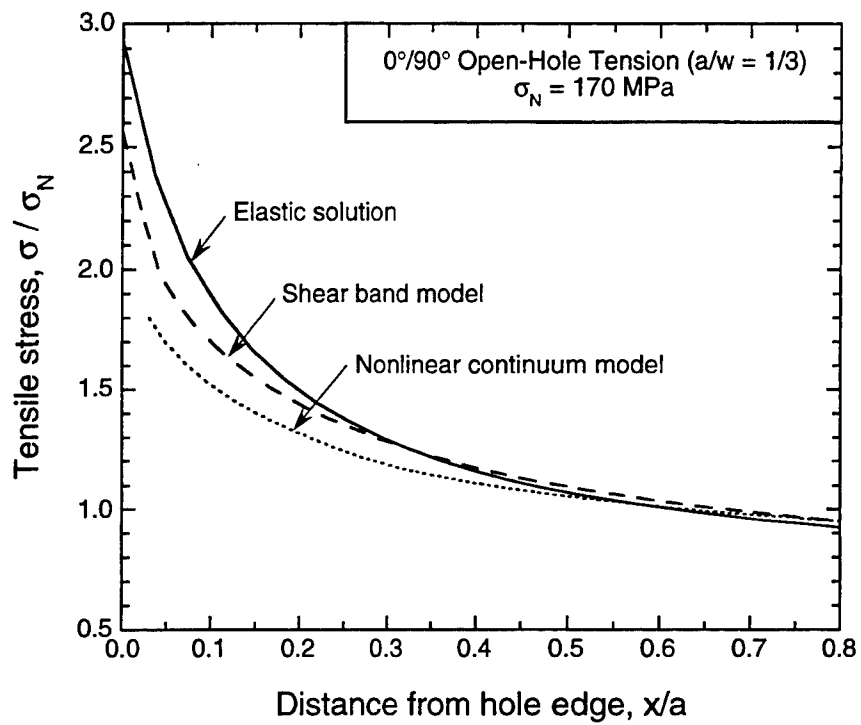


Fig. 8(a)

Figure 8. Distributions of (a) the normal axial stress, and (b) the effective plastic strain in the center-hole specimens.

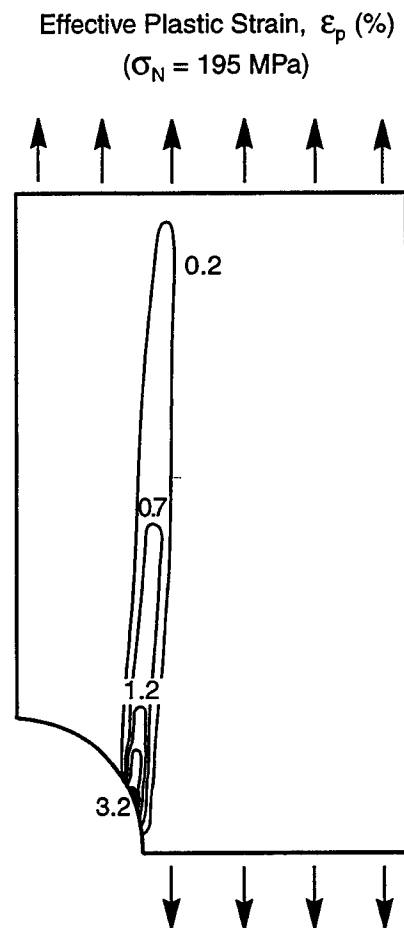


Fig. 8(b)

Figure 8. Distributions of (a) the normal axial stress, and (b) the effective plastic strain in the center-hole specimens.

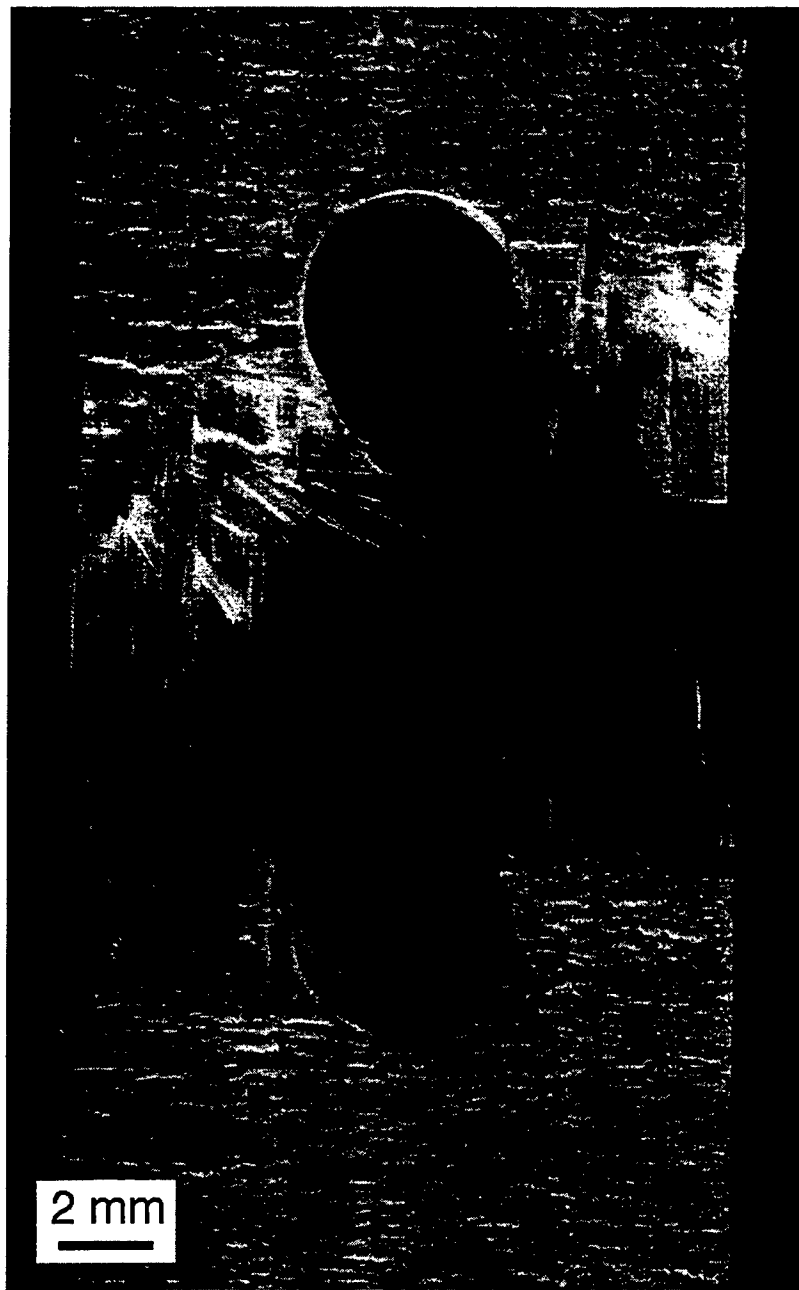


Figure 9. Macro photograph of a fractured $0^{\circ}/90^{\circ}$ specimen.

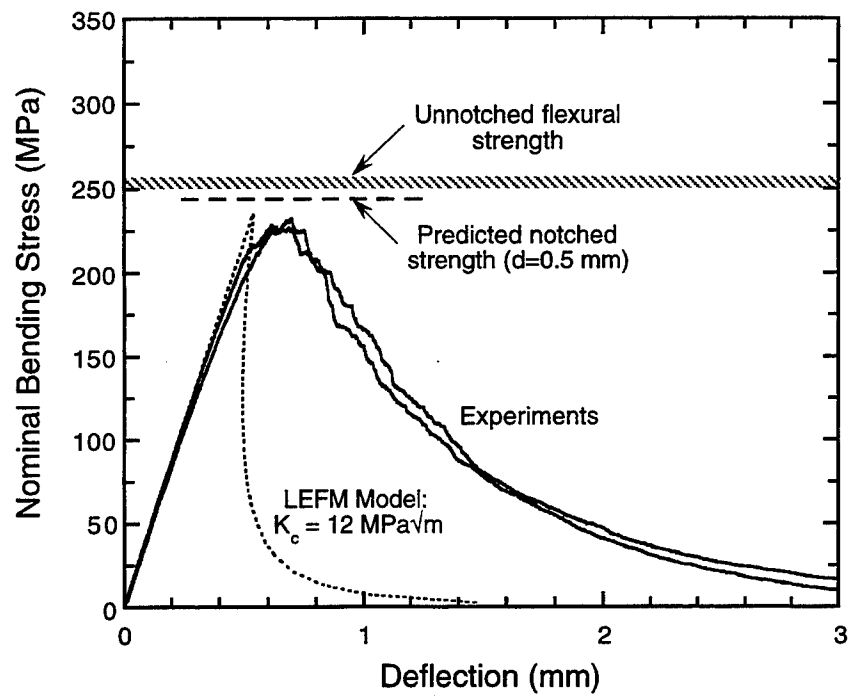


Figure 10. Stress-displacement response of an edge-notched flexure specimen ($a=6 \text{ mm}$, $w=12 \text{ mm}$). The dotted line is the predicted response for a material subject to small scale yielding. The horizontal dashed line is the predicted strength based on the shear band model and the point stress failure criterion.

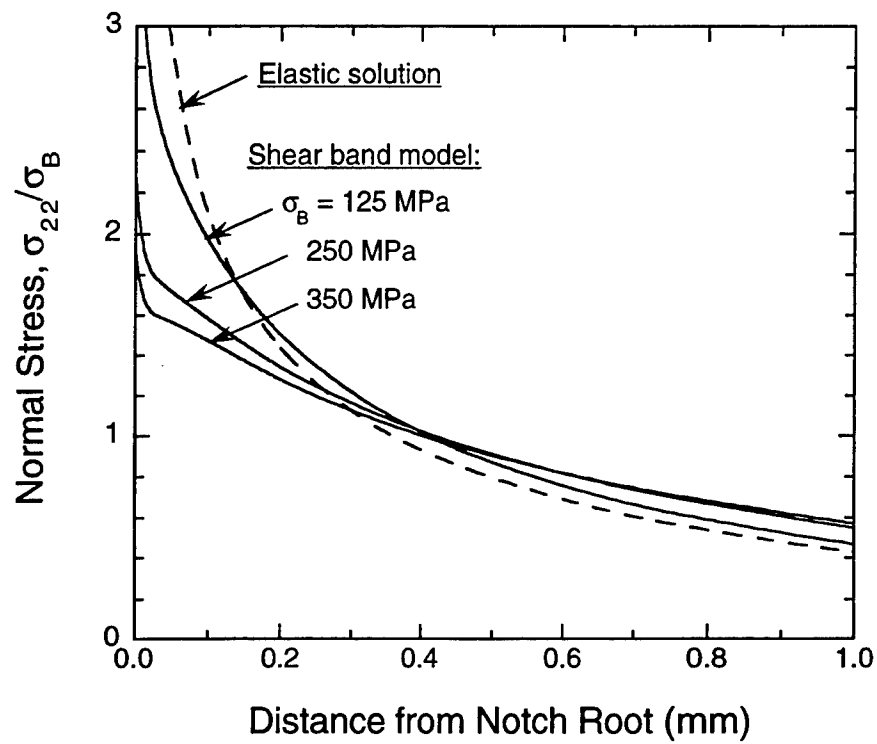


Figure 11. Distributions of normal stress in the edge-notched flexure specimen along the plane of minimum cross-section (net width, $w-a = 6$ mm).

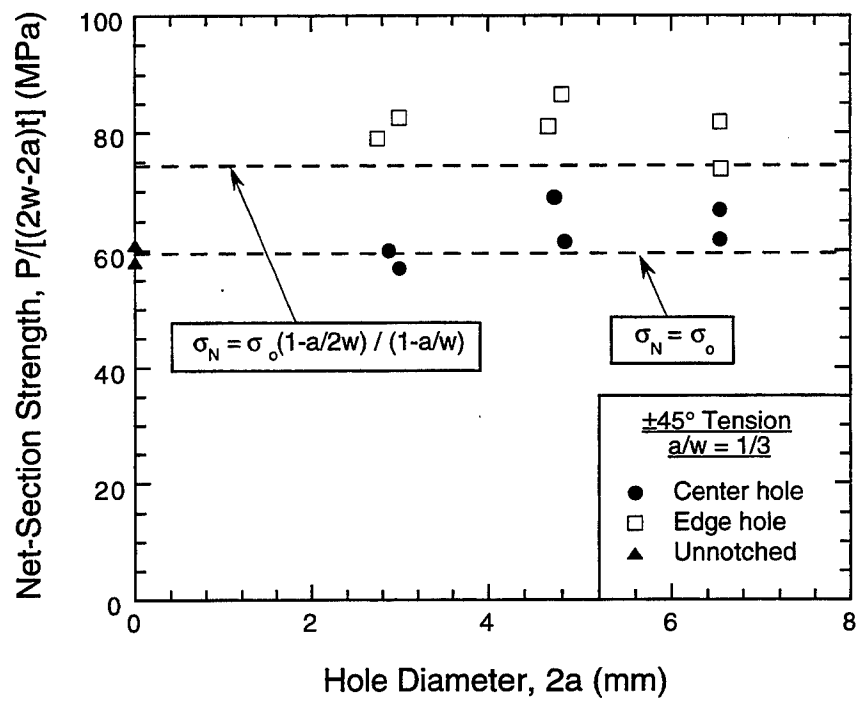


Figure 12. Notch-sensitivity of strength in the $\pm 45^\circ$ orientation.

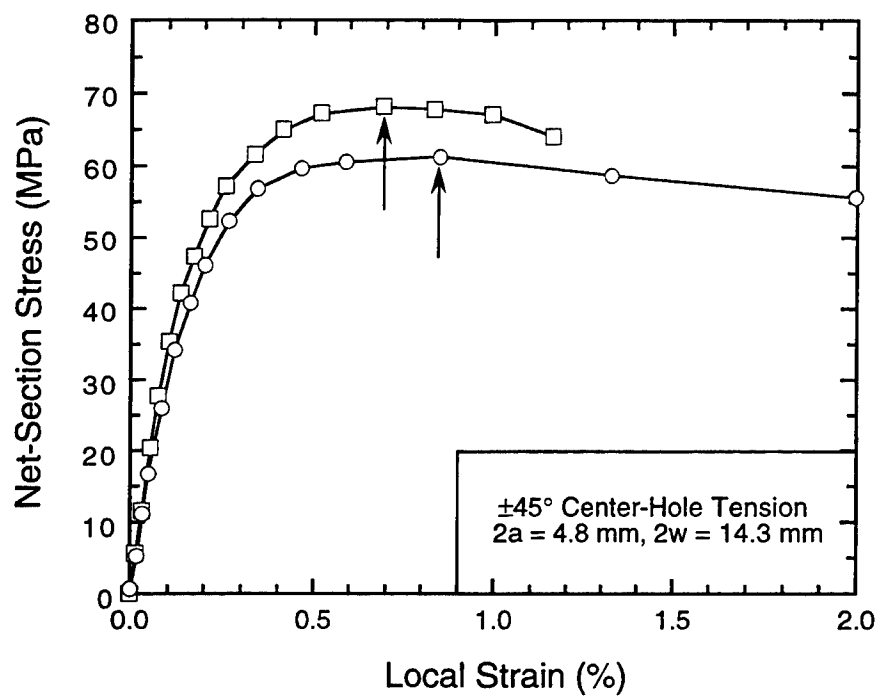


Figure 13. Development of local strain at hole edge in the center-hole specimens in the $\pm 45^\circ$ orientation. Arrows indicate strains at stress maxima.

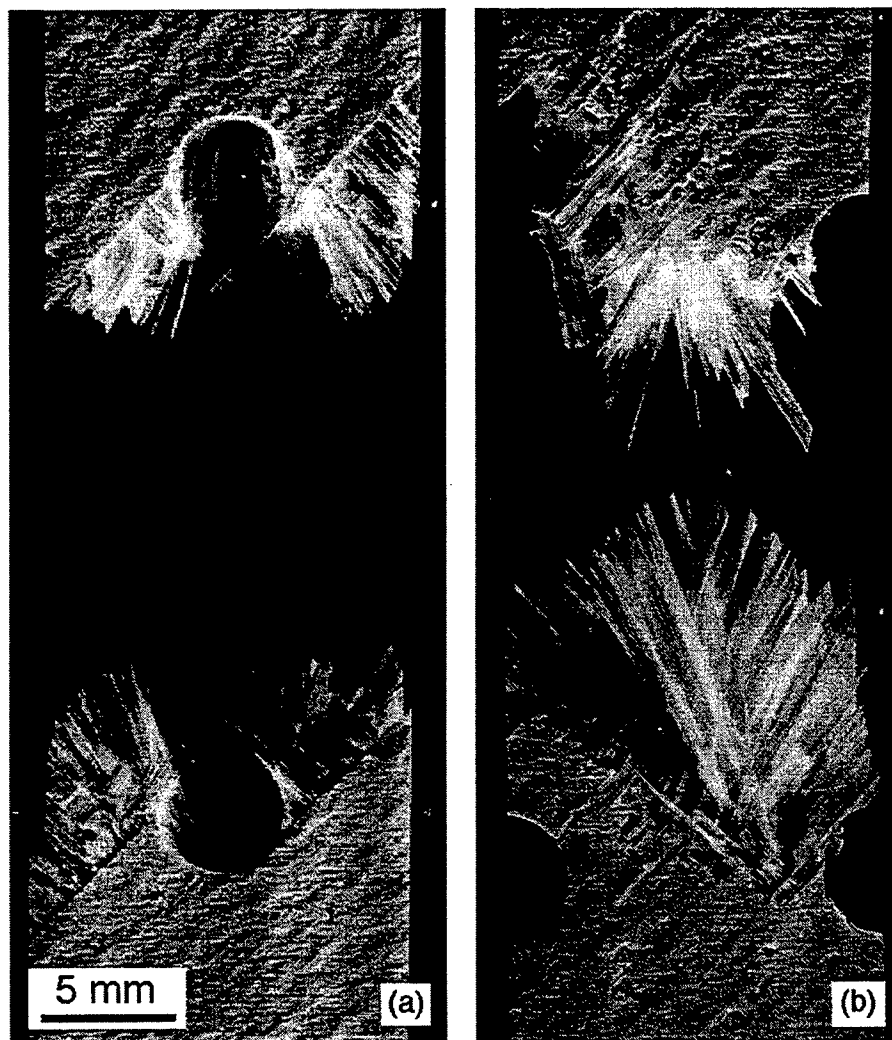


Figure 14. Macrophotographs of $\pm 45^\circ$ specimens with (a) a center-hole, and (b) edge-holes.

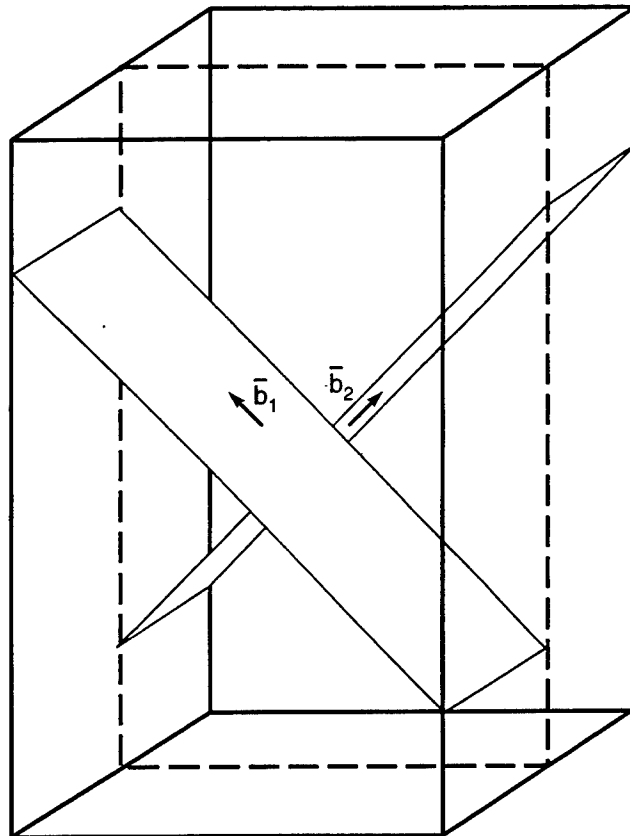


Figure 15. Schematic of a metal bicrystal, with the front and back crystals oriented for slip parallel to the Burgers vectors \vec{b}_1 and \vec{b}_2 , respectively.



*The Processing and Performance of
an All-Oxide Ceramic Composite*

C.G. Levi, J.Y. Yang, B.J. Dalgleish, F.W. Zok, and A.G. Evans*

High Performance Composites Center
Departments of Materials and Mechanical Engineering
University of California, Santa Barbara, CA, 93106-5050

* also with the Division of Applied Sciences
Harvard University, Cambridge, MA, 02138

MATERIALS



*Journal of the
American Ceramics Society*
(in press, 1997)



The Processing and Performance of an All-Oxide Ceramic Composite*

C.G. Levi, J.Y. Yang, B.J. Dalgleish, F.W. Zok, and A.G. Evans[§]

High Performance Composites Center
Departments of Materials and Mechanical Engineering
University of California, Santa Barbara, CA, 93106-5050

ABSTRACT

Continuous fiber ceramic composites (CFCCs) based on oxides are of interest for high temperature applications owing to their inherent oxidative stability. An enabling element is a matrix with an optimum combination of toughness and strength which may be achieved by incorporating a controlled amount of fine, well distributed porosity. Implementation of this concept by vacuum infiltration of aqueous mullite-alumina slurries into 2-D woven preforms of alumina fibers has been investigated. Evaluation of these materials shows stress-strain characteristics similar to other CFCCs, especially C-matrix composites. Moreover, promising notch and creep properties have been found. Microstructural and processing issues relevant to the attainment of these behaviors are discussed.

* Sponsored by the Defense Advanced Research Projects Agency under University Research Initiative Grant N00014-92-J-1808, supervised by Dr. W. Coblenz and monitored by Dr. S.G. Fishman of the Office of Naval Research.

§ A.G. Evans is also with the Division of Applied Sciences at Harvard University.

1. INTRODUCTION

Continuous fiber ceramic composites (CFCCs) with suitably tailored interfaces can exhibit inelastic deformation characteristics which enable them to retain strength in the presence of holes and notches.¹ It also renders them amenable to design and life prediction strategies developed for metals. This damage tolerance, coupled with their inherent refractoriness, has enabled CFCCs to emerge as candidates for many high temperature thermostructural applications.² Of particular interest is their use for combustors,³ wherein the ability to operate at high temperatures with reduced need for cooling air can yield substantial benefits in efficiency and also provide control of deleterious emissions, such as NO_x.⁴

Most CFCC systems are based on SiC fibers with either oxide or non-oxide matrices, and interphases consisting of various combinations of C, BN and SiC. The latter are tailored to enable interfacial debonding and crack bridging to occur upon matrix cracking, accompanied by internal friction.^{1,5} However, these systems are susceptible to embrittlement by oxygen ingress through the matrix cracks, followed by reaction with the interphase and the fibers.⁶⁻⁹ The kinetics are particularly debilitating at intermediate temperatures (500-900°C) and upon cyclic loading.^{7,9} The embrittlement problem imposes major design limitations by requiring that the stresses remain below the matrix cracking stress. This deficiency has motivated the search for CFCCs based on environmentally-stable oxide constituents.¹⁰⁻¹⁸

Development of all-oxide composites has followed two distinct microstructural design paths. One is based on the weak interface concept, typical of most CFCCs. It uses either fugitive layers¹² or stable oxide interphases with suitably low fracture toughness.¹⁷ The second implicitly accepts the formation of strong interfaces. It builds on the experience with porous interlayers as crack deflection paths^{19,20} and extends the concept to utilize a porous matrix as a surrogate. The

concept has been successfully demonstrated,^{11,14,18} but only limited information is available in the open literature. The design and stability of the matrix microstructure are arguably more critical in the latter approach than with more conventional weak-interface materials. The present investigation was undertaken to explore a concept for a stable, porous oxide matrix as well as the mechanical performance of the resulting composites.

The information is organized in the following manner. The underlying microstructural design concept for the matrix is elaborated, followed by an identification of the materials to be used. Subsequently, key elements of the processing science and technology are addressed. These include a specification of the manufacturing sequence, a sintering study that guides the choice of materials to be used for the matrix, as well as a characterization of the composite microstructure. Thereafter, several essential thermomechanical properties are measured and analyzed. Initially, the capacity of the composite to exhibit inelastic deformation is determined in the $0^\circ/90^\circ$ and $\pm 45^\circ$ orientations. Such results reveal that these composites exhibit damage tolerance comparable with other "fiber-dominated" CFCCs. Moreover, the effects of thermal exposure on the $0^\circ/90^\circ$ tensile properties are determined in order to characterize fiber degradation effects that might arise either during manufacture or in service. Finally, some preliminary results are obtained concerning the interlaminar shear properties as well as the in-plane creep strength and notch performance, which relate to design and lifing issues.

The general conclusion reached is that these materials have mechanical characteristics *comparable with those established for C-matrix materials* (such as SiC/C and C/C), with attendant implications for thermostructural performance. The key differences with the C-matrix materials concern their superior oxidative stability and their differing creep response.

2. MICROSTRUCTURAL DESIGN

The microstructure must be designed to have a sufficiently low toughness to enable crack deflection through the matrix while maintaining enough strength for adequate off-axis and interlaminar properties.¹⁸ These seemingly contradictory requirements are achievable by incorporating a controlled amount of fine, uniformly distributed porosity.^{18,21} Acceptable matrix performance dictates a stable and well bonded particle network with substantial void space, of order ~30%, on a scale comparable with the interparticle spacing. Fine matrix particles would be preferred to enhance packing density and uniformity within the fiber preform, as well as the nominal strength of the matrix. However, fine particles also reduce the stability of the matrix against densification during processing and service, promoting the evolution of undesirable flaws under the constraint imposed by the fibers.^{22, 23}

Mullite emerges as an attractive matrix material owing to its excellent creep resistance, low modulus and, as noted below, generally sluggish sintering kinetics below ~1300°C. The latter suggests adequate microstructural stability for applications in the gas turbine engine, where initial target wall temperatures are in the range ~1000 to ~1200°C. However, it presents a challenge in processing. That is, temperatures above ~1300°C would be required to achieve the requisite bonding between the matrix particles, yet most commercial oxide fibers are susceptible to microstructural degradation at these temperatures.^{16,24} Ideally, neck formation with minimal shrinkage should be promoted by operating in regimes dominated by surface and vapor transport mechanisms.²⁵ However, this approach has not provided the requisite strengths. Liquid precursor impregnation and pyrolysis provides another avenue to build the interparticle necks, but the initial matrix must have sufficient strength to withstand handling.¹⁴

The proposed matrix design concept is depicted in Figure 1. Relatively large ($\sim 1\ \mu\text{m}$) mullite particles are packed between and within tows to form a touching, non-shrinking network. Alumina particles that fit within the void spaces of this network ($\sim 200\ \text{nm}$) are added in a proportion limited primarily by the requisite levels of porosity. Since sub-micron alumina sinters readily above 800°C ,²² the fine particles form bridges between the larger mullite particles, as well as between the mullite particles and the fibers, at processing temperatures which minimize fiber degradation. Interparticle voids may locally open owing to the sintering, but the overall matrix is constrained from shrinking by the rigid mullite network. The matrix is further strengthened by adding material to the alumina "bridges" using precursor impregnation and pyrolysis, as discussed below.

3. IMPLEMENTATION

3.1 Materials

Reinforcements used in this investigation were Nextel 610TM and 720TM (a) fibers woven in 8-harness satin fabric (float length 6.5 mm). The tows in the fabric contain ~ 400 filaments with diameters of 10-12 μm . The tow denier is 1500 and the yield is 6000 m/kg. The aspect ratio of the tow cross section is ~ 10 . N610 fibers are essentially pure ($>99\%$) polycrystalline $\alpha\text{-Al}_2\text{O}_3$,^{26,27} whereas N720 consist of a mixture of fine grained mullite and alumina which exhibits improved creep strength and stability against coarsening relative to the N610 fiber.²⁸

The pristine, unwoven N610 and N720 fibers are reported to have mean filament strengths of ~ 3 and $\sim 2.1\ \text{GPa}$, respectively, for a 25 mm gauge length, with a similar Weibull shape parameter, $m \approx 10$.^{27,28} Since the difference in strengths is accompanied by a similar difference in Young's modulus, (380 and 260 GPa for N610

^a Nextel 610TM and Nextel 720TM are trademarks of the 3M Corporation, Minneapolis, MN. For simplicity they will be abbreviated hereafter as N610 and N720.

and N720, respectively,^{27,28}) the anticipated *mean* failure strain, ϵ_f , for pristine fibers is $\sim 0.8\%$ in both cases. However, some degradation may be expected to take place upon weaving. Such effects have been probed by performing fiber bundle tests on tows extracted from the as-received fabric,²⁹ using a recently developed piezo-spectroscopic technique to monitor the fiber stresses.²⁴ For the N610 fibers, these measurements yielded a dry bundle strength, $\sigma_b \approx 2.6$ GPa, and a corresponding failure strain of $\sim 0.7\%$.²⁹ The measured bundle strength is essentially identical to the value calculated on the basis of the monofilament data ($2.3 \leq \sigma_b \leq 2.7$ GPa), indicating negligible degradation in fiber strength upon weaving. In contrast, similar measurements on the N720 fibers revealed significant degradation. Notably, the strength and failure strain of the extracted tows are ~ 0.9 GPa and $\sim 0.3\%$,²⁹ respectively; approximately half of the calculated values for the pristine (unwoven) fibers (~ 1.6 GPa and $\sim 0.7\%$). The properties obtained on the *extracted* tows are thus the appropriate baseline on which the properties of the CFCCs must be assessed and the degradation effects associated with composite processing identified. Indeed, degradation effects associated with high temperature exposure have been reported for earlier generations of the N610 fibers, with dry bundle strengths diminishing from ~ 1.6 GPa to ~ 1.1 GPa after 4 h at 1200°C , and to 0.97 GPa after 1 h at 1300°C , and the accompanying failure strains dropping to $\sim 0.3\%$. Because of this susceptibility to strength degradation and the lower creep strength of the N610 fiber, studies on the elevated temperature properties have focused primarily on N720.

The mullite powder selected is MU-107 (Showa Denko K. K.), with mean particle size of ~ 1 μm and BET surface area of 7.5 m^2/g . The chemical analysis shows 75.5% Al_2O_3 and 24% SiO_2 (by weight), with only trace amounts of TiO_2 , Fe_2O_3 and Na_2O . The particle size distribution ranges from <0.5 μm to >2.5 μm , which is rather broad from a microstructural design perspective (Figure 1), but offers advantages towards attainment of reasonable packing densities. The alumina powder is

AKP-50 (Sumitomo Chemical) with a mean particle size of $\sim 0.2 \mu\text{m}$ ($0.1\text{--}0.3 \mu\text{m}$) and BET surface area of $10.6 \text{ m}^2/\text{g}$. Its chemistry is essentially pure (99.995%) $\alpha\text{-Al}_2\text{O}_3$. The precursor used to strengthen the matrix is a solution of aluminum hydroxyl-chloride, $\text{Al}_2\text{Cl}(\text{OH})_5$, which yields 8.2% of Al_2O_3 by weight.

3.2 *Manufacturing Process*

The geometry of interest is a flat panel, $200 \times 125 \times 3 \text{ mm}$, with a 2-D laminate architecture. The reinforcement content, f , was $\sim 36 \pm 4 \text{ vol.}\%$, comparable to that of other fabric CFCCs. The fabric was arranged in two different orientations: one with the fibers parallel to the panel edges (designated $0^\circ/90^\circ$) and the other rotated by $\pm 45^\circ$. The processing route is summarized in the flowchart of Figure 2. A matrix slurry containing $\sim 30\%$ solids is prepared by mixing the mullite and alumina powders in the desired proportions into deionized water, using HNO_3 to adjust the pH to ~ 3 . The latter allows repulsive interactions to develop between the oxide particles, providing the appropriate rheology to facilitate their flow into the fiber preform and their subsequent packing.³⁰ Dispersion of soft agglomerates is promoted by a combination of mechanical and ultrasonic agitation.

The cloth is cut into $200 \text{ mm} \times 125 \text{ mm}$ pieces having the desired orientation ($0^\circ/90^\circ$ or $\pm 45^\circ$). The pieces are stacked in a loose preform and de-sized by heating to 550°C for 0.5 h. The fiber content of the cloth is $9.3 \text{ mm}^3/\text{cm}^2$ and thus a 3 mm plate with a fiber volume fraction of $\sim 36\%$ requires ~ 12 layers. After de-sizing, the fiber preform is placed between two perforated stainless steel plates which act to constrain the cloth within the desired thickness during the filtration process. The assembly is then placed in the middle of a chamber with capabilities for evacuation through both top and bottom. An amount of slurry calculated to fill the preform is poured on top, whereupon the chamber is closed and evacuated from both top and bottom to eliminate air bubbles trapped within the preform. The top portion of the chamber

is then open to the atmosphere while vacuum is maintained in the bottom to drive the filtration process. Full infiltration is typically accomplished in a few hours, depending on the fiber packing and the rheology of the slurry.

After consolidation, the panels, still within the stainless steel frame, are removed from the filtration chamber and dried over a period of approximately 48 h, with the last 4 in an oven at 120°C. Once dry, the green panels are separated from the metallic frame and given an initial sintering treatment at 900°C for 2 h to promote the development of alumina bridges between the mullite particle network. The composites are subsequently impregnated with the alumina precursor solution under vacuum, dried in open air under an infrared lamp, and heated to 900°C for 2 h to pyrolyze the precursor. The materials discussed in this paper were impregnated four times. Following the last cycle, the panels are given a final sintering treatment, typically 2 h at 1200°C, which also serves to stabilize the precursor-derived alumina to the corundum (α) structure. The implications of this final step with regard to potential fiber degradation are discussed in Sections 4 and 5.

3.3 *Matrix Sintering*

Studies of the effect of alumina additions on the sintering of mullite were used to select a suitable matrix composition. Samples of unreinforced matrix, 90 x 32 x 4 mm were consolidated by vacuum filtration from slurries similar to those used to fabricate the composites. Nominally pure alumina and mullite compacts were prepared, as well as mixtures containing 10, 20, 30 and 50% Al_2O_3 by (solid) volume. The samples were first dried in ambient air for 24 h and then slowly heated to 120°C and held at this temperature overnight. Once dried, each specimen was given a 24 h treatment at 550°C and then sequential treatments at 900-1400°C in 100°C intervals. For each step the samples were heated at $\sim 3^\circ\text{C}/\text{min}$ up to the desired temperature, held for 2 h and then cooled down at $\sim 5^\circ\text{C}/\text{min}$. (The slow tem-

perature ramping was aimed at minimizing the risk of cracking or chipping which would impair the accuracy of the measurements. Examination of these samples detected no microcracking at any stage.) The packing densities were measured after each step following the ASTM C20-92 standard, as were the external dimensions of the specimens.

The results are summarized in Figure 3. The differing behaviors of the pure alumina and pure mullite compacts lend support to the proposed microstructural design concept. The porosities for the as-consolidated (wet) compacts were estimated from the packing densities after drying at 120°C and the corresponding change in volume during drying. The packing decreases slightly for alumina contents $\geq 50\%$, associated with the narrower distribution of particle sizes in the finer alumina powder. For each composition, the change in porosity relative to the as-consolidated condition is reflected in the shrinkage. All specimens experience a $\sim 1.7 \pm 0.2\%$ linear contraction upon drying, reflected as a $\sim 3\%$ change in the apparent porosity. Specimens with $< 50\% \text{ Al}_2\text{O}_3$ undergo little additional change during sintering at temperatures up to 1200°C. Since the processing temperatures are of this order, there should be no substantial impact of the Al_2O_3 content on the evolution of porosity (microstructure stability) within the mullite-rich range. However, the 1400°C data may be more relevant to the long term properties. These data suggest that the shrinkage increases more rapidly for compositions above $\sim 20\% \text{ Al}_2\text{O}_3$. (This may be related to the evolution of percolation paths between the alumina particles.) Consequently, the initial composites were based on a 20% alumina matrix.

It is noteworthy that all mullite-rich mixtures maintain porosity levels above $\sim 30\%$, even after heating to 1400°C, with attendant implications for the long term crack deflection capabilities of the matrix under service conditions. The porosity content is likely to decrease after precursor impregnation and pyrolysis,³¹ but the

initial matrix packing densities are also expected to be lower in the composites owing to the presence of the fibers.³²

3.4 *Composite Microstructure*

Views of the composite microstructure at different scales, Figure 4, reveal that the tows are well infiltrated and there are only occasional instances of large scale voids which arise from air bubbles or pockets of unconsolidated slurry trapped by the filtration front. The large particles within the matrix are mullite, and the finer particles a mixture of alumina and mullite (Figure 4a). It is also evident upon analysis of the fracture surfaces that the matrix is bonded to the fibers, presumably through the same alumina "bridges" and/or precursor "necks" present within the mullite network (see Section 4).

Examination at lower magnifications reveals the presence of crack-like shrinkage flaws within the matrix, especially in regions devoid of fibers (Figure 4d). The flaws are typically perpendicular to the fibers and tend to form 2-D arrays on planes parallel to the fiber cloth. The results in Figure 3 suggest that the flaws evolve primarily upon matrix shrinkage during drying. The phenomenon is induced by the bi-axial constraint imposed by the reinforcements, and enhanced by the presence of rather large unreinforced matrix regions owing to the limitations to fiber packing when using woven cloth. (Such cracking did not occur in unidirectional composites.^{14,18}) Because of the relatively large openings of these drying cracks, they cannot not be "healed" by the subsequent precursor impregnation and pyrolysis.

One avenue to alleviate the formation of shrinkage flaws is to reduce the scale of the unreinforced matrix regions by filling the larger spaces in the preform with short fibers. This idea was explored by coating the cloth with a paste of chopped Al_2O_3 fiber with an average aspect ratio of ~ 10 . The paste fills the cross-

over regions, as depicted in Figures 5(a,b), and attaches randomly aligned short fibers to the cloth surface. Layers of such cloth are assembled into a preform and processed in the same manner. The results in Figures 5(c,d) show that the flaws have been largely suppressed. This approach, however, further decreases the packing efficiency and limits the volume fraction of continuous reinforcement to ~25%, which is substantially below the levels typical of current CFCC composites ($\geq 35\%$). Efforts to find suitable ways to minimize flaws without sacrificing the volume fraction of reinforcement are continuing.

4. TENSILE BEHAVIOR AT ROOM TEMPERATURE

Stress-strain curves for both materials have been measured in tension in the $0^\circ/90^\circ$ and $\pm 45^\circ$ orientations, as needed for implementation in numerical design codes. The test procedures have been described elsewhere.³³ Periodic unload/reload measurements have been used to assess the incidence of damage evolution (from modulus changes), as well as the occurrence of internal friction (from hysteresis strains).^{34,35} The results are reminiscent of those found for “fiber dominated” C-matrix composites, such as C/C and SiC/C.^{5,33,36-39}

In the $0/90^\circ$ orientation the tensile response is essentially linear with only small inelastic strains, Figure 6(a), similar to that observed in SiC/C systems,^{5,39} Figure 6(b). The behavior is quite reproducible, with stress-strain curves for a given volume fraction and set of processing conditions falling within a relatively narrow band. The initial moduli (~100 and ~60 GPa for the N610 and N720 composites, respectively) are consistently larger than those expected from the axial fibers alone ($E_f/2 \approx 75$ and ~50 GPa, respectively), reflecting a contribution from the matrix and the transverse reinforcements. The average failure strain for 14 specimens from five different panels of N610 composite (33-39% fiber) sintered at 1200°C was 0.27%. These failure strains are smaller than those expected for pristine tows of comparable

gauge length, even after weaving, but are consistent with the values reported for N610 fibers subjected to thermal cycles similar to those used in composite processing.²⁴ The failure strains of the N720 composites were also of the above order, but these strains are much closer to the values measured in tows extracted from the woven fabric²⁹ (Section 3.1). These observations are in agreement with the superior stability of the N720 fiber. They also suggest that the composite manufacturing process does not cause significant degradation of the reinforcement beyond that expected from thermal exposure of the pristine fibers. Notwithstanding the higher stability of the N720 fiber, composites of the latter had significantly lower strengths at ambient temperature than those made with N610 fibers (~140 MPa vs. >200 MPa, respectively), reflecting the initially lower strength of the N720 fiber and indicating that strength retention in the N610 fiber is still adequate after processing. Further work is clearly needed to understand and quantify the effects of processing on fiber degradation and its effects on composite performance.

In the 0°/90° orientation, the fracture plane is ill-defined, with the fiber tows breaking over a wide range of axial locations, spanning a distance of ~1 cm (Fig. 7a). The location of the fiber breaks within an individual tow also exhibit a broad distribution, typically ~1 mm in length (Fig. 7b). These observations validate the efficacy of the porous matrix as a crack deflection medium both within and between the fiber tows. The apparent "pull-out" of the fibers within the tows evolves by a different mechanism than that typical of more conventional CFCCs, as there are no matrix "sockets" apparent on the fracture surface. Instead, the intervening matrix *fragments* in the region of strain localization. A fraction of particles remains attached to the fiber surfaces (e.g. Figure 7c), indicative of the sites where the matrix had bonded to the fibers by alumina "bridges" (cf. Figure 1).

In the ±45° orientation, the elastic modulus is much lower ($E_{45} \approx 35$ GPa) and inelastic deformation commences at moderately low stresses, <25 MPa, consistent

with domination by the porous matrix. Thereafter, appreciable inelastic strains develop at an essentially constant flow stress, $\sigma_o \approx 50$ MPa, as evident in Figure 6(a). Upon periodic unloading/reloading the material exhibits pronounced hysteresis with appreciable permanent strains, as illustrated in Figure 8(a), remarkably similar to the behavior observed in C/C composites, Figure 8(b).^{5,36} The inelastic deformation is accompanied by a modest reduction in modulus ($E_{45} \approx 30$ GPa upon unloading after 0.65% strain).

The conditions for failure in the $\pm 45^\circ$ orientation and the associated mechanisms are sensitive to specimen width and to lateral constraints. Specifically, in straight tensile specimens with small widths, the fibers detach from the edges and withdraw into the specimen, causing failure to occur at relatively small strains controlled primarily by the matrix. As the width increases, fiber withdrawal is delayed and the failure strain increases. For example, the $\pm 45^\circ$ specimen in Figure 6(a) had a width of 6 mm and a strain of $\sim 0.4\%$ at the maximum load whereas the 12 mm sample in Figure 8(a) achieved a strain of $\sim 0.9\%$ prior to the onset of softening. Even in the latter case, most of the tows pull out from the edge of the specimen, Figure 9(a). Matrix fragmentation also occurs, enabling the tows to rotate as they withdraw, thereby enhancing graceful failure beyond the onset of strain localization. This additional displacement is manifested in rather large apparent failure strains; for example, the specimen in Figure 8(a) fractured at an apparent strain of $\sim 2.5\%$. By using edge notches to constrain the lateral fiber displacements, the achievable strengths are enhanced to ~ 80 MPa, and the failure mechanism changes from matrix to fiber control, Figure 9(b). Such effects are characteristic of notch strengthening, clearly manifest in Figure 10. These findings highlight the need for testing methodologies that elicit the responses expected in actual components with larger dimensions, such as combustor liners.

The marked similarity between the inelastic responses of the present oxide materials and the C matrix composites suggest comparable levels of damage tolerance enabled by their capacity for deformation upon off-axis loading. This response enables stress redistribution by inelastic shear strains activated around strain concentrators, such as holes.^{5,40} These implications are verified below through preliminary measurements of the notch performance.

5. EFFECTS OF THERMAL EXPOSURE

The ambient 0°/90° tensile response after elevated temperature exposure was studied in order to assess microstructural degradation of the fiber and/or matrix. The results for N610 composites are summarized in Figure 11. In the absence of stress, thermal exposure at 1200°C does not have significant effects for times up to 100 h, Figure 11(a). The ultimate strengths after 2, 24 and 100 h are within typical experimental scatter. The fracture retains its fibrous nature, even after 100 h at 1200°C, indicating that the matrix is stable and continues to perform its function. Increasing the treatment temperature to 1300°C has a more pronounced effect, stiffening the stress-strain response but reducing the tensile strength and failure strain (Figure 11b). The reduction in strength is comparable to that observed for N610 dry bundles subjected to analogous heat treatments.²⁴ However, there is also a noticeable reduction in the extent of pull-out, suggesting some changes in the matrix or of the degree of bonding at the fiber/matrix interface.

The above results suggest that the sintering of the matrix to the fibers causes little degradation to the reinforcement beyond that expected from changes in its microstructure. The implication is that the degradation of composite properties after exposure to elevated temperatures could be reduced by using a fiber with enhanced microstructural stability such as N720. Similar studies on composites manufactured with the latter fiber are currently underway.

6. INTERLAMINAR PROPERTIES

The interlaminar response has been probed by performing 3-point flexure tests on short beam specimens (45 x 6 x 3 mm) in the 0°/90° orientation. Typical curves that relate the nominal interlaminar shear stress to the load point displacement are presented on Figure 12(a). In the N610 material, the first non-linearity occurs at stresses of $\tau \approx 8$ MPa. The subsequent response is somewhat erratic, with occasional abrupt load drops corresponding to delamination events. Delamination occurs mainly through the matrix regions between the fiber layers (Figure 12b). Evidently, the cracks propagate stably, in some instances allowing the load to increase beyond that of the first non-linearity. The peak stresses are typically in the range of 8-10 MPa. Fiber failure is minimal and the specimens retain load bearing capacity at displacements exceeding 1 mm. Even for displacements of this order, the delamination cracks close down upon removal of the load and a substantial fraction of the displacement is recovered.

Similar behavior is obtained in the N720 material. The onset of non-linearity occurs at somewhat lower stresses, but the ultimate shear strengths are comparable (~ 8 MPa). There is no significant change in the interlaminar response as the heat treatment time is increased from 2h to 50h at 1200°C, again demonstrating the stability of the matrix microstructure.

The relatively low levels of interlaminar shear strength (in comparison with other CFCCs) are attributable to the high matrix porosity. One potential strategy for improving this property involves additional cycles of precursor impregnation and pyrolysis, yielding a higher matrix density. However, excessive densification may have deleterious effects on the crack deflection characteristics of the matrix, leading to a degradation in the tensile properties along the fiber direction. An alternate solution is to introduce through-thickness reinforcing fibers. In principle, these 3-D

fiber architectures should be readily adaptable to the present manufacturing route; they will be explored in future research.

7. OTHER CHARACTERISTICS

7.1 Creep Strength

Preliminary studies of the high temperature creep characteristics have been performed to assure that there are no serious degradation phenomena occurring in these materials. The results from constant stress creep tests performed at 1200°C on the material with the Nextel 720 fibers are presented in Figure 13(a). These materials exhibit steady-state creep, unlike their counterparts with SiC fibers.⁴¹⁻⁴⁴ Moreover, they have superior, unexpectedly high, creep strengths, which render them as serious candidates for 1200°C applications. The creep rates are considerably lower than those expected from the fibers alone, at the same remote stress, as noted in Figure 13(b). The implication is that the matrix within the fiber bundles is able to sustain load by creeping at a rate comparable with that for the fibers, without extensive cracking. This behavior also differs from that for other oxide matrix CFCCs, wherein the matrix contributes minimally to the composite creep strength.⁴³ A potentially important feature of these materials is the initial shrinkage of the N720 fibers that occurs upon exposure to ~1100°C.²⁸ This shrinkage has been attributed to a change in the alumina content of the mullite phase within the fiber, which is originally synthesized at 1350°C. The possible effects on composite creep have yet to be understood.

7.2 Notch Performance

Ambient temperature tests on tensile specimens containing center holes and edge notches indicate moderate notch sensitivity, with notches causing somewhat greater strength degradation than holes (Figure 14). Comparisons with matrix-

dominated CFCCs, such as woven Nicalon/SiC and cross-ply laminates of Nicalon/MAS, indicate similar trends in the relative strength reduction associated with center holes (Figure 14a). Notably, the strength decreases by ~25% over the range of hole diameters of $0 \leq 2a \leq 10$ mm. Strong similarities are also obtained in the strength characteristics of the oxide CFCCs and C/C in the presence of sharp notches, as illustrated in Figure 14(b). Comparisons of the latter data with predictions based on linear elastic fracture mechanics (LEFM) yield an inferred fracture toughness of $\sim 10 \text{ MPa}\sqrt{\text{m}}$. However, the oxide CFCCs exhibit less notch sensitivity than the LEFM predictions (i.e. $a^{-1/2}$), as manifested in the slope of the strength vs. notch length plot (Figure 14b).

The moderate sensitivity of strength to the presence of holes in the SiC-based systems has been attributed to two mechanisms:⁴⁵ (i) the redistribution of stress around the holes, enabled by matrix cracking and fiber bridging, and (ii) a volume-dependent strength, which allows the material to sustain high stresses over the relatively small volumes that are subject to this stress concentration. In the C/C composites, the stress redistribution is associated primarily with inelastic shear deformation along the fiber directions.³⁷ Similarities in the $\pm 45^\circ$ inelastic deformation behavior of the oxide CFCCs and C/C, Figures 8(a) and (b), suggest that the oxide composites redistribute stress in a similar manner. The specific mechanisms associated with notched behavior and the role of volume-dependent strength in the oxide CFCCs are subjects of further study.

8. IMPLICATIONS

A concept for all-oxide ceramic composites based on a stable matrix consisting of mullite and alumina mixtures, in combination with polycrystalline alumina or alumina-mullite fibers, has been developed. The material has a number of attributes:

- i) It is relatively straightforward to manufacture by conventional slurry infiltration methods. It does not require a fiber coating and uses relatively low cost Nextel fibers. It thus appears to be an "affordable" material.
- ii) The mechanical performance of the material is comparable to that found for other "fiber-dominated" CFCCs, such as SiC/C and C/C.³⁶ Given the demonstrated thermostructural attributes of the C-matrix materials (in non-oxidizing environments), the implication is that components made from this material should have good performance characteristics and should behave in a similar manner. That is, at the present level of characterization, this oxide CFCC is an "oxidation resistant equivalent to C/C composites". However, it remains to be determined whether the lower thermal conductivity of the oxide material (relative to C and SiC) and its higher density constitute a detriment to thermostructural performance.
- iii) The materials containing the mullite/alumina N720 fibers have unexpectedly robust high temperature characteristics. Firstly, the sintering to the fibers of the small alumina particles in the matrix does not appear to degrade the fiber strength significantly. Secondly, the matrix within the fiber bundles seems to be quite creep resistant and apparently contributes to the creep strength of the composite up to at least 1200°C, with a well-delineated steady-state strain rate. There is no evidence of the tertiary matrix cracking phenomenon that degrades the performance of SiC/SiC composites.⁴²

Acknowledgments. The authors would like to thank Professors F.A. Leckie and F.F. Lange of UCSB, and Dr. D.M. Wilson of 3M for useful discussions. The technical assistance of Dr. U. Ramamurty and Messrs. M. Cornish, K. Fields, and D. Stave is gratefully acknowledged.

16. E. Mouchon and Ph. Colomban, "Oxide Ceramic Matrix/Oxide Fiber Woven Fabric Composites Exhibiting Dissipative Fracture Behavior," *Composites*, **26**, 175-82 (1995).
17. P.E.D. Morgan and D.B. Marshall, "Ceramic Composites of Monazite and Alumina," *J. Am. Ceram. Soc.* **78** [6] 1553-63 (1995), also **78** [9] 2574 (1995).
18. W.C. Tu, F.F. Lange, and A.G. Evans, "Concept for a Damage-Tolerant Ceramic Composite with Strong Interfaces," *J. Am. Ceram. Soc.* **79**, 417-424 (1996).
19. J.B. Davis, J.P.A. Löfvander, and A.G. Evans, "Fiber Coating Concepts for Brittle Matrix Composites," *J. Am. Ceram. Soc.* **76** [5] 1249-57 (1993).
20. T.J. Mackin, J.Y. Yang, C.G. Levi and A.G. Evans, "Environmentally Compatible Double Coating Concepts for Sapphire Fiber Reinforced γ -TiAl," *Mater. Sci. Eng.* **A161**, 285-93 (1993).
21. D.C.C. Lam, F.F. Lange, and A.G. Evans, "Mechanical Properties of Partially Dense Alumina Produced from Powder Compacts," *J. Am. Ceram. Soc.* **77** [8] 2113-7 (1994).
22. O. Sudre and F.F. Lange, "Effect of Inclusions on Densification: I - Microstructural Development in an Al_2O_3 Matrix Containing a High Volume Fraction of ZrO_2 Inclusions," *J. Am. Ceram. Soc.* **75** [3] 519-24 (1992).
23. R.K. Bordia and A. Jagota, "Crack Growth and Damage in Constrained Sintered Films," *J. Am. Ceram. Soc.*, **76** [10] 2475-80 (1993).
24. J. He and D.R. Clarke, "Determination of Fiber Strength Distribution from Bundle Tests using Optical Fluorescence," submitted to *Proceedings, Mathematical and Physical Sciences, The Royal Society*, London (1996).
25. M.F. Ashby, "A First Report on Sintering Diagrams" *Acta Metall.* **22**, 275-89 (1974).
26. T.L. Tompkins, "Ceramic Oxide Fibers: Building Blocks for New Applications," *Ceramic Industry*, (1995).
27. H. Déve and C. McCullough, "Continuous Fiber Reinforced Al Composite - A New Generation," *JOM* **47** [7] 33-37 (1995).
28. D.M. Wilson, S.L. Lieder and D.C. Lueneburg, "Microstructure and High Temperature Properties of Nextel 720 Fibers," *Ceram. Eng. Sci. Proc.* **16**, 1005-14 (1995).
29. J. He and D.R. Clarke, private communication.
30. F.F. Lange, "Powder Processing Science and Technology for Increased Reliability," *J. Am. Ceram. Soc.*, **72** [1] 3-15 (1989).
31. W.C. Tu and F.F. Lange, "Liquid Precursor Infiltration and Pyrolysis of Powder Compacts, I: Kinetic Studies and Microstructure Development," submitted to *J. Am. Ceram. Soc.*
32. F. Zok, F.F. Lange and J.R. Porter, "The Packing Density of Composite Powder Mixtures," *J. Am. Ceram. Soc.* **74** [8] 1880-5 (1991).
33. F. Heredia, S M Spearing and A. G. Evans, "Mechanical Properties of Continuous-Fiber-Reinforced Carbon Matrix Composites and Relationships to Constituent Properties," *J. Am. Ceram. Soc.*, **75** [11] 3017-3025 (1992).

34. J.-M. Domergue, F.E. Heredia and A.G. Evans, "Hysteresis Loops and the Inelastic Deformation of 0/90 Ceramic Matrix Composites," *J. Am. Ceram. Soc.* **79** [1] 161-179 (1996).
35. E. Vagaggini, J.M. Domergue and A.G. Evans. "Relationships between Hysteresis Measurements and the Constituent Properties of Ceramic Matrix Composites: I. Theory," *J. Am. Ceram. Soc.*, **78** [10] 2709-2720 (1995).
36. C. Cady, F.E. Heredia and A.G. Evans, "In-Plane Mechanical Properties of Several Ceramic-Matrix Composites," *J. Am. Ceram. Soc.* **78** [8] 2065-78 (1995).
37. F.E. Heredia, S.M. Spearing, T.J. Mackin, M.Y. He, A.G. Evans, P. Mosher and P. Brondsted. "Notch Effects in Carbon Matrix Composites," *J. Am. Ceram. Soc.*, **77** [1] 2817-2827 (1994).
38. T.J. Mackin, T.E. Purcell, M.Y. He and A.G. Evans, "Notch Sensitivity and Stress Redistribution in Three Ceramic-Matrix Composites," *J. Am. Ceram. Soc.*, **78** [7] 1719-28 (1995).
39. K.R. Turner, J.S. Speck and A.G. Evans, "Mechanisms of Deformation and Failure in Carbon-Matrix Composites Subject to Tensile and Shear Loading," *J. Am. Ceram. Soc.*, **78** [7] (1995).
40. T.J. Mackin, K.E. Perry, J.S. Epstein, C. Cady and A.G. Evans, "Strain Fields and Damage around Notches in Ceramic-Matrix Composites," *J. Am. Ceram. Soc.*, **79** [1] 65-73 (1996).
41. X. Wu and J.W. Holmes, "Tensile Creep and Creep-Strain Recovery Behavior of Silicon Carbide/Calcium Aluminosilicate Matrix Ceramic Composites," *J. Am. Ceram. Soc.*, **76** [10] 2695-2700 (1993).
42. A.G. Evans and C.H. Weber, "Creep Damage in SiC/SiC Composites," *Mater. Sci. Engr.*, **A208**, 1-6 (1996).
43. C.H. Weber, J. P.A. Löfvander and A.G. Evans, "Creep Anisotropy of a Continuous-Fiber-Reinforced Silicon Carbide/Calcium Aluminosilicate Composite," *J. Am. Ceram. Soc.*, **77** [7] 1745-1752 (1994).
44. C.H. Weber, K.T. Kim, F.E. Heredia and A.G. Evans. "High Temperature Deformation and Rupture in SiC-C Composites," to be published in *J. Mater. Sci.*
45. J. McNulty, F.W. Zok, G. Genin, and A.G. Evans, "The Effect of Holes and Notches on the Tensile Strength of Ceramic Matrix Composites," to be published.

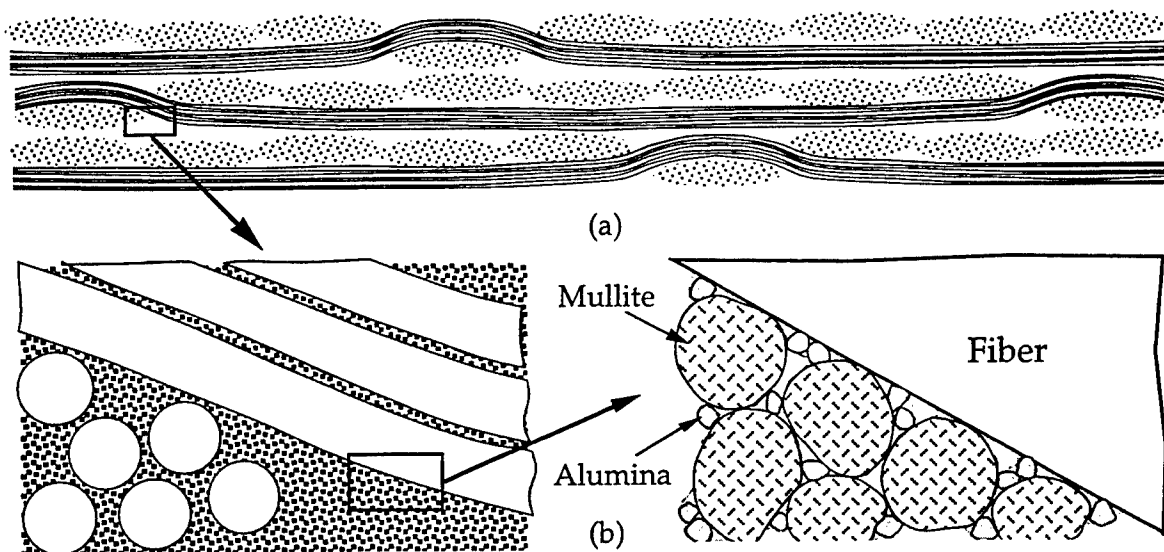


Figure 1. Microstructural design of all-oxide continuous fiber ceramic composite. The fibers are typically Nextel 610™ or 720™ from 3M. The matrix consists of a continuous network of mullite particles bonded to the fibers and among themselves by bridges consisting of smaller alumina particles and alumina produced by precursor impregnation and pyrolysis.

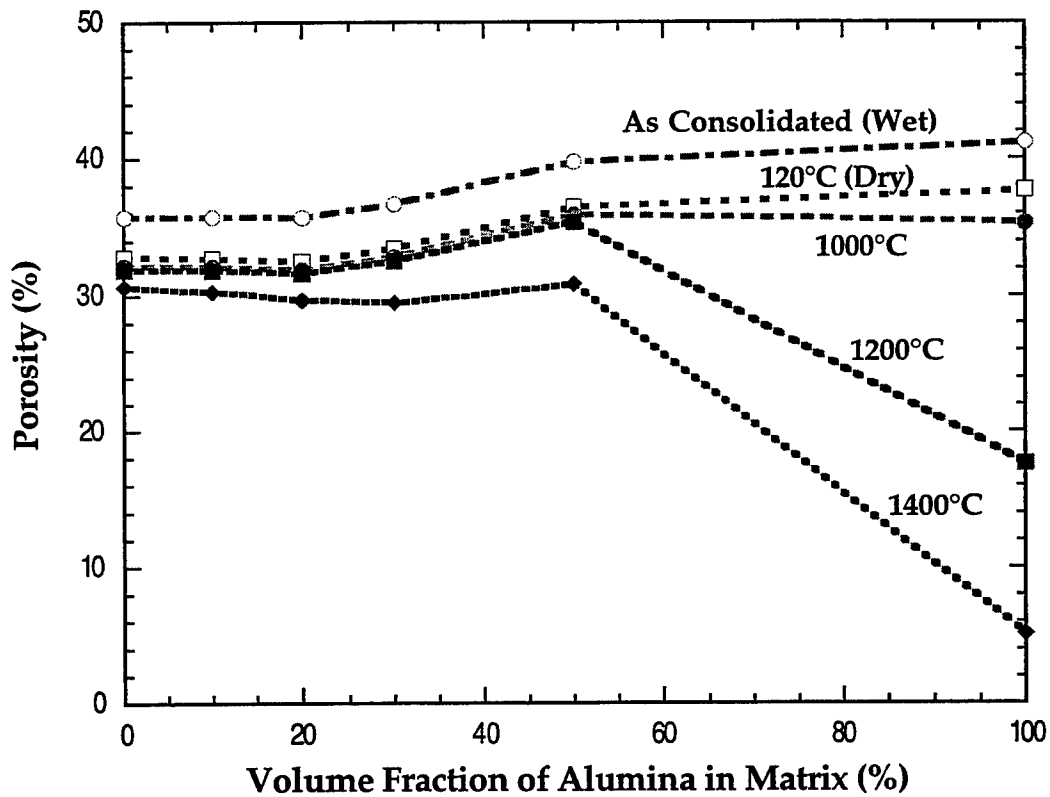


Figure 3. Evolution of porosity during heat treatment as a function of the alumina content in unreinforced mullite-alumina compacts produced by vacuum filtration under conditions similar to those used for the composites. The average particle sizes are $\sim 1 \mu\text{m}$ for mullite and $\sim 0.2 \mu\text{m}$ for alumina. Details of the heat treatment are given in the text.

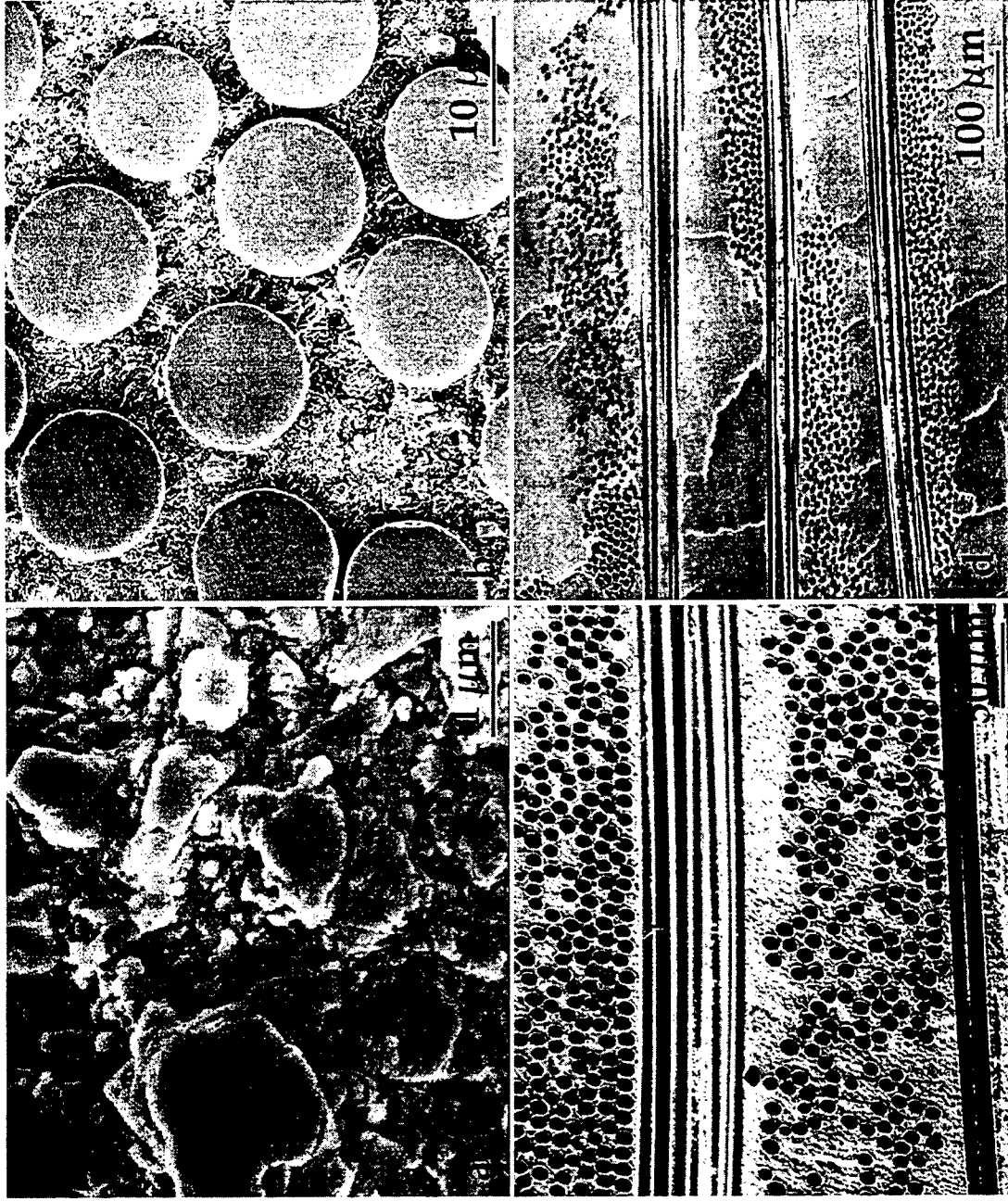


Figure 4. Microstructural views of all-oxide composites based on N610 woven fiber preforms: (a) matrix containing 20%Al₂O₃ and ~37% porosity; (b) and (c) show good levels of infiltration within and between the fiber layers, respectively; (d) matrix cracks produced during drying. The samples in (c) and (d) were given 10 impregnation cycles to facilitate polishing.

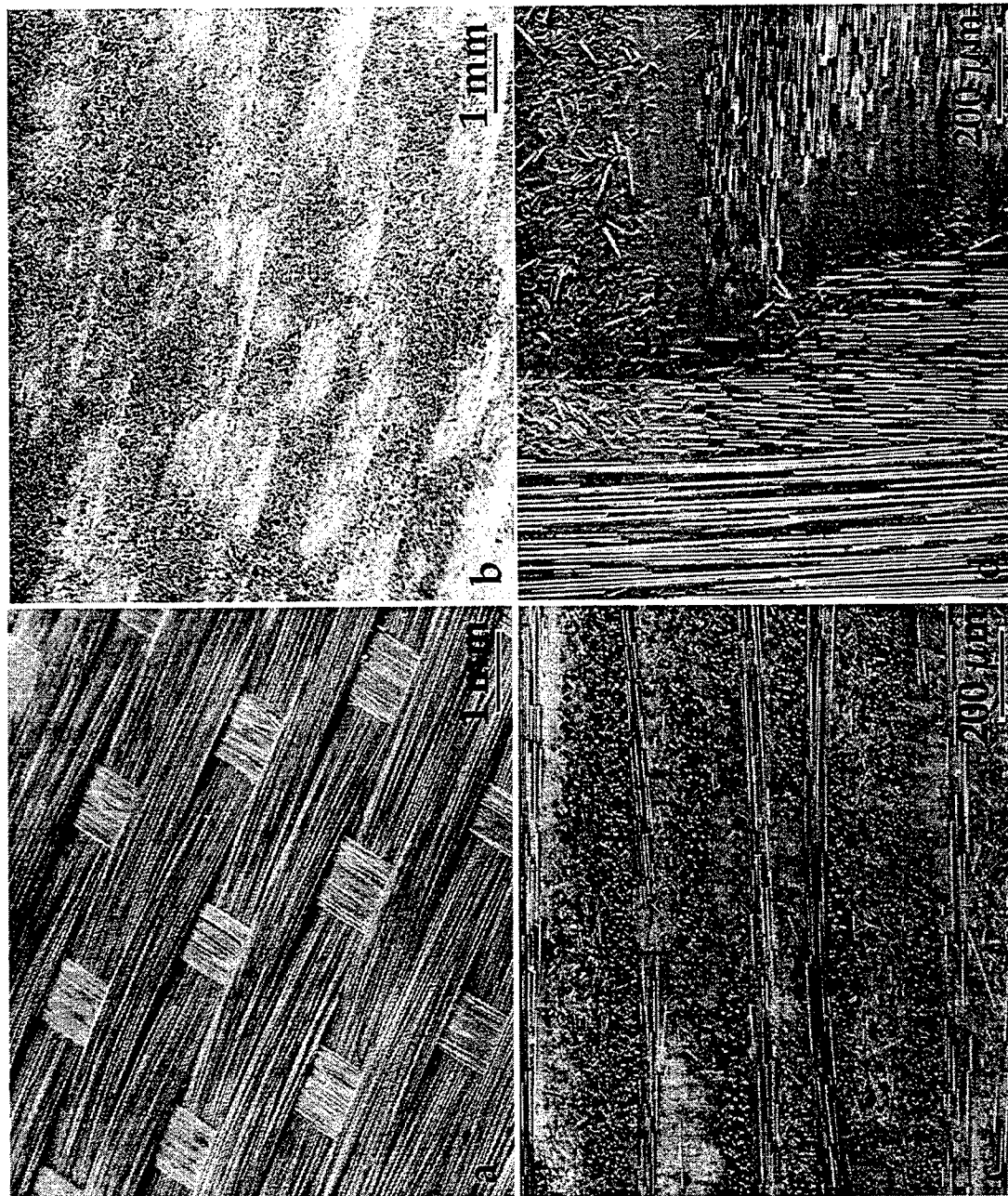


Figure 5. An approach to minimize matrix cracking in slurry infiltrated composites. (a) depicts the topography of the fiber cloth in the as-received condition, and (b) after coating with a "paste" of short alumina fiber. (c) and (d) show in-plane and cross sectional views of the resulting composites where only minimal microcracking can be detected.

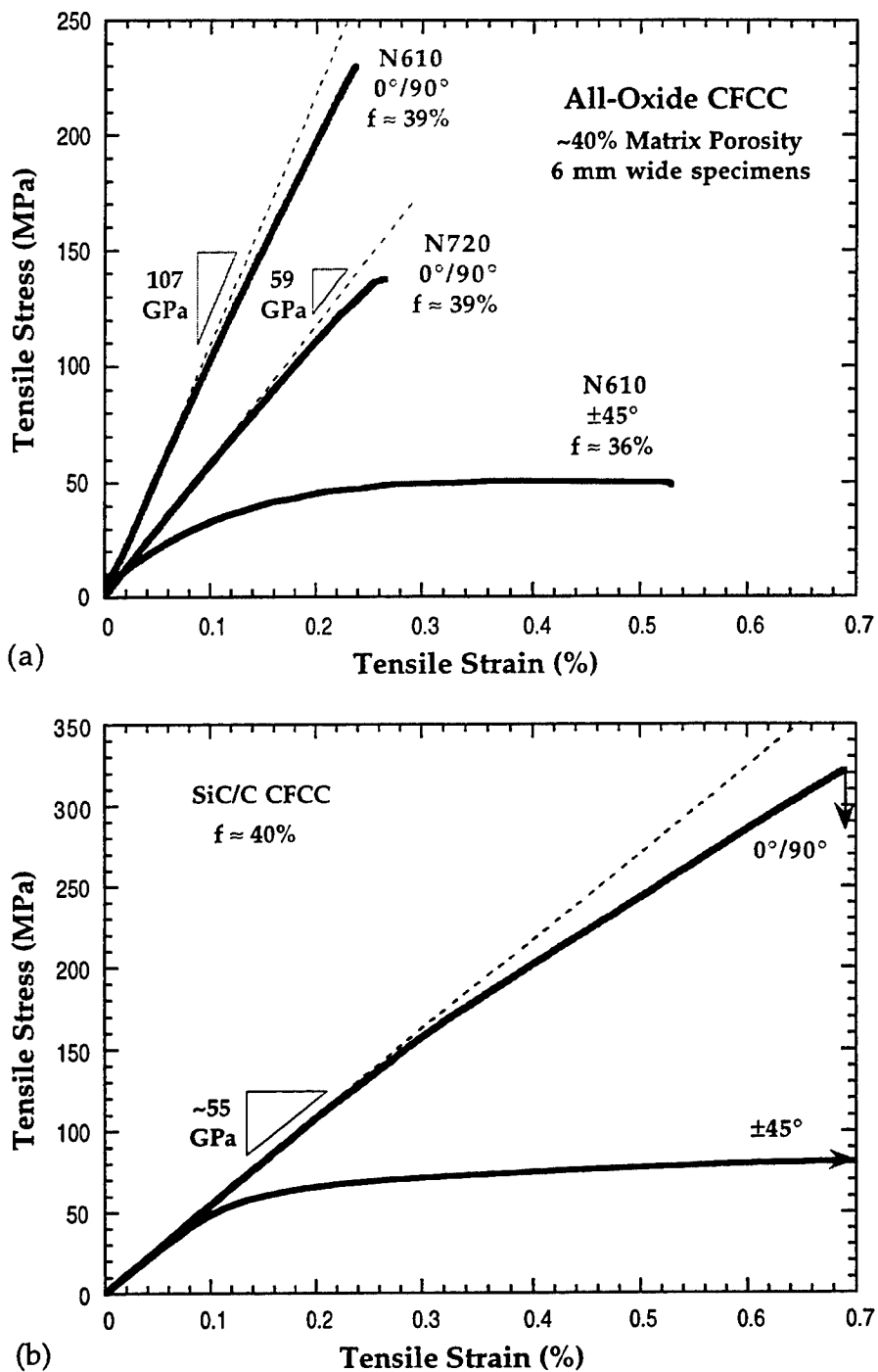


Figure 6. Tensile behavior of the oxide composites in this study (a) compared with that of SiC/C composites of similar fiber content (b), from Reference [36]. The strains at maximum load for the $\pm 45^\circ$ specimens are ~0.4% in (a) and ~0.8% in (b).

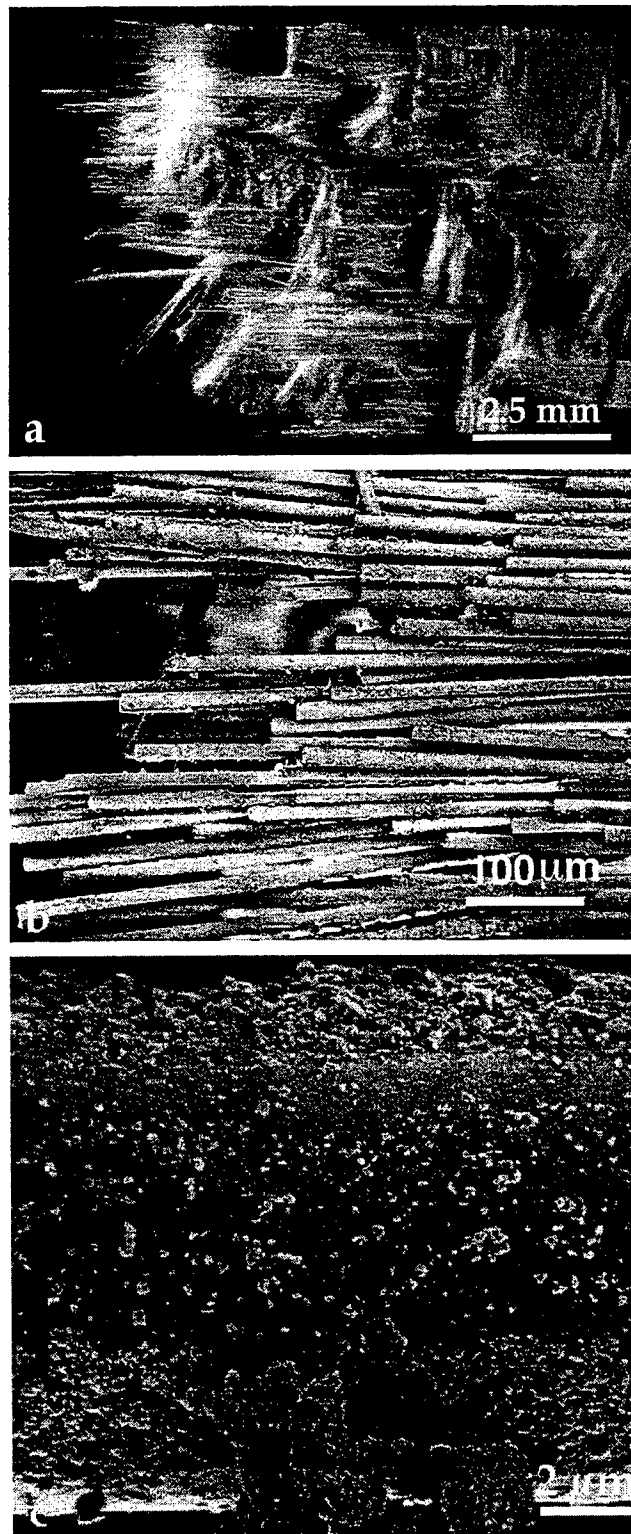


Figure 7. Fracture surfaces of N610 composites in the $0^\circ/90^\circ$ orientation. Note the fibrous fracture with extensive pull-out in (a), and the residue of matrix attached to the fibers in (b) and (c).

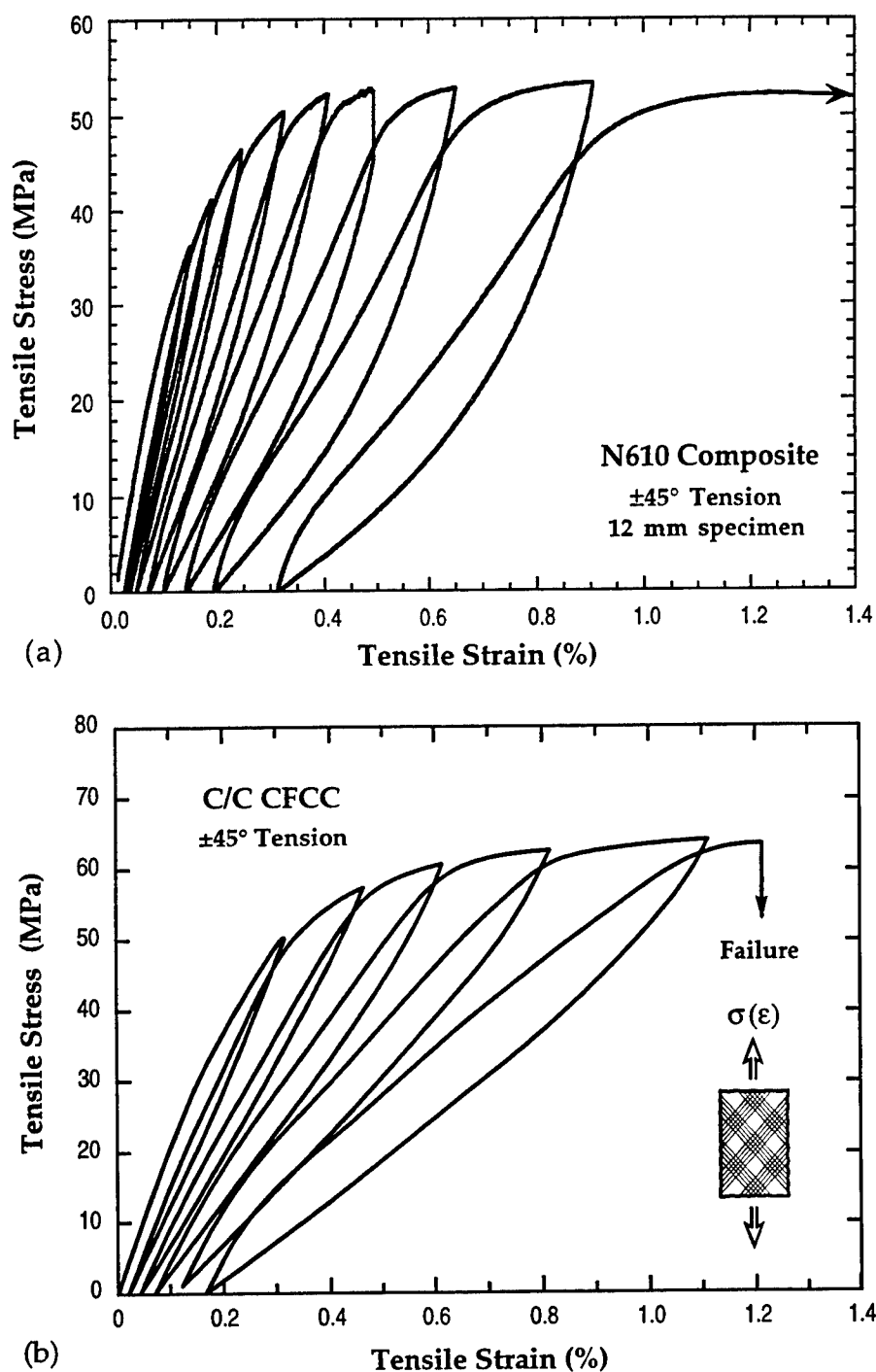


Figure 8. Hysteresis behavior in the $\pm 45^\circ$ orientation for the oxide composites in this study, (a), compared with that of C/C composites of similar fiber content, (b), from Ref. [36]. The composite in (a) reached maximum load at a strain of $\sim 0.9\%$ but supported a load of ≥ 40 MPa up to an apparent strain of $\sim 2.5\%$, when failure occurred.

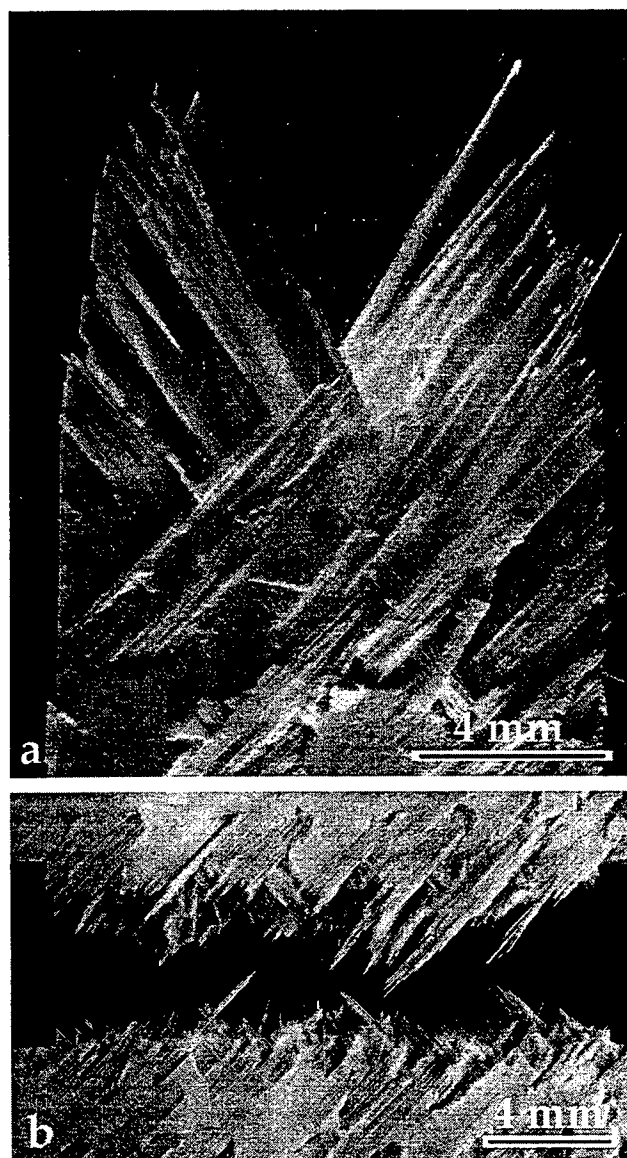


Figure 9. Fracture surfaces of composites in the $\pm 45^\circ$ orientation. (a) Unnotched N610 specimen 12 mm wide showing pull-out from the edges with minimal fiber failure. (b) Notched specimen ($a/W = 0.25$) showing extensive fiber failure on the fracture plane.

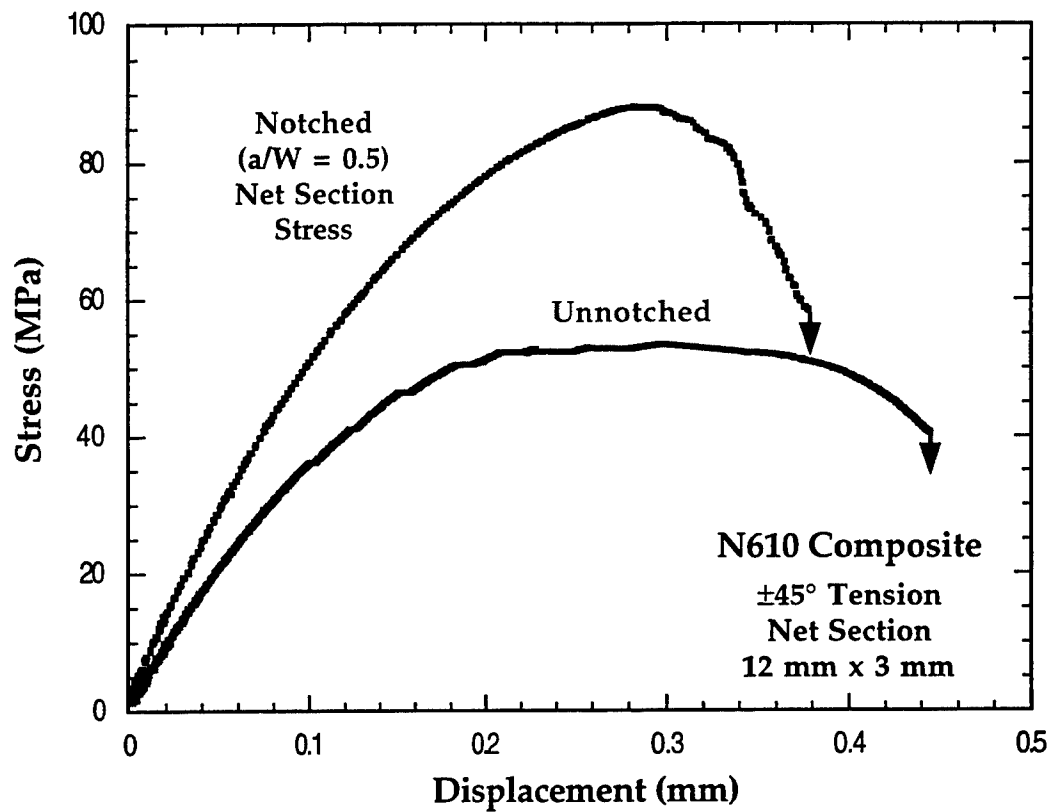


Figure 10. Notch strengthening in all-oxide ceramic composites under $\pm 45^\circ$ tension. Both specimens were cut from the same panel and had the same net section.

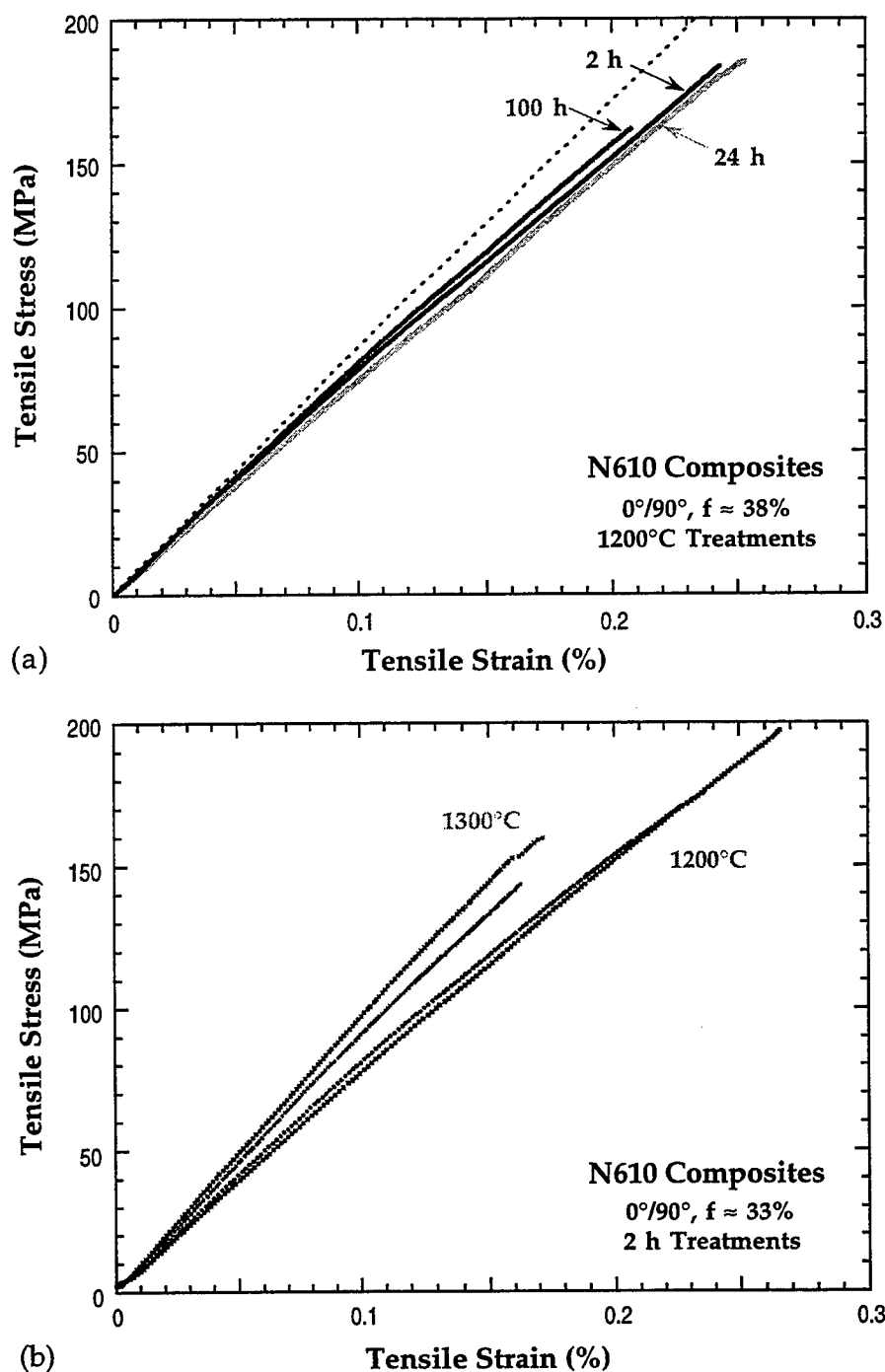


Figure 11. Effect of thermal exposure on the ambient stress-strain behavior for all-oxide composites in the 0°/90° orientation. (a) shows the effect of different times at 1200°C and (b) the effect of two different temperatures for 2 h treatments.

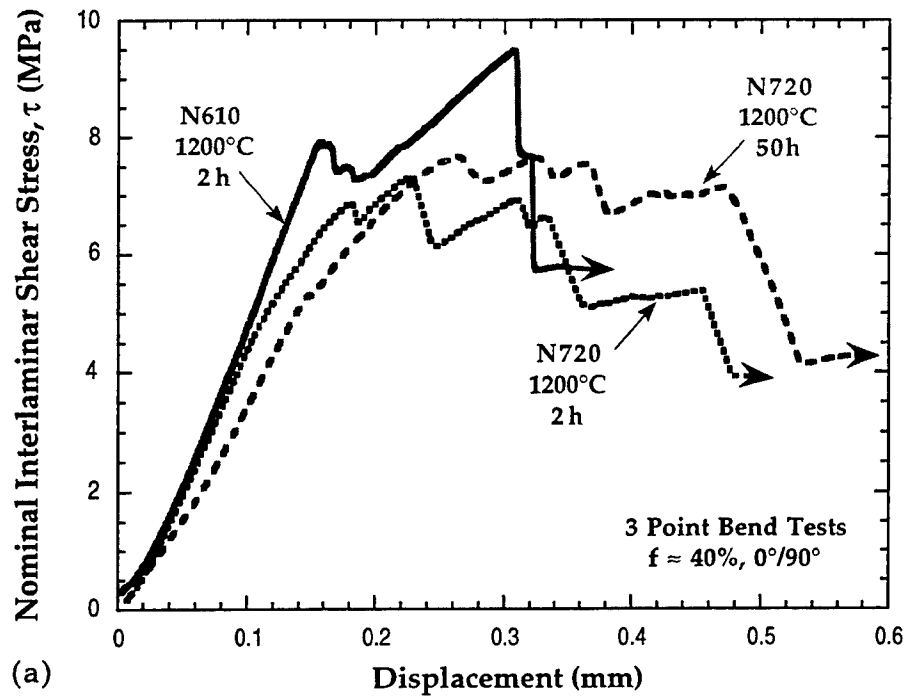


Figure 12. (a) Short beam shear behavior of all-oxide CFCCs in the $0^\circ/90^\circ$ orientation. The 2h/1200°C specimens represent the as-processed condition. The 50h/1200°C specimen of N720 composite shows no evident effect of extended heat treatment on the interlaminar properties. The nominal interlaminar shear stress is calculated using the equation $\tau = 3P/4BD$, where P , B and D are the load, thickness and depth of the specimen, respectively. (b) Micrograph showing delamination cracks after testing in a N720 composite.

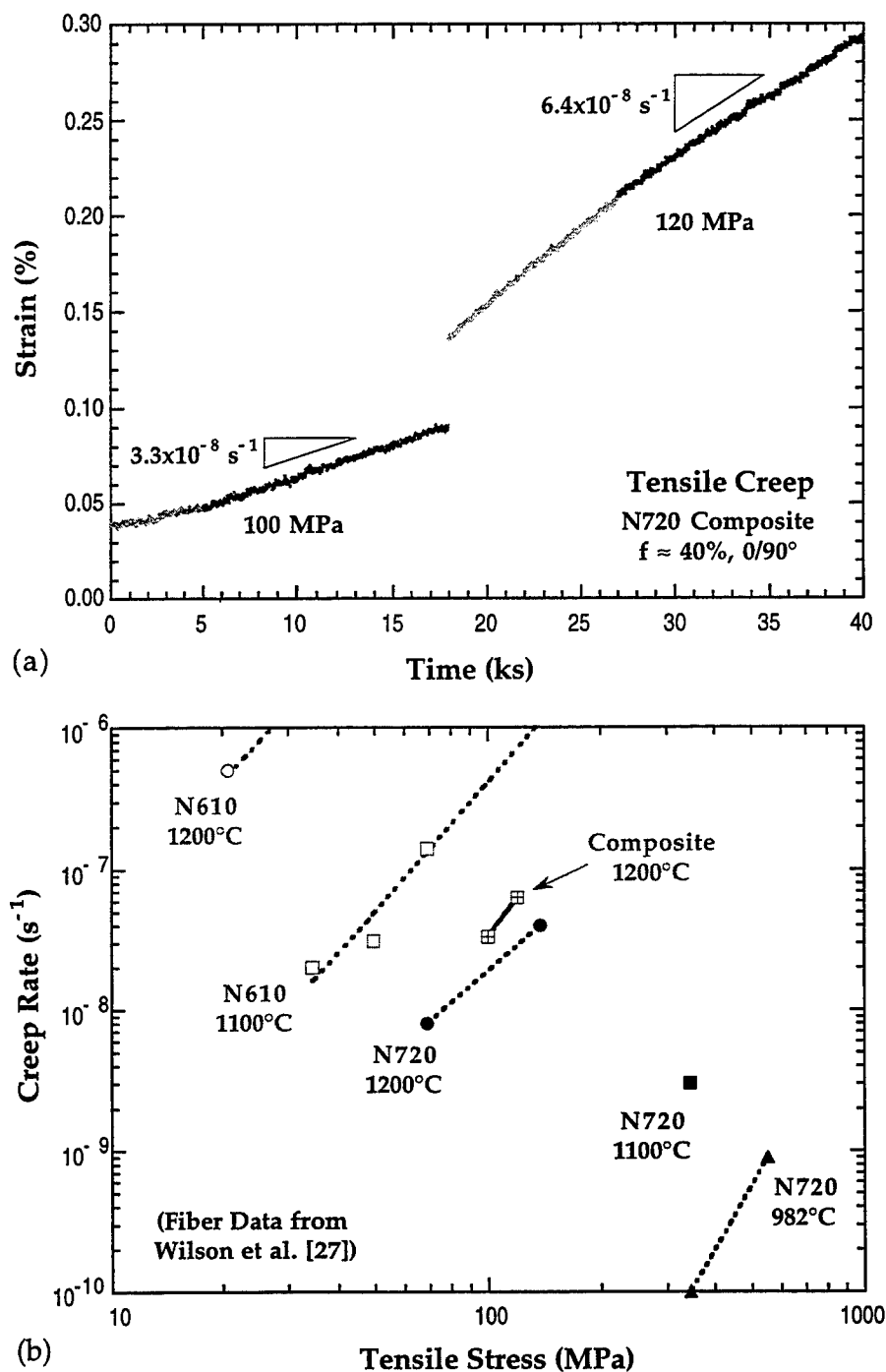


Figure 13. Tensile creep response of all-oxide CFCCs based on the N720 fiber. (a) shows the 1200°C creep response at constant load, and (b) the creep rates vs remote stress compared with data for pristine N720 fibers from Ref. [28]. Data for N610 fibers from [28] is also shown in (b) to illustrate the difference in creep properties between the two fibers.

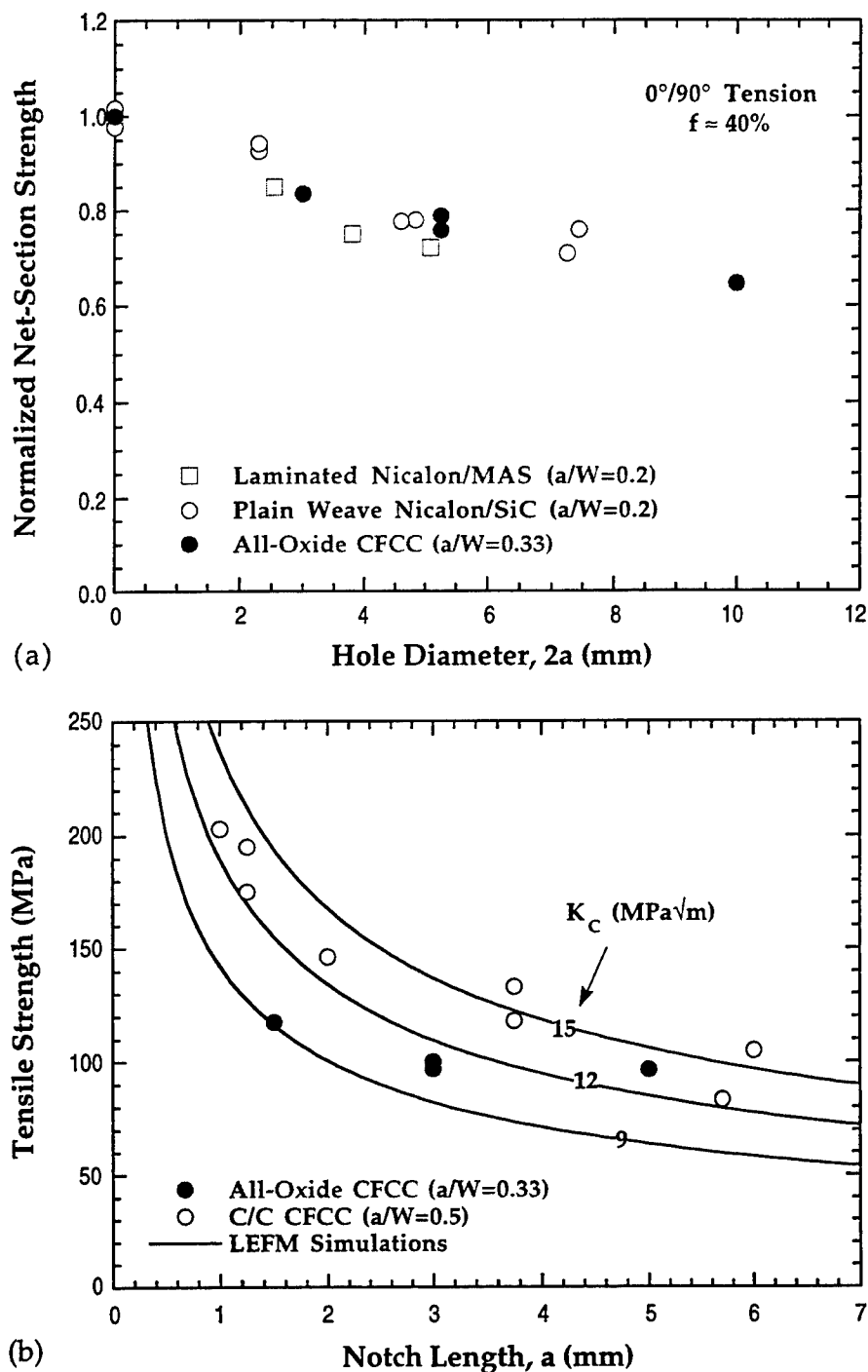


Figure 14. Effect of holes and notches on the strength of all-oxide N610 composites, compared with results from the literature for Nicalon/SiC, Nicalon/MAS and C/C composites, from Reference [37]. The tensile strengths for the unnotched composites in (b) were ~ 300 MPa for the C/C system and ~ 230 MPa for the all-oxide material.

NOTCHED STRENGTH OF CERAMIC-MATRIX COMPOSITES

W. P. Keith* & K. T. Kedward†

Mechanical Engineering Department, University of California, Santa Barbara, California 93106-5070, USA

(Received 4 April 1996; revised 31 October 1996; accepted 26 November 1996)

Abstract

Two simple approaches for characterizing the strength of notched ceramic-matrix composites are presented in non-dimensional form for finite geometries and are used to evaluate the notched strength of a woven-Nicalon-reinforced ceramic-matrix composite. Notch sensitivity can be evaluated with one parameter—the material toughness divided by the product of the unnotched strength and specimen width. For notch-insensitive behavior, a minimum toughness can be defined for the material on the basis of the Griffith criterion. For notch-sensitive behavior, an equation proposed by Suo *et al.* which envelopes many different bridging laws is used to define a material toughness and predict notched strength. Tests were conducted on two batches of the ceramic-matrix composite. One had a weak fiber/matrix interface, and the other had a strong interface. The testing and analysis revealed that the former had a toughness exceeding $10.9 \text{ MPa m}^{1/2}$ whereas the later had a toughness of only $5.4 \text{ MPa m}^{1/2}$.
 © 1997 Elsevier Science Limited

Keywords: ceramic-matrix composites, notched strength

1 INTRODUCTION

Ceramic-matrix composites (CMCs) are being developed for commercial applications in jet engines, leading edges, nose cones, and other hot, moderately stressed environments. To design flight hardware with these materials, designers need a reliable approach to assess structural integrity when notches and holes are present. Although extensive research has been conducted on notches in polymer-matrix composites, only a few investigations have been conducted on the notched behavior of CMCs.^{1,2} In this paper two approaches for characterizing their notched strength will be examined: the classical Griffith approach and a

recent approach developed by Suo *et al.* which incorporates the transition between brittle and ductile behavior.^{3,4} Particular emphasis will be placed on the importance of specimen size, which has been largely neglected in previous work. Following the development, the approaches will be used to interpret notched test results conducted on a CMC manufactured by McDonnell Douglas Technologies Inc.

2 NOTCH SENSITIVITY

Engineers typically distinguish between two classes of failure: notch insensitive and notch sensitive. For notch-insensitive behavior, damage mechanisms at the crack tip diffuse stress gradients to prevent localized failure and crack extension, and the composite strength is governed by the average net-section stress. Quantitatively, the strength, σ_c , can be defined by

$$\sigma_c = \sigma_0 \left(1 - \frac{a}{b}\right) \quad (1)$$

where σ_0 is the unnotched strength, a is half the notch size, and b is half the specimen width.

For notch-sensitive behavior, stress concentrations promote crack extension which propagates through the composite, causing failure. For sharp cracks which result in a $r^{-1/2}$ singular stress field, composite failure can be characterized by the Griffith criterion which can be expressed as

$$\sigma_c = \frac{K_c}{Y\sqrt{\pi a}} \quad (2)$$

σ_c is the critical stress which will cause propagation of a crack-like flaw, a . K_c is a material property referred to as the toughness, and Y is a factor which accounts for the specimen geometry.⁵ The Griffith criterion applies to flawed or notched materials with low toughness. As the notch size is reduced towards zero, the Griffith strength becomes infinitely large and a notch-sensitive to notch-insensitive (brittle-to-ductile) transition occurs.

Current engineering practice does not recognize the existence of any transitional behavior between these two regimes. It implicitly regards notch-insensitive

* Present address: McDonnell Advanced Transport Aircraft, Systems Division, Long Beach, California, USA.

†To whom correspondence should be addressed.

behavior and notch-sensitive behavior as being governed by separate mechanisms. Thus, engineers typically apply both the net-section stress and the Griffith criterion and use the most conservative result.

Recently, Suo *et al.* have forwarded several papers addressing the transition between brittle and ductile behavior.^{3,4} Their work evaluates crack propagation when non-linear deformation ahead of the crack tip is sufficient to suppress the development of a $r^{-1/2}$ stress field. They studied the effect that different bridging laws (rectilinear, linear, linear softening, and quadratic) had on the critical stress needed for crack extension. Although there were subtle differences depending upon the choice of the bridging law, they found that the critical stress was well represented by

$$\sigma_c = \frac{\sigma_0}{\sqrt{\left(1 - \frac{a}{b}\right)^{-2} + \pi a Y^2 \left(\frac{\sigma_0}{K_c}\right)^2}} \quad (3)$$

For large flaw sizes and low toughness, the strength given by eqn (3) asymptotically approaches the Griffith strength, whereas for small flaw sizes and high toughness, it approaches the net-section strength of the material. Equation (3) provides a unifying expression for predicting the notched strength for both large and small notches which conservatively encompasses both ductile and brittle behavior and the transition between them.

As a historical note, Waddoups *et al.*⁶ proposed an equivalent criterion for the case when $a/b \approx 0$ to explain the behavior of notched polymer composites. They postulated the existence of an inherent material defect, c_0 , at the tip of a notch such that the effective notch size was $a + c_0$. The modified notch size was used to evaluate the material toughness and predict the strength (via LEFM) for other notch lengths. The size of the inherent defect was evaluated from the unnotched strength by using the Griffith criterion. The resulting strength criterion was equivalent to eqn (3).⁶ An excellent review of this and other early work on the notched strength of polymer-matrix composites is given by Awerbuch and Madhukar.⁷ Although eqn (3) can be originally attributed to Waddoups *et al.*, the recent work by Suo and colleagues provides the micromechanics basis for this criterion. Therefore, to acknowledge both sets of researchers, eqn (3) will be subsequently referred to as the WS (Waddoups-Suo) criterion.

Before proceeding with an evaluation of these two separate approaches, i.e. the net-section and Griffith versus the Waddoups-Suo criteria, a third and more rigorous approach for addressing notch sensitivity should be mentioned. That is to use experimental means to define a material's notch-tip deformation behavior explicitly, i.e. a bridging law, and then to determine the notched strength computationally for various loads and notch geometries. The complication

and cost of this latter approach raises the question of whether there is a simpler engineering solution; thus, the interest in the former two approaches.

A better understanding of the combined net-section and Griffith criteria and the WS criterion can be obtained by examining them graphically. First, define a non-dimensional strength (Σ), a non-dimensional toughness (κ), and a relative notch size (α) as follows:

$$\Sigma = \frac{\sigma_c}{\sigma_0}, \quad \kappa = \frac{K_c}{\sigma_0 \sqrt{b}} \quad \text{and} \quad \alpha = \frac{a}{b} \quad (4)$$

eqns (1)–(3) can then be rewritten in non-dimensional form as

$$\Sigma_{\text{net}} = (1 - \alpha) \quad (5)$$

$$\Sigma_{\text{Griffith}} = \frac{\kappa}{Y \sqrt{\pi \alpha}} \quad (6)$$

and

$$\Sigma_{\text{WS}} = \frac{1}{\sqrt{\frac{1}{(1 - \alpha)^2} + \frac{\pi \alpha Y^2}{\kappa^2}}} \quad (7)$$

The Griffith and net-section criteria are plotted versus α for different values of κ in Fig. 1, and the WS criterion is plotted in Fig. 2. Y was calculated from the expression for the double-edge-notch geometry:⁸

$$Y = \left[1 + 0.122 \cos^4\left(\frac{\pi a}{2b}\right) \right] \sqrt{\frac{2b}{\pi a} \tan\left(\frac{\pi a}{2b}\right)} \quad (8)$$

First, we examine Fig. 1. For small κ (e.g. $\kappa = 0.35$), the Griffith criterion defines failure; whereas for large κ , the net-section criterion defines failure. The transition between notch-sensitive behavior (Griffith) and notch-insensitive behavior (net-section) is governed by κ . Thus, notch sensitivity depends upon the parameters which define κ ; namely the toughness, unnotched strength, and specimen width. The importance of specimen width is often overlooked in the literature (or at least not addressed explicitly). As will be shown in Section 4, the quantitative interpretation of notch test results depends sig-

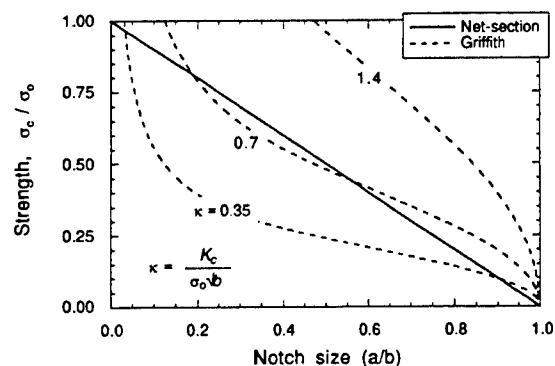


Fig. 1. Notched strength for Griffith and net-section criteria (double-edge-notch geometry).

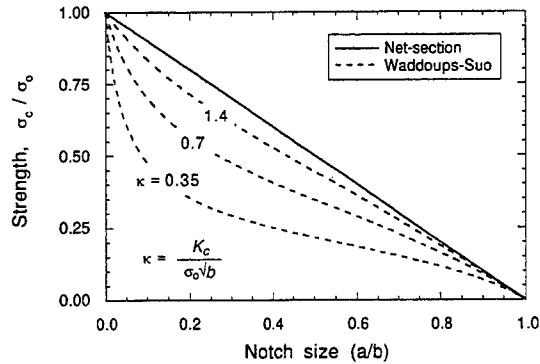


Fig. 2. Notched strength for WS and net-section criteria (double-edge-notch geometry).

nificantly on the specimen width. For intermediate values of κ , the notch sensitivity also depends weakly upon the relative notch size, α , as shown in Fig. 1 for $\kappa = 0.7$.

The WS criterion is plotted in Fig. 2. For small κ , the WS criterion is nearly identical with the Griffith criterion—compare the $\kappa = 0.35$ curves in Figs 1 and 2. For large κ , the WS criterion asymptotically approaches the net-section criterion. For the WS criterion, there is no definitive transition between notch-insensitive and notch-sensitive behavior, which implies that the presence of a notch always reduces the net-section strength. The WS criterion predicts notch-insensitive behavior only in the limit as $\kappa \rightarrow \infty$. This is a potential problem for the WS criterion since, in practice, notch-insensitive behavior will be observed whenever the measurement scatter is of the same order as the difference between the net-section and WS criteria and whenever notch strengthening mechanisms are activated. The latter will be addressed further in the analysis.

The two criteria make distinctly different predictions in the transition regime, $0.5 \leq \kappa \leq 1.5$. In the former, the net-section criterion applies once κ exceeds approximately 0.7. Whereas for the WS criterion, the predicted strength is as much as 20% below the net-section criterion when $\kappa = 0.7$. The question arises as to which criterion better represents actual material behavior. The bridging-law computations of Suo *et al.* indicate that the WS criterion should better represent actual materials. The strength predictions of the Griffith-based approach for transitional values of κ are likely to be inaccurate because a fully developed $1/\sqrt{r}$ singular stress field will not exist at the crack tip. But this answer represents ideal behavior, the reality can only be addressed with experiments. Unfortunately, the limited experimental results presented in the following sections can only make a small contribution towards answering this question. Yet, they do show how the framework outlined in this section can be used to better interpret notched test data.

3 EXPERIMENTS

The experiments were conducted on a 2D CMC manufactured by McDonnell Douglas Technologies Inc. (MDTI). The CMC is reinforced with eight-harness satin-weave SiC (Nicalon) cloth, NL202 grade with an 11.8% oxygen content, manufactured by Nippon Carbon Company. The matrix is a proprietary aluminum phosphate system.

For this research, MDTI supplied plates from two batches of the CMC which were designated batch #1 and batch #2. The plates were made from four plies and were nominally 1.27 mm thick. Although the constituents of both batches were the same, push-out testing indicated that the batch #2 material had a stronger interface.⁹ As a result, the two batches have distinct tensile properties and will be considered as two separate materials.

Notched and unnotched tensile tests were conducted on both batches of material with an Instron 8562 test frame. Aluminum tabs were epoxied to the ends to enable gripping. For the notched specimens, a double-edge-notch configuration was utilized with notch length to half width ratios (a/b) of 0.25 and 0.5. In this configuration, the length of each edge notch is denoted by a and total width by $2b$ (see Fig. 3). The edge notches were created with a 0.3 mm thick diamond wafering blade. The notch tip radii were 150 μm . All the batch #1 specimens were tested with a 12.7 mm width in the gage section. Unfortunately, the specimens had been pre-cut from the plates by MDTI, and no additional material was available to make wider specimens. For the batch #2 material, two specimen widths, 12.7 and 50.8 mm, were tested. This allowed notch size effects to be evaluated in this material.

The results of the strength testing are plotted in Fig. 4. The open circles denote the measured strengths of all the 12.7 mm wide, batch #1 specimens. The closed circles denote the strength of the 12.7 mm wide, batch

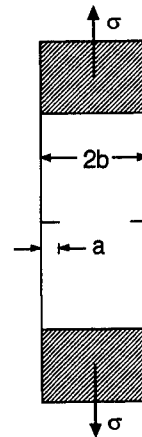


Fig. 3. Double-edge-notch specimen configuration.

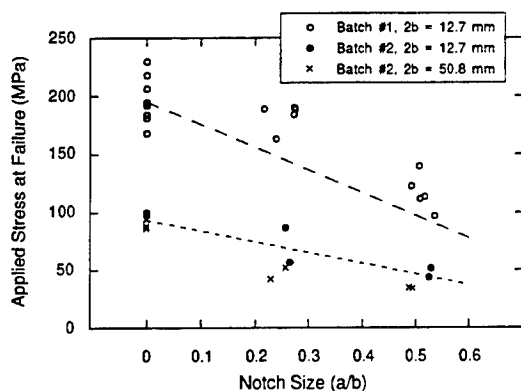


Fig. 4. Tensile strengths of the 2D MDTI materials.

#2 specimens, and the \times s denote the strength of the 50.8 mm wide, batch #2 specimens. The dashed lines represent an extrapolation of the unnotched strength on the basis of the reduction of the net-section area.

The much lower strength of the batch #2 material can be attributed to a stronger interface which promotes crack extension and brittle failure. Figure 4 provides insight into the notch sensitivity of the two materials. The notched strengths of the batch #1 material all lie above the anticipated net-section strength, indicating notch insensitivity. Similarly, the notched strengths of the 12.7 mm batch #2 specimens lie roughly on the line of net-section strength, indicating notch insensitivity. On the other hand, the 50.8 mm batch #2 specimens clearly lie below the line indicating notch sensitivity.

4 ANALYSIS

Figure 4 reveals that the strength of the longitudinally oriented batch #1 material is notch-insensitive. The two approaches outlined in Section 2 yield different quantitative interpretations of this behavior. If we use the WS criterion (see Fig. 2), notch insensitivity implies that $\kappa = \infty$ and in turn that $K_{Ic} = \infty$. Whereas, if we use the Griffith criterion (see Fig. 1), notch insensitivity implies that κ exceeds 0.7. Thus, from the measured unnotched strength of batch #1, $\sigma_0 = 195$ MPa, and the specimen width, $2b = 12.7$ mm, the Griffith criterion provides a lower-bound estimate of the toughness of $10.9 \text{ MPa m}^{1/2}$.

An infinite toughness cannot be physically justified. The high notched strengths observed for the batch #1 material—above the extrapolated net-section strength—may probably be attributed to notch strengthening. The strength of brittle materials (including many CMCs) is governed by the largest inherent defect. For a notched specimen, the high stresses are localized at the notch. Since the critical defect in this vicinity is likely to be smaller, the net-section strength will statistically exceed the area-weighted unnotched strength of the composite.

Such mechanisms are not incorporated in the WS criterion. Thus, use of the Griffith criterion provides the most effective approach for interpreting these data.

The actual toughness of the batch #1 material may be much higher than the $10.9 \text{ MPa m}^{1/2}$ estimate, but only by testing larger specimens can the true value be ascertained. In lieu of tests on larger specimens, the lower bound can be used as conservative estimate of the fracture toughness and may be sufficient for design purposes.

The 12.7 mm wide, batch #2 specimens also showed notch insensitivity, but the 50.8 mm wide specimens showed notch-sensitive behavior. The former tests indicate a lower bound for the toughness of $5.5 \text{ MPa m}^{1/2}$. Figure 5 shows a least-squares fit to the latter data which estimates the actual toughness as $5.4 \text{ MPa m}^{1/2}$ from the WS criterion. The slightly lower value in the latter case can be attributed to the lower unnotched strength of the 50.8 mm wide specimens.

5 CONCLUSIONS

Two approaches for predicting notched strength have been examined: (1) the net-section criterion combined with the Griffith criterion and (2) the Waddoups–Suo criterion. Notch sensitivity depends upon a non-dimensional parameter κ which is equal to the material toughness divided by the product of the unnotched strength and specimen width. The dependence of κ on the specimen width in addition to the material parameters implies that a material can only be designated as ‘notch insensitive’ if specific size limitations are included. For notch-insensitive behavior, the Griffith criterion provides a means of defining a minimum toughness based upon the unnotched strength and specimen size. For notch-sensitive behavior, the WS criterion should provide a more accurate estimate of the material toughness although more experimental data are needed to support this.

Notched tests were conducted on two batches of a

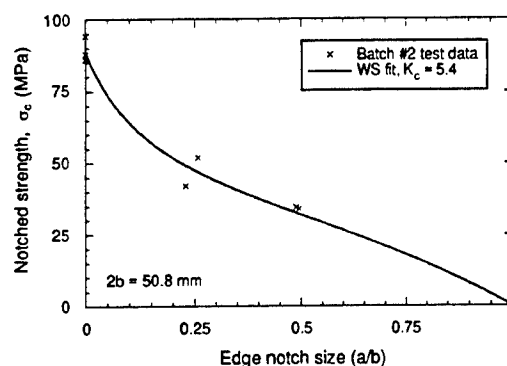


Fig. 5. Test data for 50.8 mm wide, batch #2 specimens and least-squares fit using the WS criterion given by eqn (3).

CMC manufactured by MDTI. The 12.7 mm specimens of the batch #1 (weak interface) material were notch insensitive, i.e. the net-section stress at failure exceeded the unnotched strength. A lower bound for the toughness was estimated as $10.9 \text{ MPa m}^{1/2}$. The 12.7 mm specimens of the batch #2 (strong interface) material were also notch insensitive, but the 50.8 mm specimens were notch sensitive. By the WS criterion, the toughness of the batch #2 material was calculated to be $5.4 \text{ MPa m}^{1/2}$.

ACKNOWLEDGEMENTS

The authors are grateful to Professor Z. Suo for helpful discussions. This work was funded by the ARPA University Research Initiative at UCSB.

REFERENCES

1. Heredia, F. E., Spearing, S. M., Mackin, T. J., He, M. Y., Evans, A. G., Mosher, P. and Brondsted, P., Notch effects in carbon matrix composites. *J. Am. Ceram. Soc.*, 1994, **77**, 2817–2827.
2. Cady, C. M., Mackin, T. J. and Evans, A. G., Silicon carbide/calcium aluminosilicate: a notch-insensitive ceramic-matrix composite. *J. Am. Ceram. Soc.*, 1995, **78**, 77–82.
3. Suo, Z., Ho, S. and Gong, X., Notch ductile-to-brittle transition due to localized inelastic band. *J. Eng. Mater. Technol.*, 1993, **115**, 319–326.
4. He, M.-Y., Wu, B. and Suo, Z., Notch-sensitivity and shear bands in brittle matrix composites. *Acta Metall. Mater.*, 1994, **42**, 3065–3070.
5. Rolfe, S. T. and Barsom, J. M., *Fracture and Fatigue Control in Structures—Applications of Fracture Mechanics*. Prentice-Hall, Englewood Cliffs, NJ, 1977.
6. Waddoups, M. E., Eisenmann, J. R. and Kaminski, B. E., Macroscopic fracture mechanics of advanced composite materials. *J. Compos. Mater.*, 1971, **5**, 446–454.
7. Awerbuch, J. and Madhukar, M. S., Notched strength of composite laminates: predictions and experiments—a review. *J. Reinf. Plast. Compos.*, 1985, **4**, 3–159.
8. Tada, H., Paris, P. C. and Irwin, G. R. (eds), *Stress Analysis of Cracks Handbook*. Del Research Corporation, Hellertown, PA, 1973, Section 2-6.
9. Keith, W. P. and Kedward, K. T., Shear damage mechanisms in a woven, Nicalon reinforced ceramic-matrix composite. *J. Am. Ceram. Soc.*, 1997, **80**, 357–364.

Shear Damage Mechanisms in a Woven, Nicalon-Reinforced Ceramic-Matrix Composite

William P. Keith* and Keith T. Kedward

Mechanical Engineering Department, University of California, Santa Barbara, California 93106

The shear response of a Nicalon-reinforced ceramic-matrix composite was investigated using Iosipescu tests. Damage was characterized by X-ray, optical, and SEM techniques. The large inelastic strains which were observed were attributed to rigid body sliding of longitudinal blocks of material. These blocks are created by the development and extension of intralaminar cracks and ply delaminations. This research reveals that the debonding and sliding characteristics of the fiber-matrix interface control the shear strength, strain softening, and cyclic degradation of the material.

I. Introduction

A LOW-COST ceramic-matrix composite (CMC) is being developed by McDonnell Douglas Technologies Inc. (MDTI). It has potential commercial applications in jet engine exhaust ducts, leading edges, nose cones, and other hot moderately stressed environments. An understanding of the mechanical behavior of this material is needed to help make improvements and to design components.

Research on CMCs has generally focused on their tensile behavior. Recent investigations have defined the relationship between matrix cracking, sliding, and the tensile inelastic strains and hysteresis.¹⁻³ With this research, the tensile behavior is fairly well understood. More recently, investigators have begun to examine CMC behavior when shear loads are applied.⁴⁻⁷ These studies indicate that many CMCs have significant inelastic shear deformations and large shear failure strains. Although the ultimate tensile strains of the constituents are less than 1%, the composite shear strains at failure exceed 2-3%. There is no clear understanding of the damage mechanisms which are responsible for this behavior. To address this issue, this research examines the shear damage mechanisms in the MDTI CMC.

This paper is organized as follows. First, Iosipescu shear and push-out test results are presented. These are supported with X-ray, optical, and SEM observations. Second, a damage model is proposed which attributes the inelastic shear deformations to a rigid body sliding mechanism and predicts the shear strength from the interfacial sliding properties. The model is then assessed and corroborated with the experimental results. Finally, several pertinent issues are discussed and conclusions are drawn.

II. Experimental

(I) Material

The MDTI CMC is manufactured by passing fiber cloth through a matrix slurry and then air drying until tacky. Several

cloth plies are combined to produce the desired thickness and can be laid up to form complex geometric shapes using polymer composite techniques. The formed part is then vacuum bagged and fired in an autoclave.

The fiber cloth consists of many tows in 15 μm diameter SiC filaments in an eight-harness satin weave architecture. The SiC (NicalonTM), NL202 grade with 11.8% oxygen content, is manufactured by Nippon Carbon Co. There are 8.7 tows/cm running in each direction with each tow containing approximately 500 filaments.

The matrix slurry is created by mixing alumina particles in phosphoric acid. The alumina and phosphoric acid react to form aluminum phosphate (AlPO_4). The resulting matrix is highly porous and contains particles of aluminum phosphate in both quartz and cristobalite forms and unreacted alumina.⁸

For this research, MDTI supplied plates from two batches of the CMC. The plates were made from four plies and were nominally 1.27 mm thick. A micrograph of a polished cross section is shown in Fig. 1. The batches are compositionally identical—40% fibers, 40% matrix, and 20% porosity by volume. Yet, tensile tests indicated a dramatic difference in the

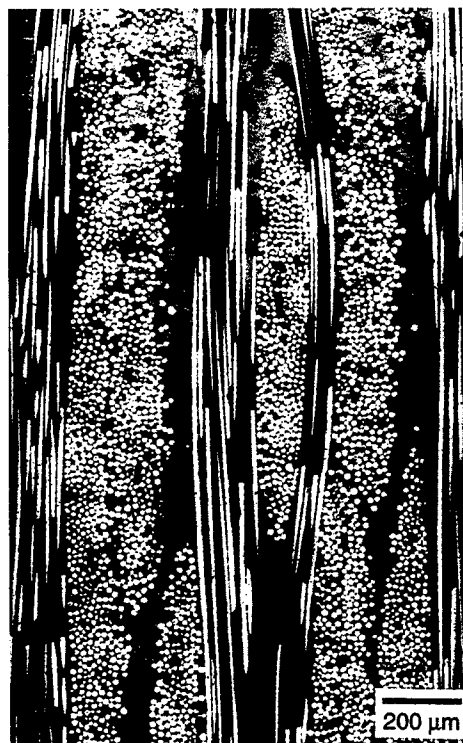


Fig. 1. Polished cross section of MDTI woven CMC. The fibers are the light phase, the matrix is the gray phase, and the pores (filled with epoxy) are the dark phase.

R. J. Kerans—contributing editor

Manuscript No. 192377. Received August 14, 1995; approved August 8, 1996. Presented at the 97th Annual Meeting of the American Ceramic Society, Cincinnati, OH, May 3, 1995 (Engineering Ceramics Division, Paper No. C-40-95).

Based in part on the dissertation submitted by W. P. Keith for the Ph.D. degree in mechanical engineering, University of California, Santa Barbara, California, 1995.

Supported by the ARPA University Research Initiative Program at the University of California, Santa Barbara.

*Member, American Ceramic Society.

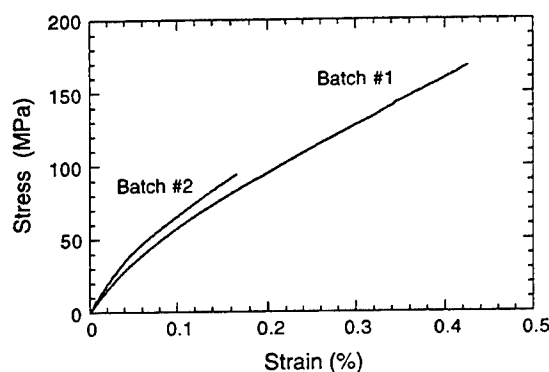


Fig. 2. Tensile stress-strain behavior to failure for the batch 1 and 2 materials.

strength of these batches as shown by Fig. 2. The batch 1 material has a tensile strength of 170 MPa, whereas the batch 2 material has a strength of only 93 MPa. This difference is attributed to the respective strengths of the fiber-matrix interface, and is corroborated by push-out testing reported here. These differences were likely engendered by alterations in the CMC processing. Unfortunately, since these batches were produced before MDTI's processing procedure was rigorously defined, the processing deviations which effected the change are unknown. Nevertheless, these unintended differences were welcomed as they provided a platform to better explore the role of the interface on the shear behavior.

(2) Procedures

The CMC material was cut into Iosipescu specimens as shown in Fig. 3 with the fibers oriented in the directions of the maximum shear stress. The 110° notch was used because it has yielded good results in shear tests on other CMCs.⁵ To measure strain, a two gage $\pm 45^\circ$ rosette (Measurement Group, Inc., EA-06-062TH-120) was mounted on each face between the notches. Each gage had an active length of 1.57 mm. A modified Wyoming Iosipescu test fixture^{9,10} was used to apply a pure shear load to the region between the notches. The response of the material to monotonic and low cyclic, less than 10 cycles, shear loadings was investigated. A series of tests were conducted to explore the range of mechanical response and to provide multiple samples for destructive examination. Table I presents a summary of these tests which were conducted on both the batch 1 and batch 2 materials. Fully reversed cyclic strains were achieved by reorienting the specimen, switching the front face to the back, in the test fixture between load applications.

Surface replication, X-ray radiography, and optical microscopy techniques were used to assess damage. To assess the extent of matrix cracking, acetate replicas were taken at regular intervals during two monotonic Iosipescu tests, one test for each material. Strain gages were applied only to the back face of these specimens to make the front face available for replicating. After testing, a few specimens were sectioned and soaked in a ZnI solution for 24 h. X-ray radiographs were then taken of the damaged specimens. The ZnI was preferentially adsorbed

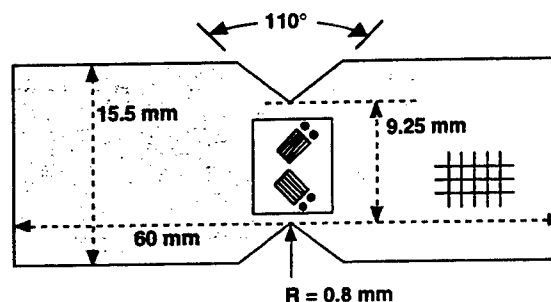


Fig. 3. Iosipescu specimen configuration.

in the damaged regions. Because the ZnI was impervious to X-rays, the damaged areas were revealed as dark regions on the X-ray image. Sections were also impregnated with a low-viscosity epoxy under vacuum, polished to a 1 μm finish, and examined optically. Further, a batch 1 specimen delaminated into two separate pieces after being sectioned between the notches. This provided a unique opportunity to examine the delaminated surface. These pieces were mounted (uncoated) on stubs, and the delaminated surfaces were examined in a JEOL 6300 field emission scanning electron microscope (SEM).

To evaluate the fiber-matrix interface properties directly, bundle push-out tests¹¹ were conducted—four on the batch 1 material and three on the batch 2 material. Thin wafers (~ 0.8 mm thick) were cut and polished on both faces; 4 to 6 μm of matrix were etched from one face with a 10% HF acid solution. The wafer was placed on an aluminum base containing a 220 μm diameter hole. A 140 μm diameter silicon carbide fiber (SCS6) push-rod was placed on the protruding fibers of a tow normal to the surface. The push-rod was used to push out, unexpectedly, a cylinder of the composite into the 220 μm hole. The backside displacement was measured using a small rod placed within the hole and attached to a cantilever beam displacement gage. After each test, the perimeters of these irregularly shaped sections were measured from optical micrographs with a thread and pins. The debond and sliding stresses were calculated by dividing the push-out load by the product of the specimen thickness and the perimeter length. Additionally, a specimen from each batch was examined in the SEM.

(3) Mechanical Response

The monotonic shear stress-strain curves for both batch 1 and batch 2 materials are shown in Fig. 4. The average shear strain is computed using the gages from both faces. Note, there were slight variations between gages due to material inhomogeneities, but the average response of the four gages provided reproducible results. The curves show an initial elastic behavior, a transition to a plateau shear stress, and finally a softening behavior as the shear strain reaches 2–3%. The tests were stopped when one or more of the strain gages failed. The maximum shear stresses were 29 and 49 MPa in the batch 1 and 2 materials, respectively. The shear strain exceeded 3% for both materials.

The first three and tenth cycles from the fully reversed 1% cyclic testing of the batch 1 material are shown in Fig. 5. This behavior typifies the response observed in the cyclic testing

Table I. Iosipescu Test Summary

Load type	Maximum shear strain (%)	Cycles	Comments
Monotonic	1		
Monotonic	>3		Tests stopped because of gage failure
Cyclic ($R = 0$)	>2	≤ 5	Strain level increased with each cycle
Cyclic ($R = -1$)	± 0.5	≤ 10	$\pm 0.5\%$ strain applied in each cycle
Cyclic ($R = -1$)	± 1.0	≤ 10	$\pm 1.0\%$ strain applied in each cycle
Cyclic ($R = -1$)	± 2.5	≤ 10	Strain level increased with each cycle

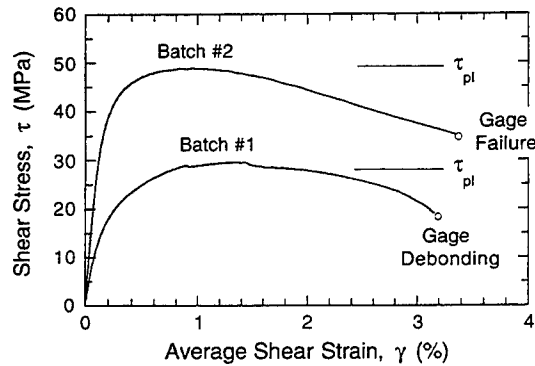


Fig. 4. Monotonic Iosipescu response of the batch 1 and batch 2 materials, and the predicted shear strengths, τ_{pl} , based on push-out results.

of both batches. Several features are worth highlighting. The unloading shear modulus—defined as the tangent modulus after load reversal—and the peak cyclic shear stress decrease with each cycle. Secondly, the tangent modulus decreases continuously as the load application is reversed from positive to negative until the shear strain reaches zero. Then, the composite stiffens before again softening as the peak stress is reached. These general characteristics were observed consistently in the various specimens. Note, the irregularities at zero shear stress are associated with the dismantling and remounting procedures needed to apply the fully reversed cyclic loads.

To assess the phenomenological nature of the damage development, the unloading modulus and cyclic peak stress were evaluated for the multiple cycles of each test. In Fig. 6, the unloading modulus is plotted versus the inelastic strain range. The inelastic strain range was determined by subtracting the elastic strain range from the measured strain range associated with each cycle. The elastic strain range was calculated as the product of the initial tangent shear modulus and the cyclic shear stress range. The results from all the tests listed in Table I are included in Fig. 6. Despite the different loading histories in these tests, a consistent trend is seen between the unloading modulus and inelastic strain range. The graph shows that the unloading modulus decreases rapidly with increases in the strain until it reaches 6–8 GPa, where it tends to level off. Note, the absolute strains never exceeded 2.5%. The high inelastic strain ranges were achieved by the fully reversed loading. The batch 2 material exhibits higher unloading moduli particularly at low strain levels.

In Fig. 7, the peak cyclic stress is plotted versus the cumulative inelastic strain, which is the sum of the inelastic strains from each cycle. Again, a consistent trend is observed. The

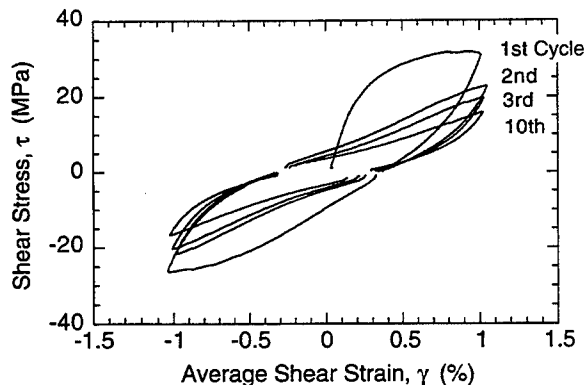


Fig. 5. Fully reversed cyclic behavior of a batch 1 specimen.

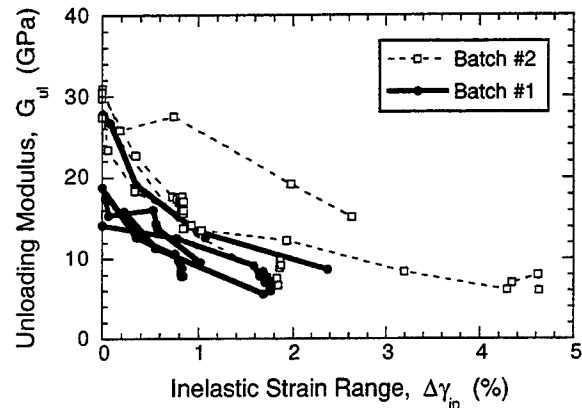


Fig. 6. Degradation of the unloading modulus as a function of the inelastic strain.

peak cyclic shear stress decreases rapidly initially and then tends to level off as the cumulative inelastic strain increases.

(4) Observations

A well-defined array of matrix cracks does not develop in this composite. Instead, an irregular array of porosity and matrix microcracks was observed. Although much of this array was present initially, the acetate replicates did reveal additional microcracking from pores and in matrix-rich regions as shown in Fig. 8.

Figure 9 shows the X-ray images obtained from the batch 1 material specimen cyclically tested to $\pm 1.0\%$ shear strain. Note, this specimen was sectioned with seven lengthwise cuts creating six central sections and four pieces adjacent to the notches. The sectioning ensured even penetration of the ZnI. For the X-ray image shown in Fig. 9(a), all the pieces were reassembled in their original positions adjacent to one another. Small gaps in the assembly resulted in the white space seen between the pieces on the X-ray image. The much darker region between the notches in Fig. 9(a) reveals the localization of the shear damage. The images in Figs. 9(b) were taken with each of the six central sections rotated 90° . These images show distinct narrow black lines suggesting the presence of delamination planes. Similar damage observations were seen in the batch 2 specimens.

At large strains ($\gamma > 3\%$), the ply delaminations lead to macroscopic buckling of the surface plies. The buckling ran diagonally across the specimens and was normal to the principal compressive stress. Although buckling typically caused

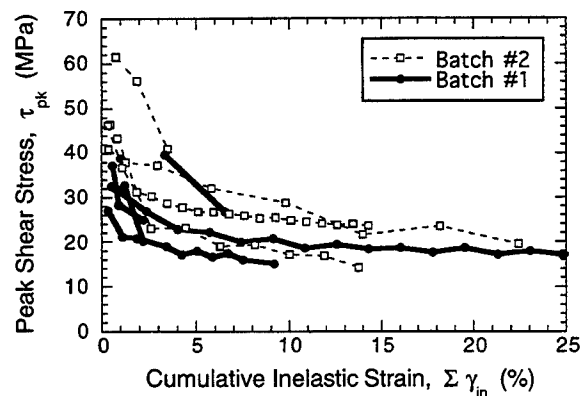


Fig. 7. Degradation of the peak cyclic shear stress as a function of the cumulative inelastic strain.

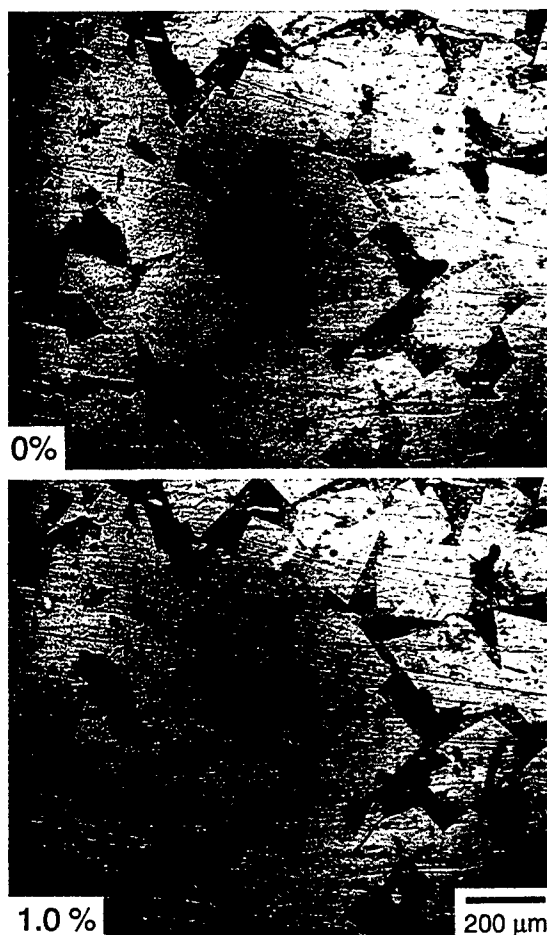


Fig. 8. Surface replicas of monotonically tested Iosipescu specimens showing the presence of matrix cracks at 1.0% strain in the matrix-rich surface region where no cracks were seen prior to loading, 0% strain.

gage failures, the composite was still able to sustain 30–50% of the peak load.

Figure 10(b) shows the polished surface of an Iosipescu specimen which has been strained to $\pm 0.7\%$ and sectioned between the notches. For comparison, an identically polished section of virgin material is also shown in Fig. 10(a). The tested Iosipescu specimen shows considerable interface damage and matrix cracks running between fibers. There also appear to be edge cracked fibers which were probably caused by polishing. The interface damage likely made these fibers susceptible to this polishing damage.

The SEM examination of the specimen which delaminated during sectioning indicated that separation occurred almost entirely along the fiber–matrix interface as shown in Fig. 11. The delamination path alternately traverses cylindrical fiber surface and cylindrical matrix surface where it is evident that the fiber has been pulled away. Longitudinally, the continuity of the matrix is interrupted by large cavities (pores) and occasionally fine cracks. There was no evidence of damage to the fibers.

(5) Push-out Tests

Typical results from the push-out tests are shown in Fig. 12. The batch 2 material showed a gradual load drop after debonding as the push-out proceeded. The average debond stress was 28 MPa with a standard deviation of 3.6 MPa, and the average sliding stress was 19 MPa with a standard deviation of 4.0 MPa. In the batch 1 material, no load drop was observed. Debonding and sliding were coincident. Further, the sliding stresses remained fairly constant as the fibers were pushed out. The

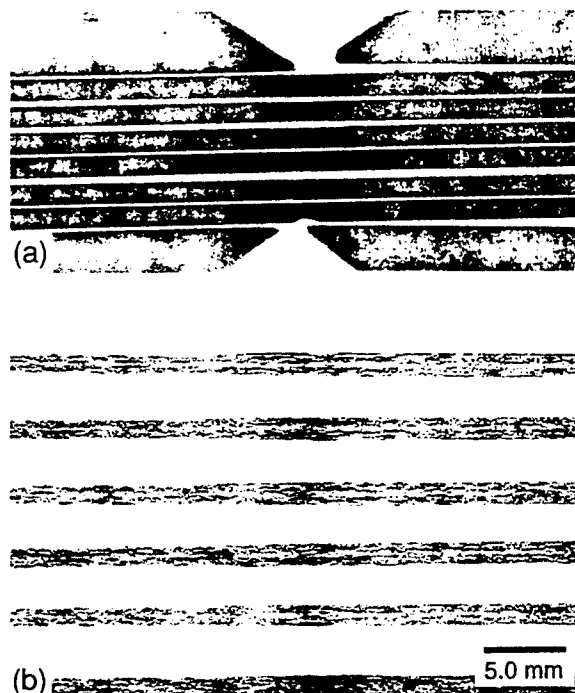


Fig. 9. X-ray images of the shear damage in a batch 1 specimen strained to $\pm 1.0\%$: (a) The much darker central region shows the localization of the damage between the notches, and (b) the distinct black lines suggest delaminations.

batch 1 debonding and sliding stresses averaged 16 MPa with standard deviations of 4.9 and 3.2 MPa, respectively. In both materials, an entire cylinder of fibers and matrix was pushed out (Figs. 13 and 14). For both batches, the perimeter of these irregularly shaped cylinders predominantly followed the fiber–matrix interface. It is estimated that less than 10% of the perimeter path traverses the matrix. In the batch 2 material, the interface had small matrix fragments adhering to the surface, whereas in the batch 1 material, the interface was clean. The perimeter of the pushed-out cylinders for both batches averaged 0.81 mm with a standard deviation of 0.13 mm and typically contained 25–35 fibers.

III. Analysis

In the previous section, the test results and observations were presented in a sequential, matter-of-fact manner. This was done to provide an efficient, unbiased report to the reader. Unfortunately, the results, so reported, seem unconnected and lack a unifying theme. To rectify this deficiency, a model will be presented, in this section, which provides a simple representation of the composite architecture and shear-induced damage. This model provides a basis for interpreting and connecting the experimental results and observations. With the model, an analytic expression will be derived to predict the composite shear strength from the push-out test results. Then, the model will be assessed by using the push-out test results and examining the shear stress–strain response of the composite.

(1) Model

The nonlinear stress–strain behavior can largely be explained and the shear strength predicted with a simple damage model. First, the woven 2-D CMC is idealized as a $0^\circ/90^\circ$ laminate as shown in Fig. 15. Second, primary damage is assumed to exist in the form of porosity and matrix cracks. To a large extent, this damage exists before loading although some additional matrix cracking occurs upon loading (see Figs. 8(a) and (b)). The

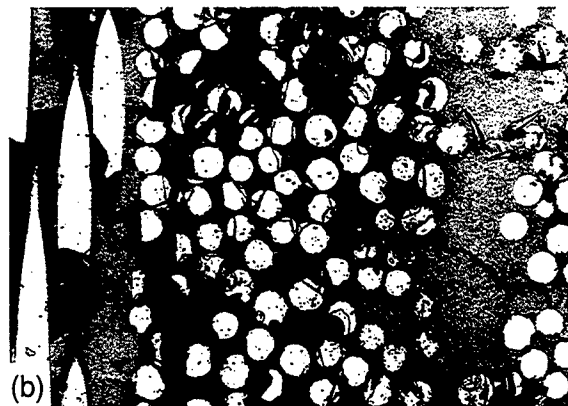
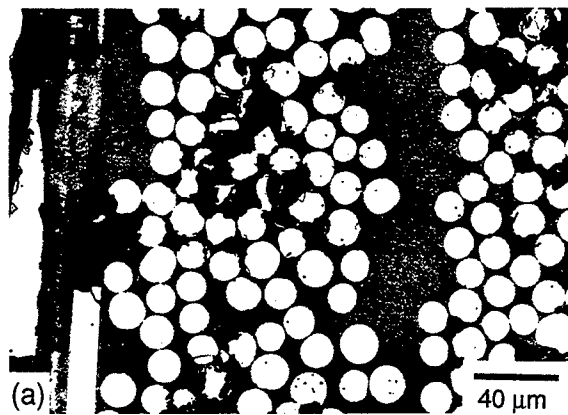


Fig. 10. Polished section of composite (a) untested material and (b) Iosipescu specimen strained to $\pm 0.7\%$ showing fiber-matrix interface damage and matrix cracking.

primary damage gives rise to stress concentrations which promote secondary damage in the form of intralaminar cracks and ply delaminations. The term "intralaminar cracks" is being used very specifically as a label for hypothesized cracks which run along the fiber-matrix interface and span fibers through the ply thickness as shown in Fig. 15. The existence of these intralaminar cracks was supported by the interface damage and matrix cracks observed in Fig. 10, while the presence of ply

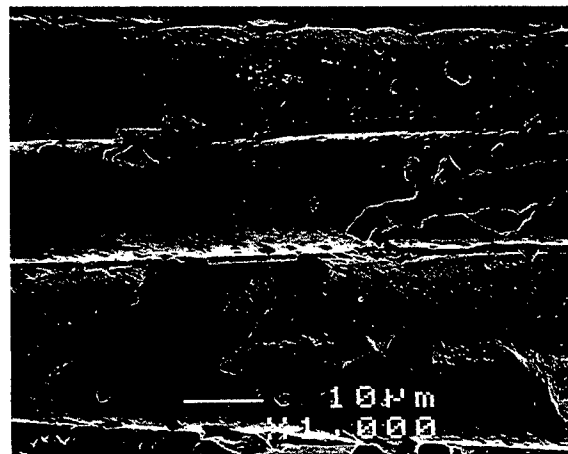


Fig. 11. SEM image of delaminated surface indicating separation at the fiber-matrix interface.

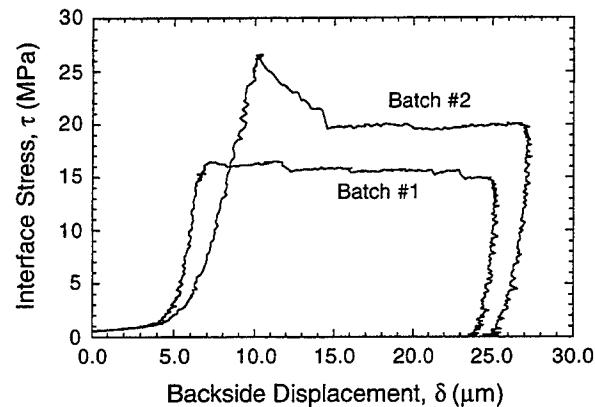


Fig. 12. Typical stress-displacement push-out test results.

delaminations was demonstrated by the X-ray images (Fig. 9), observations of surface ply buckling, and ply separation during sectioning. As shown in Fig. 15, the average distance between these intralaminar cracks has been denoted l_c and the ply thickness has been denoted t_{ply} .

It is this secondary damage which controls the shear strength and enables the large shear strains. The intralaminar cracks break the plies into long blocks. With the intralaminar cracks and ply delaminations, shear deformation is achieved by slip between adjacent blocks and relative ply rotation. The relative ply rotation is needed to maintain compatibility between laminae. This allows for a rigid body shear deformation constrained only by frictional sliding along the intralaminar and delamination crack surfaces. The sliding within one 0° ply is illustrated in Fig. 16. It should be pointed out that in an unconstrained $0^\circ/90^\circ$ laminate, once intralaminar cracking and delamination occur the composite is likely to come apart. In the Iosipescu test of the woven composite, the weave and membrane stresses in the longitudinal fibers will help keep the composite intact.

The anticipated shear stress-strain behavior of this idealized laminate is illustrated in Fig. 16. This is derived from physical arguments. Initially no sliding occurs, and the shear response is linear and elastic. As the primary damage induces sliding and the secondary damage initiates, the tangent modulus decreases and nonlinear behavior is observed. The modulus continues to decrease until the secondary damage is fully developed. Then, rigid body deformation ensues and the shear stress plateaus.

The development of an analytical expression which describes the complete stress-strain behavior is beyond the intent of this

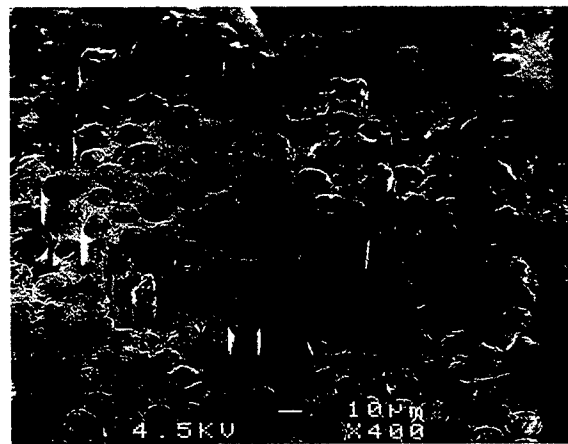


Fig. 13. Example of contiguous cylinder of fibers and matrix displaced in the push-out testing of a batch 2 specimen.



Fig. 14. Push-out interfaces of the (a) batch 1 material and (b) batch 2 material.

research. Rather, the model has been developed to derive a relationship between the plateau stress and the interfacial sliding stresses. It is assumed that the intralaminar crack and delamination surfaces can be characterized by constant sliding stresses, τ_s and τ_r , respectively—the *s* denotes translational sliding at the intralaminar crack surfaces and the *r* denotes rotational sliding at the ply delaminations. Further, to account

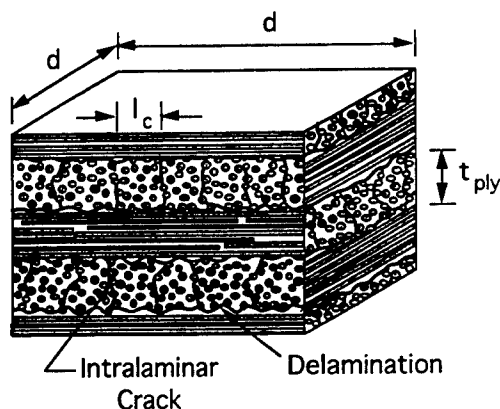


Fig. 15. Idealized 0°/90° laminate showing intralaminar cracks and delaminations.

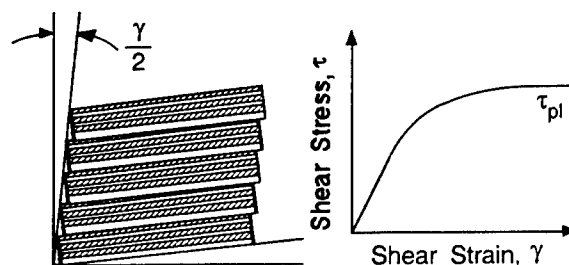


Fig. 16. Schematics of the shear deformation due to sliding along intralaminar crack surfaces and of the anticipated shear stress-strain response of the idealized laminate.

for irregular interfaces, topography coefficients are introduced for each interface and denoted by β_s and β_r . If an interface was flat, β would equal 1.0. Since the observations indicate (see Fig. 11) that these surfaces tend to follow a semicircular path, β is presumed to be equal to $\pi/2$. Based upon these assumptions, the relationship between the plateau stress, τ_{pl} , and the interfacial sliding stress is determined by an energy balance. The work done by the applied shear stress is equated with the energy dissipated by frictional sliding to show that

$$\tau_{pl} = \beta_s \tau_s + 0.38 \beta_r \frac{l_c}{t_{ply}} \tau_r \quad (1)$$

The details of this derivation are provided in the Appendix.

(2) Model Assessment

The push-out test results can be used in conjunction with the model, i.e., Eq. (1), to independently predict the shear strength of the composite. The polished sections indicated that cracking was narrowly spaced within the tows (25–50 μm apart) but more widely spaced in matrix-rich regions ($\sim 100 \mu\text{m}$ apart). Using this larger value as an estimate of the intralaminar crack spacing, along with the ply thickness of 310 μm , and a topography coefficient of $\pi/2$ for both surfaces, Eq. (1) can be rewritten as

$$\tau_{pl} = 1.57 \tau_s + 0.19 \tau_r \quad (2)$$

Equation (2) reveals that the estimates for l_c and t_{ply} are not critical since the first term dominates. If the debond stresses obtained from the push-out tests are used as estimates for both τ_s and τ_r , then Eq. (2) yields predictions of 28 and 49 MPa for the shear strength of the batch 1 and 2 materials, respectively. These values have been plotted alongside the monotonic test results in Fig. 4 and show remarkable agreement.

In addition, the overall responses of the monotonic shear and push-out tests show a strong correlation which supports the conclusion that the shear response is controlled by debonding and sliding along the fiber–matrix interface. First, the stress–displacement plots obtained from the push-out tests (Fig. 12) mimic the monotonic shear stress–strain response (Fig. 4). In both plots, the stronger interface batch 2 material achieves higher stresses and exhibits greater strain softening. Second, the boundary of the ejected material observed in the push-out tests (Figs. 13 and 14) matches the topology of the proposed intralaminar cracks, i.e., one which traverses the matrix and fiber–matrix interface, and justifies the use of the push-out test results in the model.

Further, the experimentally observed cyclic shear stress–strain behavior is consistent with the proposed damage mechanism. The initial response is elastic and then smoothly transitions to a plateau shear stress analogously to that predicted by the model. The continuous reduction in the tangent modulus as the applied load is reversed is consistent with sliding along the fiber–matrix interface. If the reduction in modulus was due to matrix cracking normal to the principal tensile stress, the composite modulus would increase significantly upon the application of negative shear stresses as these matrix cracks closed,

but this is not observed. Instead, the modulus continues to decrease until the shear strain reaches zero. If the delaminated plies reseal at zero strain, the moderate increase in the modulus at this point may be attributed to the additional force needed to again unseat the delaminated plies.

On a separate note, the push-out of a composite cylinder rather than individual fibers can be attributed to tight fiber packing and a low matrix shear strength. The perimeter of 30 fibers pushed out individually would be 1.4 mm, yet the measured perimeter of the cylindrical blocks averaged 0.81 mm. Thus, the cylindrical push-out mode reduces the perimeter length and is energetically favored when the matrix is weak.

IV. Discussion

This model is clearly an idealization. The MDTI CMC has a woven architecture with tightly packed tows and matrix-rich regions. The microscopic evidence indicates profuse cracking within the tows and only moderate cracking in the matrix-rich zones (see Fig. 10(b)). This suggests that uniformly sized blocks spanning each layer are unlikely to form. Instead, the damage will tend to be localized in the tows, which implies smaller values should be chosen for the intralaminar crack spacing and ply thickness. Yet, this would not change the model predictions significantly since, for one, these parameters only affect the relatively small rotational term in Eq. (1) and, two, it's their ratio which affects its magnitude.

The cyclic degradation of the peak shear stress can be attributed to cyclic wear reducing the sliding stress of the interfaces. This is consistent with cyclic behavior reported for other CMC systems.^{12,13} Identifying the mechanisms responsible for the decrease in the unloading modulus is more difficult. It is likely attributed to an increase in the density of matrix cracking and to interface degradation which inhibits shear load transfer, but further work is needed to definitively link the degradation of the unloading modulus with specific composite damage.

Finally, the shear mechanism proposed for this CMC relies to an extent upon the existence of a weak matrix. The porous MDTI CMC fulfills this requirement as best demonstrated by the push-out of a cylindrical composite block rather than individual fibers. It is yet unclear whether this mechanism will apply to a broader class of CMCs which have stronger matrices.

V. Conclusions

Shear loading in this material promotes primary damage in the form of matrix cracking and secondary damage in the form of intralaminar cracks and ply delaminations. These intralaminar cracks run primarily along the fiber-matrix interfaces but also traverse the matrix extending through the ply thickness. The intralaminar cracks and delaminations permit shear deformations by rigid body sliding along their surfaces.

Thus, it is the debonding and sliding characteristics of these interfaces which control the mechanical behavior of the CMC. From the correlation with push-out tests, the shear strength depends upon the debond strength of the fiber-matrix interface. The high failure strains (>3%) and permanent strains are achieved by extensive sliding along the intralaminar and delamination crack surfaces.

APPENDIX

Plateau Stress Evaluation

In the following an expression for the plateau shear stress, τ_{pl} , in terms of the interfacial sliding stresses at the intralaminar and delamination surfaces, τ_s and τ_r , will be derived. The expression is obtained by calculating and equating the work done by the external force to the energy dissipated internally due to sliding.

(1) Work Done by External Force

A simple way of calculating the work done by the external force, τ_{pl} , is to calculate the work done by τ_{pl} along the principal

axis, (x, y) . The external work can therefore be written as the sum of the tensile work done along the x -axis and the compressive work done along the y -axis. Note, the factor of 4 in the following equation accounts for the four plies used in the MDTI CMC as shown in Fig. 15, and d represents the size of a representative block of material deforming in the manner specified by the model:

$$W_{ex} = 4t_{ply}d\tau_{pl}\Delta x + 4t_{ply}d(-\tau_{pl})\Delta y \quad (A-1)$$

This can be simplified to

$$W_{ex} = 4t_{ply}d\tau_{pl}(\Delta x - \Delta y) \quad (A-2)$$

The displacements in the x and y directions are given by the strains

$$\Delta x = \epsilon_x d, \quad \Delta y = \epsilon_y d \quad (A-3)$$

Thus,

$$W_{ex} = 4t_{ply}d^2\tau_{pl}(\epsilon_x - \epsilon_y) \quad (A-4)$$

For pure shear, the difference of the principal strains is equivalent to the shear strain, γ . Thus, the external work can be written as

$$W_{ex} = 4t_{ply}d^2\tau_{pl}\gamma \quad (A-5)$$

(2) Energy Dissipated Because of Sliding within Each Ply

The energy dissipated at the intralaminar crack surfaces due to sliding is just the sum of the work done at each sliding surface (see Fig. A1). Thus,

$$E_{dis}^{int} = \sum_{j=1}^n A_{int} \tau_s \delta_j \quad (A-6)$$

where A_{int} is the area of each interface, τ_s is a constant sliding stress which characterizes these surfaces, and δ_j is the relative displacement of each longitudinal block. The area, A_{int} , can be rewritten as

$$A_{int} = 4\beta_s t_{ply} d \quad (A-7)$$

where β_s is a topography coefficient to account for nonflat interfaces. Substituting Eq. (A-7) into Eq. (A-6) and replacing $\sum \delta_j$ with δ_{tot} yields

$$E_{dis}^{int} = 4\beta_s t_{ply} d \tau_s \delta_{tot} \quad (A-8)$$

Since the total displacement equals the product of the shear strain and the block size ($\delta_{tot} = \gamma d$), then

$$E_{dis}^{int} = 4\beta_s t_{ply} d^2 \tau_s \gamma \quad (A-9)$$

(3) Energy Dissipated Because of Relative Rotation between Plies

Finally, the energy dissipated by rotational sliding between plies must be calculated. Each square ($l_c \times l_c$), l_c represents the

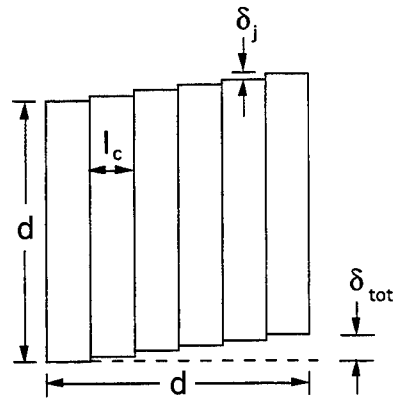


Fig. A1. Sliding shear deformation within a single ply.

distance between intralaminar cracks, rotates relative to the corresponding square in the adjacent ply by an angle equivalent to shear strain. If we examine a differential element on a representative square, the differential work done (dW) by sliding is the product of the sliding force ($\tau_r dA$) and shear strain displacement (γr). Specifically,

$$dW = \tau_r dA \gamma r \quad (\text{A-10})$$

where dA is the area of the differential element and r is its radial distance from the center of the square. The differential area can be expressed as

$$dA = \beta_r r d\phi dr \quad (\text{A-11})$$

where β_r again represents a topography coefficient and $r d\phi$ and dr are the differential arc and radial lengths. To obtain the total energy dissipated in a block ($d \times d$) with four ply interfaces (see Fig. 15), the differential work must be integrated over the square and multiplied by a prefactor which accounts for the four interfaces and the size of the block, d . Thus,

$$E_{\text{dis}}^{\text{rot}} = 4 \frac{d^2}{l_c^2} \left[8 \int_0^{\pi/4} d\phi \int_0^{l_c/2 \cos \phi} \beta_r \tau_r \gamma r^2 dr \right] \quad (\text{A-12})$$

When this integral is solved and simplified, it gives the energy dissipated as a result of rotational sliding as follows:

$$E_{\text{dis}}^{\text{rot}} = 4[0.3826\beta_r d^2 \tau_r \gamma l_c] \quad (\text{A-13})$$

(4) Equating External Work with the Energy Dissipated

The plateau stress can now be evaluated by equating the right-hand side of Eq. (A-5) to the sum of the right-hand sides

of Eqs. (A-9) and (A-13). After simplifying, the following expression for τ_{pl} is obtained:

$$\tau_{\text{pl}} = \beta_s \tau_s + 0.3826\beta_r \frac{l_c}{l_{\text{ply}}} \tau_r \quad (\text{A-14})$$

References

- ¹A. W. Pryce and P. A. Smith, "Matrix Cracking in Ceramic Matrix Composites under Quasi-Static Tensile Loading," *Acta Metall. Mater.*, **41** [4] 1269–81 (1993).
- ²E. Vagaggini, J.-M. Domergue, and A. G. Evans, "Relationships between Hysteresis Measurements and the Properties of Ceramic Matrix Composites: I. Theory," *J. Am. Ceram. Soc.*, **78** [10] 2709–20 (1995).
- ³W. P. Keith and K. T. Kedward, "The Stress–Strain Behaviour of a Porous Unidirectional Ceramic Matrix Composite," *Composites*, **26** [3] 163–74 (1995).
- ⁴K. R. Turner, J. S. Speck, and A. G. Evans, "Mechanisms of Deformation and Failure in Carbon Matrix Composites Subject to Tensile and Shear Loading," *J. Am. Ceram. Soc.*, **78** [7] 1841–48 (1995).
- ⁵P. Brondsted, F. E. Heredia, and A. G. Evans, "In-plane Shear Properties of 2-D Ceramic Matrix Composites," *J. Am. Ceram. Soc.*, **77** [10] 2569–74 (1994).
- ⁶N. J.-J. Fang and T.-W. Chou, "Characterization of Interlaminar Shear Strength of Ceramic Matrix Composites," *J. Am. Ceram. Soc.*, **76** [10] 2539–48 (1993).
- ⁷C. Cady, F. E. Heredia, and A. G. Evans, "The In-Plane Mechanical Properties of Several Ceramic Matrix Composites," *J. Am. Ceram. Soc.*, **78** [8] 2065–78 (1995).
- ⁸H. Li, "Fracture of Aluminum Phosphate/Alumina Matrix Silicon Carbide Fiber Reinforced Laminated Composites," Ph.D. Dissertation, University of Nevada, Reno, NV, February 1992.
- ⁹N. Iosipescu, "New Accurate Procedure for Single Shear Testing of Metals," *J. Mater.*, **2** [3] 537–66 (1967).
- ¹⁰D. E. Walrath and D. F. Adams, "The Iosipescu Shear Test as Applied to Composite Materials," *Exp. Mech.*, **23**, 105–10 (1983).
- ¹¹T. J. Mackin and F. W. Zok, "Fiber Bundle Pushout: A Technique for the Measurement of Interfacial Sliding Properties," *J. Am. Ceram. Soc.*, **75** [11] 3169–71 (1992).
- ¹²J. W. Holmes and C. Cho, "Experimental Observations of Frictional Heating in Fiber-Reinforced Ceramics," *J. Am. Ceram. Soc.*, **75** [4] 929–38 (1992).
- ¹³A. G. Evans, F. W. Zok, and R. M. McMeeking, "Overview No. 18 Fatigue of Ceramic Matrix Composites," *Acta Metall. Mater.*, **43** [3] 859–75 (1995). □

Effect of Matrix Grain Growth Kinetics on Composite Densification

Olivier Sudre^{*,†} and Fred F. Lange^{*}

Materials Department, University of California, Santa Barbara, California 93106

The effect of matrix grain growth kinetics on the densification behavior of a particulate composite has been investigated. Large alumina inclusions were added to two types of zirconia matrices having different grain growth kinetics, i.e., Zr(8Y)O₂ and Zr(3Y)O₂. Despite the evolution of different grain sizes, both matrices reached an end-point relative density of 0.92 and 0.94, respectively, even though they contained 0.25 volume fraction of inclusions (based on total solid volume). However, the morphology and spatial distribution of the residual pores were distinct. The Zr(8Y)O₂ matrix, which developed very large grains, had a dual microstructure with porous regions surrounded by a connective, denser region, as previously reported for an alumina matrix containing zirconia inclusions. Conversely, the Zr(3Y)O₂ matrix was fully dense and uniform, but the composite contained large cracklike voids at inclusion/matrix interfaces. The large opening displacement of these cracklike voids locally relaxed the constraint to matrix shrinkage imposed by the inclusion network.

I. Introduction

THE effect of large inclusions on the matrix densification behavior has been a subject of interest for the past 10 years. Numerous observations have outlined the retardation effect on matrix densification and detailed some characteristic microstructural features (for example, Refs. 1–3). Most of the prominent mechanisms of this phenomenon have already been reviewed.^{4,5}

In particular, a phenomenological model for composite densification has been proposed and several parameters pertaining to both the inclusions and the matrix have been identified.^{4,6,7} The densification process was separated into two stages. In the first stage, inhomogeneous densification of the matrix produced a constraining network whose morphology depended on the inclusion volume fraction, shape, and distribution.^{4,8} In the subsequent stage, the matrix properties determined whether the interstitial porous regions reached full density or developed cracklike pores. In this model, it appeared that the end-point density of the matrix was determined by the creep rate of the dense regions relative to the rate that damage would evolve in the porous regions.⁷ These two competing processes were closely related to the grain growth and the coarsening behaviors of the matrix. In particular, it was inferred from the microstructural observations that grain growth in the dense regions of the matrix would increase the creep resistance of these regions, and thereby limit the final densification. With this hypothesis, it is expected that the densification of a composite matrix that exhibited slow grain growth kinetics should be beneficial in allowing more creep deformation of the constraining dense regions, and thus a denser composite.

Therefore, the objective of this work was to test the hypothesis that slow grain growth and, hence, a low creep strength of the dense regions are necessary conditions for composite densification. This goal can be tested with a zirconia-based

matrix since its grain growth kinetics depends strongly on the amount of yttria in solid solution.⁹ Consequently, experiments based upon two different Zr(Y)O₂ matrices, i.e., Zr(3Y)O₂ and Zr(8Y)O₂, that exhibit different grain growth kinetics, each containing 25 vol% Al₂O₃ inclusions, were designed to test the hypothesis.

II. Experimental Procedure

Two zirconia (ZrO₂) matrices (TZ-3Y and TZ-8Y, Tosoh U.S.A., Inc., Atlanta, GA) containing either 3 or 8 mol% yttria (Y₂O₃) were chosen in order to control the grain size during the densification of the matrix. Grain growth in zirconia is very slow in the two-phase region of the ZrO₂–Y₂O₃ between ≈1 to ≈7 mol%, whereas on either side of this compositional range, grain growth is rapid.⁹

The ZrO₂ + 3 mol% Y₂O₃ (Zr(3Y)O₂) and ZrO₂ + 8 mol% Y₂O₃ (Zr(8Y)O₂) powders were colloidal prepared.¹⁰ The powder was dispersed at pH 3 by adding HNO₃ to an aqueous solution, and then subjected to an ultrasonic treatment to break up soft agglomerates. The dispersed powder was then sedimented to remove hard agglomerates >1 μm. The slurries were subsequently concentrated to a higher solid loading by centrifugation. Flocculation of the slurry was avoided to prevent the addition of salts and to facilitate the redispersion of the slurry after concentration; this centrifugation technique had the drawback of removing a portion of the smallest particles. During the slurry concentration process, some HNO₃ was added to maintain a pH of 3. The final aqueous slurries of ZrO₂–3 mol% Y₂O₃ and ZrO₂–8 mol% Y₂O₃ had a solid content of 40 and 37 vol%, respectively.

Dense Al₂O₃ inclusions, 38–53 μm in size, were prepared by sieving coarse, fused Al₂O₃ powder (Alcoa, T-64/325LI, Bauxite, AR). Al₂O₃–Zr(Y)O₂ composites containing 0.25 volume fraction of Al₂O₃ inclusions, based on total solid content, were prepared by thoroughly mixing the inclusions with the dispersed slurry. Both slurries were sufficiently viscous to prevent mass segregation of the Al₂O₃ inclusions. Disk-shaped specimens (2.5 cm diameter × 0.8 cm) were consolidated by using pressure-filtration¹¹ at 5 MPa. After consolidation, the bodies were dried at room temperature over a period of a few days and then oven-dried at 60°C. The matrix particle packing prior to drying was determined by measuring the weight before and after drying.

The disks were initially heated to 1000°C for 30 min to impart some strength to the powder compacts before they were sectioned into six specimens. The different specimens were subsequently heated at a rate of 5°C/min to temperatures ranging from 1100° to 1600°C without any isothermal hold and furnace cooled. Additional specimens were heated for 5 h at 1600°C. Density was measured using the Archimedes principle in deionized water. Specimens were ground, polished, and thermally etched to reveal grain boundaries. Microstructural observations were performed by scanning electron microscopy (SEM) (840-ASM, JEOL, Peabody, MA).

III. Results

The densification behaviors of the two composites and of the respective matrices without inclusions are shown in Fig. 1. The

L. C. De Jonghe—contributing editor

Manuscript No. 191831. Received May 13, 1996; approved January 11, 1997.
*Member, American Ceramic Society.
Now at ONERA, F-92322 Chatillon Cedex, France.

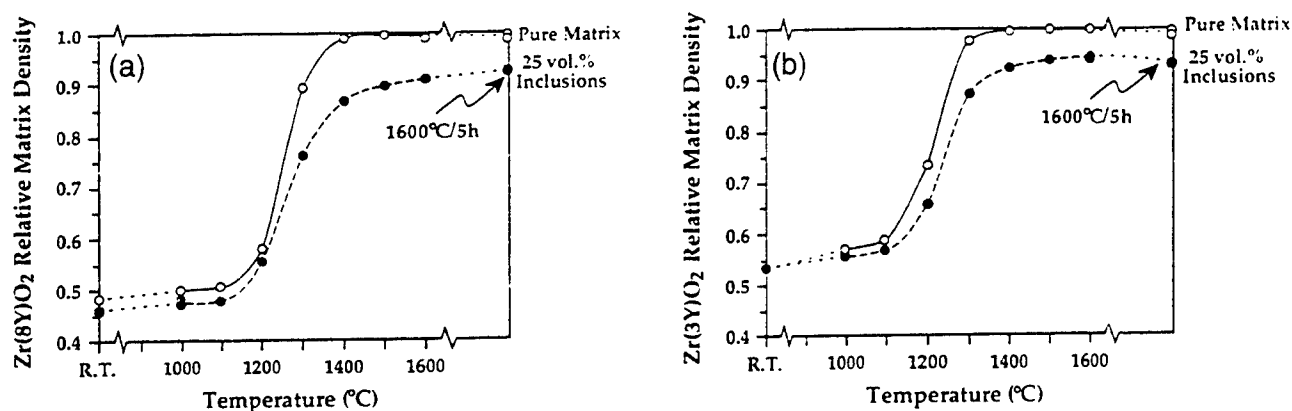


Fig. 1. Densification behavior of (a) $0.25\text{Al}_2\text{O}_3\text{-Zr(8Y)O}_2$ composite and (b) $0.25\text{Al}_2\text{O}_3\text{-Zr(3Y)O}_2$ composite and of their respective pure matrices.

relative density of the powder matrix without inclusions was 0.48 and 0.54 for the Zr(8Y)O_2 and Zr(3Y)O_2 powders, respectively. Calculations based on the composite density showed that the Zr(3Y)O_2 matrix had a relative density identical to that of the matrix without inclusions, whereas the Zr(8Y)O_2 matrix was reduced by 2%. The Zr(3Y)O_2 matrix without inclusions densified to nearly theoretical density at 1300°C , whereas the Zr(8Y)O_2 matrix became fully dense at 1400°C . As expected, the presence of the inclusions perturbed the densification of both matrices. Even though matrix densification in the composite was constrained by the inclusions, a maximum density of 0.92 and 0.94 was achieved for the Zr(8Y)O_2 and Zr(3Y)O_2 composites, respectively, at a higher temperature, relative to the matrix alone. As shown in Fig. 1, densification appeared more rapid for the Zr(3Y)O_2 composite.

Composite densities were correlated to microstructural observations. Both composites had a well-dispersed inclusion phase. Microstructures for a heat treatment at 1500°C are shown for the two composites in Fig. 2. The microstructure of the Zr(8Y)O_2 matrix resembles that of the previously reported⁴ Al_2O_3 matrix containing ZrO_2 inclusions (Fig. 2(a)). It has a dual microstructure composed of porous regions surrounded by a connective, denser material. The grain size in the porous regions is small, but larger than the initial particle size. In the denser regions, the grains grew to several micrometers, similar to the dense material without inclusions. In addition, large cracklike voids are observed at some inclusion/matrix interfaces. After heat treatment at 1600°C for 5 h, the grain size increased to several micrometers in most regions. The porous regions retained some residual, isolated porosity, resulting, in part, from trapped porosity during grain growth. The large

cracklike voids at the inclusion interface were still present after the $1600^\circ\text{C}/5\text{ h}$ heat treatment.

As shown in Fig. 2(b), the microstructure of the Zr(3Y)O_2 matrix evolved in a more homogeneous manner. No differential densification could be observed after the 1200° and 1500°C heat treatments. The main feature of this microstructure is the presence of a large number of cracklike voids. These voids, with a size comparable to the inclusion size, were primarily located along the inclusion/matrix interface. Grain bridges were often observed across the void as shown in Fig. 3. These bridges were often elongated, and on the verge of desintering (Fig. 3(b)), as described elsewhere.⁷ Upon reaching the edge of the inclusion, the cracklike void apparently blunted, and opened during subsequent heat treatments. As expected, the grain size of the Zr(3Y)O_2 matrix remained small, on the order of $0.4\text{ }\mu\text{m}$, throughout the matrix for specimens heat-treated below 1500°C .

IV. Discussion

The presence of the Al_2O_3 inclusions constrained the densification of both matrices. Although the end-point densities of the Zr(8Y)O_2 and Zr(3Y)O_2 matrices were nearly identical, i.e., 0.92 and 0.94, respectively, the location of the residual porosity was different. Most of the residual porosity was located within the Zr(8Y)O_2 matrix in the form of density variations similar to that previously observed⁴ for the Al_2O_3 matrix containing ZrO_2 inclusions. Some cracklike voids at matrix/inclusion interfaces can also be noticed. For the Zr(3Y)O_2 matrix, the matrix became fully dense, and the residual porosity was solely located along inclusion/matrix interfaces, in the form of cracklike voids with large opening displacements. Microstructural observations

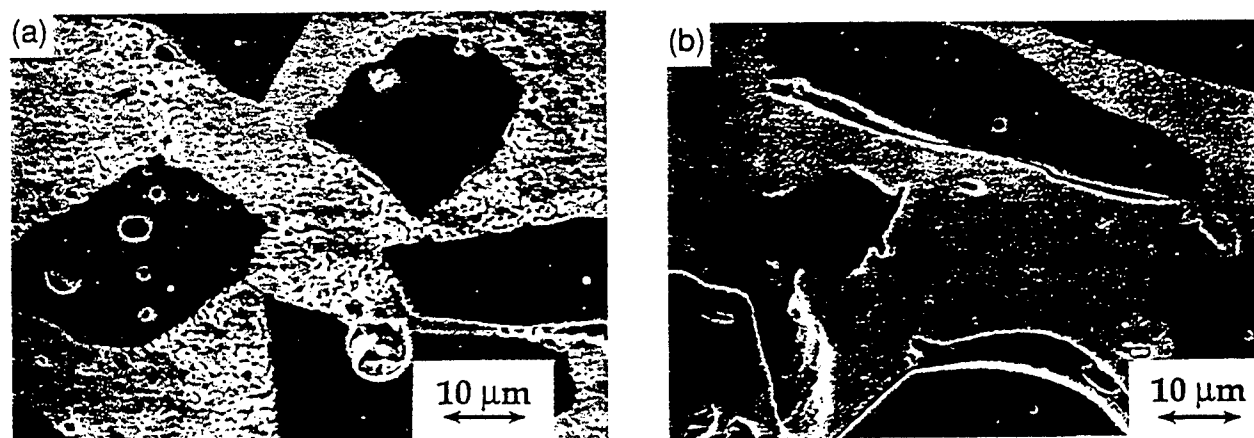


Fig. 2. Microstructural observations of (a) the $0.25\text{Al}_2\text{O}_3\text{-Zr(8Y)O}_2$ composite sintered at 1500°C , showing the inhomogeneous matrix densification and the grain size differential. (b) the $0.25\text{Al}_2\text{O}_3\text{-Zr(3Y)O}_2$ composite sintered at 1500°C showing the formation of large cracklike voids and the full densification of the matrix.

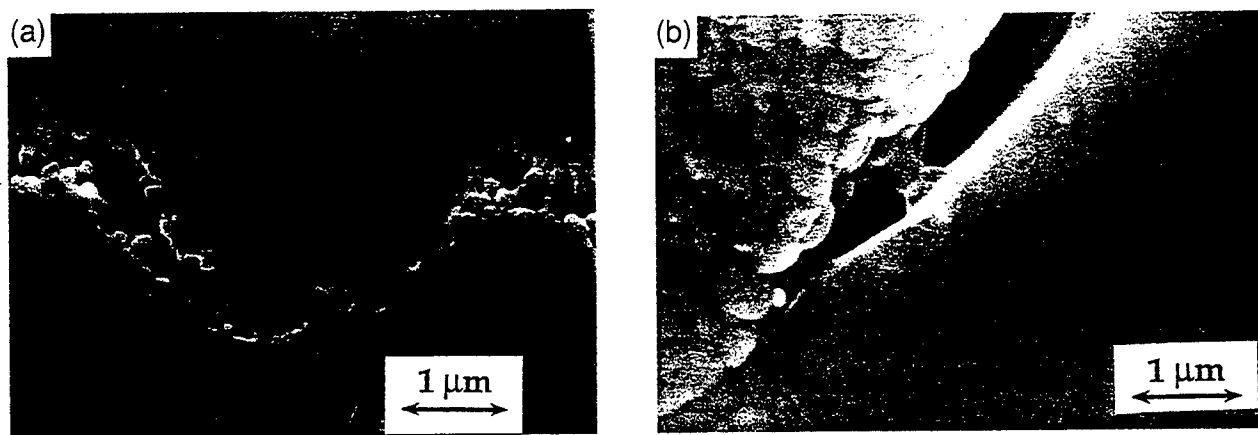


Fig. 3. Matrix/inclusion interface showing the elongated bridges at the tip of a cracklike void: (a) 1200°C and (b) 1500°C.

represented by Fig. 3 clearly show that the desintering of grain bridges was a dominating phenomenon at matrix/inclusion interfaces. Why the desintering phenomenon is more rapid and prevalent at the matrix/inclusion interface for the Zr(3Y)O_2 matrix, relative to within the matrix for the Zr(8Y)O_2 material, might be explained by the grain size difference of the two matrices.

The initial green microstructure of the two composites can be assumed to be equivalent. In particular, both matrices have comparable packing densities but they certainly exhibit a lower powder packing density next to the inclusion surface as detailed elsewhere.¹² Therefore, similar incipient flaws preexist in both composites. During the initial stage of densification, both matrices are relatively unconstrained up to the point where regions between closely spaced inclusions become dense and begin to constrain other remaining porous regions. After this similar initial densification stage, the porous regions are kinematically constrained from densifying and the microstructure will tend to reduce its surface to volume energy by a desintering mechanism.

The difference of behavior of the two matrices certainly occurs during the course of densification due to three causes. First, the much smaller grain size of the Zr(3Y)O_2 material maintains a larger driving potential to densify the matrix. Therefore, the force acting upon any given grain bridge in the matrix would be larger in the Zr(3Y)O_2 matrix, relative to the Zr(8Y)O_2 matrix. Second, the desintering phenomenon depends on a grain pair achieving a critical bridge length between adjacent regions; this critical bridge length depends on grain size.⁷ That is, the smaller the grain size, the smaller the displacement needed to "break" the grain bridge by desintering. Third, the desintering process localizes preferentially at the inclusion/matrix interface because the weakest site in the Zr(3Y)O_2 composite is next to the inclusion surface due to its lower initial packing density. Once a cracklike void has nucleated along the inclusion surface, stress and strain concentrations arise at the tip of the crack and scale with the square root of crack length. Therefore, the combination of a large crack opening driving force, a small grain size, and an increasing crack length all contribute to the rapid growth of these large defects along the inclusion/matrix interface. This mechanism is closely related to that described in creep-crack growth theories,¹³ except that in our case, the applied stress is provided by the driving force for densification of the adjacent porous region. On the contrary, subsequent to the rapid matrix grain growth in the Zr(8Y)O_2 in the initial densification stage, the driving force is smaller and most pores along the inclusion surface become of a size comparable to that in the bulk of the matrix, thereby not providing a preferential site for cracklike void nucleation and growth.

Thus it can be argued that the much smaller grain size in the Zr(3Y)O_2 matrix allows it to achieve a higher density because

of its higher driving potential for densification, where concurrently, the relaxation of the constraint produced by the inclusions occurs by the opening of cracklike voids at the most porous site, i.e., at the matrix/inclusion interface. According to that same grain size argument, the microstructure evolves rapidly to reach the end-point density. Because of its much larger grain growth kinetics, the microstructure of the Zr(8Y)O_2 matrix becomes more resistant to a localized desintering instability. The porous regions are more homogeneous and the time required to reach the final microstructure appears beyond the experimental time frame of the current experiments. The final microstructure might also be different because of the more widespread location for cracklike void growth.

V. Conclusion

Decreasing the grain growth kinetics in the ZrO_2 matrix apparently affected the densification kinetics and the spatial distribution and kinetics of the damage formed in the porous regions as it certainly influenced the deformation rate of the initially denser regions. Because of these different competing phenomena, the differential grain size of the two matrix phases did not have the profound effect on composite density as initially expected, but it did hasten the development and alter the morphology of the end-point microstructure.

References

1. C. De Jonghe, M. N. Rahaman, and C. H. Hsueh, "Transient Stresses in Bimodal Compacts During Sintering," *Acta Metall.*, **34** [7] 1467-71 (1986).
2. R. K. Bordia and R. Raj, "Sintering of TiO_2 - Al_2O_3 Composites: A Model Experimental Investigation," *J. Am. Ceram. Soc.*, **71** [4] 302-10 (1988).
3. W. H. Tuan, E. Gilbart, and R. J. Brook, "Sintering of Heterogeneous Ceramic Compacts, Part I: Al_2O_3 - Al_2O_3 ," *J. Mater. Sci.*, **24**, 1062-68 (1989).
4. O. Sudre and F. F. Lange, "Effect of Inclusions on Densification: I. Microstructural Development in an Al_2O_3 Matrix Containing a High Volume Fraction of ZrO_2 Inclusions," *J. Am. Ceram. Soc.*, **75** [3] 519-24 (1992).
5. C.-L. Fan and M. N. Rahaman, "Factors Controlling the Sintering of Ceramic Particulate Composites: I. Conventional Processing," *J. Am. Ceram. Soc.*, **75** [8] 2056-65 (1992).
6. O. Sudre, G. Bao, B. Fan, F. F. Lange, and A. G. Evans, "Effect of Inclusions on Densification: II. Numerical Model," *J. Am. Ceram. Soc.*, **75** [3] 525-31 (1992).
7. O. Sudre and F. F. Lange, "Effect of Inclusions on Densification: III. The Desintering Phenomenon," *J. Am. Ceram. Soc.*, **75** [12] 3241-51 (1992).
8. W. Hong and L. R. Dharani, "Pressureless Sintering of a Ceramic Matrix with Multiple Rigid Inclusions: Finite Element Model," *J. Am. Ceram. Soc.*, **78** [6] 1593-600 (1995).
9. F. F. Lange, "Transformation Toughened ZrO_2 : Correlations Between Grain Size Control and Composition in the System ZrO_2 - Y_2O_3 ," *J. Am. Ceram. Soc.*, **69** [3] 240-42 (1986).
10. F. F. Lange, B. I. Davis, and E. Wright, "Processing-Related Fracture Origins: IV. Elimination of Voids Produced by Inorganic Inclusions," *J. Am. Ceram. Soc.*, **69** [1] 66-69 (1986).
11. K. T. Miller and F. F. Lange, "Pressure Filtration: Consolidation Kinetics and Mechanics," *Am. Ceram. Soc. Bull.*, **66** [10] 1498-504 (1987).
12. D. Bouvard and F. F. Lange, "Correlation Between Random Dense Packing and Random Dense Packing for Determining Particle Coordination Number in Binary Systems," *Phys. Rev. A*, **45** [8] 5690-93 (1992).
13. M. Thouless, "Models of Creep Crack Growth in Ceramics," Ph.D. Thesis, University of California, Berkeley, CA, July 1984.

ANISOTROPIC DAMAGE EVOLUTION IN UNIDIRECTIONAL FIBER REINFORCED CERAMICS

Y. M. Liu, T. E. Mitchell

Center for Materials Science, Mail Stop K765

Los Alamos National Laboratory, Los Alamos, NM 87545, U. S. A.

and

H. N. G. Wadley

Department of Materials Science and Engineering

School of Engineering and Applied Science

University of Virginia, Charlottesville, VA 22903, U. S. A.

Abstract

Damage transverse to the loading direction of a unidirectionally reinforced ceramic matrix composite has been observed and characterized by ultrasonic methods and acetate replicas. A laser-ultrasonic technique was developed and used to measure the ultrasonic velocity anisotropy, thus the complete elastic stiffness tensor, during uniaxial tensile loading/unloading of calcium aluminosilicate (CAS) composites reinforced by Nicalon™ SiC fibers. Acoustic emission and surface replica observations link degradation of the axial stiffness to the accumulation of matrix cracks normal to the loading (and fiber) direction. The substantial loss of transverse stiffness is proposed to originate from fiber/matrix

interface debonding near matrix cracks. These observations may significantly impact the constitutive models used to design multiaxially loaded ceramic matrix composites.

1. INTRODUCTION

Ceramic matrix composites (CMCs) have attracted interest for high temperature structural applications because of their substantial toughness enhancement compared to monolithic ceramics and their high specific elastic moduli. The enhanced toughness is only obtained when the fiber/matrix interface is relatively weak [1-6]. This can be achieved when a thin carbon-rich layer exists between a Nicalon SiC fiber and its calcium aluminosilicate (CAS) matrix. CAS/SiC glass-ceramic composites with weak interfaces exhibit a large nonlinear deformation and have significant damage tolerance under tensile loading, as a result of extensive multiple matrix cracking and interfacial debonding/sliding [5,7,8]. These materials are then relatively notch-insensitive because the stress at concentrators (such as attachments and holes) is redistributed through inelastic strain (matrix cracking process), and the risk of their catastrophic failure is significantly reduced from that of conventional ceramics [9-11].

In the past, CMC damage in the form of matrix cracking was often characterized by the change of Young's modulus measured by the partial unloading of a sample during tensile testing [7,12,13]. The stiffness reductions were observed to accompany nonlinear deformation, and were experimentally correlated to the change of matrix crack density in the loading direction. These observations have formed the experimental basis for the subsequent development of micromechanical constitutive models that are now used for mechanical design [8,10]. However, the Young's modulus measurements provide little insight about damage that might occur in other orientations due, for example, to fiber-matrix interface debonding. Degradation of moduli in these other orientations could lead

to premature failure under multiaxial loading near points of attachments, holes or at notches. An efficient experimental methodology is therefore needed to measure and assess the complete anisotropic stiffness degradation. Such information could lead to a better understand of the damage mechanisms as well as providing essential information for constitutive modeling and for CMC design. In this study, nondestructive laser-ultrasonic and acoustic emission techniques have been used to explore the anisotropic, strain dependent, damage evolution of unidirectional CAS/SiC under uniaxial tension. The ultrasonic approach extends early work by Baste *et. al* [14] who used a water bath to conduct conventional ultrasonic measurements and found a correlation between the wave velocity and CMC damage.

The ultrasonic evaluation of anisotropic damage is based on a reduction in elastic stiffness tensor components as a result of the collective effect of microcracks. The elastic stiffness components can be deduced from measurements of ultrasonic wave velocities in different propagation directions. Elastic wave propagation velocities in anisotropic media are given by solutions to the well-known Christoffel equation [15]

$$\det[C_{ijkl} n_j n_l - \rho V^2 \delta_{ik}] = \Omega(V, \mathbf{n}) = 0, \quad (1)$$

where C_{ijkl} are the elastic stiffness constants of the material, \mathbf{n} is a unit vector in the wave propagation direction, ρ is the density of the medium, V is the elastic wave's phase velocity and δ_{ik} is the Kroneker delta. Wave velocities measured along various propagation directions can be used to determine the elastic constants C_{ijkl} using Eq. (1).

Elastic constant measurements have been made in undeformed CAS/SiC composites using a resonant ultrasonic spectroscopy (RUS) technique [16]. Results have

shown that undamaged unidirectional CAS/SiC composites are transversely isotropic with the elastic constants given in Table 1. For a transversely isotropic material, there are five independent elastic stiffness components: C_{11} , C_{33} , C_{44} , C_{12} , and C_{13} , while $C_{22} = C_{11}$, $C_{23} = C_{13}$, $C_{55} = C_{44}$ and $C_{66} = (C_{11} - C_{12})/2$, where the $1-2$ directions form the plane perpendicular to the fiber direction. Based on transversely isotropic symmetry, analytical expressions for the three unique phase velocities in the $1-3$ plane ($n_2 = 0$) can be derived from Eq. (1) [15]. Two of these correspond to a quasi-longitudinal (QL) mode with a velocity

$$V_{QL} = \sqrt{\frac{a + \sqrt{b}}{2\rho}}, \quad (2)$$

and a quasi-shear (or quasi-transverse) mode (QT) with a velocity

$$V_{QT} = \sqrt{\frac{a - \sqrt{b}}{2\rho}}, \quad (3)$$

where

$$a = (C_{11} + C_{55})\cos^2 \theta + (C_{33} + C_{55})\sin^2 \theta, \quad (4)$$

and

$$b = [(C_{11} - C_{55})\cos^2 \theta - (C_{33} - C_{55})\sin^2 \theta]^2 + 4(C_{13} + C_{55})^2 \sin^2 \theta \cos^2 \theta. \quad (5)$$

The third is a pure shear (or pure transverse) mode (PT) with velocity

$$V_{PT} = \sqrt{\frac{C_{66} \cos^2 \theta + C_{44} \sin^2 \theta}{\rho}}, \quad (6)$$

where θ is the angle between the wave propagation direction and the 1 -axis.

Similarly, in the $1-2$ transversely isotropic plane ($n_3 = 0$), it is easy to show that

$$V_{PL} = \sqrt{\frac{C_{11}}{\rho}} \quad (7)$$

$$V_{PT1} = \sqrt{\frac{C_{44}}{\rho}} \quad (8)$$

$$V_{PT2} = \sqrt{\frac{C_{66}}{\rho}} \quad (9)$$

Point source laser ultrasonic techniques enable precise measurements of wave propagation speeds between precisely defined locations on a sample. In a laser-ultrasonic approach, an ultrasonic pulse is generated by optical absorption, and its time of flight over a known distance is sensed either optically or in the study here, using point-like piezoelectric transducers. Since one measures the time of flight of a pulse, one strictly measures a group velocity. The RUS results for CAS/SiC indicated however that the difference between the phase velocity and group velocity was negligible, consistent with the small elastic anisotropy of this material system.

It should be pointed out that at the microscopic scale, composites are heterogeneous media with differing elastic constants in each phase. However, when the ultrasonic wave length is long compared with the length scale of the inhomogeneity, the medium responds as an equivalent homogeneous medium [17]. This is the case for the composite material used in this study. In this situation, the complexity of wave reflection and refraction at the interfaces between the different material phases can be neglected, and elastic constants approximate well those of an equivalent homogeneous medium.

In addition to the wave velocity measurements, damage evolution can also be detected by acoustic emission (AE) techniques. This approach has previously been used to

detect matrix crack initiation and damage evolution in CMCs [18,19] Acoustic emissions are elastic waves generated by sudden changes in the stress state within a body. In ceramics, these are usually associated with the formation of cracks [20,21]. The radiated elastic waves cause surface displacements that can be detected by piezoelectric sensors attached to the sample surface [21]. In the present work, AE events were recorded during loading/unloading and were combined with surface replica observations to link the evolution of damage to the macroscopic stress-strain behavior. We note that laser-ultrasonic and AE techniques are both examples of dynamic elastic test methods. Laser-ultrasonic measurements convey information about the accumulated damage state; AE signals reveal when, during loading, the individual damage events occur. We have explored the use of both measurements to try and better understand the damage mechanisms and their evolution in a representative unidirectional ceramic matrix composite.

2. EXPERIMENTAL PROCEDURE

2.1 Specimens

Unidirectional CAS/SiC composite material was provided by Corning Inc. (New York). It consisted of multiply laminae with the fibers aligned in one direction. The manufacturing procedure and material properties have been described elsewhere [7,16]. The Nicalon™ SiC fiber volume fraction was about 0.35, the average fiber diameter was 15 μm , the Young's modulus of the fiber was 200 GPa and that of the matrix was 97 GPa.

A carbon-rich interface was formed between fiber and matrix during fabrication, and plays an important role in the deformation of Nicalon fiber reinforced ceramics [1,2,5,6]. The CAS matrix has a higher thermal expansion coefficient ($\sim 5 \times 10^{-6} \text{ }^{\circ}\text{C}^{-1}$) than that of the fiber ($\sim 4 \times 10^{-6} \text{ }^{\circ}\text{C}^{-1}$) [7]. Thus, the matrix is under axial residual tension and the interface is under radial compression after cooling from processing [7,22]. Fiber push-out tests indicate a modest interface sliding resistance of about 16 MPa [23].

Tensile test specimens were cut from the plate using a low-speed diamond saw. The specimens were 150 mm in length, 10 mm in width and 3 mm in thickness. The fibers were oriented parallel to the loading direction (the long direction of the specimen). Aluminum tabs were bonded to the sample ends using a modified epoxy. To metallographically detect matrix cracks, the side surfaces of two of the samples were polished prior to tensile testing and acetate replicas were taken at different stress levels during continuous loading test. Fracture surfaces of testing samples were also analyzed by scanning electron microscopy (SEM) using a JOEL JSM 6300 FXV.

2.2 Tensile testing

Tensile testing was performed at a cross-head speed of 0.02 mm/min using a computer controlled screw driven machine equipped with a 50 kN load cell. Axial strain was measured with a one-inch gauge length extensometer in contact with the sample in the gauge section. Care was taken to avoid over-tightening the extensometer which could lead to premature failure at its contact positions with the sample.

Load-extension information during testing was recorded and stored in a personal computer using LabVIEW program (National Instrument). For each experiment, load was allowed to increase to a pre-set level and then held at that level while laser-ultrasonic measurements were made. The stress was then reduced to 10 MPa, and the laser-ultrasonic measurements repeated. The entire measurement procedure was repeated to progressively higher stress levels. Acoustic emission events were also recorded throughout both the loading and unloading process.

2.3 Laser-ultrasonic measurements

The use of a pulsed laser to generate a broad band acoustic pulse is now well established [24,25]. Three basic mechanisms of ultrasonic generation have been identified:

(I) The thermoelastic regime. Absorption of a low power pulse causes a rapid localized rise of temperature, which results in a transient (dilatational) thermoelastic stress. Stress components normal to the surface are relaxed at the surface and the stress is approximately biaxial in the plane of the surface. In isotropic materials, the elastic waves generated from this type of thermoelastic expansion mechanism are most energetic in a cone at $\sim 60^\circ$ to the surface.

(II) The constrained surface source. In this regime, the ultrasonic amplitude of the thermoelastic mechanism is enhanced by applying a transparent coating to the irradiated surface. This constrains the stress relaxation normal to the sample surface and significantly enhances the signal strength, especially normal to the sample surface.

(III) The plasma regime. At high incident power densities, surface melting and evaporation occur, resulting in material ablation, and the formation of a plasma above the sample surface. The momentum of the evaporated material exerts a force on the sample, causing a reactive stress at the surface. This generates an intense broad-band ultrasonic source, whose strongest components are directed normal to the surface.

In this study, vacuum grease was applied to the sample surface to enhance the signal, and ultrasound was thus generated by a combination of I, II and III above.

Fig. 1 is a schematic diagram of the test set up. Fig. 2 shows the positions of the piezoelectric sensors and defines material coordinates used later. The laser source was a 7 ns duration Q-switch Nd:YAG laser pulse with a wavelength of 1.064 μm . To deliver the laser pulse to the sample during loading, a multimode step-index 5m long optical fiber with a 600 μm core diameter was used [26,27]. A pulse energy of about 5 mJ was chosen to avoid damage to both the optical fiber and the specimen. A small convex lens conveniently coupled the laser beam into one end of the optical fiber. A two convex lens setup was used to focus the outcoming beam from the fiber onto to the sample. This was attached to a PC controlled two axis positioner that provided source position control to about a micron level of precision. Laser source scanning along the two principal directions shown in Fig. 2 was thus accomplished.

A small portion of the laser pulse was deflected onto a photodiode and used to trigger a pair of 8-bit, 1 GHz digital oscilloscopes to which the signals from the two ultrasonic transducers were also connected. These transducers were of a broad band conical design with a small (1.0 mm) aperture [28]. Their signals were amplified and low

pass filtered at 10 MHz before digitization and recording. The arrival time of the acoustic pulse was measured by observing the difference in time between the photodiode and transducer pulse. The systematic delay arising from the propagation of laser pulses through the optical system was measured and subtracted from the wave arrival time detected by the sensor attached to the sample. The time of flight measured in this way had a precision of ± 5 ns.

Using the ultrasonic velocities measured within the principal I -2 and I -3 planes, we were able to determine the elastic constants of CAS/SiC at different damage states. C_{11} was determined directly from the longitudinal wave velocity at the epicenter position using Eq. (7). In the transversely isotropic plane, C_{44} and C_{66} can be deduced from the shear wave speed. However, the magnitude of C_{44} and C_{66} are too close to each other (Table 1), and it is difficult to distinguish the signals in the wave forms. As a result, we used the approximation $C_{44} \approx C_{66}$, and determined C_{44} (C_{66}) by averaging the shear velocity at different scan positions in the I -2 transversely isotropic plane.

After C_{11} , C_{44} and C_{66} were determined, the longitudinal wave velocities along fifteen different directions within the principal I -3 plane were used for curve fitting to determine the unknown elastic constants C_{33} and C_{13} , using the solution of the Christoffel equation. Again, the two shear modes are not clearly distinguished, thus identifying C_{33} and C_{13} was based on the longitudinal wave speeds using Eq. (2) through a nonlinear curve fitting process. Once all the independent elastic constants were determined, the ultrasound velocities for various modes were calculated as a function of propagation direction.

2.4 Acoustic emission

During loading and unloading, acoustic emission events were detected by the same two transducers used to detect the laser generated ultrasound. These signals were band pass filtered between 20 kHz and 2 MHz to reduce background noise. AE waveforms were recorded on the digital oscilloscopes. A total of 20,000 data points were recorded with a 2.5 nsec sample interval and the integrated root-mean square (RMS) average of the waveform amplitude was calculated for every recorded waveform.

3. RESULTS

3.1 Stress-strain and acoustic emission behavior

Fig. 3 shows a typical loading/unloading stress-strain curve and the accompanying acoustic emissions. In the nominally linear portion of the stress-strain curve (up to the elastic limit ~ 140 MPa), a few AE events were detected. The deformation processes responsible for these emissions have no discernible effect on the macroscopic deformation behavior, and are presumed to arise from extension of defects created either during fabrication or machining of the test samples. Young's modulus obtained from the slope of the stress-strain curve for several tensile specimens was in the range of 125 GPa to 133 GPa.

Beyond the linear regime, AE events started to accelerate. This can be seen in Fig. 3 and more clearly by the accumulation of the AE in Fig. 4 (a). This acceleration of AE

events near 140 MPa was also observed in two of the other tested samples. It was accompanied by macroscopic nonlinear deformation and a composite stiffness decrease. This could be characterized by the reduction of Young's modulus measured by partial unloading. Effective Young's moduli at various peak stress levels determined by partial unloading ($\Delta\sigma = 20$ MPa) are given in Fig. 4(b) (solid line). The unloading modulus started to decrease rapidly when the stress reached 200 MPa, where wide-spread matrix cracking was observed to have occurred (see below). The effective elastic modulus had changed little when the sample was unloaded from either 270 MPa or 320 MPa. During later deformation stages, the fibers carried an increased fraction of the load, and the stress-strain curve showed a "stiffening" effect, as indicated in Fig. 3. Acoustic emission events recorded in the later deformation stage could be the result of fiber fracture, and continued localized (short) matrix cracking.

During unloading from 320 MPa, a number of AE events (~25) were observed. In contrast, only one or two AE signals were recorded when unloading from lower stress either 200 MPa or 270 MPa. AE events during unloading could have originated from crack closure (rubbing) or the nucleation of new matrix cracks. For most reloading paths, AE did not occur until near the previous stress level, in agreement with previous acoustic emission studies [18,19]. However, at higher stress loading, AE events reoccurred well before reaching the previous stress level (e.g. when 270 MPa was reached). These observations suggest that unloading/reloading does not contribute to significant additional damage when the previously applied stress was moderately low, but that it can occur in more highly stressed samples.

3.2 Matrix cracking during loading

The development of matrix surface cracks was observed from optical micrographs of acetate replicas ($\sim 3 \text{ mm} \times 10 \text{ mm}$) taken during *continuous* testing up to failure (stress-strain behavior and AE are not presented here). Figs. 5(a)~(e) show matrix cracks at five progressively higher stresses. Surface cracks were first detected at a stress level of $\sim 140 \text{ MPa}$ (see arrow in Fig. 5(a)). At a lower stress level, no visible surface damage was detected, even though a few AE events were recorded. These AE events are therefore attributed to internal cracks that do not extend to the sample surface. When the stress was increased to 168 MPa , the original crack presented in Fig. 5(a) (indicated by the arrow) extended, and new cracks were nucleated nearby, Fig. 5 (b). These two micrographs clearly show that the matrix cracks formed early in the loading process do not spread over the entire sample cross section, and the cracks are not uniformly distributed in the loading direction, as usually assumed in current modeling approaches [10, 29]. Replicas made on another sample loaded up to 220 MPa also showed the same crack initiation behavior.

The stress-strain curve started to deviate from its original linear slope with the development of the matrix cracking. Fig. 5(c) shows that at 200 MPa matrix cracks had spread to a wider area compared to Fig. 5(b). By the time the stress had reached 230 MPa , the surface replicas indicated that matrix cracks were approximately evenly distributed, Fig. 5(d). The crack density continued to increase rapidly up to a stress level of $\sim 270 \text{ MPa}$, Fig. 5(e), and saturated. The matrix crack density as a function of stress is plotted (dashed line) in Fig. 4(b). In tests that were not used for laser-scan measurements,

AE events were observed to increase in the same stress range over which the matrix crack density increased rapidly (according to the replica results on the same sample). The increase of the matrix crack density was thus strongly correlated with a reduction of the axial elastic modulus, and increased AE.

As an aside we have noted that when tests were interrupted, as shown in Fig. 3, relatively few AE events subsequently occur in the stress range 200-240 MPa where nonlinear deformation is prevalent. We observed a substantial amount of inelastic strain while holding at 200 MPa to perform ultrasonic measurements (piezoelectric sensors recorded laser-generated ultrasound, *not* AE during this period). A significant amount of damage seemed to have accumulated at this constant stress level, and the relative absence of AE in interrupted tests might indicate that subsequent inelastic deformation was accommodated by crack opening (a relatively silent process) rather than crack extension or the formation of new cracks.

Surface replicas revealed interactions of matrix cracks with fiber/matrix interfaces. The form of this is illustrated in Fig. 6 (a)-(c), corresponding to the same surface area at stress levels of 140 MPa, 270 MPa and 430 MPa, respectively. We observed increased acetate penetration into the interfaces near matrix cracks. This is shown by the gradually *exposed* "boundary" between the fiber and the matrix on the replica at two sites marked by arrows. These "boundaries" remained visible after final failure. There was a strong correlation between matrix cracks and the observed damage along the interface. Acetate replicas did not reveal interface damage in regions where no matrix cracks existed.

3.3 Fracture surface observations

Fracture surfaces of tested samples show considerable fiber pullout, and fiber debonding from the surrounding matrix, as shown in Fig. 7 (indicated by an arrow). Other SEM observations also indicate the occasional presence of radial matrix cracks (Fig. 8). These observations will be discussed in section 4.2.

3.4 Elastic properties determined from laser-ultrasonic measurement

The measured longitudinal wave velocities are plotted in Fig. 9 for four different stress levels (0, 200, 270 and 320 MPa). Similar measurements and calculations were also performed for a second sample at stress levels of 180 and 240 MPa. The elastic constants determined from the velocity data at each stress level are given in Fig. 10. The results at 0 MPa are also listed in Table 1 for comparison with those previously determined with the sensitive RUS technique [16]. The agreement between these two test methods is clearly good.

Uncertainties in C_{11} ($\pm 1.4\%$), C_{66} and C_{44} ($\pm 3.3\%$), C_{12} ($=C_{11}-2C_{66}$) ($\pm 7.1\%$) were estimated based on the precision of wave arrival time determination and wave travel distance. The errors for C_{33} ($\sim \pm 3.0\%$) and C_{13} ($\sim \pm 10\%$) (deduced from nonlinear curve fitting) are determined according to a 95% confidence limit setting during the nonlinear curve fitting process. The relatively large range of scatter for the off-diagonal elastic stiffness constants has also been found in other ultrasonic studies [30].

The Young's moduli of the composite can be deduced from the ultrasonically determined C_{ij} values. Using the coordinate system defined in Fig. 2, the ultrasonically deduced axial Young's modulus E' for transverse isotropic material is:

$$E' = C_{33} - 2 \frac{C_{13}^2}{C_{11} + C_{12}} \quad (10)$$

The dependence of E' upon stress is plotted in Fig. 11, together with the elastic moduli E^* (unloading elastic modulus determined from partial unloading) and \bar{E} (average modulus determined from the hysteresis loop as illustrated in Fig. 3) obtained from tensile testing [29]. All the moduli are normalized to the initial Young's modulus, E , measured in the nominally elastic region. They show a similar degradation trend with stress. However, the rate of degradation varies from one to the other.

Similar measurements were also performed after unloading to 10 MPa from successively higher stress levels. In general, the wave arrival times were reduced slightly compared with those before unloading. Values of the elastic constants for sample #1 before and after loading at different stress levels are listed in Table 2. The elastic constants after unloading are slightly higher, especially after unloading from 270 and 320 MPa, presumably due to the narrowed matrix crack opening after unloading. However, the overall change of elastic constants upon unloading is small, indicating that the majority of matrix cracks and damage still contribute to softening even after unloading.

4. DISCUSSION

4.1 Damage evolution

An experimental study of damage evolution in unidirectional CAS/SiC under tension has been conducted using *in situ* laser-ultrasonic, acoustic emission, mechanical property measurements and observations of surface cracking via replicas. The stress-strain curve (Fig. 3) shows a plateau region from 200 MPa to 270 MPa, as a result of damage accumulation associated with the formation of new matrix cracks, interface debonding/sliding and additional crack opening under loading. This is reflected by the rapid increase of matrix crack density, the reduction of axial Young's modulus (Fig. 4(b)), and the significant decrease of ultrasound velocity (Fig. 9) in this region. The results demonstrate that matrix crack density, ultrasound velocity and elastic stiffness are closely related during damage evolution, and that the laser-ultrasonic technique is an effective tool for the measurement of damage evolution in CMCs.

4.2 Transverse elastic stiffness degradation

The laser-ultrasonic measurements show that the stiffness decreases not only in the *1-3* plane but also in the transverse *1-2* plane. Changes in the transverse elastic stiffness C_{11} and C_{66} (Fig. 10) reveal a *progressive* deterioration in the transverse plane under loading. Replicas have linked this to interface debonding (Figs. 6 and 7) at the weakly bonded carbon-rich interface near matrix cracks. When matrix cracks run into interfaces, they are deflected along the interfaces; the resulting damage traces on the surface are

recorded by acetate replicas (Fig. 6). Numerical calculations have also shown matrix cracking can change the radial interface stress from compressive to tension (due to radial stress concentration) [31], which may explain the easy penetration of acetate into the interfacial damage area.

Radial cracks of the type shown in Fig. 8 are also able to contribute to the transverse softening. Since the CAS matrix is under hoop tensile residual stress after processing, radial cracks could be a result from thermal mismatch between the fiber and the matrix. However, laser-ultrasonic and RUS measurements (Table 1) have indicated that, for the as-received CAS/SiC, the transverse elastic stiffness C_{11} (~147 MPa) is high (axial C_{33} ~154 MPa), implying that the initial radial crack density is very low, as verified by SEM. It may be that the shock wave generated by final fracture produced the additional cracks [32,33]. In that case, the splitting in Fig. 7 and 8 would not have contributed to the ultrasonically observed softening prior to final fracture.

Based on above, we concluded that interface damage (debonding) caused by matrix cracks interactions with fibers is the dominant factor responsible for the decrease of the elastic constants in the transverse direction during loading.

4.3 Comparison of axial elastic modulus obtained by mechanical testing and laser-ultrasonic technique

The elastic modulus E' calculated from the ultrasonic determined C_{ij} decreases with increasing stress, consistent with the results from mechanical testing. As shown in Fig. 11, most values of the axial elastic modulus determined from the laser-ultrasonic

method lie between E^* and \bar{E} . However, some discrepancy exists between the magnitude of E' and E^* . We note that the laser-ultrasonic measurement is an *in-situ* testing method, whereas mechanical determination of the elastic modulus must be done using loading/unloading. In the elastic region where little or no damage is present, these two approaches should yield the same results, as observed in this study. However, once damage occurs in the CMCs, bridging fibers can exert frictional forces on the matrix, which tend to oppose crack closure during unloading and resist crack opening during loading [1]. For CAS/SiC, a moderate sliding resistance (~ 16 MPa) at the fiber/matrix interface [23] results in a smaller unloading strain compared to the case without interfacial friction; this consequently “stiffens” the composite and yields a higher unloading modulus E^* . On the other hand, the dynamic stresses activated in the laser-ultrasonic method are small, the cracks remain open and the modulus is lower. We also note that C_{12} and C_{13} determined by ultrasound measurement have relatively large uncertainties, which affect the precise determination of the elastic modulus E' (see Eq.(10)).

5. CONCLUSIONS

Anisotropic damage evolution in unidirectional CAS/SiC has been observed using laser-ultrasonic and acoustic emission techniques. Matrix cracking, observed by both surface replicas taken under loading and acoustic emission monitored during testing, is responsible for the significant drop in axial elastic stiffness constants. The form of the

reduction of the effective axial Young's modulus from laser-ultrasonic measurements is similar to that observed from mechanical test, but discrepancies remain.

Significant degradation of the transverse stiffness elastic constants C_{11} is also observed. Surface replicas indicate that this transverse "softening" is linked to interfacial debonding, that results from interactions between matrix cracks and nearby fibers. These results indicate that the laser-ultrasonic technique is a useful tool for the *in situ* measurement of anisotropic damage in CMCs.

ACKNOWLEDGMENTS

This work has been supported by the Defense Advanced Research Projects Agency through the University Research Initiative at University of California at Santa Barbara under ONR Contract No. N00014-92-J-1808. Y. M. Liu and T. E. Mitchell are also grateful to the US Department of Energy, Office of Basic Energy Sciences for support. We would like to thank Dr. Y. Lu, D. Sypeck (University of Virginia), C. Cady (Los Alamos National Laboratory) and A. G. Evans (Harvard University) for helpful discussions. We also thank the referee for making several helpful comments and suggestions.

TABLE 1

Elastic constants of unidirectional CAS/SiC composites with transversely isotropic symmetry (Units: GPa). The 3-axis is parallel to the fiber direction [16].

C_{11}	C_{33}	C_{13}	C_{12}	C_{44}	$*C_{66}$
147.21	153.83	50.36	53.30	47.72	46.95

$$*C_{66}=(C_{11}-C_{12})/2$$

** Laser- ultrasonic results at 0 MPa:

$$C_{11} = 146, C_{33} = 158, C_{13} = 55, C_{12} = 52, C_{44} = 47$$

TABLE 2.

Elastic constants (unit: GPa) before/after unloading to 10 MPa at different stress level (sample #1).

Stress (MPa)	Before unloading					After unloading to 10 MPa				
	C ₁₁	C ₁₂	C ₁₃	C ₃₃	C ₄₄	C ₁₁	C ₁₂	C ₁₃	C ₃₃	C ₄₄
200	136.6	49.9	60.0	150.6	44.3	135.5	52.36	60	151	41.6
270	101	34.6	48.4	116.7	33.2	107	37.9	56.9	125.0	34.6
320	99.7	35.5	41.9	111.0	32.1	104.3	36.3	51	121.4	34.0

FIGURE CAPTIONS

Fig. 1 Schematic experimental setup for laser-ultrasonic study.

Fig. 2 Material coordinates and the positions of piezoelectric sensors.

Fig. 3 Loading/unloading stress-strain curve and the corresponding AE events. E is the Young's modulus in the elastic region, \bar{E} is the average Young's modulus determined from the hysteresis loop, and E^* represents the unloading modulus.

Fig. 4 (a) Accumulated AE events as a function of stress; (b) The matrix crack density (dashed line) and the reduction of the unloading elastic modulus E^* (solid line) as a function of stress.

Fig. 5 Optical micrographs of replicas showing surface matrix cracks at different loading stages: (a) 140 MPa; (b) 168 MPa; (c) 200 MPa; (d) 230 MPa; (e) 270 MPa.

Fig. 6 Optical micrographs of replicas taken under the same area showing interfacial damage: (a) 140 MPa; (b) 270 MPa; (c) 430 MPa, two sites are marked by arrows.

Fig. 7 SEM micrograph of fracture surface showing interface debonding, as indicated by an arrow.

Fig. 8 SEM micrograph of fracture surface showing matrix radial cracks.

Fig. 9 Longitudinal wave velocity in the I -3 plane at different stress levels for a tested sample. Symbols: experimentally measured velocities. Solid lines: longitudinal velocity calculated using the experimentally determined elastic constants.

Fig. 10 Elastic constants at various stress levels determined from laser-ultrasonic velocities.

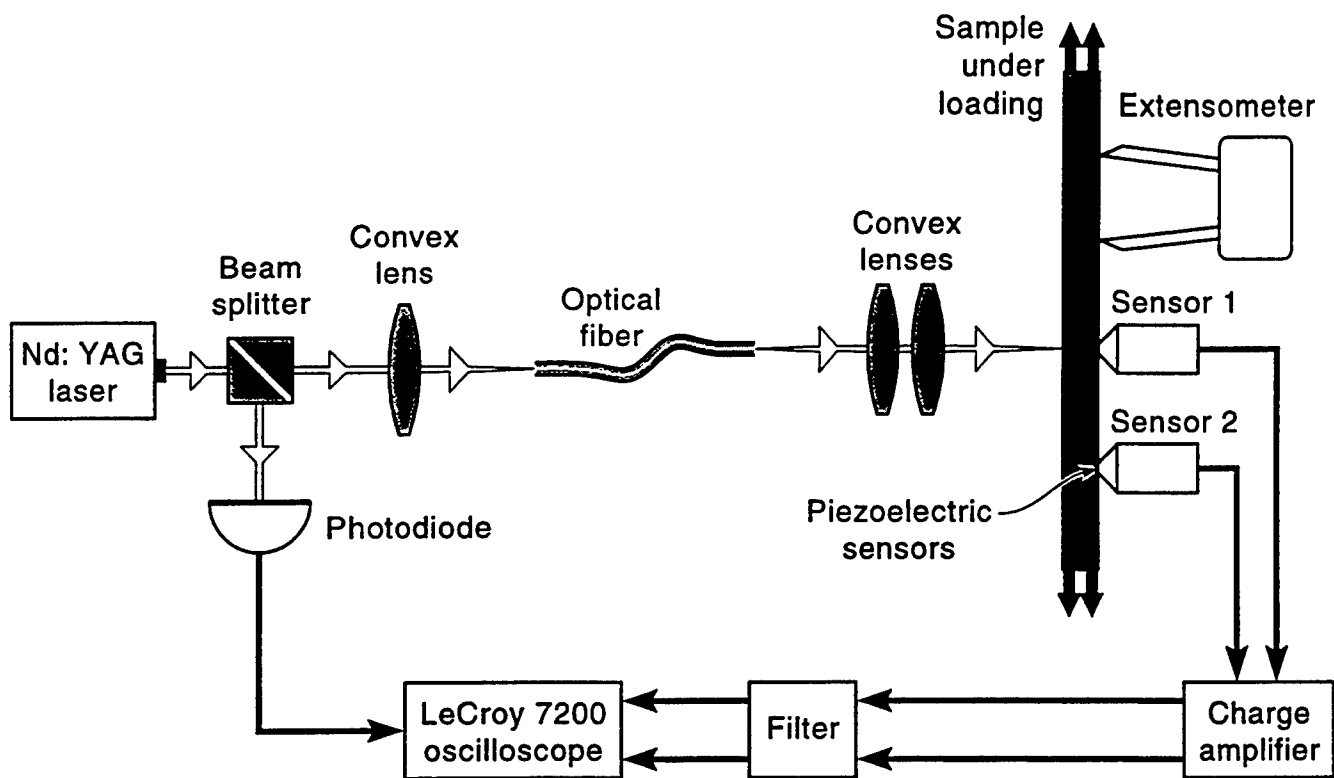
Fig. 11 Normalized elastic modulus determined by laser-ultrasonic method and mechanical testing.

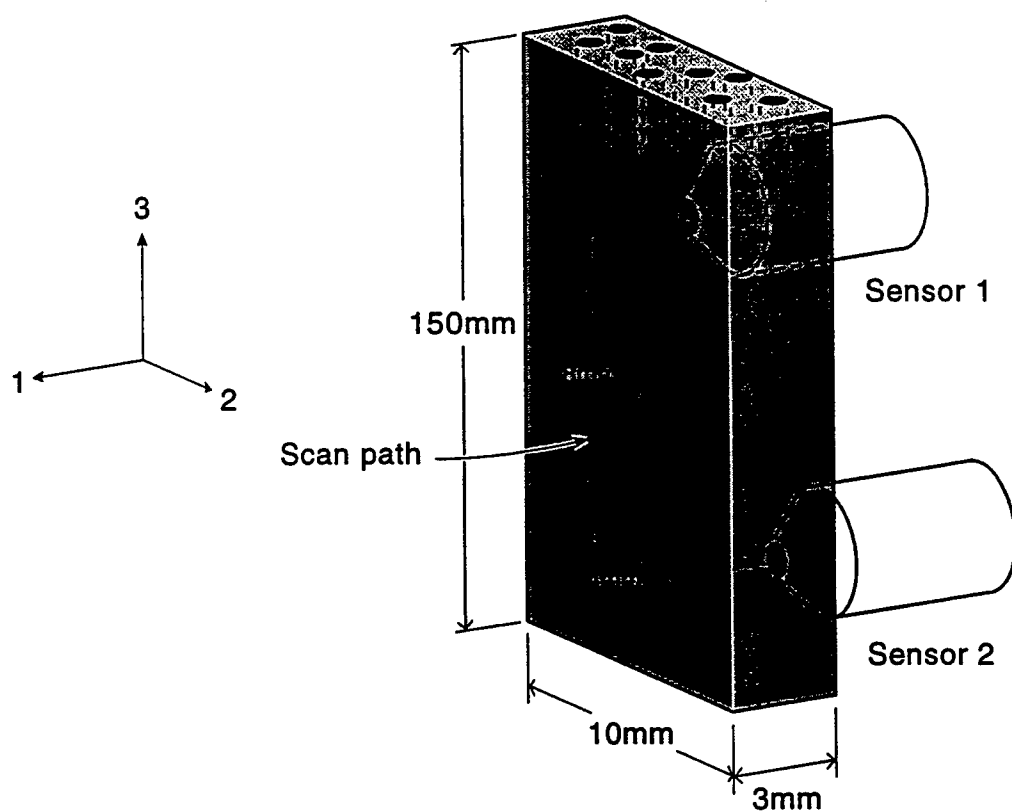
REFERENCES

- [1] D. B. Marshall and A. G. Evans, *J. Am. Ceram. Soc.*, **68**, 225 (1985).
- [2] A. G. Evans and D. B. Marshall, *Acta Metall.*, **37**, 2567 (1989).
- [3] M. D. Thouless, O. Sbaizero, L. S. Sigl, and A. G. Evans, *J. Am. Ceram. Soc.*, **72**, 525 (1989).
- [4] R. N. Singh, *J. Am. Ceram. Soc.*, **72**, 1764 (1989).
- [5] J. J. Brennan, in *Fiber Reinforced Ceramic Composites* (edited by K. S. Mazdiyasni) pp. 222-259, Noyes Publications, Park Ridge, New Jersey, (1990).
- [6] K. M. Prewo and J. J. Brennan, *J. Mater. Sci.*, **17**, 2731 (1982).
- [7] D. S. Beyerle, S. M. Spearing, F. W. Zok, and A. G. Evans, *J. Am. Ceram. Soc.*, **75**, 2719 (1992).
- [8] A. G. Evans, F. W. Zok, and T. J. Mackin, in *High Temperature Mechanical Behavior of Ceramic Composites* (edited by S. V. Nair and K. Jakus), pp. 3-83, Butterworth-Heinemann, Massachusetts, U. S. A. (1995).
- [9] C. Cady, F. E. Heredia, and A. G. Evans, *J. Am. Ceram. Soc.*, **78**, 2065 (1995).
- [10] M. Y. He, B.-X. Wu, A. G. Evans, and J. W. Hutchinson, *Mech. Mater.*, **18**, 213 (1994).
- [11] C. Cady, T. J. Mackin, and A. G. Evans, *J. Am. Ceram. Soc.*, **78**, 77 (1995).
- [12] D. S. Beyerle, S. M. Spearing, and A. G. Evans, *J. Am. Ceram. Soc.*, **75** 3321 (1992).
- [13] M. Drissi-Habti, *Scripta Metall. Mater.*, **33**, 967 (1995).
- [14] S. Baste, R. E. Guerjouma and B. Audoin, *Mechanics of Materials*, **14**, 15 (1992).

- [15] B. A. Auld, *Acoustic Fields and Waves in Solids*, Krieger Publishing Company, Malabar, Florida (1990).
- [16] Y. M. Liu, Y. He, F. Chu, T. E. Mitchell and H. N. G. Wadley, *J. Am. Ceram. Soc.*, **80**, 142 (1997).
- [17] R. M. Christensen, *Mechanics of Composite Materials*, Wiley, New York (1979).
- [18] R. Y. Kim and N. Pagano, *J. Am. Ceram. Soc.*, **75**, 1082 (1991).
- [19] J.-J. Luo, S.-C. Wooh, and I. M. Daniel, in *Review of Progress in Quantitative Nondestructive Evaluation*, vol. **13** (edited by D. O. Thompson and D. E. Chimenti), Plenum Press, New York (1994).
- [20] C. B. Scruby, H. N. G. Wadley, and J. J. Hill, *J. Phys. D: Appl. Phys.*, **16**, 1069 (1983).
- [21] D. G. Eitzen and H. N. G. Wadley, *Journal of Research of the National Bureau of Standards*, **89**, 75 (1984).
- [22] Y. M. Liu, T. E. Mitchell, and H. N. G. Wadley, to be submitted to *J. Am. Ceram. Soc.*
- [23] T. J. Mackin and F. W. Zok, *J. Am. Ceram. Soc.*, **75**, 3169 (1992).
- [24] S. J. Davies, C. Edwards, G. S. Taylor, and S. B. Palmer, *J. Phys. D.: Appl. Phys.*, **26**, 329 (1993).
- [25] C. B. Scruby, and L. E. Drain, *Laser Ultrasonics*, Adam Hilger (1990).
- [26] R. J. Dewhurst, A. G. Nurse, and S. B. Palmer, *Ultrasonics*, **26**, 307 (1988).
- [27] S. Geckeler, "Physical Principles of Optical Waveguides", *Telcom Report*, **6** (1983).

- [28] D. J. Sypeck, and H. N. G. Wadley, in *Review of Progress in Quantitative Nondestructive Evaluation*, vol. **15** (1995).
- [29] E. Vagaggini, J.-M. Domergue, and A. G. Evans, *J. Am. Ceram. Soc.*, **78**, 2709 (1995).
- [30] B. Castagnede, K. Y. Kim, W. Sachse and M. O. Thompson, *J. Appl. Phys.*, **70**, 150 (1991).
- [31] N. J. Pagano and H. W. Brown, *Composites*, **24**, 69 (1993).
- [32] I. M. Daniel, *J. Composite Mater.*, **4**, 178 (1970).
- [33] H. W. Herring, J. L. Lytton, and J. H. Steele, *Metal. Trans.*, **4**., 807 (1973).





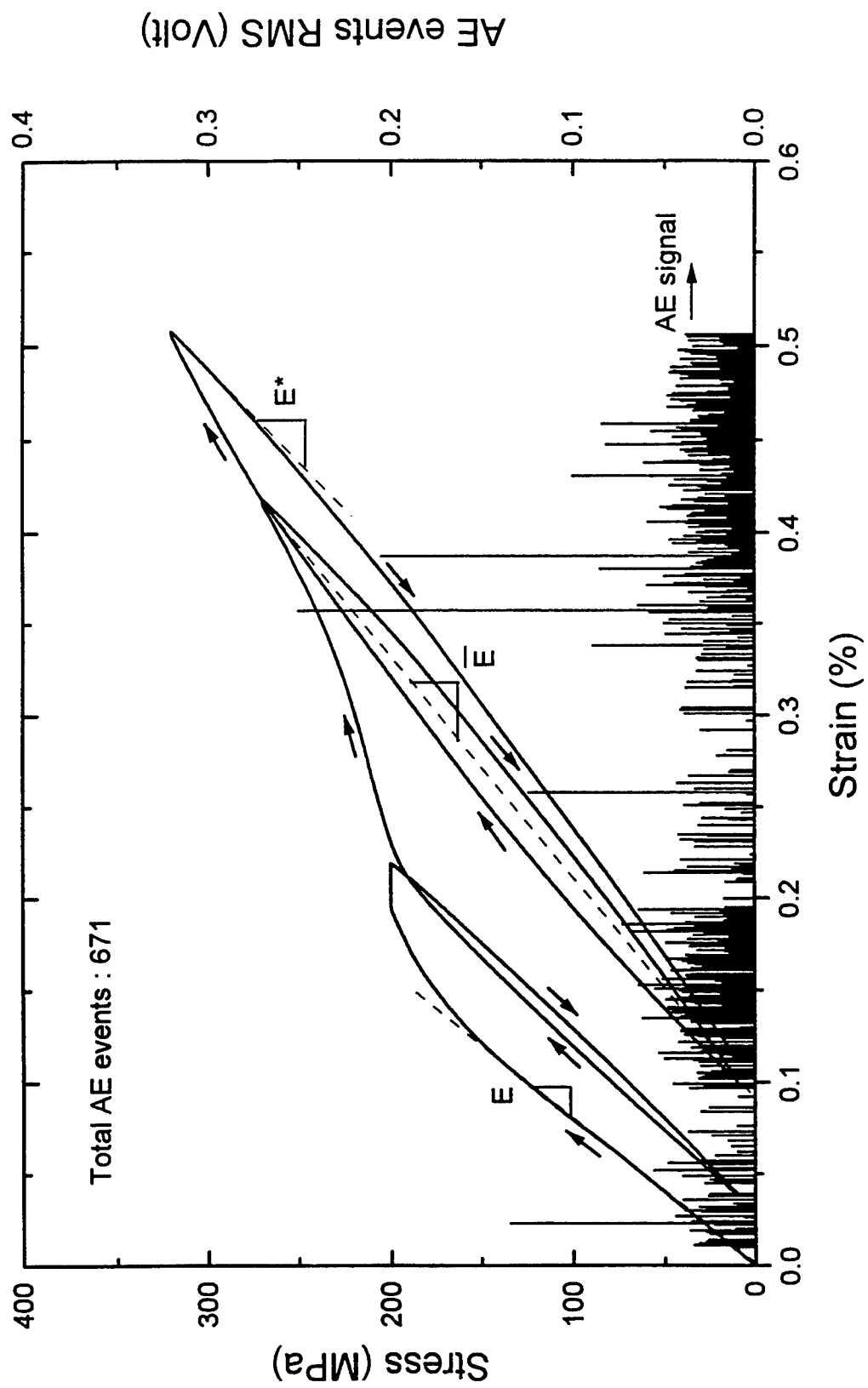
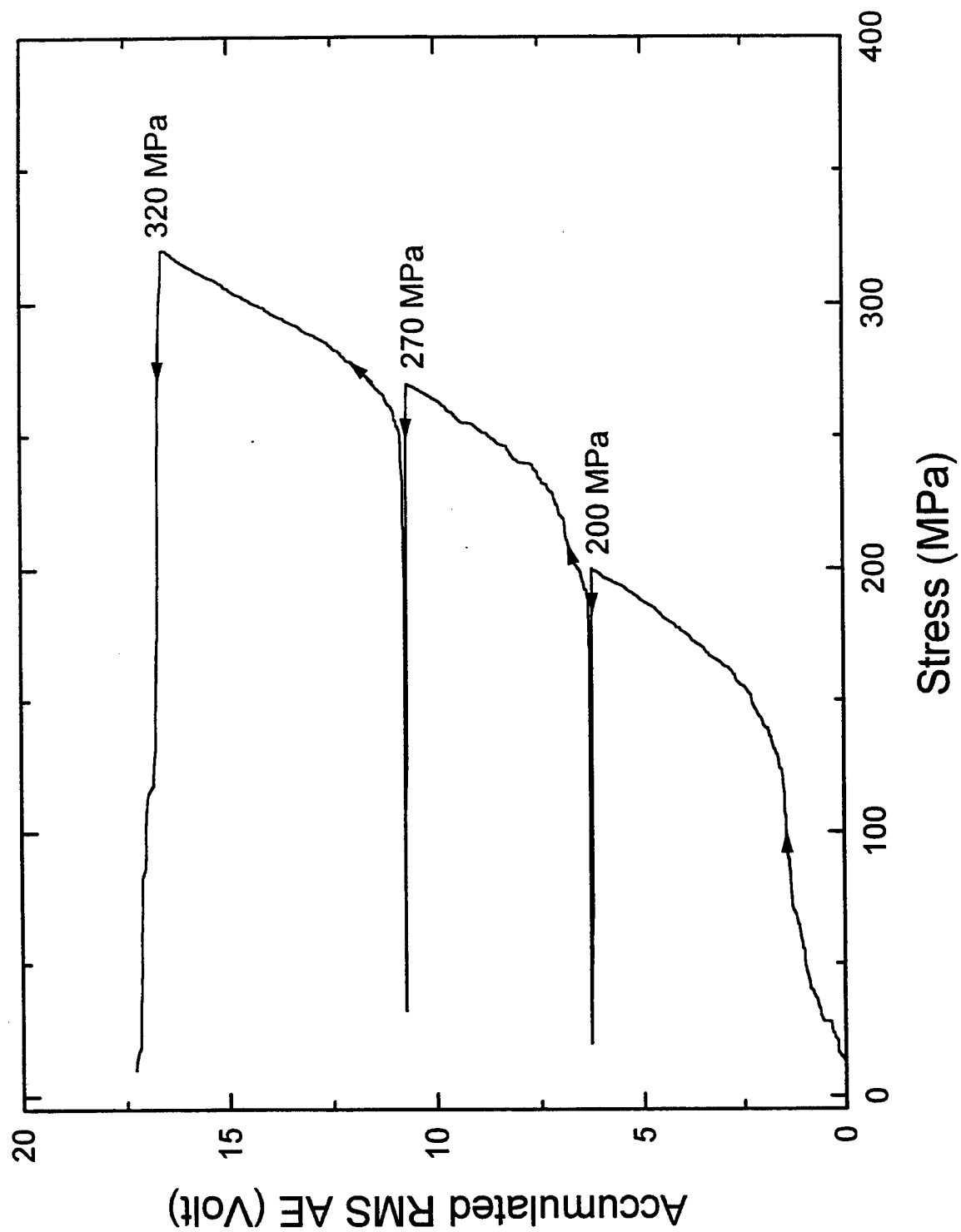


Fig 3



ae0328.org

Fig 4(a)

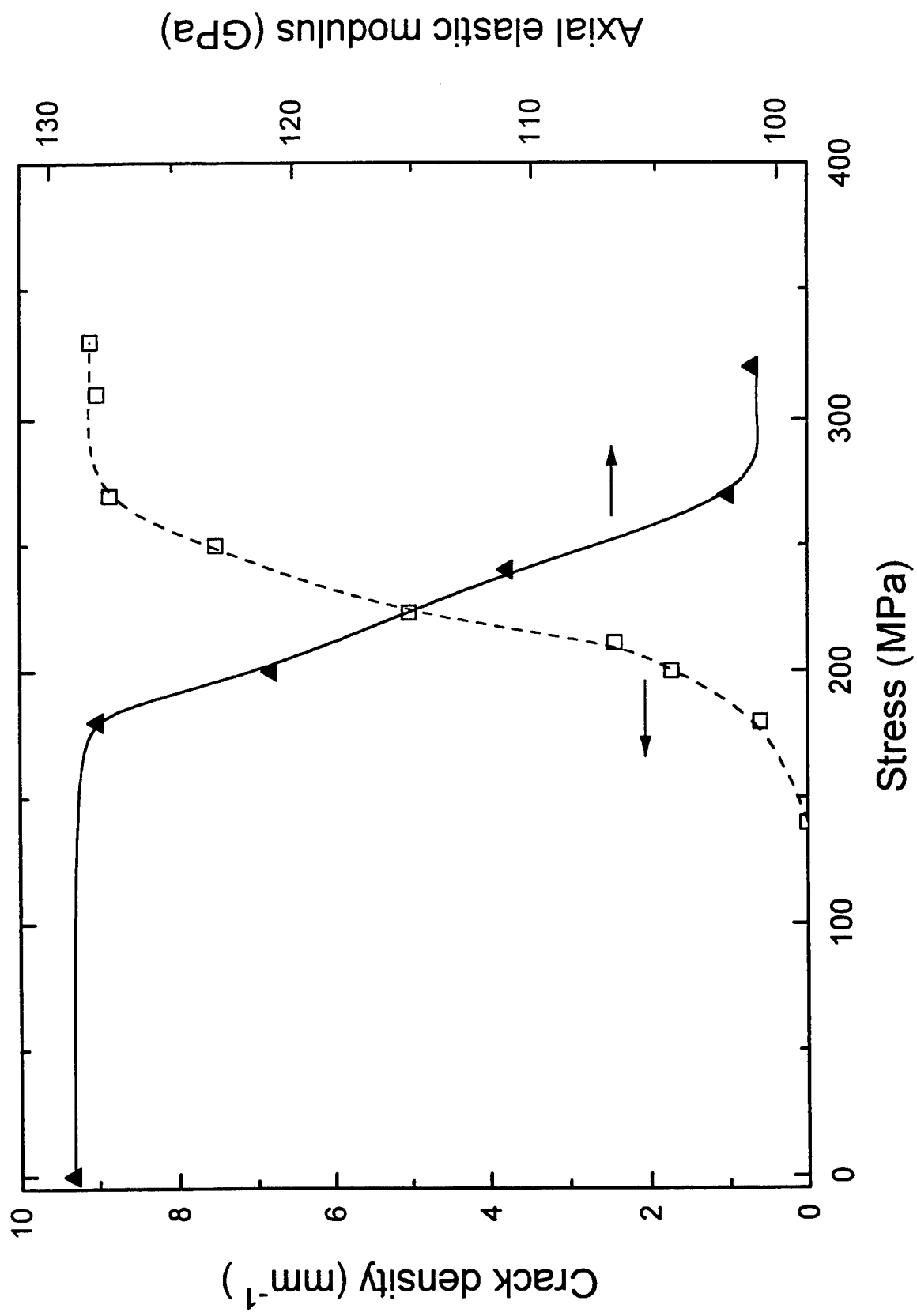
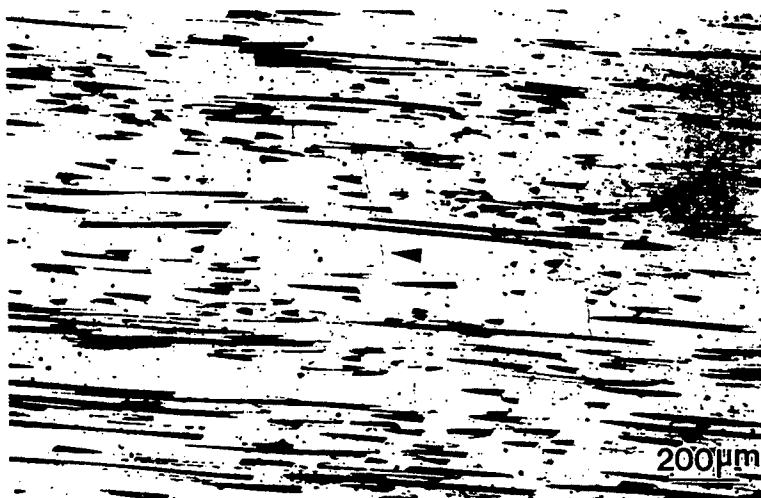


Fig. 4(6)

(a) 140 MPa



(b) 168 MPa



(c) 200 MPa



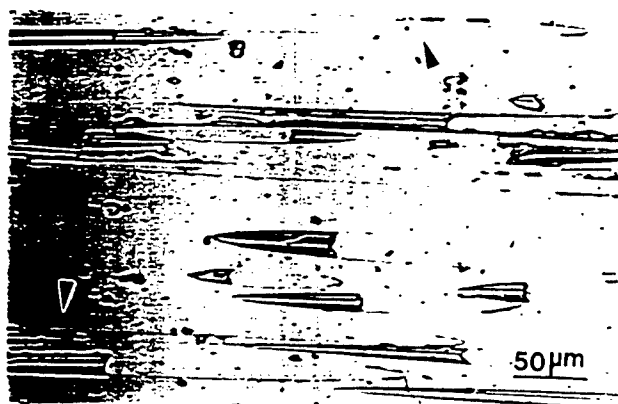
(d) 230 MPa



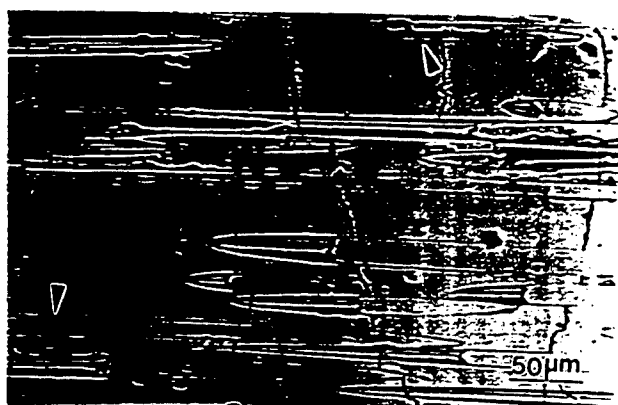
(e) 270 MPa



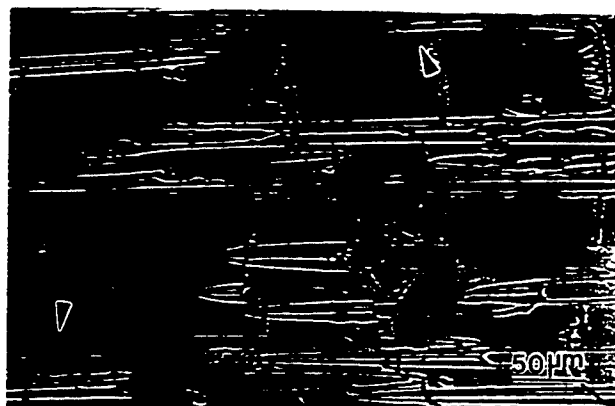
Fig. 5 (continued)



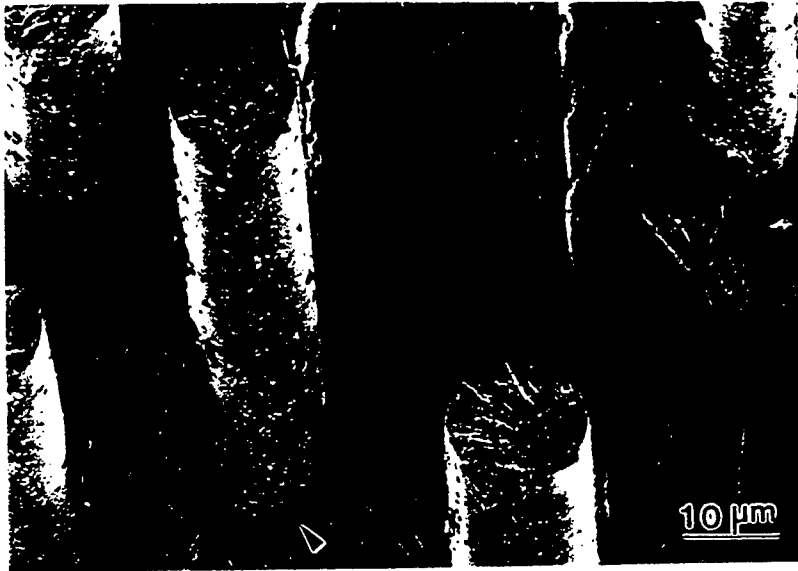
(a)



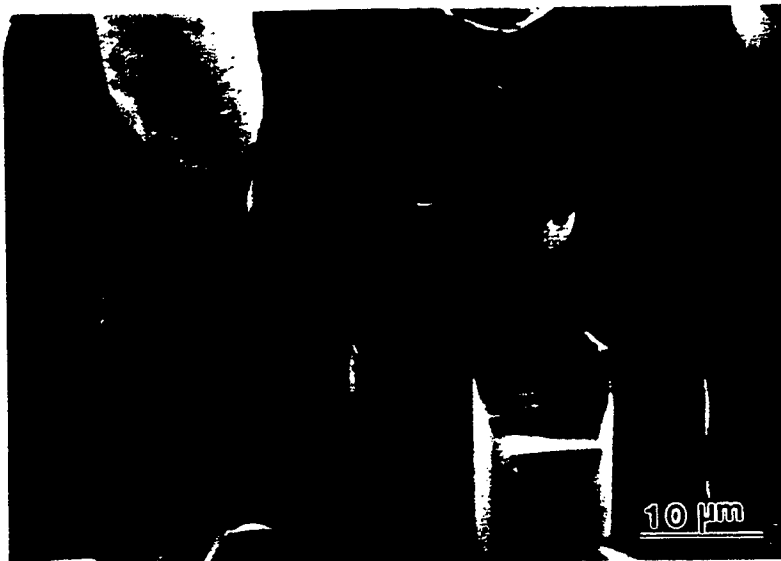
(b)



(c)



7.7



7.8

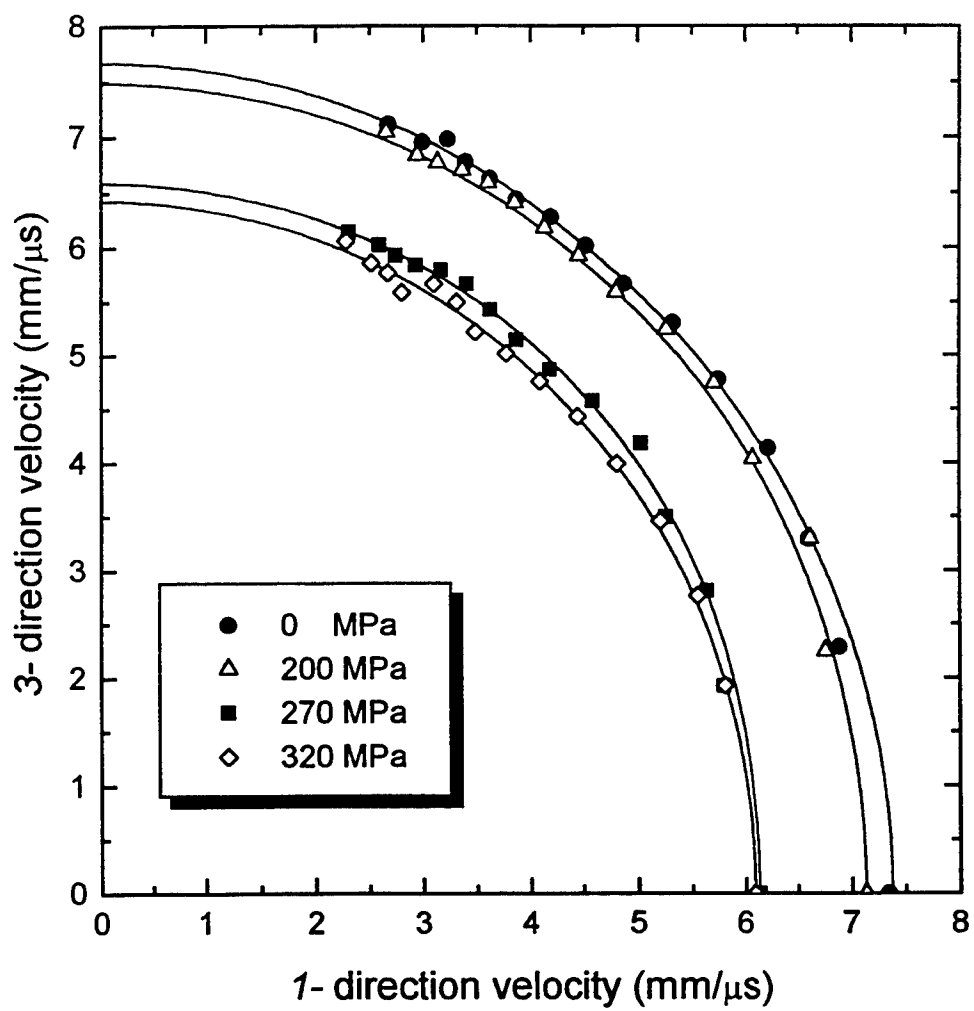
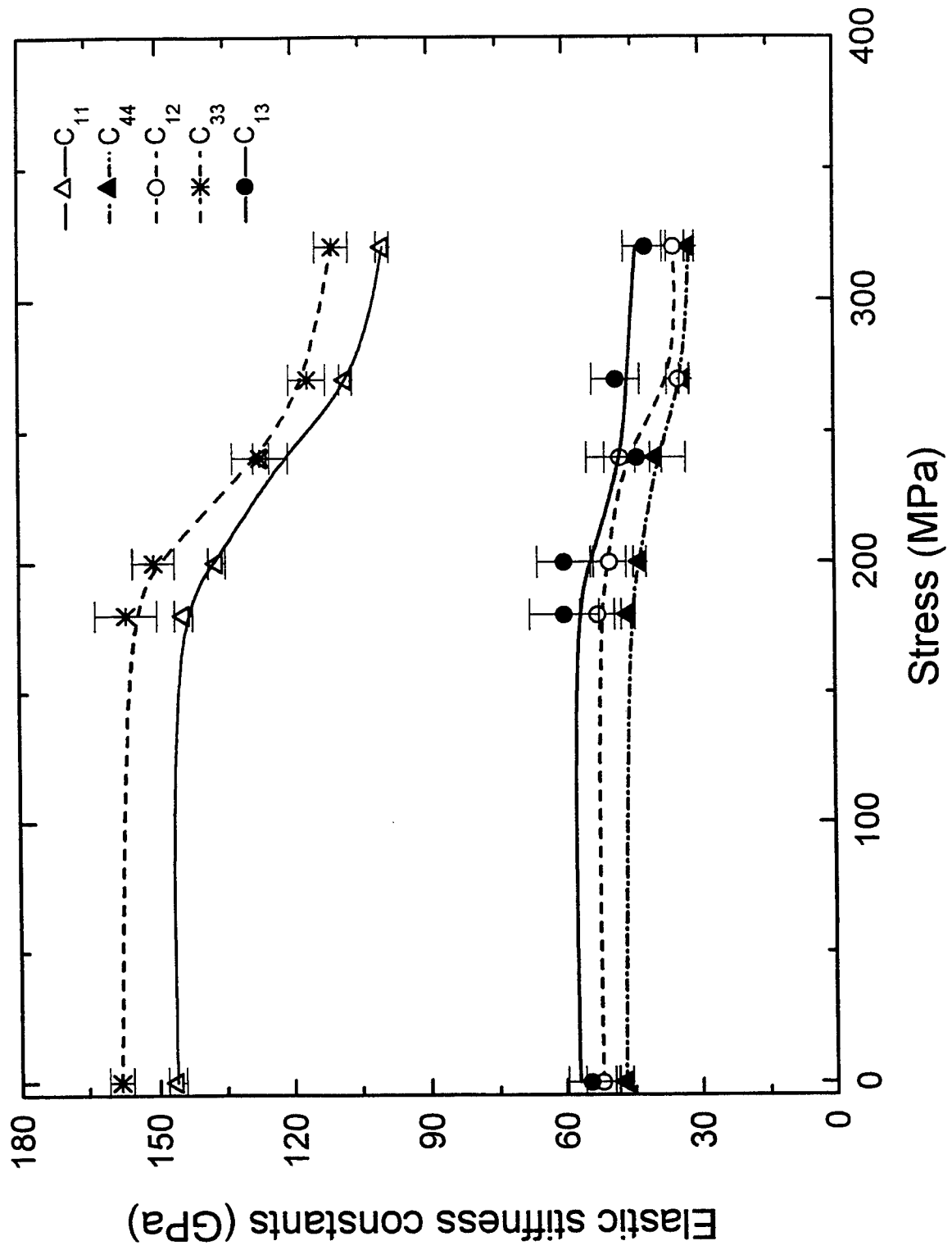
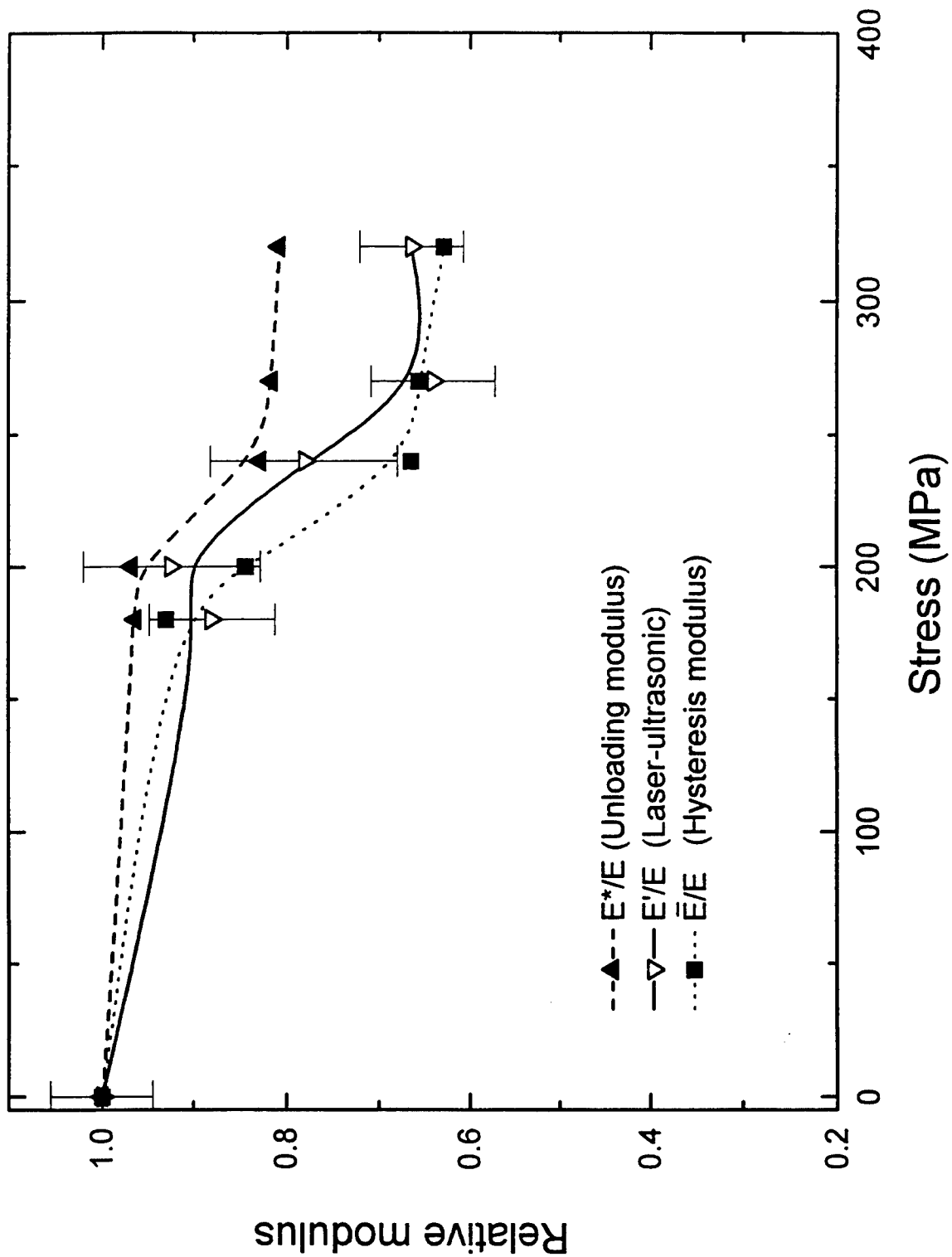


Fig. 9





Elastic Properties of Laminated Calcium Aluminosilicate/Silicon Carbide Composites Determined by Resonant Ultrasound Spectroscopy

Yongmei Liu, Yi He, Fuming Chu, and Terence E. Mitchell*

Center for Materials Science, Los Alamos National Laboratory, Los Alamos, New Mexico 87545

Haydn N. G. Wadley

Department of Materials Science and Engineering, School of Engineering and Applied Science,
University of Virginia, Charlottesville, Virginia 22903

The elastic properties of unidirectional and 0°/90° crossply Nicalon-SiC-fiber-reinforced calcium aluminosilicate (CAS/SiC) ceramic-matrix composites have been measured using a resonant ultrasound spectroscopy (RUS) technique. This approach has allowed the nondestructive determination of the complete set of independent second-order elastic stiffness constants of these ceramic composites. These stiffness data have been used to obtain the orientation dependence of Young's modulus and the shear modulus. The results are in reasonably good agreement with the limited experimental data obtained from mechanical testing. The RUS measurements reveal that the unidirectional CAS/SiC composite is well modeled by transverse isotropic symmetry, indicating relatively isotropic fiber spacing in the transverse plane. The analysis indicates that the overall elastic anisotropy is also small for unidirectional and 0°/90° laminated CAS ceramic-matrix composites, a result that can be attributed to the relatively low modulus ratio of the Nicalon SiC fiber to the CAS matrix and to the moderate fiber volume fraction.

I. Introduction

CERAMIC-MATRIX composites (CMCs) have generated significant interest as potential high-temperature structural materials, because of their low density, high elastic moduli, high strength, and, for those with weak interfaces, surprisingly good damage tolerance.¹⁻⁵ The use of inexpensive glass and glass-ceramics as a composite matrix has facilitated the development of inexpensive synthesis techniques. The viscous flow characteristics of the glass make easy densification of an appropriately oriented composite lay-up possible by applying pressure at an elevated temperature. Then, matrices can be crystallized to form fiber-reinforced composites with high thermal stability.² Many applications have been proposed for these relatively affordable materials.^{2,4,5} In structural applications, a multiaxial stress state is often encountered and unidirectional composites are susceptible to failure by transverse cracking.^{6,7} For these applications, multi-ply laminates are normally necessary. These also are synthesized by hot pressing a lay-up of appropriately oriented unidirectional laminae arranged to carry load in different directions.^{2,8}

Several aluminosilicate matrices have been explored for the design of composites with weak interfaces. Composites of calcium aluminosilicate (CAS) reinforced with Nicalon™ (Nippon

Carbon Co., Tokyo, Japan) SiC fibers have been the subject of particularly active investigation.^{7,9-11} In this system, a thin carbon-rich layer between the fiber and matrix leads to a composite with a high toughness and good damage tolerance.^{1,2,12} This class of composite exhibits nonlinear deformation above a critical tensile stress, a result of multiple matrix cracking.^{3,4,10,11} These materials are designated as Class II ceramic composites, based on their fracture mechanism.^{11,13} Class II materials are "matrix-dominated" materials; they have a relatively large initial tensile modulus, exhibit appreciable inelastic strain, and achieve a steady-state matrix-cracking condition before fiber failure.^{7,10,11} These materials are relatively notch insensitive, because the stress is redistributed through the inelastic strain (matrix cracking). This is of significant importance for structural applications, because the stress concentration near notches and attachments can be mitigated by inelastic deformation, and the risk of catastrophic failure is consequently reduced.

Because the initial elastic modulus and the subsequent inelastic strain behavior of composites are expected to be sensitive to the fiber orientation and its volume fraction, complete elastic constant data are needed for the design of components subjected to multiaxial loads. In the past, the Young's modulus in a specific direction has been used for design purposes. It has been measured in a tensile test and is of limited value, because it conveys little information about the shear and off-axis properties that frequently govern the useful strength.^{4,11} To obtain a more complete elastic constant data set, a variety of different mechanical tests must be used and considerable effort is required to obtain data that are sufficiently precise.⁴ The problem is considerably complicated by the occurrence of damage at interfaces and in the matrix at low stress levels. Here, we explore the application of a resonant ultrasound spectroscopy (RUS) technique¹⁴ to obtain all the independent elastic constants simultaneously for unidirectional and 0°/90° crossply CAS/Nicalon SiC composites.

The RUS technique is a nondestructive technique based on ultrasonic excitation and the measurement of the mechanical resonant frequencies of a small sample having a regular shape.¹⁴ The mechanical resonant response of a solid is dependent on its elastic moduli, shape, and density.¹⁴ The resonant spectrum can be predicted based on these parameters. However, no analytical solution exists for the inverse problem (i.e., for deducing elastic constants from a measured spectrum). Thus, to deduce the elastic constants via the RUS technique, a least-square modeling approach is used. The resonant frequency spectrum is first calculated from an initial estimate for each of the elastic constants. The calculated spectrum is then compared with the measured one, and a least-square difference between the measured and predicted resonant frequencies is calculated and summed for all the spectral peaks to find a residual, F , given by

$$F = \sum_i w_i (f_i^* - f_i)^2 \quad (1)$$

where f_i (where $i = 1, 2, \dots, n$) is the i th measured resonant frequency, f_i^* the predicted frequency, and w_i a weight factor

F. W. Zok—contributing editor

Manuscript No. 191934. Received March 21, 1996; approved July 5, 1996.
Supported by the ARPA-funded UCSB-URI and the U.S. Department of Energy, Office of Basic Sciences.
*Member, American Ceramic Society.

Table I. Mechanical Properties of CAS/SiC Class II Glass-Ceramic Composites*

Property	0°	0°/90°
Longitudinal (0°) tensile properties at 25°C		
Ultimate strength (MPa)	450	194
Ultimate strain (%)	0.95	0.74
Elastic limit stress (MPa)	207	100
Elastic limit strain (%)	0.1–0.15	0.16
Elastic modulus (GPa)	124	111
Poisson's ratio	0.25	0.22–0.24
Off-axis properties at 25°C		
Transverse (90°) tensile strength (MPa)	28	
In-plane shear strength at ±45° (MPa)	65	
Transverse elastic modulus (GPa)	117	
Shear modulus at ±45° (GPa)	48	48

*Supplied by Corning. Fiber modulus, E_f , is ~200 GPa; matrix modulus, E_m , is ~97 GPa; and fiber volume fraction, V_f , is ~0.35. Density, ρ , for each is 2.7 g/cm³.

reflecting the degree of confidence in the measured frequency. The minimum value of F is obtained by varying the estimated elastic constants in the forward problem that predicts f^* . The elastic constants that minimize F are then considered to be the actual elastic constants of the material. This method has already been successfully used to identify the complete elastic constants of many single-crystal materials, intermetallic compounds,^{15–17} and, recently, boron-fiber-reinforced aluminum composites.¹⁸

Choosing a symmetry for the RUS approach is necessary. In the work presented here, transversely isotropic symmetry and orthotropic symmetry have been used for determining the elastic constants of unidirectional CAS/Nicalon SiC. For 0°/90° crossply composite materials with even numbers of 0° and 90° laminae, tetragonal symmetry has been assumed.

II. Experimental

(1) Materials

The materials used in this study were supplied by Corning, Inc. (Corning, NY). The fabrication started with the infiltration of a CAS matrix slurry into a Nicalon fiber yarn. The resulting sheets were dried, cut, and stacked in the appropriate orientation.² The plies were then consolidated to final composites by hot pressing. The mechanical properties of 0° and 0°/90° materials provided by Corning are summarized in Table I. The fiber volume fractions for unidirectional (0°) and 0°/90° laminated composites were ~35%. The Young's modulus for the matrix, E_m , was ~97 GPa and for the fibers, E_f , was ~200 GPa.

(2) Resonant Ultrasound Spectroscopy

Rectangular parallelepiped specimens were cut from the 0° and 0°/90° laminated composites and then polished. The unidirectional sample was ground to the dimensions $a_1 = 2.976$ mm, $a_2 = 4.023$ mm, and $a_3 = 3.317$ mm, where the fiber direction was parallel to the 3-axis and the 1-axis was the thickness direction of the laminate (Fig. 1(A)). For the 0°/90° crossply

composite, the final sample dimensions were $a_1 = 2.794$ mm, $a_2 = 3.967$ mm, and $a_3 = 3.185$ mm, where the 3-axis was parallel to the thickness direction of the laminate, as shown in Fig. 1(B).

To make a RUS measurement, the sample was lightly clamped between two piezoelectric transducers along one of its body diagonals. One of the transducers generated a continuously swept frequency ultrasonic signal of constant amplitude. The mechanical resonances of the sample were detected by a second transducer. In this study, the excitation frequency varied over a range of 0.3–1.9 MHz. To detect all the resonant frequencies in this range, the measurement was repeated several times, while the sample position, with respect to the transducers, was altered slightly each time. This practice ensured that all possible vibrational modes were detectable. The 70 lowest resonant peak frequencies were measured and used for determination of the elastic constants. The error for the individual elastic constants was estimated by examining the curvature of the minimum F value (in Eq. (1)) for a particular elastic stiffness constant, C_{ij} .¹⁴

III. Results

(1) Microstructure Characterization

As-received materials were characterized using a field-emission scanning electron microscope (SEM) (Model 6300, JEOL, Tokyo, Japan). Figures 2(A) and (B) are SEM micrographs showing the cross sections of the unidirectional and 0°/90° composites, respectively. The nominal ply thickness was ~200 μ m, and the fiber diameter was ~15 μ m.

The fiber volume fraction of the unidirectional laminated CAS/SiC composite was determined by using image analysis on the SEM micrographs of the cross sections using a software package (Mocha) developed by Jandel Scientific (Corte Madera, CA). The matrix and fiber were classified based on their gray level. The number of matrix and fiber pixels was individually counted. The fiber volume fraction was then determined from the ratio of the number of fiber pixels to the total number of the pixels. Twelve micrographs were used to calculate the average fiber volume fraction, V_f , found to be 34%, which was very similar to the value supplied by Corning.

The as-received material was almost fully dense, as shown by the micrographs in Fig. 2. A few pores were observed, usually where a triangular group of touching fibers had hindered infiltration. The macroscopic density, ρ , was determined to be 2.685 ± 0.005 g/cm³ by measuring the mass and dimensions of polished rectangular parallelepiped specimens. This result was confirmed by a density measurement using the Archimedes principle. The porosity was estimated to be <1% based on SEM micrographs.

(2) Resonant Frequency Spectrum

The first 70 resonant frequencies were measured for unidirectional and 0°/90° laminates. Figure 3 shows an example of a portion of the resonant frequency spectrum, 600–750 kHz, for the unidirectional sample. The first 33 peaks were used to

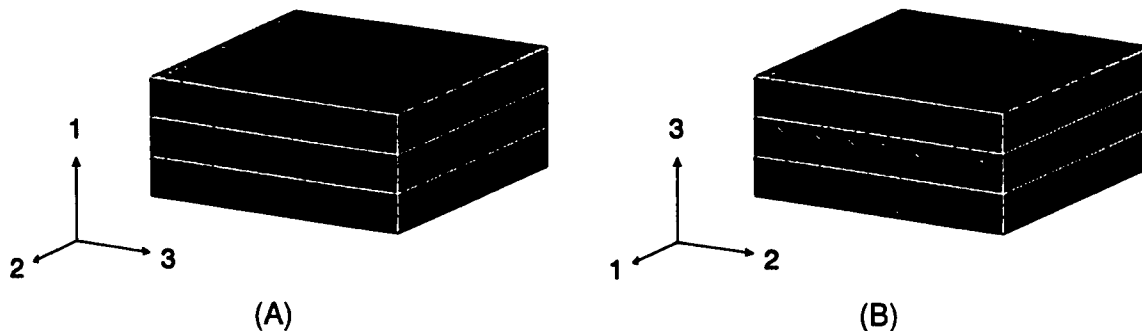


Fig. 1. Coordinate system for (A) unidirectional and (B) 0°/90° laminated composites.

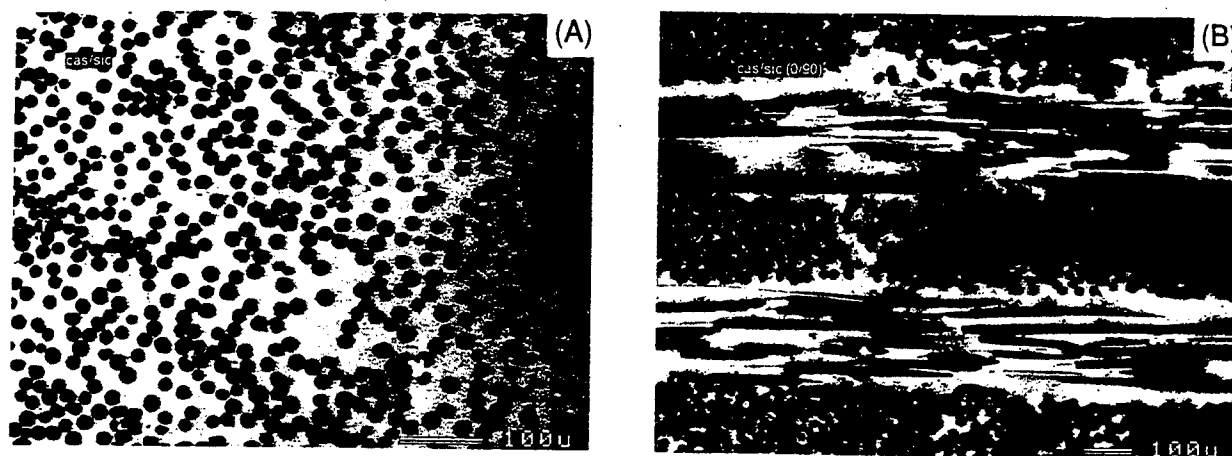


Fig. 2. SEM micrographs of cross sections of (A) unidirectional and (B) 0°/90° crossply CAS/SiC composites.

deduce the elastic stiffness constants, C_{ij} ; the remaining measured resonant frequencies were then used as an independent check of the result, by comparing them with the calculated frequencies of the "best-fit" constants.

(3) Elastic Stiffness Constant Determination

(A) *Unidirectional CAS/SiC Composites*: For the unidirectional laminates, the measured resonant frequency spectrum was fitted by imposing transversely isotropic and orthotropic symmetries. For transversely isotropic symmetry, five independent elastic constants exist: C_{11} , C_{33} , C_{12} , C_{13} , and C_{44} ($C_{22} = C_{11}$, $C_{23} = C_{13}$, $C_{55} = C_{44}$, and $C_{66} = (C_{11} - C_{12})/2$). For a material with orthotropic symmetry, these nine elastic constants are independent. Table II lists the elastic constants deduced by fitting the resonant spectrum by assuming either transversely isotropic or orthotropic symmetry. Table III lists the first ten

measured resonant frequencies and the calculated frequencies based on the two different symmetries.

(B) *0°/90° Crossply Composites*: For a 0°/90° crossply composite with an even number of 0° and 90° plies, the symmetry must be tetragonal. A tetragonal system has six independent elastic constants: C_{11} , C_{33} , C_{12} , C_{13} , C_{44} , and C_{66} . The elastic constants of the 0°/90° crossply composite material, deduced by resonant spectrum fitting, are listed in Table IV.

IV. Discussion

(1) Elastic Constants

(A) *Unidirectional Composites*: For unidirectional composites, transversely isotropic symmetry in the plane perpendicular to the fiber direction is generally accepted to be appropriate.

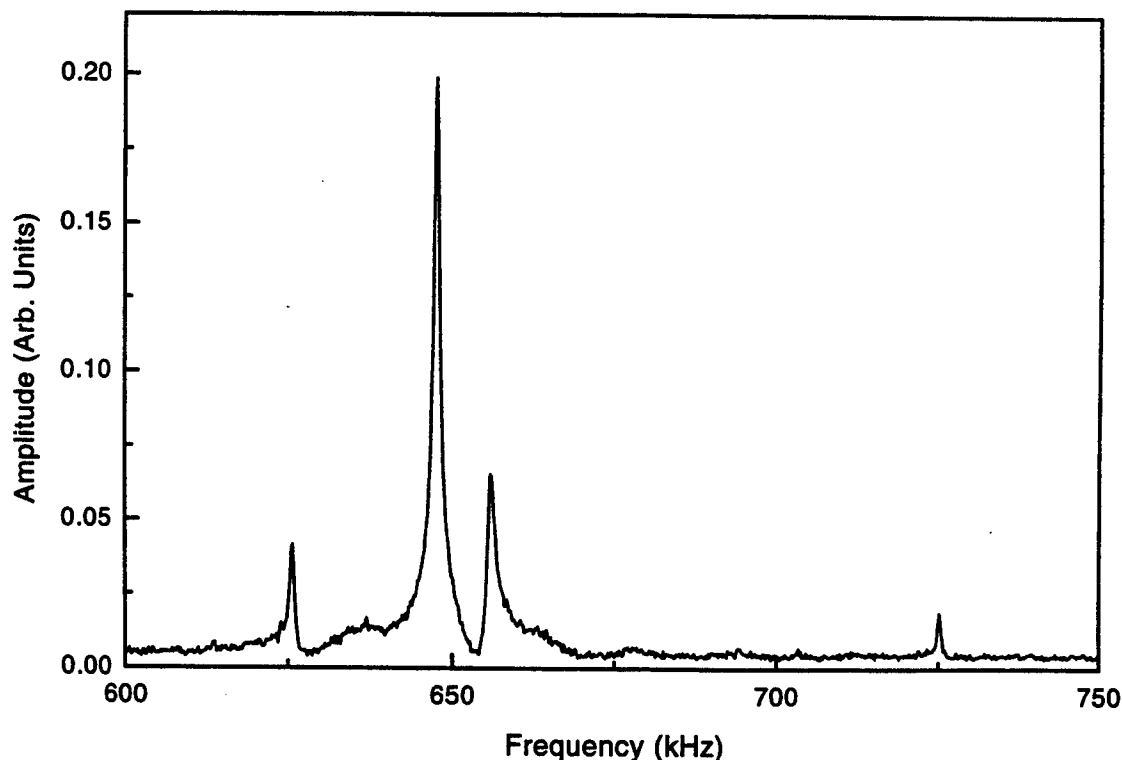


Fig. 3. Portion of the resonant frequency spectrum, 600–750 kHz, of a unidirectional CAS/SiC composite.

Table II. Elastic Stiffness Constants, C_{ij} , of Unidirectional CAS/SiC Composites with either Transversely Isotropic Symmetry or Orthotropic Symmetry*

Symmetry	Elastic stiffness constant, C_{ij} (GPa)									RMS [†] error (%)
	C_{11}	C_{22}	C_{33}	C_{23}	C_{13}	C_{12}	C_{44}	C_{55}	C_{66}	
Transversely isotropic	147.21 (0.20)	147.21 (0.20)	153.83 (0.14)	50.36 (0.24)	50.36 (0.24)	53.30 (0.51)	47.72 (0.01)	47.72 (0.01)	46.95 (0.04)	0.2572
Orthotropic	146.50 (0.06)	148.53 (0.07)	154.12 (0.10)	50.49 (0.28)	50.43 (0.52)	54.00 (0.35)	48.20 (<0.01)	47.17 (<0.01)	46.86 (0.01)	0.1869

*Value given in parentheses is the error (in %). [†]Root mean square.

Table III. First Ten Measured and Calculated[†] Frequencies of Unidirectional CAS/SiC Composites

Frequency (kHz)		$\frac{f_{\#} - f}{f}$ (%)	Calculated frequency, $f_{\#}$ (kHz)	$\frac{f_{\#} - f}{f}$ (%)
Measured, f	Calculated, $f_{\#}$			
472.97	470.92	-0.43	472.09	-0.19
625.71	624.48	-0.20	626.12	0.07
647.45	646.19	-0.20	648.09	0.10
654.59	657.53	0.42	655.37	0.09
725.18	721.14	-0.53	724.82	-0.05
759.29	758.92	-0.05	758.49	-0.10
791.89	789.03	-0.36	790.98	-0.12
818.76	822.90	0.51	820.22	0.18
850.12	848.79	-0.16	847.84	-0.27
859.96	858.07	-0.22	858.74	-0.14

[†] $f_{\#}$ is the frequency calculated assuming the sample has transversely isotropic symmetry; $f_{\#}$ is the frequency calculated assuming orthotropic symmetry.

Table IV. Elastic Stiffness Constants, C_{ij} , of 0°/90° Crossply CAS/SiC Composites with Tetragonal Symmetry*

Elastic stiffness constant, C_{ij} (GPa)						RMS [†] error (%)
C_{11}	C_{33}	C_{13}	C_{12}	C_{44}	C_{66}	
147.45 (0.11)	145.19 (0.28)	52.23 (0.39)	49.96 (0.88)	46.12 (0.01)	46.35 (0.02)	0.4537

*Value given in parentheses is the error (in %). [†]Root mean square.

However, transverse anisotropy can occur if the fiber distributions in the principal directions of the 1-axis and 2-axis are not uniform. This could occur because of fiber rearrangement during hot pressing. When this occurs, the symmetry of the material would be orthotropic, and all nine elastic constants mentioned above would be independent.

From Table III, the calculated frequencies based on transversely isotropic symmetry agree well with the measured values. The relative errors between the measured and calculated resonant frequencies are <1% for all 70 measured peaks. In fact, the root-mean-square (RMS) deviation of the fitting is as low as 0.25%, and, to a good approximation, these materials can be viewed as transversely isotropic. However, when orthotropic symmetry is assumed for the fitting, the differences between the measured and calculated resonant frequencies are smaller; the RMS error is reduced to 0.19%. Thus, the unidirectional CAS/SiC composite is not a perfectly transversely isotropic material; a small anisotropy exists in the plane perpendicular to the fiber direction. The in-plane anisotropy is clearly small, and the data shown in Table II indicate that, for orthotropic symmetry, $C_{11} \approx C_{22}$, $C_{13} \approx C_{23}$, $C_{44} \approx C_{55}$, and $C_{66} \approx (C_{11} - C_{12})/2$. Thus, we will assume transversely isotropic symmetry for the unidirectional CAS/SiC for the remainder of the discussion.

Because the fibers are stiffer than the matrix and they are packed along the direction of the 3-axis, C_{33} should be higher than C_{11} and C_{22} . For the shear moduli, one would expect $C_{44} \approx C_{55} \geq C_{66}$, because C_{66} ($= C_{1212}$) represents the shear modulus for a shear stress in the 1-3 plane along the direction of the 1-axis or in the 2-3 plane along the direction of the 2-axis. Thus, the main contribution to C_{66} comes from the matrix, because the fibers are parallel to the shear plane. The results in Table II reveal that this is indeed the case. Previous studies on boron-aluminum-metal-matrix composites reached a similar conclusion.¹⁸ However, in the CAS/Nicalon SiC system, this

effect is rather weak, because C_{44} , C_{55} , and C_{66} are all quite similar to each other, again indicating that the elastic anisotropy of this composite is small.

(B) *0°/90° Crossply Composites:* The 0°/90° crossply composite material has been assumed to possess tetragonal symmetry. This approximation is based on the assumption that the number of 0° and 90° plies are equal and that they have identical thickness with the same fiber volume fraction. However, SEM micrographs of the 0°/90° crossply composite show that the ply thicknesses along the 0° and 90° layers are not completely uniform, which can, therefore, contribute to a variation in the respective C_{ij} . Indeed, the relative differences between the measured and calculated ultrasonic resonant frequencies are slightly larger than those for the unidirectional material.

(2) Orientation Dependence of the Elastic Moduli

(A) *Unidirectional Composites:* Based on the C_{ij} values, the elastic compliance constants, S_{ij} , can be calculated using $[C][S] = [I]$, where $[I]$ is a 6×6 unit matrix. The determination of S_{ij} is especially necessary if one wants to know the elastic moduli as a function of fiber orientation, because the orientation dependence of Young's modulus and the shear modulus can be easily calculated from a proper transformation of the compliance matrix S_{ij} .¹⁹ The S_{ij} values for the unidirectional and 0°/90° CAS/SiC composite materials are listed in Table V.

Because the unidirectional CAS/SiC composite material is transversely isotropic, the Young's modulus along a transverse direction, E_T , within the plane perpendicular to the fiber direction (1-2 plane) is a constant: $E_T = E_1 = 1/S_{11} = 120.35$ GPa, which is similar to the value provided by Corning ($E_T = 117$ GPa).

When the tensile axis is confined within the 1-3 plane, the corresponding Young's modulus, as a function of orientation, can be expressed by^{8,15,19}

$$\frac{1}{E} = S'_{11} = S_{11} \sin^4 \theta + S_{33} \cos^4 \theta + \frac{1}{4}(2S_{13} + S_{44}) \sin^2 2\theta \quad (2)$$

where θ is the angle between the tensile axis and the 3-axis (which also is the fiber direction). The orientation dependence of Young's modulus in the 1-3 plane is plotted in Fig. 4(A). When $\theta = 0^\circ$, $E = E_L = 1/S_{33} = 128.53$ GPa, which is the Young's modulus along the longitudinal or fiber direction, and is consistent with that provided by Corning (see Table I) and other results obtained from tensile^{10,20} and compressive tests.²¹

The Young's moduli along the longitudinal and transverse directions can also be estimated using

$$E_L = E_f V_f + E_m (1 - V_f) \quad (3)$$

and

$$\frac{1}{E_T} = \frac{V_f}{E_f} + \frac{1 - V_f}{E_m} \quad (4)$$

although Eq. (4) gives a lower-bound estimate of E_T . Assuming $E_f = 200$ GPa, $E_m = 97$ GPa, and $V_f = 0.34$, we obtain $E_L = 132.0$ GPa and $E_T = 117.6$ GPa, which are in good agreement with our results deduced from the RUS measurements, although the agreement of E_T is probably due to the modest degree of elastic mismatch.

Similarly, the shear modulus within the 1-2 plane is a constant independent of the shear-stress direction: $G = 1/S_{44} = C_{44} = 47.72$ GPa. When the shear plane is the 1-3 plane, the shear modulus is determined by¹⁵

$$\frac{1}{G} = S_{66} \sin^2 \theta + S_{44} \cos^2 \theta \quad (5)$$

where θ is the angle between the shear stress axis and the 3-axis. When $\theta = 0^\circ$, $G = 1/S_{44} = C_{44} = 47.72$ GPa, as expected; when $\theta = 90^\circ$, $G = 1/S_{66} = C_{66} = 46.95$ GPa. The orientation dependence of the shear modulus also is shown in Fig. 4(A).

From Fig. 4(A), the elastic anisotropy for the unidirectional CAS/SiC composites is evidently weak. This could be justified by the following factors: the fiber volume fraction is only moderate; the magnitude of E_f is only twice that of E_m ; and a relatively stronger fiber-matrix interfacial bond exists in CAS/SiC compared to lithium aluminosilicate/SiC (LAS/SiC), in which the system transverse elastic modulus is significantly lower.⁴

(B) 0°/90° Crossply Composites: For the 0°/90° laminated CAS/SiC composites, the sample has tetragonal symmetry with respect to the thickness direction, which is the direction of the 3-axis in Fig. 1(B). Following a similar approach to that discussed above and using the S_{ij} data of Table V, we plot the orientation dependence of Young's modulus for a tensile stress within the 1-3 plane. In this case, Eq. (2) also is valid, and θ is now defined as the angle between the lamina thickness direction (3-axis) and the stress direction; the result is plotted in Fig. 4(B). When the tensile direction is along the thickness direction, the corresponding Young's modulus, E_3 , is 117.44 GPa, whereas the longitudinal Young's modulus along either one of the fiber directions, $E_L = E_1 = E_2$, is 121.07 GPa.

The crossply material used in this study has an even number of laminae laid on each other, with the fiber direction alternating between 0° and 90° orientations, and double 0° (or 90°) layers present in the center. Consequently, this is a symmetric laminate. Assuming that the in-plane strains are identical in each ply, one can calculate E_L along the fiber direction of the 0°/90° crossply composite using the elastic moduli of a single ply:⁶

$$E_L = \frac{\frac{1}{4} \left(1 + \frac{E_L^s}{E_T^s} \right) - \nu^2}{\frac{1}{2} \left(1 + \frac{E_L^s}{E_T^s} \right) \left(\frac{E_L^s}{E_T^s} - \nu^2 \right)} E_L^s \quad (6)$$

where E_L^s and E_T^s are the longitudinal and transverse elastic moduli, respectively, of a single ply, and ν is its Poisson's ratio.

Assuming that the elastic moduli of a single ply are the same as those for unidirectional laminates—i.e., $E_L^s = 128.53$ GPa, $E_T^s = 120.36$ GPa, and $\nu = 0.25$ — E_L is calculated to be 124.45 GPa, which is in good agreement with the value deduced from our measurements. The expected order, $E_L^s > E_L > E_T^s$, is observed.

RUS measurements on the 0°/90° crossply composite provide $E_L = 121.07$ GPa and $E_T = 117.44$ GPa, whereas for a unidirectional laminated material, we have $E_L = 128.53$ GPa and $E_T = 120.36$ GPa. If the fiber volume fraction were the same for the 0° and 0°/90° laminates, the transverse modulus E_T (in the laminate thickness direction) would be the same for both cases. The small discrepancy between these two transverse elastic moduli suggests a slightly smaller fiber volume fraction in the 0°/90° laminated composite.

The E_L value for the 0°/90° crossply composite deduced from our RUS measurements is ~9% larger than that provided by Corning (Table I). Early work by Beyerle *et al.*,⁷ using mechanical testing, showed that $E_L \approx 100$ GPa, which was consistent with the calculated results using a separated interface model. However, a recent investigation by Cady *et al.*,¹¹ again using mechanical testing, resulted in $E_L \approx 120$ GPa, which is in good agreement with our result. The different experimental results might be due to sample processing variations. Also, the RUS technique is a nondestructive evaluation technique, whereas cracks may be initiated in the matrix during mechanical testing, even at low stress levels, consequently changing the effective elastic modulus.

The orientation dependence of the shear modulus in the 1-3 plane for the 0°/90° crossply composite can be calculated using Eq. (5), as for unidirectional composites, and the result is plotted in Fig. 4(B). The shear modulus for a shear stress in the 1-2 plane is again independent of the shear stress direction, and $G = C_{44} = 46.12$ GPa. From Fig. 4(B), we can conclude that the elastic anisotropy for the 0°/90° crossply composite is further reduced, compared to the unidirectional composites.

(3) Poisson's Ratio

The Poisson's ratio is an important property of a material in mechanical design. If we apply a longitudinal stress along the direction of the 1-axis, the Poisson's ratio ν_{12} is defined as $-\epsilon_2/\epsilon_1$, where ϵ_1 is the longitudinal strain and ϵ_2 is the strain in the direction of the 2-axis, transverse to the direction of the 1-axis. The Poisson's ratio ν_{ij} can easily be calculated, using the elastic stiffness constants S_{ij} :

$$\nu_{ij} = -\frac{S_{ij}}{S_{ii}} \quad (7)$$

The values of Poisson's ratio for the unidirectional and 0°/90° crossply composites are listed in Table VI. For unidirectional composites, ν_{ij} obtained from RUS is 0.235–0.282, whereas the average value using Hill's averaging scheme,²² ν_H , is 0.260. These values are in good agreement with those provided by Corning. Because the direction of the 3-axis (the fiber direction) is stiffer than the transverse direction, one can naturally expect that $\nu_{31} > \nu_{13} = \nu_{23}$.

(4) Bulk Modulus

The volume compressibility, κ , of a material can be expressed in terms of its elastic compliance constants, S_{ij} :¹⁹

$$\kappa = -\frac{1}{V} \left(\frac{\partial V}{\partial p} \right) = S_{11} + S_{22} + S_{33} + 2(S_{12} + S_{23} + S_{13}) \quad (8)$$

The bulk modulus, K , is then $1/\kappa$. Thus, for unidirectional CAS/SiC composites, $K = 84.0$ GPa, whereas for 0°/90° crossply composite materials, $K = 83.3$ GPa.

V. Conclusions

We have demonstrated that the RUS technique is an efficient method for determining all the independent elastic stiffness

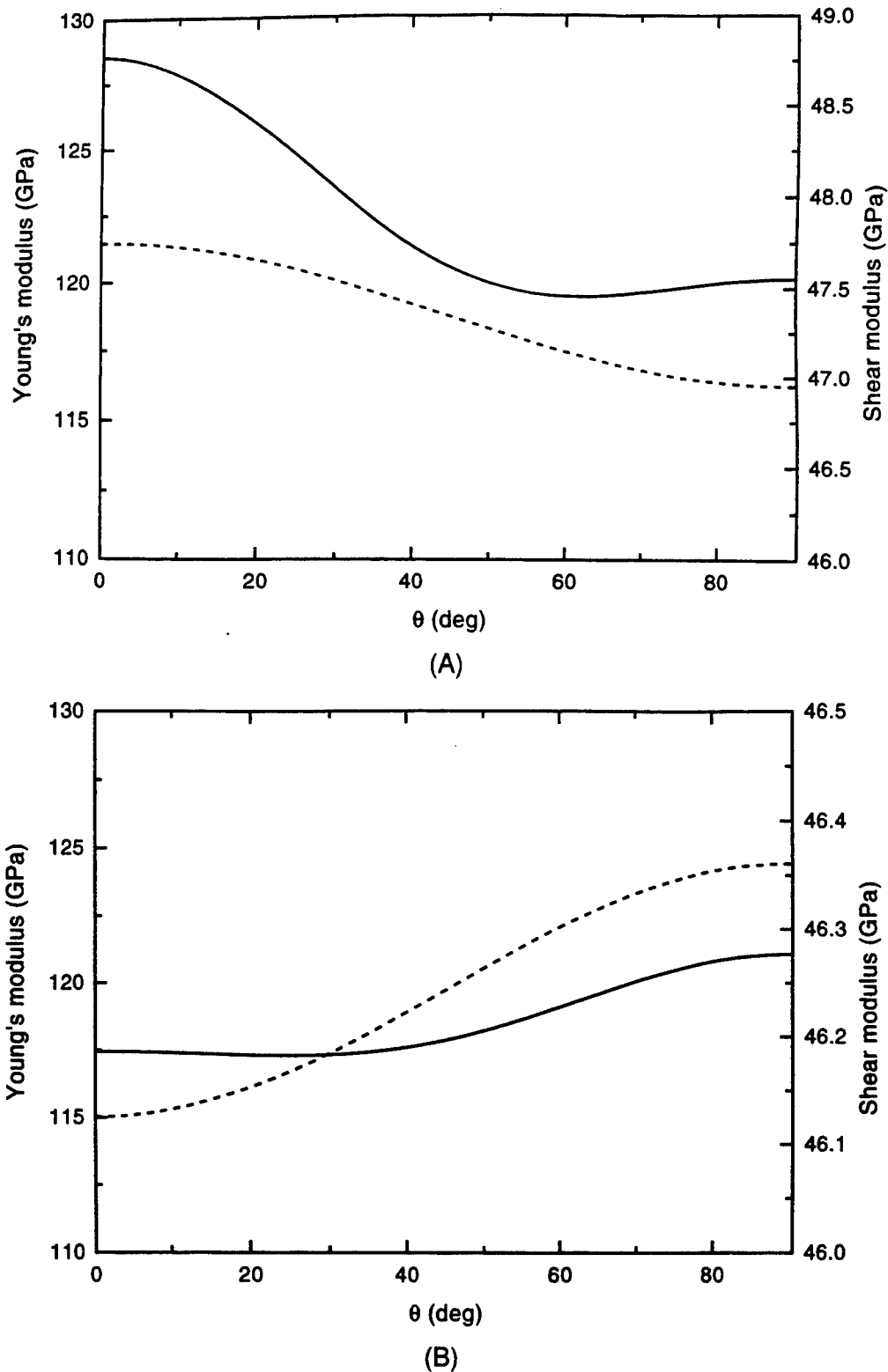


Fig. 4. Orientation dependence of (—) Young's modulus and (---) shear modulus for (A) unidirectional and (B) 0°/90° crossply composite material.

Table V. Elastic Compliance Coefficients, S_{ij} , of Unidirectional* and 0°/90° Crossply Composite Materials

	Elastic compliance coefficient, S_{ij} (10^{-11} m ² /N)					
	S_{11}	S_{22}	S_{33}	S_{12}	S_{44}	S_{66}
0°	0.8309	0.7780	-0.1954	-0.2340	2.0956	2.1299 [†]
0°/90°	0.8260	0.8515	-0.2257	-0.1998	2.1683	2.1575

*Unidirectional calculation is based on transversely isotropic symmetry. [†] $S_{66} = 2(S_{11} - S_{22})$.

Table VI. Poisson's Ratio for Unidirectional¹ and 0°/90° Crossply Composite Materials

	Poisson's ratio, ν_{ij}					
	ν_{11}	ν_{12}	ν_{21}	ν_{22}	ν_{13}	ν_H^2
0°	0.2512	0.2512	0.2816	0.2352	0.2816	0.260
0°/90°	0.2651	0.2651	0.2419	0.2733	0.2419	0.263

¹For the unidirectional composites, the calculation was made based on transversely isotropic symmetry. ² ν_H is the average Poisson's ratio, based on Hill's averaging scheme.

constants of fiber-reinforced glass-ceramic-matrix composites accurately. For a unidirectional CAS/Nicalon SiC composite, the elastic stiffness constants have been deduced based on a transversely isotropic symmetry and an orthotropic symmetry assumption, whereas tetragonal symmetry has been used for the 0°/90° laminated composite. Our results indicate that the unidirectional material is slightly orthotropic; however, because the transverse anisotropy is small, the assumption that the material is isotropic transverse to the fiber direction is a good one for most applications.

The orientation dependence of Young's modulus and the shear modulus was calculated from the elastic compliance constants. For the unidirectional composite, the longitudinal and the transverse Young's moduli were 128.53 and 120.35 GPa, respectively. These values are in reasonable agreement with those obtained from mechanical testing. Based on the RUS measurements, the Young's moduli along the fiber direction and the laminate thickness direction of the 0°/90° crossply composite were 121.07 and 117.44 GPa, respectively. These values are slightly smaller than those calculated based on the elastic moduli of a single ply and are slightly larger than those provided by Corning. The small discrepancy among these results may be attributed to small variations of the fiber volume fractions.

For unidirectional and 0°/90° laminated composites, the shear modulus and Poisson's ratio show very little variation with orientation. The results reveal that the elastic anisotropy for unidirectional and 0°/90° laminated materials is small. This is due to the fact that Young's modulus of the fiber (E_f) is only twice that of the matrix (E_m) and the volume fraction of fiber (V_f) is moderate. If E_f had been much larger than E_m and with a much higher V_f , one would have expected a much larger elastic anisotropy in these materials. High transverse modulus also is achieved by a relatively stronger fiber-matrix interfacial bond in CAS/SiC, compared to LAS/SiC composites.⁴

Acknowledgments: The authors are grateful to K. Chyung and D. C. Larsen (Corning, Inc.), for supplying the material and discussion, and to A. Migliori, T. Darling, and C. Cady (Los Alamos National Laboratory), together with Anthony Evans, for helpful discussions.

References

¹K. M. Prewé and J. J. Brennan, "Silicon Carbide-Fiber-Reinforced Glass-Ceramic Matrix Composites Exhibiting High Strength and Toughness," *J. Mater. Sci.*, **17**, 2371–83 (1982).

²J. J. Brennan, "Glass and Glass-Ceramic Matrix Composites," pp. 222–59 in *Fiber Reinforced Ceramic Composites*. Edited by K. S. Mazziyasni. Noyes, Park Ridge, NJ, 1990.

³A. G. Evans and D. B. Marshall, "The Mechanical Behavior of Ceramic Matrix Composites," *Acta Metall.*, **37** [10] 2567–83 (1989).

⁴D. C. Larsen and S. L. Stuchly, "The Mechanical Evaluation of Ceramic Fiber Composites," see Ref. 2, pp. 182–221.

⁵R. W. Rice, "Ceramic Composites: Future Needs and Opportunities," see Ref. 2, pp. 452–95.

⁶Z. C. Xia, R. R. Carr, and J. W. Hutchinson, "Transverse Cracking in Fiber-Reinforced Brittle Matrix, Cross-Ply Laminates," *Acta Metall. Mater.*, **41** [8] 2265–76 (1993).

⁷D. S. Beyerle, S. M. Spearing, and A. G. Evans, "Damage Mechanisms and the Mechanical Properties of a Laminated 0/90 Ceramic/Matrix Composite," *J. Am. Ceram. Soc.*, **75** [12] 3321–30 (1992).

⁸R. M. Jones, *Mechanics of Composite Materials*. Hemisphere Publishing, New York, 1975.

⁹R. Y. Kim and N. Pagano, "Crack Initiation in Unidirectional Brittle-Matrix Composites," *J. Am. Ceram. Soc.*, **74** [5] 1082–90 (1991).

¹⁰D. S. Beyerle, S. M. Spearing, F. W. Zok, and A. G. Evans, "Damage and Failure in Unidirectional Ceramic-Matrix Composites," *J. Am. Ceram. Soc.*, **75** [10] 2719–25 (1992).

¹¹C. Cady, F. E. Heredia, and A. G. Evans, "In-Plane Mechanical Properties of Several Ceramic-Matrix Composites," *J. Am. Ceram. Soc.*, **78** [8] 2065–78 (1995).

¹²D. B. Marshall and A. G. Evans, "Failure Mechanisms in Ceramic Fiber/Ceramic Matrix Composites," *J. Am. Ceram. Soc.*, **68** [5] 225–34 (1985).

¹³T. J. Mackin, K. E. Perry Jr., J. S. Epstein, C. Cady, M. Y. He, and A. G. Evans, "Strain Fields and Damage around Notches in Ceramic-Matrix Composites," *J. Am. Ceram. Soc.*, **79** [1] 65–73 (1996).

¹⁴A. Migliori, J. L. Sarrao, W. M. Visscher, T. M. Bell, M. Lei, Z. Fisk, and R. G. Leisure, "Resonant Ultrasound Spectroscopic Techniques for Measurement of the Elastic Moduli of Solids," *Physica B (Amsterdam)*, **183**, 1–24 (1993).

¹⁵Y. He, R. B. Schwarz, A. Migliori, and S. H. Whang, "Elastic Constants of Single Crystal γ -TiAl," *J. Mater. Res.*, **10**, 1187–95 (1995).

¹⁶A. Migliori, W. M. Visscher, S. Wong, S. E. Brown, I. Tanaka, H. Kojima, and P. B. Allen, "Complete Elastic Constants and Giant Softening of C_{66} in Superconducting $\text{La}_{1-x}\text{Sr}_x\text{CuO}_4$," *Phys. Rev. Lett.*, **64** [20] 2458–61 (1990).

¹⁷F. Chu, M. Lei, A. Migliori, S. P. Chen, and T. E. Mitchell, "Anomalous Elastic Properties in a C15 Laves-phase Compound," *Philos. Mag. B*, **70** [4] 867–80 (1994).

¹⁸H. Ledbetter, C. Fortunko, and P. Heyliger, "Orthotropic Elastic Constants of a Boron-Aluminum Fiber-Reinforced Composite: An Acoustic-Resonance-Spectroscopy Study," *J. Appl. Phys.*, **78** [3] 1542–46 (1995).

¹⁹J. F. Nye, *Physical Properties of Crystals*. Oxford Scientific Publications, New York, 1985.

²⁰Y.-M. Liu, T. E. Mitchell, and H. N. G. Wadley, "Anisotropic Damage Evolution in Unidirectional Fiber Reinforced Ceramics," to be submitted to *Acta Metall. Mater.*

²¹C. Cady, private communication.

²²E. Schreiber, O. L. Anderson, and N. Soga, *Elastic Constants and Their Measurements*. McGraw-Hill, New York, 1973. □

THE INFLUENCE OF FIBER/MATRIX INTERFACE ON THE MECHANICAL BEHAVIOR OF NICALON SiC FIBER REINFORCED GLASS-CERAMIC COMPOSITES

Y. M. Liu *, T. E. Mitchell *, H. N. G. Wadley **

* Center for Materials Science, Mail Stop K 765, Los Alamos National Laboratory, Los Alamos, NM 87545

** Department of Materials Science and Engineering, School of Engineering and Applied Science, University of Virginia, Charlottesville, VA 22903

ABSTRACT

The mechanical properties of unidirectional Nicalon SiC fiber reinforced calcium aluminosilicate (CAS/SiC) and magnesium aluminosilicate (MAS/SiC) glass-ceramic composites have been investigated by tensile testing and a nondestructive laser-ultrasound technique. The barium-stuffed MAS was either undoped or doped with 5% borosilicate glass. The degradation of the elastic stiffness constant C_{11} in the transverse direction due to interface damage was monitored *in-situ* by measuring the laser-generated ultrasound wave velocity. The three composite materials show distinctly different macroscopic deformation characteristics, which are correlated strongly to the interface degradation. A stronger reduction trend of the elastic constant C_{11} is associated with a larger degree of inelastic deformation. Observations of the fracture surfaces also reveal the close relation between fiber pullout length and interfacial characteristics. Interfaces of these composites have been studied by TEM, and their influence on inhibiting and deflecting matrix cracks is discussed.

INTRODUCTION

It is well known that the fiber/matrix interface has a profound influence on the mechanical behavior of ceramic matrix composites (CMCs).^{1,2} Since the failure strain of the matrix is usually smaller than that of the fiber, matrix cracking occurs first under tensile loading.³ Matrix cracks run into nearby fibers and are deflected along the fiber/matrix interface if the interface is relatively weak. CMCs exhibit nonlinear deformation behavior as a result of multiple matrix cracking and interface debonding/sliding.⁴

Although the importance of the interface has long been recognized, little has been done to investigate the interface damage *in situ* and correlate it to macroscopic deformation. In this study, a laser-ultrasound technique has been applied to reveal the relation between interface degradation and axial deformation under uniaxial tension. Laser-generated ultrasound velocities in transverse plane are measured at various stress (damage) levels. The transverse elastic stiffness can then be determined from these measurements. The deterioration of transverse elastic stiffness due to interface damage is reflected by the reduction of ultrasound velocity measured in the transverse plane. Three Nicalon SiC fiber reinforced glass-ceramic matrix systems, calcium aluminosilicate (CAS), barium-stuffed magnesium aluminosilicate (MAS) undoped or doped with 5% borosilicate glass (BSG), are used in this investigation. BSG functions as a source of boron and diffuses into the interface and fiber during hot consolidation, which affects the interfacial layer formation.⁵ The degree of stiffness reduction in the transverse and axial directions will be studied for the above CMCs. The important role of fiber/matrix interface on the macroscopic deformation behavior will be discussed.

EXPERIMENTAL

Nicalon SiC fiber reinforced unidirectional CAS and MAS composite panels were supplied by Corning Inc. The manufacturing procedure and material properties are described elsewhere^{6,7}. The Nicalon SiC fiber volume fraction is about 0.35 ~ 0.4, and the average fiber diameter is 15 μm . There is a carbon-rich interface formed during fabrication, which plays an important role in the deformation of Nicalon fiber reinforced ceramics.^{1,2,8,9}

Tensile specimens were $\sim 150 \text{ mm} \times 10 \text{ mm} \times 3 \text{ mm}$. Side surfaces of some samples were polished before tensile testing in order to take acetate replicas of surface matrix cracks during loading. Cross-head speed of 0.03 mm/min was used. Axial strain was measured with a one-inch gauge length extensometer. Both continuous and loading/unloading tests¹⁰ were conducted for each CMC system.

Detailed procedures for the laser-ultrasound test have been given previously.¹⁰ The laser pulse from a Q-switch Nd:YAG laser with an operating wavelength of 1.064 μm was delivered to the sample under loading by an optical fiber with a 600 μm core diameter.¹¹ The laser beam was coupled into one end of the optical fiber by a small convex lens, and the outcoming beam from the fiber was focused onto the sample by two convex lenses. A small portion of the laser pulse was deflected onto a photodiode and used to trigger a pair of 8-bit, 1 GHz digital oscilloscopes. The signals from two ultrasonic transducers were also connected to the oscilloscopes. These signals were amplified and low pass filtered at 10 MHz. The arrival time of the ultrasound wave was measured by observing the difference in time between the photodiode and the transducer pulse. The systematic delay arising from the propagation of the laser pulse through the optical system was measured and subtracted.

Thin sections parallel to the fiber direction were cut from as-received material, mechanically polished to $\sim 20 \mu\text{m}$, and ion-milled. The fiber/matrix interface was then analyzed by transmission electron microscopy (TEM).

RESULTS AND DISCUSSION

The stress-strain behavior of CAS/SiC, MAS0/SiC, and MAS5/SiC composites are shown in Fig. 1. MAS0 refers to undoped MAS and MAS5 refers to MAS doped with 5% BSG. Axial Young's modulus E_L is almost identical ($\sim 150 \text{ GPa}$) for MAS5/SiC and MAS0/SiC, and is $\sim 130 \text{ GPa}$ for CAS. Deformation beyond the linear elastic regime is quite different for the three CMCs. CAS/SiC has a plateau region in the stress range of 200~270 MPa, and shows a "stiffening" effect in the final deformation stage. MAS0/SiC deviates appreciably from linear elastic behavior near 300 MPa, and deforms nonlinearly up to failure without a plateau regime, while MAS5/SiC displays very little nonlinear deformation.

The above characteristics are closely correlated to their interfacial characteristics and corresponding transverse stiffness degradation. The transverse elastic stiffness C_{11} is directly related to the ultrasound velocity by $C_{11} = \rho V_L^2$, where ρ is the density of the composite and V_L is the longitudinal velocity in the transverse direction. The change of C_{11} as a function of applied stress is illustrated in Fig. 2, where symbols are the experimental data from various tests, and continuous lines are from curve fitting to show the general reduction trends. Among the three Nicalon SiC reinforced glass-ceramics, CAS/SiC exhibits the largest degree of reduction of C_{11} , while MAS5/SiC shows the least reduction. The same order applies for axial nonlinear deformation. A large amount of nonlinear deformation from 200 to 270 MPa for CAS/SiC is also

associated with the rapid reduction of C_{11} in this range, where the matrix cracking density increases significantly.¹⁰

Since matrix cracks are nearly parallel to the transverse direction, transverse stiffness is insensitive to the presence of matrix cracks. The reduction of C_{11} is attributed to the degradation of interfacial adhesion as a result of the interaction between transverse matrix cracks and the interface. Although MAS5/SiC shows little nonlinear deformation, matrix cracking is found from surface replicas. Matrix cracking of MAS5/SiC at a stress level of 255 MPa is illustrated in Fig. 3. The absence of a reduction of C_{11} in MAS5/SiC indicates that interfacial damage in the form of debonding/sliding is inhibited substantially in a strongly bonded interface system, and results in negligible reduction of transverse elastic stiffness. The above observations demonstrate that, to exhibit appreciable amount of nonlinear deformation, significant interfacial damage must occur in addition to multiple matrix cracking. Strong fiber/matrix interface prohibits matrix crack opening considerably and results in small inelastic strain. This observation also confirms that, as pointed out by Kim *et. al.*¹², defining the initiation of matrix cracking from stress-strain curves using the deviation point from the linear regime is inappropriate in CMCs. For CMCs where multiple matrix cracking occurs, the beginning of macroscopic nonlinear deformation is a result of *damage accumulation* due to interface debonding/sliding and consequent matrix crack opening.

As expected, the fiber pull-out length after failure in MAS5/SiC is quite short compared to that of MAS0/SiC and CAS/SiC. This is illustrated in Figs. 4 (a)-(c).

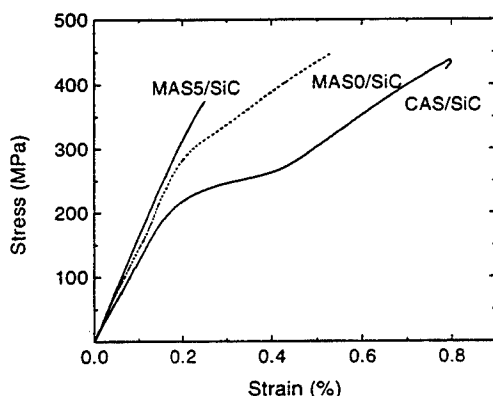


Fig. 1 Stress-strain curves for CAS/SiC, MAS0/SiC, and MAS5/SiC composites.

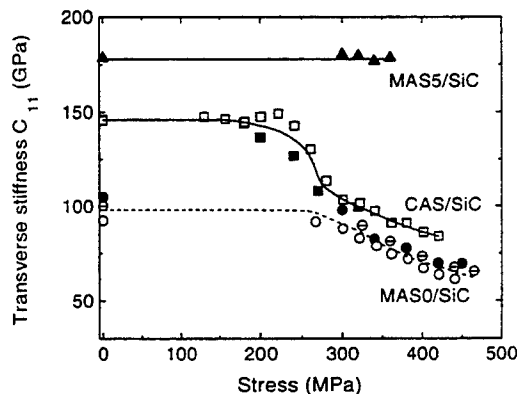


Fig. 2 Reduction of transverse elastic stiffness C_{11} with the increase of stress.



Fig. 3 Optical micrograph of surface replica of MAS5/SiC revealing matrix cracking at 255 MPa.

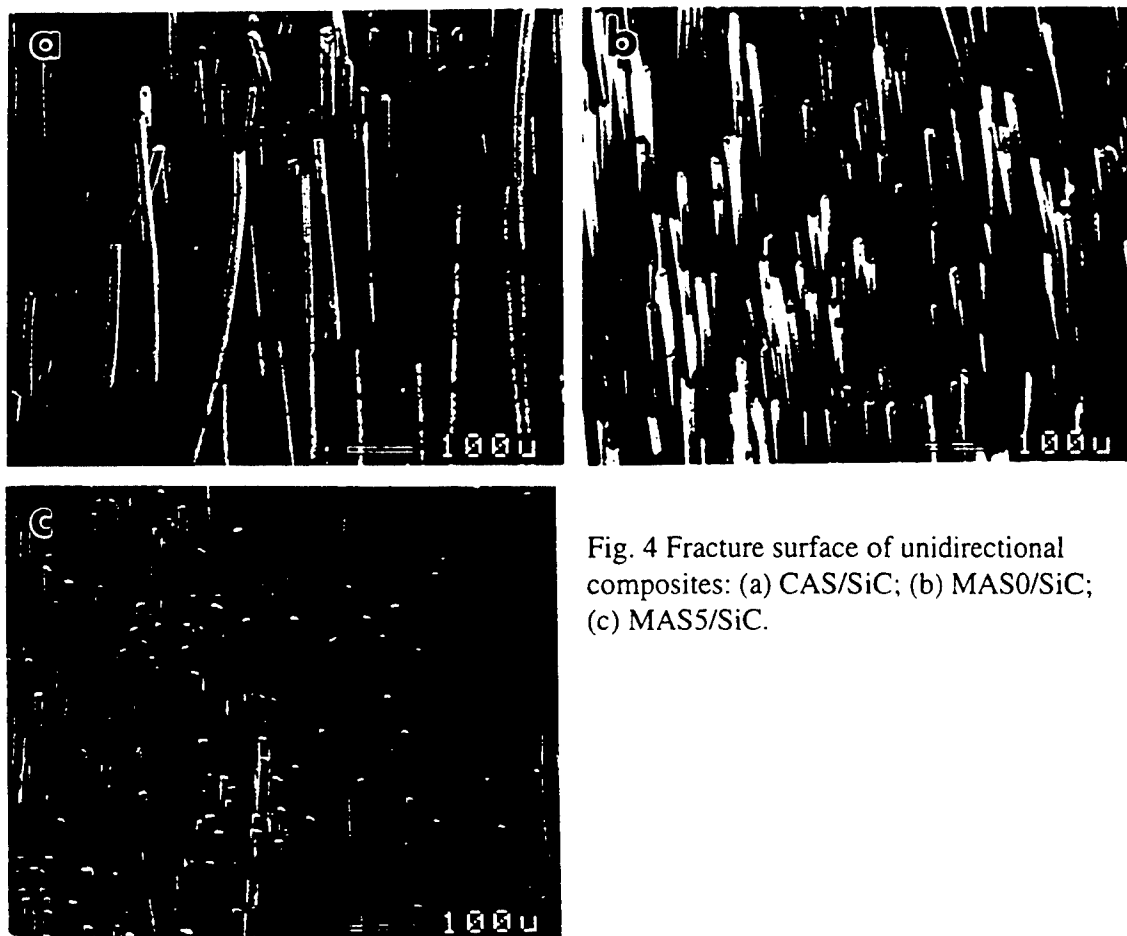


Fig. 4 Fracture surface of unidirectional composites: (a) CAS/SiC; (b) MAS0/SiC; (c) MAS5/SiC.

C_{11} is seen to be quite low for as-processed MAS0/SiC (~ 100 GPa) compared to MAS5/SiC (~ 175 GPa). Because the MAS matrix has a lower thermal expansion coefficient ($\sim 2.6 \times 10^{-6} \text{ K}^{-1}$) than that of the fiber ($4.0 \times 10^{-6} \text{ K}^{-1}$),¹³ the fiber/matrix interface is under residual tension after processing, which could result in local gaps at the interface. Whereas for MAS5/SiC, this gap is filled by reaction layers because of doping, and strong adhesion at the interface is achieved. This is reflected by the higher value of C_{11} in as-processed MAS5/SiC. Transverse tensile testing also confirms that the transverse Young's modulus E_T of MAS0/SiC is much lower than that of MAS5/SiC.¹⁴ However, the interfacial bonding has little effect on the initial E_L of MAS5 and MAS0 (before matrix cracking occurs). It is the interaction between matrix cracking and the interface that determines the nonlinear deformation behavior.

TEM thin foil observations of MAS5/SiC and MAS0/SiC reveal that a uniform interaction layer formed in MAS5 compared to a slightly porous interfacial structure in MAS0. This is illustrated in Figs. 5 (a)-(b). Preliminary chemical analysis on MAS5/SiC by X-ray energy dispersive spectroscopy (EDS) reveals there is barium segregation at fiber/matrix interface.¹⁵ XPS investigation on 7.5% doped MAS by Larsen *et al.* indicated that boron is present at interfaces in the form of B_2O_3 and BN.⁵ We have attempted to detect B or N on MAS5/SiC by parallel energy loss spectroscopy (PEELS) but have so far been unsuccessful due to the low concentration of B and N.¹⁵ A stronger bond does form at fiber/matrix interface because of doping in the MAS system, as revealed by laser-ultrasonic measurements and transverse tensile

testing. More study is underway to characterize the chemistry and microstructure of the interface in the MAS system.

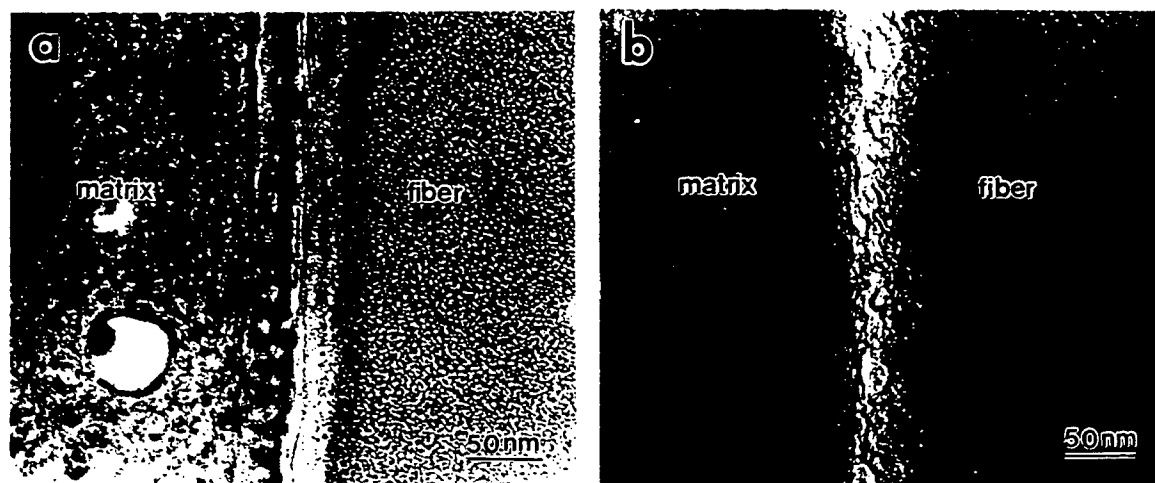


Fig. 5 TEM bright field images of fiber/matrix interfacial region:(a) MAS5/SiC; (b) MAS0/SiC

CONCLUSIONS

Using a laser-ultrasonic technique, progressive interface damage has been monitored *in situ* during uniaxial tension. A strong correlation between interface debonding/sliding and axial nonlinear deformation is found. A strong reduction in the transverse elastic constant C_{11} is associated with large inelastic deformations. Among the three CMCs investigated, MAS5/SiC shows little nonlinear deformation (as a result of doping), consistent with a negligible reduction in the transverse stiffness and a short fiber pull-out length after failure. Results confirm that the interaction between matrix cracking and the interface has a significant role on the nonlinear deformation of CMCs. Strongly bonded fiber/matrix interfaces inhibit matrix crack opening and result in little inelastic deformation in the axial direction.

ACKNOWLEDGMENTS

The authors would like to acknowledge the financial support by Department of Energy, Office of Basic Sciences and DARPA funded UCSB-URI program (S. Fishman, Program Manager).

REFERENCES

- ¹ D. B. Marshall and A. G. Evans, J. Am. Ceram. Soc. **68**, p. 225 (1985).
- ² K. M. Prewo and J. J. Brennan, J. Mater. Sci. **17**, p. 2371 (1982)
- ³ D. C. Larsen and S. L. Stuchly, in Fiber Reinforced Ceramic Composites, edited by K. S. Mazdizyasni, Noyes Publications, Park Ridge, New Jersey, p. 182-221 (1990).
- ⁴ M. Y. He, B.-X. Wu, A. G. Evans, and J. W. Hutchinson, Mech. Mater. **18**, p. 213 (1994).
- ⁵ D. C. Larsen, private communication.
- ⁶ D. S. Beryerle, S. M. Spearing, F. W. Zok, and A. G. Evans, J. Am. Ceram. Soc. **75**, p. 2719 (1992).

- ⁷ Y.- M. Liu, Y. He, F. Chu, T. E. Mitchell and H. N. G. Wadley, J. Am. Ceram. Soc. **80**, p. 142 (1997).
- ⁸ J. J. Brennan, in Fiber Reinforced Ceramic Composites, edited by K. S. Mazdiasni, Noyes Publications, Park Ridge, New Jersey, p. 222-59 (1990).
- ⁹ A. G. Evans and D. B. Marshall, Acta. Metall. **37**, p. 2567 (1989).
- ¹⁰ Y. M. Liu, T. E. Mitchell, H. N. G. Wadley, to be submitted to Acta. Mater.
- ¹¹ R. J. Dewhurst, A. G. Nurse, and S. B. Palmer, Ultrasonics, **26**, p.307 (1988).
- ¹² R. Y. Kim, and N. J. Pagano, J. Am. Ceram. Soc.**74**, p. 1082 (1991).
- ¹³ W. A. Cutler, private communication.
- ¹⁴ Y.M. Liu, T. E. Mitchell, and H. N. G. Wadley, unpublished work.
- ¹⁵ Y. M. Liu, K. Sickafus, P. Katula, T. E. Mitchell, and H. N. G. Wadley, unpublished work.

Effects of Off-Axis Loading on the Tensile Behavior of a Ceramic-Matrix Composite

Christopher S. Lynch*

G. W. Woodruff School of Mechanical Engineering, Georgia Institute of Technology, Atlanta, Georgia 30332-0405

Anthony G. Evans*

Division of Applied Sciences, Harvard University, Cambridge, Massachusetts 02138

A 0°/90° ceramic-matrix composite (CMC) comprised of Nicalon fibers in magnesium aluminosilicate (MAS) has been loaded in tension in three orientations relative to the fiber direction: 0°, 30°, and 45°. The off-axis loaded samples exhibit inelastic deformation at appreciably lower stresses than samples loaded at 0°. Matrix cracking governs the inelastic strains in all orientations. But, important differences in the morphologies and sequencing of the cracks account for the differences in the stress levels. Off-axis failure also occurs at substantially lower stresses than on-axis failure. On-axis composite failure is governed by fiber fracture, but off-axis failure involves matrix-crack coalescence. To facilitate interpretation and modeling of these behaviors, the interface friction and debond stresses have been determined from hysteresis measurements.

I. Introduction

THE design of ceramic-matrix composite (CMC) components capable of reliable operation is facilitated by devising inelastic constitutive laws that can be implemented in finite-element (FEM) schemes.¹⁻³ For this development, a thorough understanding of the stress/strain behavior in tension, compression, and shear is required.^{4,5} The design requirements are exemplified (Fig. 1) by the performance of a mechanical attachment between a CMC component and its support structure (typically titanium or nickel alloys).⁵ The loading through the attachment produces multiaxial states of strain, with an associated strain concentration.^{2,5} The inelastic deformation that occurs in response to these strains redistributes the stresses and reduces the stress concentration.^{1,2,5} A capability for calculating this stress concentration is an essential aspect of the design process. A phenomenological deformation law has been devised and implemented in the FEM code ABAQUS.¹⁻³ To complement this and to support further developments, experimental results are required on a range of CMCs, as well as diagnosis of the mechanisms and their relation to constituent properties. The intent of this study is to provide experimental information on the deformation and failure characteristics of a silicon carbide/magnesium aluminosilicate (SiC/MAS) composite.

The tensile behavior of CMCs on loading in the direction of the fibers has been relatively well established.⁶⁻¹³ This has led to a methodology for characterizing the inelastic strains in terms of the properties of the constituents and their interactions.^{4,6,14} These concepts have not yet been successfully extended to off-axis or shear-loaded CMCs. The experiments performed in this study emphasize these off-axis characteristics

and provide insight into the associated nonlinear behavior as well as the failure mechanisms.

II. Experimental Methods

(1) Basic Approach

CMC samples are subjected to on-axis and off-axis tensile loading. The stress/strain behavior is measured with strain gauges and a load cell. Acetate replicas give the matrix microcrack density at various loads. Birefringent film illustrates the development of damage prior to failure, especially in the off-axis loading samples. Optical examinations during the tests and after failure give information about the failure mechanisms. Grinding of the composite into a bilayer and then measuring the resulting curvature provides a measure of the interply residual stress.^{13,15,16}

(2) Material Description

The composite is a SiC/MAS material (Corning Glass Works, Corning, NY) that is comprised of Nicalon™ (Nippon Carbon, Tokyo, Japan) (SiC) fibers 15 μm in diameter in a borosilicate-doped cordierite matrix. The fibers are in a [0°/90°]_{3s} crossply arrangement with a ply thickness of 200 μm. The total thickness of the CMC is 2.5 mm. The constituent properties (fibers and matrix) are listed in Table I. The fibers are in residual tension, and the matrix is in residual compression, induced primarily by differential thermal expansion on cooling from the processing temperature.

(3) Tensile Testing

Tensile samples were cut from a billet in three orientations, with a width of 6.35 mm (Fig. 2). The cuts resulted in specimens with three stacking sequences: [0°/90°]_{3s}, [±45°]_{3s}, and [+30°/-60°]_{3s}. Fiberglass/epoxy tabs were laminated on each end of the sample to provide a compliant layer for the test-frame grips. A gauge section of 50 mm remained between the grips. Multiple strain gauges attached to the center of each sample in the orientations depicted in Fig. 3 gave information about the elastic and inelastic deformation. The tensile-loaded [0°/90°]_{3s} samples (Fig. 3(A)) had strain gauges oriented to measure strain at three orientations to the applied load: 0°, 45°, and 90°. The tensile-loaded [±45°]_{3s} samples (Fig. 3(B)) had gauges oriented to measure strain in four orientations relative to the applied load: 0°, 45° (parallel and perpendicular), and 90°. The tensile-loaded [+30°/-60°]_{3s} samples (Fig. 3(C)) had gauges oriented to measure strain in four orientations relative to the applied load: 0°, 30°, 60°, and 90°.

Tensile tests were performed with unload/reload cycles used to establish the hysteresis. The loading was imposed by using a servohydraulic test frame, at a displacement rate of 50 μm/min.

(4) Microscopy and Acetate Replication

Acetate replicas provided *in-situ* measurement of matrix-crack densities.^{3,12} The displacement was fixed prior to an

F. W. Zok—contributing editor

Manuscript No. 192153. Received December 4, 1995; approved May 23, 1996.

*Member, American Ceramic Society.

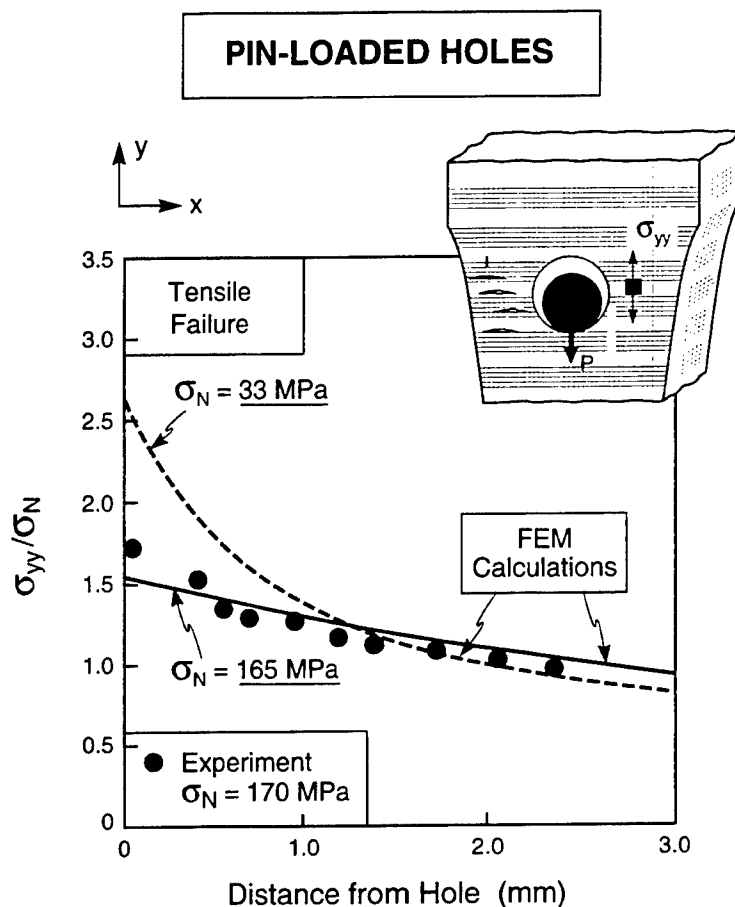


Fig. 1. Pin-loaded sub-element indicating the role of inelastic strain in stress redistribution. Plot shows σ_{yy} stresses, normalized by the net section stress, calculated as a function of the distance from the hole.² Calculations shown are for two values of σ_N (33 and 165 MPa). Note that the peak stress at the hole decreases appreciably as σ_N (i.e., the load) increases, because additional inelastic strain is activated. Also shown are experimental measurements obtained by Moiré interferometry,⁵ at $\sigma_N = 170$ MPa. Correspondence with the calculated stresses at a similar load ($\sigma_N = 165$ MPa) provides credence in the constitutive law.

Table I. Properties of Constituent Materials

Property	Symbol	Value
Fiber modulus (GPa)	E_f	200
Fiber Poisson's ratio*	ν_f	0.19
Matrix modulus (GPa)	E_m	115
Matrix Poisson's ratio	ν_m	0.25
Fiber volume fraction	f	0.37
Fiber thermal expansion ($\times 10^6 \text{ K}^{-1}$)	α_f	4.9
Matrix thermal expansion ($\times 10^6 \text{ K}^{-1}$)	α_m	2.4
Cooling range (K)	ΔT	1000

*Poisson's ratio of SiC.²⁵

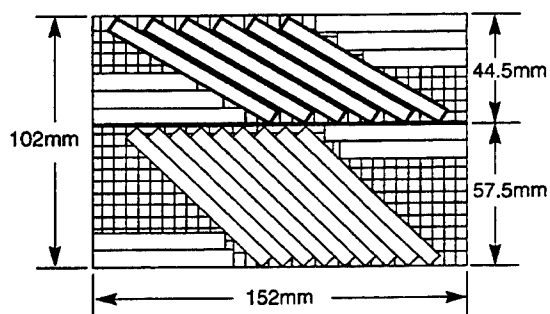


Fig. 2. Layout of samples cut from the as-received billet. Underlying grid represents the fiber directions. Samples are cut at 0°, 30°, and 45° to the fibers.

unload/reload cycle. A small drop of acetone was placed onto acetate in contact with the surface. The acetone dissolved the acetate into the microcracks and then evaporated, allowing the acetate to resolidify. The acetate was peeled off and adhered to a microscope slide with adhesive tape. The acetate replicas were viewed using optical microscopy.

After completion of the loading tests, the samples were sectioned and polished, lightly etched in hydrofluoric acid (HF),

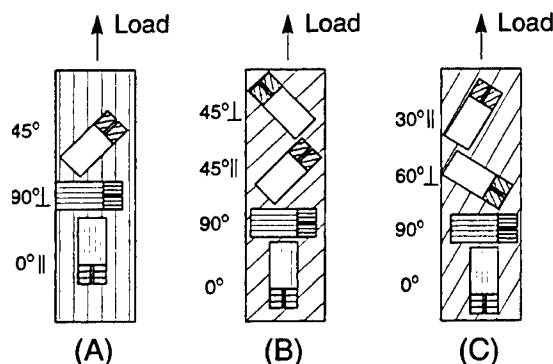


Fig. 3. Orientation of strain gauges on the samples. Lines on the samples represent the direction of the fibers in the top ply. Figures depict the strain-gauge orientation for (A) on-axis loading ($[0^\circ/90^\circ]_{3s}$), (B) 45° off-axis loading ($[+45^\circ]_{3s}$), and (C) 30° off-axis loading ($[+30^\circ/-60^\circ]_{3s}$).

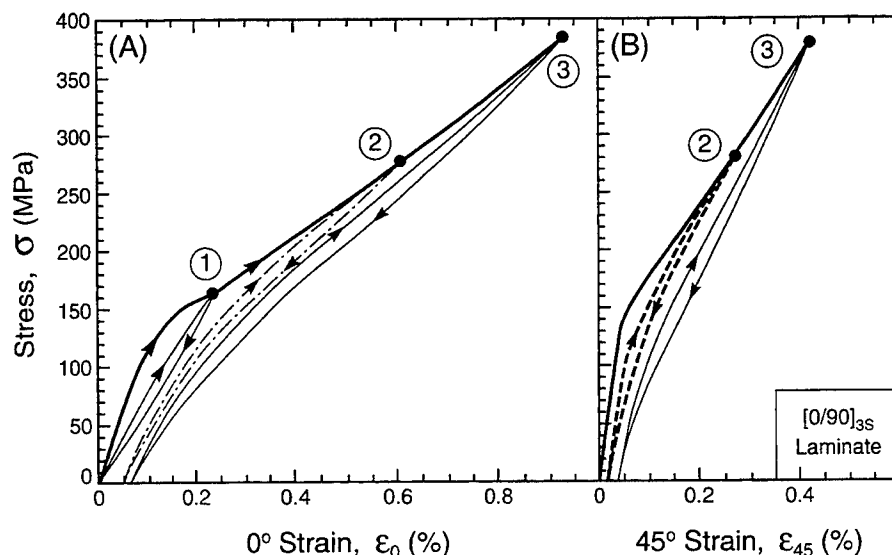


Fig. 4. Stress/strain curves for on-axis $[0^\circ/90^\circ]_{3s}$ loading ((A) 0° strain (in the direction of applied stress) and (B) 45° strain).

and then viewed using optical microscopy. The saturation crack density was determined in this manner. Some tests were observed *in situ* using optical microscopy; the development of matrix cracks also was monitored using optical microscopy. Scanning electron microscopy (SEM) was used to examine the samples after failure.

(5) Bilayer Residual Stress

Residual stress was measured from the curvature of a bilayer.^{13,15,16} A sample with the fibers in the length direction was cut into a long narrow strip. The strip was ground on a surface grinder until the ply interface was reached. The sample was then turned and ground until a bilayer 400 μm thick remained. The bilayer spontaneously deformed to a uniform curvature on removal from the holding fixture. This curvature provided a direct measure of the interply residual stress (Appendix A). Measurements for this CMC gave a radius of curvature, ρ , of 0.54 m.

III. Stress/Strain Diagrams

(1) $[0^\circ/90^\circ]_{3s}$ Tensile Loading

The stress/strain diagrams (Figs. 4–9) correspond to the strain-gauge orientations shown in Fig. 3. The stress/ 0° -strain diagram (Fig. 4(A)) is linear at stress levels up to ~ 125 MPa, with modulus, E , of 130 GPa; thereafter, inelastic strain develops. The ultimate tensile strength, S_u , is ~ 400 MPa. The saturation modulus just before failure, E_s , is 75 GPa. The stress/ 45° -strain diagram (Fig. 4(B)) is similar to that at 0° strain, although the strains are smaller. A typical unload/reload cycle (Fig. 5) indicates that the unload strain is initially parabolic and then becomes linear. At ~ 50 MPa, the strains are again parabolic, but with *opposite* curvature. Initial reloading has essentially the same slope as the virgin composite. The subsequent portions are parabolic and then linear.

The stress/ 90° -strain diagram, plotted on an expanded scale (Fig. 6), indicates the initial contraction expected from the Poisson effect.¹¹ But, at 45–50 MPa, a negative deviation from linearity exists, and at ~ 130 MPa, an abrupt positive strain is present. This behavior is similar to that found in silicon carbide/calcium aluminosilicate (SiC/CAS).¹¹ Removal of the load leaves a positive, remnant strain (attaining 0.02% at the highest loads). Hysteresis is not present in this orientation; only the first cycle is shown, because subsequent cycles overlap the first. Comparison of the initial portions of the stress/strain diagrams

for the three orientations (Fig. 7) reveals that a positive nonlinear strain increment is present on all three strain gauges, indicative of dilatation during matrix cracking.

(2) $[\pm 45^\circ]_{3s}$ Tensile Loading

In the $[\pm 45^\circ]_{3s}$ symmetric orientation, the onset of nonlinear behavior occurs at lower stresses than for $[0^\circ/90^\circ]_{3s}$ loading. Moreover, the failure stresses are substantially lower (Fig. 8). The stress/ 0° -strain diagram (Fig. 8(A)) is linear to ~ 115 MPa, with a modulus, E_{45} , of 110 GPa. But thereafter, the tangent modulus decreases dramatically. The material fails at 0.57% strain and 140 MPa. The unload/reload cycle is similar in shape to that for $[0^\circ/90^\circ]_{3s}$ loading, but the hysteresis loops are substantially wider. In contrast to $[0^\circ/90^\circ]_{3s}$ loading, the 90° strain is negative throughout (Fig. 8(D)) and hysteretic (again similar to SiC/CAS¹¹).

The stress/ 45° -strain diagrams (Figs. 8(B) and (C)) are similar to each other and to that at 0° strain, although the strains are smaller. Hysteresis is present, and the stress/strain envelope exhibits a small slope increase near failure. A small residual strain perpendicular to the fibers exists, and the elastic modulus is slightly smaller than that measured parallel to the fibers.

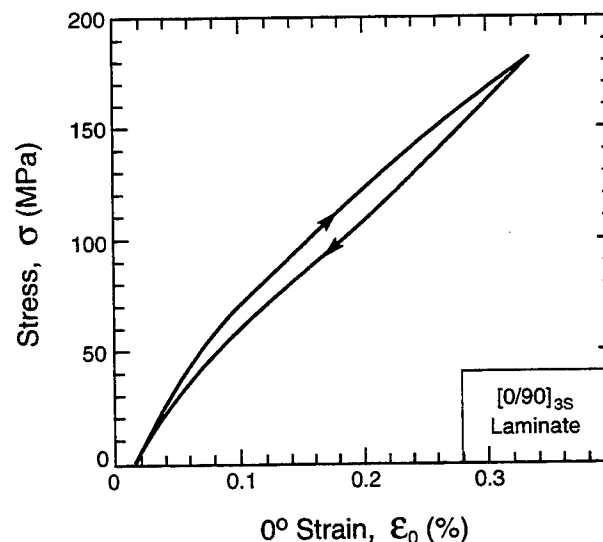


Fig. 5. Unload/reload cycle for on-axis $[0^\circ/90^\circ]_{3s}$ loading.

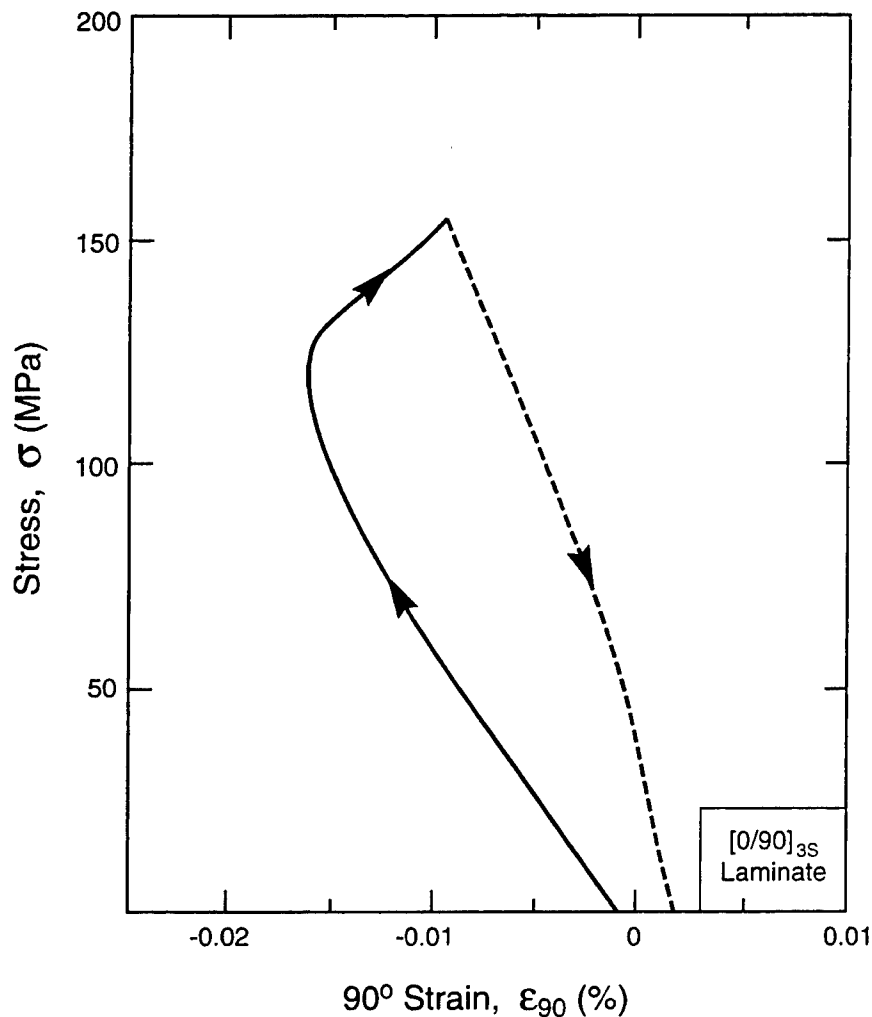


Fig. 6. Stress/90° strain (perpendicular to the applied stress) for on-axis $[0^\circ/90^\circ]_{3s}$ loading.

(3) $[+30^\circ/-60^\circ]_{3s}$ Tensile Loading

The $[+30^\circ/-60^\circ]_{3s}$ tensile loading is not a balanced laminate. Yet, the occurrence of nonlinearity and failure are similar to the balanced samples. The stress/0°-strain diagram (Fig. 9(A)) is linear to stress levels of ~ 105 MPa with a modulus, E_{30° , of

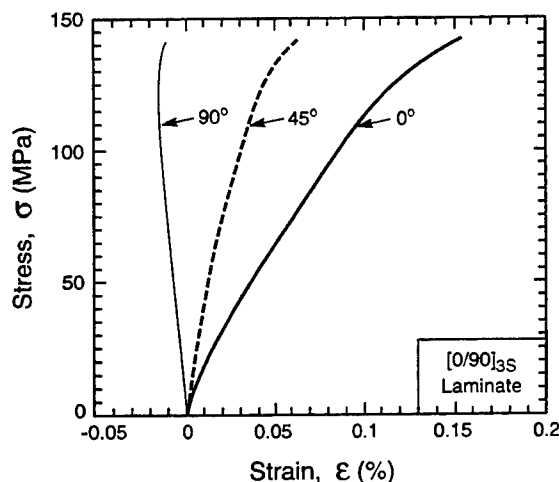


Fig. 7. Comparison of the initial loading curves for the three gauge orientations under on-axis $[0^\circ/90^\circ]_{3s}$ loading.

~ 120 GPa. Above this stress, a reduction in tangent modulus exists. The stress at failure, 130 MPa, is even lower than that measured in $[\pm 45^\circ]_{3s}$ loading. The unload/reload cycle is hysteretic and has parabolic and linear portions. The 30° strain in the direction of the fibers (Fig. 9(C)) is zero during elastic loading and becomes positive with the onset of nonlinearity; the nonlinear strain also is the smallest in this orientation. The 60° strain (Fig. 9(B)) is positive and smaller than that at 0° strain. The 90° strain (Fig. 9(D)) is similar to that at 30° strain, but of opposite sign.

In summary, the strains vary with orientation. This variance is in accordance with the following sequence: 0° large positive strain, 60° intermediate positive strain, 90° small negative strain.

IV. Damage Mechanisms

Each sample was sectioned through the center to create a side view and polished down several layers to reveal a front view in the absence of surface effects. Optical micrographs of these sectioned, polished, and etched samples (Fig. 10) display the fully developed microcrack system. The dominant matrix cracks were perpendicular to the tensile stress in the $[0^\circ/90^\circ]_{3s}$ and $[\pm 45^\circ]_{3s}$ loading configurations (Figs. 10(A) and (B)), as in SiC/CAS,⁴ and slightly tilted in the $[+30^\circ/-60^\circ]_{3s}$ configuration (Fig. 10(C)).

Under $[\pm 45^\circ]_{3s}$ tensile loading, other cracks became apparent just before failure. These cracks extended *along the fibers*. They were apparent on the front of the sample and extended into the ply at the edge (Fig. 10(B)). A similar cracking mode (parallel to

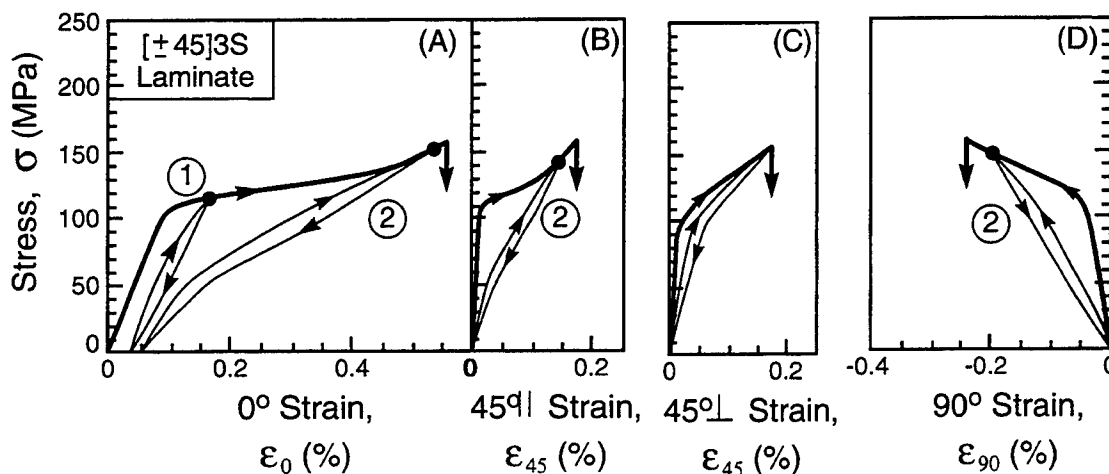


Fig. 8. Stress/strain curves for 45° off-axis $[\pm 45]_3$ loading ((A) 0° strain in the direction of applied stress, (B) 45° strain in the direction of the fibers in the surface ply, (C) 45° strain perpendicular to the direction of the fibers in the surface ply, and (D) 90° strain perpendicular to the applied stress).

the fibers) was evident on the $[+30^\circ/-60^\circ]_3$ specimens. In this case, the cracks were apparent substantially before failure and exhibited stable propagation on increasing the load. After failure, such cracks were visible along the fibers at the surface plies.

The implication of these observations is that, in addition to the matrix cracks that form normal to the applied tensile load, matrix *debonds* are present, which develop parallel to the fibers as deformation continues beyond the "matrix-cracking" strain (Fig. 11). The precise strain levels at which they originate have yet to be ascertained, because the small opening displacements impede imaging. The situation is comparable to the interface debonds that form on 0° loading¹⁷ and to matrix shear cracks in SiC/carbon composites,¹⁸ which can only be imaged using high-resolution methods.

V. Analysis and Interpretation

(1) Calibrations

The stress/strain behavior can be analyzed, in principle, by using the formulas summarized in the Appendices. In practice, preliminary calibration of the unknown constituent properties is needed. Two such unknowns exist:

(1) The composite response is sensitive to the initial state of the interfaces—bonded or unbonded—because the thermal expansion of the matrix is less than that for the fibers (Table I).

The bonding state is reflected in the magnitude of the transverse Young's modulus, E_T .¹⁹ The formulas must be iterated with the experimental data to establish E_T . When the relevant E_T has been established, it can be used explicitly in all the subsequent analyses and interpretations.

(2) Independent information about the cooling range, ΔT , is not available. Initially, it is assumed to be the difference between the ambient and consolidation temperatures, $\sim 1000^\circ\text{C}$ for this composite.¹¹ Then, the calculations of the residual stresses are iterated with the measurements until a reasonable and consistent interpretation is achieved. The same ΔT value is used for all subsequent calculations.

(2) Initial Properties

The elastic moduli and the residual stresses calculated from the formulas, on using the data from Table I, are presented in Table II. The composite modulus calculated for an attached interface¹⁹ ($E = 140$ GPa) appreciably exceeds the measured value ($E = 130$ GPa). This infers that the residual tensile stress at the fiber/matrix interface (Table II) partially debonds the fibers. This is affirmed by the calculated modulus for a fully separated interface¹⁹ ($E = 105$ GPa), which underestimates the measured value. Thus, E_T is inferred from the measured composite modulus to be 100 GPa; this value is used for all further analyses.

The mismatch in the thermal expansion coefficients (Table I) indicates that the interply residual stresses, σ_x , are tensile in the

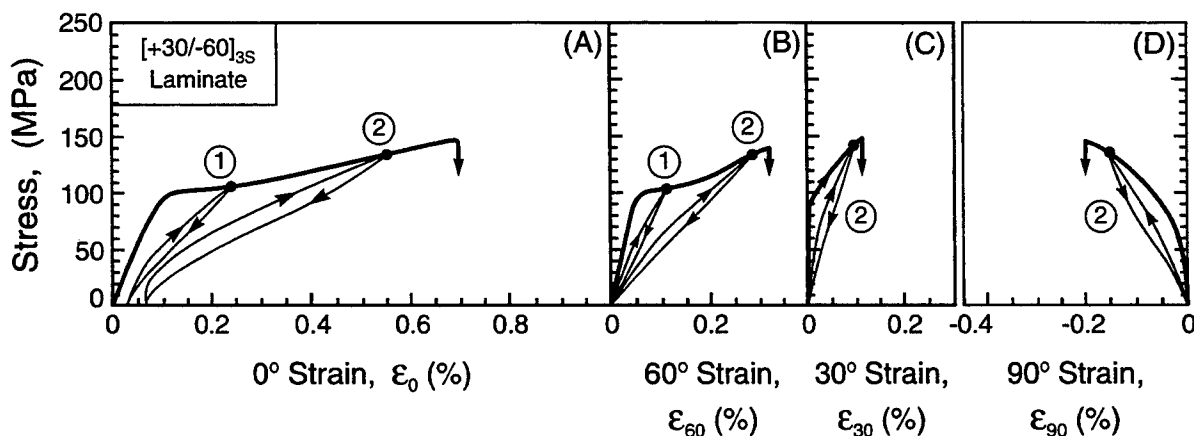


Fig. 9. Stress/strain curves for 60° off-axis $[+30^\circ/-60^\circ]_3$ loading ((A) 0° strain in the direction of applied stress, (B) 60° strain perpendicular to the direction of fibers of the surface ply, (C) 30° strain in the direction of the fibers of the surface ply, and (D) 90° strain perpendicular to the applied stress).

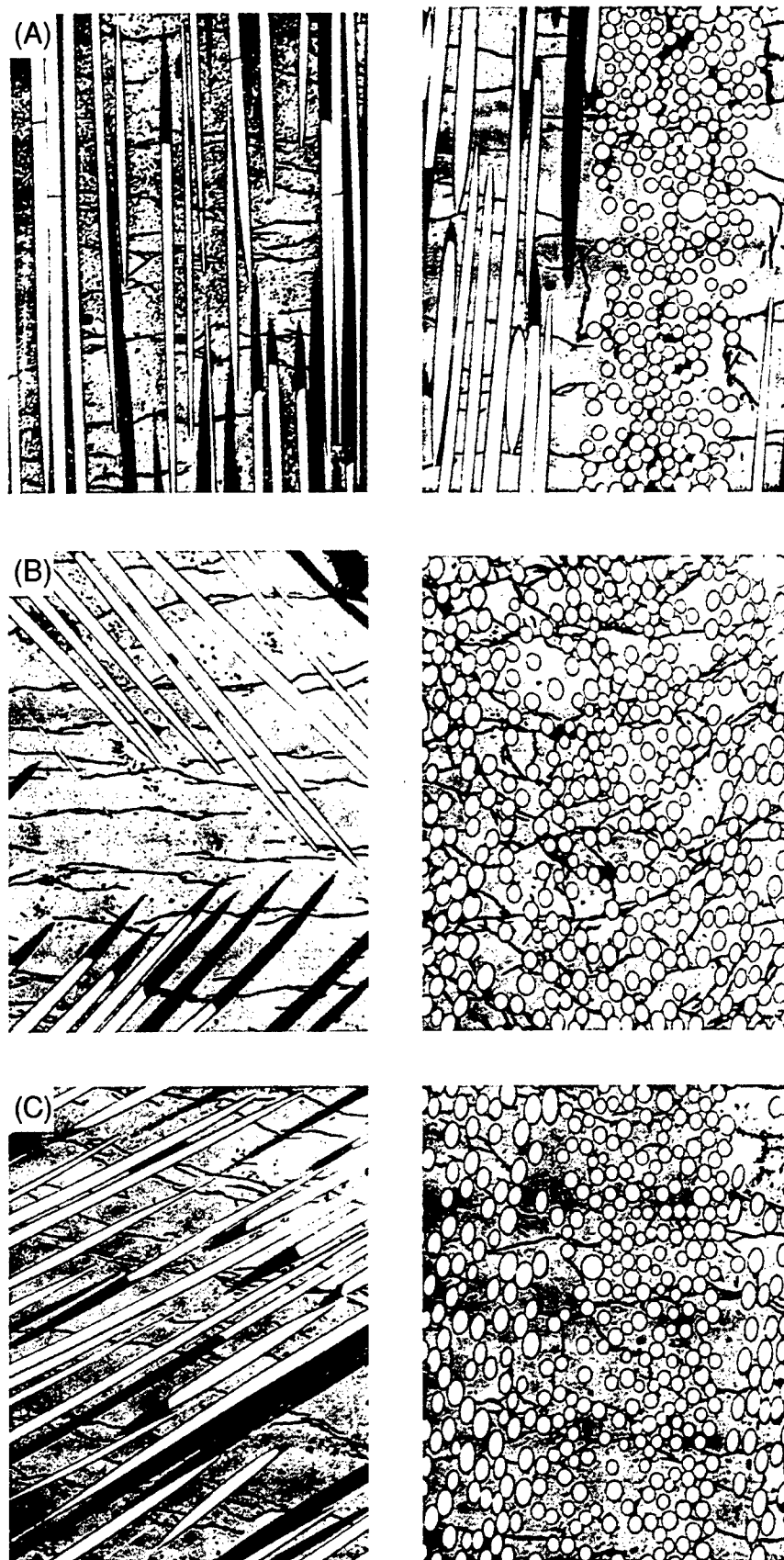


Fig. 10. Optical micrographs of matrix cracks and debonds; width of field is 400 μm . Samples are polished to show a front view (micrographs on left-hand side) and sectioned to show a side view (micrographs on right-hand side). (A) On-axis loading produces microcracks perpendicular to the fibers in the longitudinal plies. (B) 45° off-axis loading produces microcracks perpendicular to the applied load; the side view displays the complexity of the microcrack systems. (C) 30° off-axis loading produces a microcrack system that is tilted relative to the applied load; this corresponds to the loss of symmetry of the load relative to the fibers.

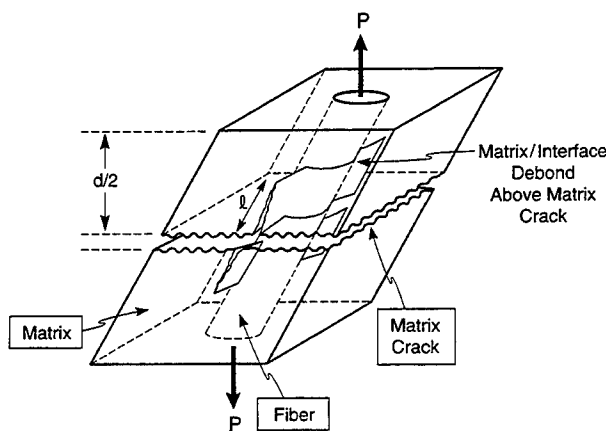


Fig. 11. Matrix cracks develop perpendicular to the applied stress. As the stress is increased, the fibers debond and pull out. At higher stress, cracks develop along the fibers, leading to ultimate failure with delamination between the plies.

fiber direction and compressive in the transverse direction. The σ_R value calculated from the thermal expansion mismatch²⁰ by using the above value of E_T with Eq. (A-7) and on requiring $\Delta T = 1000^\circ\text{C}$ is 38 MPa. The measured σ_R value obtained from Eq. (A-9) by using the bilayer curvature (and the inferred E_T) is 35 MPa. This consistency provides credence in ΔT , as well as affirming the magnitudes of each of the initial properties needed to calculate σ_R .

(3) Inelastic Strains

(A) $[0^\circ/90^\circ]_2$ Tensile Loading: The first appearance of non-linearity, evident in the 90° stress/strain curve (Fig. 6) at ~ 50 MPa, coincides with the load at which the net stress in the transverse plies (residual compression plus applied tension) becomes tensile. However, appreciable inelastic strain does not initiate until matrix cracks penetrate the longitudinal plies, at 125–140 MPa. At this stage, debonding occurs along the fiber/matrix interfaces, accompanied by friction.^{8,9,14} The positive 90° strain that originates at this load (Fig. 4) suggests that debonding relieves the residual radial tensile stress at the interface, causing the matrix to expand. Additional expansion may then occur because of displacements caused by asperities on the slipping surfaces. The hysteresis (Fig. 5) is the result of sliding at the fiber/matrix interface, in accordance with the following sequence:^{6,14}

(1) On initial unloading, reverse slip commences, accompanied by nonlinear strains; when this slip reaches the debond, the unloading curve becomes linear, and a state of steady-state sliding prevails.

(2) At ~ 70 MPa, the residual compression in the matrix begins to close the cracks; further slip is suppressed, and a diminished compliance ensues.

(3) During reloading, the matrix cracks are still initially closed, and the compliance is similar to that of the virgin composite; as the reload stress increases, the cracks open and the behavior then mirrors that on unloading—comprising nonlinear slip-zone evolution, followed by steady-state slip.

These features may be used to evaluate the debond and friction parameters that characterize the inelastic strains. The procedure involves determination of the tangent compliances from the hysteresis strains.^{4,14} These compliances have three principal characteristics (Fig. 12):

(1) The plateau compliance, I_p , equal to $1/E_p$; this compliance depends on the fiber/matrix interface friction, τ , the crack spacing, d , and the fiber pullout length below the crack saturation stress, σ_s . At stresses exceeding σ_s , these parameters are constant and are equal to $0.5fE_f$ in the crossply arrangement.

(2) The transition stress, σ_{tr} , at the onset of steady-state slip; this stress relates to the debond stress, σ_i , needed to propagate the crack at the fiber/matrix interface.

(3) The slope, L , of the variable-slip region; this is related to the debond stress and the debond length.

These characteristics are better defined on reloading than on unloading (Fig. 13), as in other CMCs^{1,14,21} (although the characteristic behavior is partially obscured in this CMC by the early onset of matrix-crack closure). The subsequent interpretation uses these compliance parameters. The results are augmented by estimations of the debond length, l , using an approach developed in Appendix B. The parameters obtained by these procedures are summarized in Table III.

The progression of the plateau compliance, I_p , with stress (Fig. 13) suggests that matrix cracks continue to evolve in the 0° -strain plies at stresses up to ~ 340 MPa, with crack saturation prevailing at higher stresses. This is affirmed by the trends in the debond fraction, $2l/d$ (Fig. 14). It also is consistent with the tangent modulus above this stress having the saturation magnitude.

The product of the friction stress, τ , and the crack spacing, d (τd), has been independently obtained from three measurements:^{4,6,21–24} (i) the slope of the reload compliance with stress, (ii) the plateau compliance, and (iii) the width of the hysteresis loop. Such measurements reveal that τd approaches ~ 350 N/m as the matrix cracks saturate. With the saturation crack spacing, d_s , being ~ 70 μm (Table III), the value of τ becomes ~ 5 MPa. Such a small value of τ is consistent with the state of residual tension normal to the interfaces, which causes asperity contact to be the only source of frictional resistance.²³

The transition stresses, σ_{tr} (Fig. 12) obtained from the compliances indicate that the debond stress, σ_i , changes, ranging from ~ 170 to ~ 260 MPa, as the load increases. This is similar to the behavior found for SiC/SiC²⁴ and SiC/Al₂O₃.²¹

Table II. Calculated Properties

Property	Symbol	Value
Longitudinal modulus (GPa)	E_L	147
Poisson's ratio	ν_{LT}	0.21
Transverse modulus (GPa)		
Separated interface	E_T	60
Bonded interface	E_T	135
Composite modulus (GPa)		
Separated interface	E	105
Bonded interface	E	125
Longitudinal thermal expansion coefficient (K^{-1})	α_L	3.6
Transverse thermal expansion coefficient (K^{-1})		
Separated interface	α_T	3.0
Bonded interface	α_T	2.4
Interface residual stress (MPa)	σ_i^R	138
Ply-level residual stress (MPa)	σ_R	35

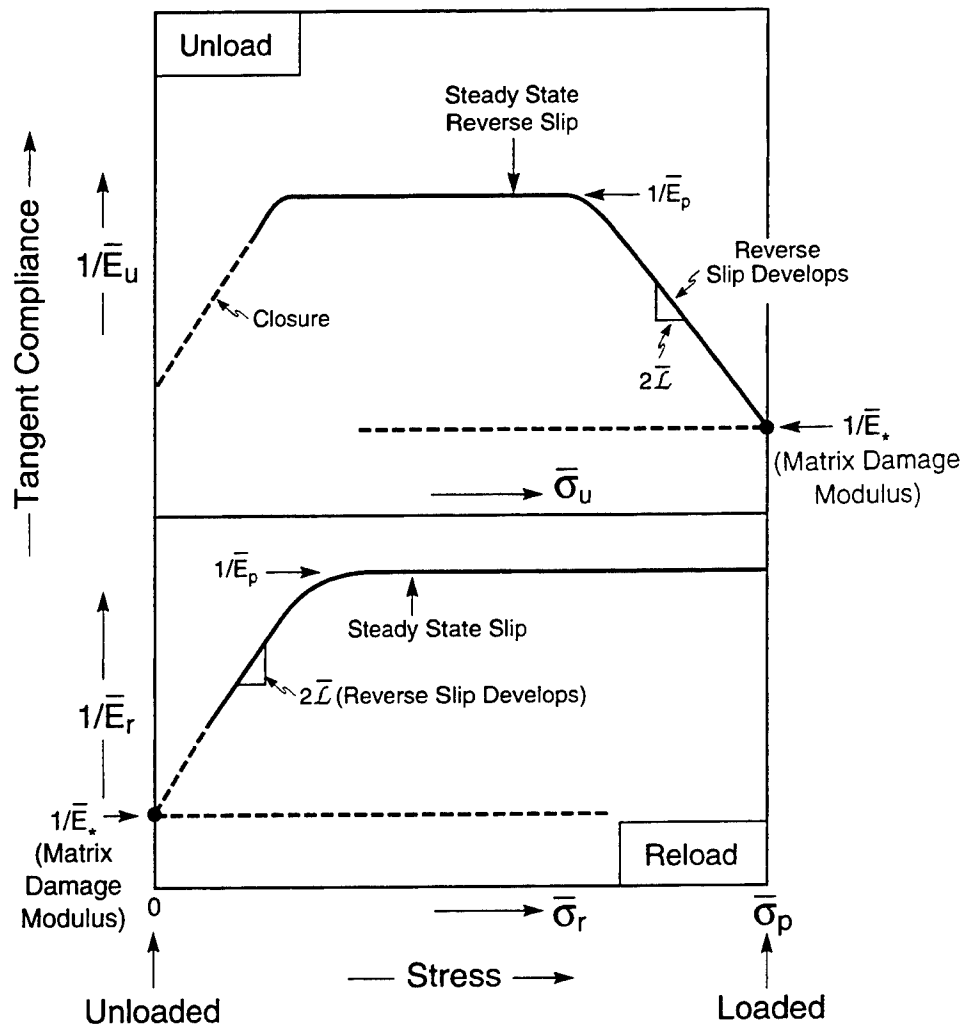


Fig. 12. Schematic of the expected trends in the unload and reload tangent compliances in the absence of matrix-crack closure.¹⁴

(B) $[\pm 45^\circ]_{3s}$ and $[+30^\circ/-60^\circ]_{3s}$ Tensile Loading: The present results affirm major differences between $[0^\circ/90^\circ]_{3s}$ loading and $[\pm 45^\circ]_{3s}$ and $[+30^\circ/-60^\circ]_{3s}$ loadings in CMCs:^{4,11} (i) the stresses needed to develop appreciable inelastic strains are smaller for $[\pm 45^\circ]_{3s}$ and $[+30^\circ/-60^\circ]_{3s}$ loadings than for $[0^\circ/90^\circ]_{3s}$ loading; (ii) minimal strain hardening exists in these off-axis orientations, but appreciable hardening is present for $[0^\circ/90^\circ]_{3s}$ on-axis orientations; and (iii) the transverse strains for $[\pm 45^\circ]_{3s}$ and $[+30^\circ/-60^\circ]_{3s}$ loadings are *negative* (Poisson's ratio, ν , of ~ 0.4), but they are essentially zero for $[0^\circ/90^\circ]_{3s}$ loading strains.

These characteristics cannot be explained by the $[0^\circ/90^\circ]_{3s}$ cell models,⁹ in which debonding and slip are confined to the fiber/matrix interfaces. These models predict that debonding and slip become increasingly difficult as the loading axis deviates from 0° . Such characteristics are *opposite* to those found experimentally. This paradox might be resolved by a model that allows matrix debonds to evolve *parallel* to the fibers, as proposed in Fig. 11. These debonds facilitate frictional slip and allow appreciable inelastic strains to occur. They also enhance the matrix-crack opening and thereby diminish the stress needed for steady-state propagation. A model based on these notions is presented in a separate article.²²

The large reduction in the saturation modulus, E_s (relative to that for $[0^\circ/90^\circ]_{3s}$ loading), might be rationalized through an analysis presented in Appendix C. Beyond saturation, all of the load is supported by the fibers, in accordance with the simple spring configuration depicted in Fig. 15. The role of the matrix

is to resist the rotation of the fibers toward the loading axis. This is achieved by exerting compressive forces normal to the load. This model predicts Eq. (C-9):

$$E_s = 0.5fE_f(\cos^4 \phi + \sin^4 \phi)$$

The predicted values are $E_s = 18.5$ GPa, at 45° , and 23 GPa, at 30° , compared to the measured values of 18.8 and 18.5 GPa, respectively.

VI. Conclusion

On-axis and off-axis tensile loadings of a SiC (Nicalon)/MAS CMC have been used to elucidate inelastic deformation and failure mechanisms, especially on off-axis loading. Implementation of an on-axis cell model has allowed determination of interface debond and friction parameters. These parameters govern the inelastic strain and the unload/reload hysteresis.

The corresponding off-axis phenomena are qualitatively similar but occur at appreciably lower stresses. These effects are not explicable by the on-axis cell models. The present experiments, augmented by some simple models, suggest directions for further modeling that may lead to a rational characterization of the inelastic off-axis behavior.

APPENDIX A

Thermoelastic Properties

The elastic moduli of a ply in longitudinal tension, E_L , and transverse tension, E_T , are well-established quantities.^{19,20} They are related to the constituent moduli by^{19,20}

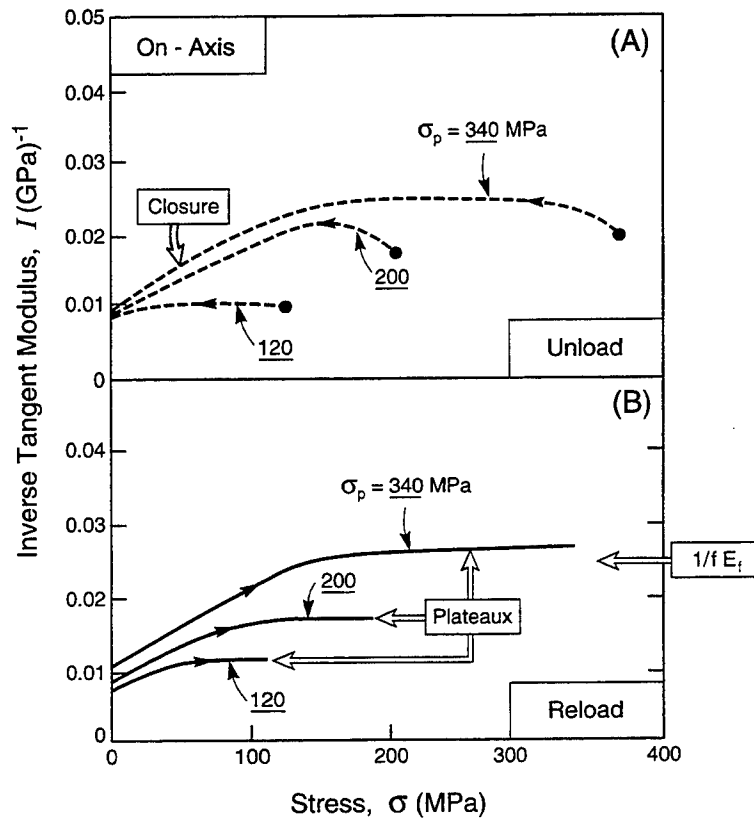


Fig. 13. (A) Inverse tangent modulus against unload stress for the on-axis cycles. Initial unload from high stress is linear as reverse slip develops. Slope is related to the interface friction stress; the plateau is the region of steady-state slip. As the stress is reduced, the matrix cracks close and the curve is again linear. (B) Inverse tangent modulus against reload stress for the on-axis cycles. Initial reload has a modulus similar to that of the virgin composite; the plateau designates steady-state slip. When the stress is sufficiently high to propagate the debond interface, the curve increases dramatically.

Table III. Constituent "Damage" Parameters

Property	Symbol	Value
Debond fraction*	$\frac{2l}{d}$	
Saturation crack spacing (μm)	d_s	70
Fiber sliding stress (MPa)	τ	5

*Evolves with load, Fig. 14.

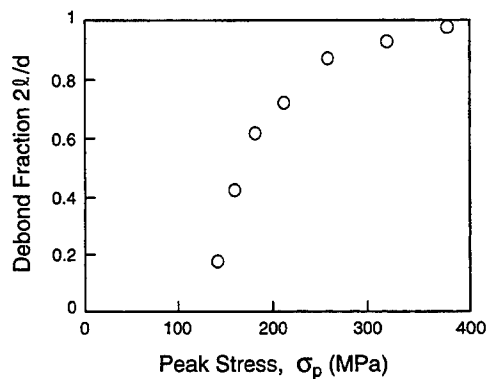


Fig. 14. Fiber debond fraction as a function of the peak stress. Debond fraction is calculated from the inverse tangent modulus during steady-state slip. At the matrix-cracking stress (130 MPa), debonds develop rapidly. As the stress increases, the debond fraction approaches unity. Curve shape dictates the inelastic strain evolution.

$$E_L = f_b E_f + (1 - f_b) E_m \quad (\text{A-1})$$

$$E_T = \frac{(1 + 2\eta f_b) E_m}{(1 - \eta f_b)} \quad (\text{A-2})$$

The fibers and matrix are referenced as f and m , respectively, with f_b being the fiber volume fraction in the ply. For an attached interface,

$$\eta = \frac{(E_f/E_m) - 1}{(E_f/E_m) + 2} \quad (\text{A-3})$$

For a separated interface, $\eta = 0$. These moduli are related to that of a 0°/90° crossply material by¹⁹

$$\bar{E} = \frac{E_T + E_L}{2[(E_L/E_T) - \nu_{LT}^2]} \quad (\text{A-4})$$

The thermal expansion coefficient difference between the fibers and matrix typically causes residual stress at the ply level. These stresses are governed by the thermal expansion anisotropy of each ply: α_L in the longitudinal direction and α_T in the transverse direction. These thermal expansions are, in turn, related to those of the fiber, α_f , and matrix, α_m , by²⁰

$$\alpha_L = \alpha_m - \frac{f_b E_f (\alpha_m - \alpha_f)}{E_L} \quad (\text{A-5})$$

and

$$\alpha_T = (1 - f_b) \alpha_m + f_b \alpha_f + (\alpha_m - \alpha_f) H f_b \quad (\text{A-6a})$$

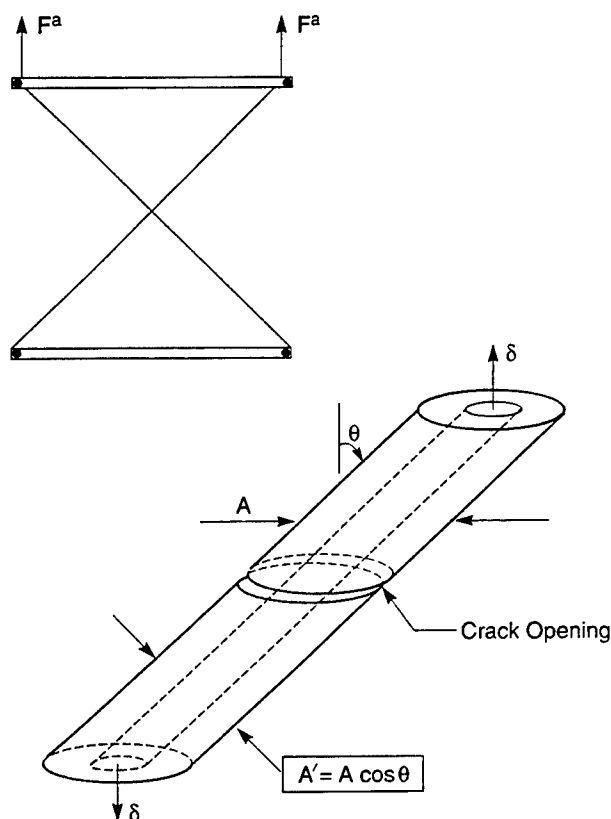


Fig. 15. Spring configuration used to model the off-axis compliance beyond matrix-crack saturation.

where

$$H = \frac{(1 - f_b)(E_m - E_f)[(2 - 3\nu)E_L - \nu E_f]}{E_L[E_f + (1 - 2\nu)E_L]} \quad (\text{A-6b})$$

with ν being the Poisson's ratio of the fiber and matrix (assumed to be the same).

The thermal expansion anisotropy ($\alpha_T - \alpha_L$) governs the axial residual stress in the 90° plies, σ_R , in accordance with²⁰

$$\begin{aligned} \alpha_R &= \frac{(\alpha_T - \alpha_L)\Delta TE_L E_T}{2\bar{E}} \\ &= \frac{f_b(\alpha_m - \alpha_f)[(E_f/E_L) - 1 + H]\Delta TE_L E_T}{2\bar{E}} \end{aligned} \quad (\text{A-7})$$

where ΔT is the temperature change from processing to ambient conditions. The stress in the 0° -strain plies has the same magnitude but opposite sign when the plies have equal thickness.

The residual stress is experimentally determined from the radius of curvature, ρ , of a bilayer. For a bilayer with equal ply thickness, h , in each layer, the neutral axis shifts into the stiffer material by an amount a .¹⁶

$$\frac{a}{h} = \frac{1 - (E_f/E_L)}{2[1 + (E_f/E_L)]} \quad (\text{A-8})$$

The residual stress is then

$$\sigma_R = \frac{E_T h}{3l} \left[1 + \frac{3a}{h} + 3\left(\frac{a}{h}\right)^2 \right] + \frac{E_L h}{3l} \left[1 - \frac{3a}{h} + 3\left(\frac{a}{h}\right)^2 \right] \quad (\text{A-9})$$

APPENDIX B

Debond Length

The debond length can be derived from the strains in the following manner. The total strain of the composite is given by

the weighted sum of the average fiber strain in the debonded portion, $\bar{\epsilon}_f^d$, and the elastic strain, ϵ_f^e , in the intact portion:

$$\epsilon_{zz} = \bar{\epsilon}_{zz}^d \left(\frac{2l}{d} \right) + \epsilon_{zz}^e \left(1 - \frac{2l}{d} \right) \quad (\text{B-1})$$

where the bar refers to the average value, and the ratio $2l/d$ is the fraction of debonded material. During reloading, the average stress in the fibers in the debonded section, on steady-state slip, is

$$\bar{\sigma}_{zz}^d = \frac{\lambda \sigma_{zz}}{f} - \frac{\tau l}{R} \quad (\text{B-2})$$

where λ is the stress-partitioning factor for the 0° strain plies, typically 1.5–2.²⁴ The corresponding result during unloading is

$$\bar{\sigma}_{zz}^d = \frac{\lambda \sigma_{zz}}{f} + \frac{\tau l}{R} \quad (\text{B-3})$$

The strains on reloading in the steady-state slip (linear) region, thus, are

$$\epsilon_{zz/\text{load}} = \left(\frac{\lambda \sigma_{zz}}{f} - \frac{\tau l}{R} - \sigma_f^R \right) \frac{2l}{E_f d} + \frac{\sigma_{zz}}{\bar{E}} \left(1 - \frac{2l}{d} \right) \quad (\text{B-4})$$

and strains during unloading are

$$\epsilon_{zz/\text{unload}} = \left(\frac{\lambda \sigma_{zz}}{f} + \frac{\tau l}{R} - \sigma_f^R \right) \frac{2l}{E_f d} + \frac{\sigma_{zz}}{\bar{E}} \left(1 - \frac{2l}{d} \right) \quad (\text{B-5})$$

where σ_f^R is the residual stress in the fibers. Subtraction of these strains to obtain the loop width $\Delta \epsilon$ at the same stress cancels all terms except that containing the friction stress:

$$\Delta \epsilon = \frac{4\tau l^2}{RE_f d} \quad (\text{B-6})$$

This result can be used to estimate $2l/d$ from the hysteresis loop width when d is known.

APPENDIX C

Off-Axis Saturation Modulus

When the matrix cracks have attained their saturation density, steady-state frictional slip occurs at the interfaces. All of the subsequent increase in load is borne by the fibers. Hence, for on-axis loading of a single ply, the saturation tangent modulus, E_s , is

$$E_s = fE_f \quad (\text{C-1})$$

The analogous situation for off-axis loading is simulated by the spring configuration depicted in Fig. 15. The diagonal springs each represent a unit cell comprising a fiber encompassed by matrix having a saturation density of cracks and with dimensions that ensure the correct fiber volume fraction, f . One spring is representative of fibers in the 0° -strain orientation, and the other is representative of fibers in the 90° -strain orientation. The horizontal springs represent the intact matrix between the cracks. This matrix restricts the rotation of the fibers on off-axis loading and allows them to remain essentially straight. The composite consists of many such spring configurations.

The spring constants are found by noting that a load applied along one fiber direction causes a linear deformation with elastic modulus given by Eq. (C-1), such that the fiber stress, σ_f , and strain, ϵ_f , are related by

$$\sigma_f = \epsilon_f E_f \quad (\text{C-2})$$

Force equilibrium at area A requires that

$$F_A = F_f \cos \phi \quad (\text{C-3})$$

where F_f is the force acting along the diagonal spring, F_A the force associated with the applied load, and ϕ the angle indicated in Fig. 15. The cross-sectional areas A and A' are related by

$$A' = A \cos \phi \quad (\text{C-4})$$

The stresses ($\sigma = F/A$) are, thus, related by

$$\sigma_A = f\sigma_f \cos^2 \phi \quad (\text{C-5})$$

During steady-state slip, the matrix experiences almost constant load, such that the strain perpendicular to the load is essentially zero. On uniaxial straining in the direction of the applied load, ϵ_f and ϵ_A are related by

$$\epsilon_A = \frac{\epsilon_f}{\cos^2 \phi} \quad (\text{C-6})$$

Combining the results for the stresses (Eq. (C-5)) and strains (Eq. (C-6)) with Eq. (C-1), the contribution to the modulus from the 0° -strain fibers becomes

$$E_{s,0} = fE_f \cos^4 \phi \quad (\text{C-7})$$

The corresponding result for the 90° -strain fibers is

$$E_{s,90} = fE_f \sin^4 \phi \quad (\text{C-8})$$

The final result for the composite is

$$E_s = 0.5fE_f(\cos^4 \phi + \sin^4 \phi) \quad (\text{C-9})$$

Acknowledgment: The authors would like to thank John McNulty for his many helpful comments and discussions.

References

- ¹G. W. Genin and J. W. Hutchinson, "Composite Laminates in Plane Stress: Constitutive Modeling and Stress Redistribution due to Matrix Cracking"; pp. 23-42 in Ceramic Transactions, Vol. 57, *High-Temperature Ceramic-Matrix Composites I: Design, Durability, and Performance*. Edited by A. G. Evans and R. Naslain. American Ceramic Society, Westerville, OH, 1995.
- ²G. W. Genin and J. W. Hutchinson; unpublished calculations.
- ³A. C. F. Cocks and F. A. Leckie, "Design with Ceramic Matrix Composites"; see Ref. 1, pp. 483-500.
- ⁴C. Cady, F. E. Heredia, and A. G. Evans, "In-Plane Mechanical Properties of Several Ceramic-Matrix Composites," *J. Am. Ceram. Soc.*, **78** [8] 2065-78 (1995).
- ⁵C. Cady, A. G. Evans, and K. E. Perry Jr., "Stress Redistribution around Mechanical Attachments in Ceramic Matrix Composites," *Composites*, **26** [10] 683-90 (1995).
- ⁶E. Vagaggini, J.-M. Domergue, and A. G. Evans, "Relationships between Hysteresis Measurements and the Constituent Properties of Ceramic Matrix Composites: I, Theory," *J. Am. Ceram. Soc.*, **78** [10] 2709-20 (1995).
- ⁷A. G. Evans, J.-M. Domergue, and E. Vagaggini, "Methodology for Relating the Tensile Constitutive Behavior of Ceramic-Matrix Composites to Constituent Properties," *J. Am. Ceram. Soc.*, **77** [6] 1425-35 (1994).
- ⁸M. Y. He, B. X. Wu, A. G. Evans, and J. W. Hutchinson, "Inelastic Strains Caused by Matrix Cracking in Fiber-Reinforced Composites," *Mech. Mater.*, **18**, 213-29 (1994).
- ⁹J. W. Hutchinson and H. Jensen, "Models of Fiber Debonding and Pull-Out in Brittle Composites with Friction," *Mech. Mater.*, **9**, 139-63 (1990).
- ¹⁰J. Aveston, G. A. Cooper, and A. Kelly, "Single and Multiple Fracture"; pp. 15-26 in *The Properties of Fiber Composites* (NPL Conference Proceedings). IPC Science and Technology Press, Teddington, U.K., 1971.
- ¹¹A. G. Evans and F. W. Zok, "The Physics and Mechanics of Fiber-Reinforced Brittle Matrix Composites," *J. Mater. Sci.*, **29**, 3857-96 (1994).
- ¹²B. Harris, F. A. Habib, and R. G. Cooke, "Matrix Cracking and the Mechanical Behaviour of SiC-CAS Composites," *Proc. R. Soc. London, A*, **37**, 109-31 (1992).
- ¹³D. S. Beyerle, M. S. Spearing, and A. G. Evans, "Damage Mechanisms and the Mechanical Properties of a Laminated 0/90 Ceramic/Matrix Composite," *J. Am. Ceram. Soc.*, **75** [12] 3321-30 (1992).
- ¹⁴J. M. Domergue, E. Vagaggini, and A. G. Evans, "Relationships between Hysteresis Measurements and the Constituent Properties of Ceramic Matrix Composites: II, Experimental Studies on Unidirectional Materials," *J. Am. Ceram. Soc.*, **78** [10] 2721-31 (1995).
- ¹⁵D. S. Campbell, *Handbook of Thin Film Technologies*. McGraw-Hill, New York, 1970.
- ¹⁶A. G. Evans and J. W. Hutchinson, "The Thermomechanical Integrity of Thin Films and Multilayers," *Acta Metall. Mater.*, **43** [7] 2507-19 (1995).
- ¹⁷H. C. Cao, E. Bischoff, O. Sbaizero, M. Rühle, A. G. Evans, D. B. Marshall, and J. J. Brennan, "Effect of Interfaces on the Properties of Fiber-Reinforced Ceramics," *J. Am. Ceram. Soc.*, **73** [6] 1691-99 (1990).
- ¹⁸K. R. Turner, J. S. Speck, and A. G. Evans, "Mechanisms of Deformation and Failure in Carbon-Matrix Composites Subject to Tensile and Shear Loading," *J. Am. Ceram. Soc.*, **78** [7] 1841-48 (1995).
- ¹⁹Z. C. Xia, R. R. Carr, and J. W. Hutchinson, "Transverse Cracking in Fiber-Reinforced Brittle Matrix, Cross-Ply Laminates," *Acta Metall. Mater.*, **41** [8] 426-40 (1993).
- ²⁰T. J. Lu and J. W. Hutchinson, "Effects of Matrix Cracking on the Thermal Conductivity of Composites," *Philos. Trans. R. Soc. London, A*, **351**, 595-610 (1995).
- ²¹F. E. Heredia, A. G. Evans, and C. A. Andersson, "Tensile and Shear Properties of Continuous Fiber-Reinforced SiC/Al₂O₃ Composites," *J. Am. Ceram. Soc.*, **78** [10] 2790-800 (1995).
- ²²M. Y. He, A. G. Evans, and J. W. Hutchinson, unpublished work.
- ²³D. B. Marshall, "Analysis of Fiber Debonding and Sliding Experiments in Brittle Matrix Composites," *Acta Metall. Mater.*, **40**, 427-41 (1992).
- ²⁴J.-M. Domergue, F. E. Heredia, and A. G. Evans, "Hysteresis Loops and the Inelastic Deformation of 0/90 Ceramic/Matrix Composites," *J. Am. Ceram. Soc.*, **79** [1] 161-70 (1996).
- ²⁵D. W. Richerson, *Modern Ceramic Engineering*. Marcel Dekker, New York, 1982. □

RUPTURE SIMULATIONS FOR UNIDIRECTIONAL CERAMIC MATRIX FIBER COMPOSITES

R.M. McMeeking*, M.A. McGlockton* and B.N. Cox[‡]

*Mechanical and Environmental Engineering Department
University of California, Santa Barbara, CA 93106

[‡]Rockwell International Science Center
1049 Camino Dos Rios
Thousand Oaks, CA 91360

ABSTRACT

A model for the behavior of unidirectional fiber reinforced ceramic matrix materials with weak interfaces is used to simulate the stochastic failure process leading to ultimate stress and the transition to pullout controlled extension. Brittle cracking of the matrix is assumed to limit the axial load sustained by the matrix, does not damage the fibers, but allows the matrix to retain shear stiffness. Fiber element fracture nuclei consistent with a Weibull distribution of strengths fail stochastically with increasing load. Fiber-matrix load transfer at fiber failure sites is governed by uniform shear strength representing frictional constraint at unbonded interfaces. The results prior to peak load are shown to be consistent with sparse fiber damage with modest stress concentrations on neighboring fibers. Localization is shown to dominate the post peak pullout.

KEYWORDS

Ceramic matrix composites, stress-strain, rupture, simulation.

INTRODUCTION

The strength and toughness of ceramic matrix composites (CMCs) exhibit a strong dependence upon the mechanical properties of the fiber-matrix interface. The interface properties must be tailored to control the fracture of fibers and load transfer near flaws (Evans and Zok, 1994). Damage in the composite commences with flaws within the matrix, since the failure strain of the matrix is usually much less than that of the reinforcing fibers. Under tensile loads, the matrix develops cracks which propagate across the composite and which may cause the fibers to fail if the interface is too strong. For intact fibers to survive and bridge the matrix cracks, the interface debond energy must be sufficiently low to prevent matrix cracks from penetrating the fibers. Furthermore, to avoid brittle failure of the composite, upon matrix cracking, it is desirable for the matrix fracture strength to be lower than the stress which will fail the majority of the fibers. After

matrix cracking, the strength of the interface shear strength τ . The interfacial shear stress which develops at debonded interfaces governs load transfer between the fibers and the matrix, with low τ leading to gradual load transfers (over a length L_T) and low stress concentrations in neighboring fibers. When L_T is much less than the gauge length of the composite, multiple fiber failures are expected at high stress along the length of the composite and its strength is governed by the weakest link in a chain of fiber bundles (of length L_T) simultaneously supporting the composite load (Curtin, 1991). Higher τ diminishes the load transfer length at fiber failures and increases the stress concentration in neighboring fibers.

SIMULATIONS OF RUPTURE

Calculations are carried out for composites with arrays of fibers which experience fracture in a stochastic manner. Displacement control is used to impose strain on the composite by specification of a uniform x-displacement of each fiber at the end planes of a model as shown in Fig. 1. Fibers having slip zones protruding through the end of the model are omitted from the displacement control process. The model is stretched until significant damage has occurred and the ultimate strength has been established. Calculations were carried out with 11×11 arrays of 121 fibers with 12 elements representing each fiber.

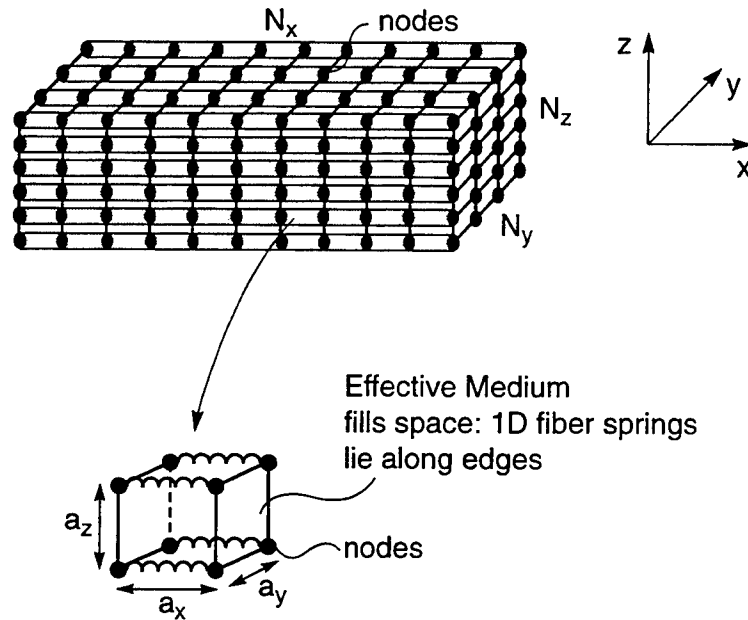


Fig. 1 The finite element model for the simulations.

The finite element program used is a special version of the Binary Model code (Cox et al., 1994; Xu et al., 1995; McGlockton, et al., 1996) developed to simulate the behavior of unidirectional fiber reinforced ceramic matrix composites subjected to strain parallel to the fibers. The finite element nodes coincide with the fibers so that there are N_x fiber elements along the length of the cuboid. The fiber elements are 1-dimensional units between the nodes and prior to failure are simple uniaxial elastic springs. Their spring constant is chosen to represent a fiber with a finite cross-section; i.e. $E_f \pi R^2 / a_x$ where E_f is the fiber modulus, R is the fiber radius and a_x is the fiber element length. Upon fiber failure, the fiber segment stiffness is eliminated from the finite element model.

The space among the nodes is filled with cuboidal effective medium elements which have 8 nodes per element. The purpose of these elements is to simulate the phenomena not represented by the fiber elements. Thus they represent the matrix properties in the longitudinal direction. The effective medium elements have zero stiffness in the longitudinal and transverse directions to represent a matrix cracked at the outset of the computation. The shear moduli of the effective medium elements, G_{xy} and G_{xz} , are both equal to $E/2(1+\nu)$ with $E = 400$ GPa and $\nu = 0.22$. The shear moduli are therefore 164 GPa. Similarly, the fiber modulus $E_f = E = 400$ GPa. These values are representative of alumina/alumina composites. Only the axial displacements are relevant and are decoupled from the transverse displacements by the effective medium properties. Efficiency is gained by tailoring the computer program to calculate them only and not the transverse displacement.

The fiber elements are given strengths according to a random number procedure, and are consistent with a Weibull model given by

$$P_f(S_f) = 1 - \exp \left[- \frac{a_x}{L_o} \left(\frac{S_f}{\sigma_o} \right)^m \right] \quad (1)$$

where P is the probability of survival of an element of length a_x subject to a fiber stress S_f . The Weibull parameters for the strength statistics are chosen as $\sigma_o = 1.5$ GPa and $L_o = 25$ mm with m chosen to be 2 or 10. The interface shear strength between matrix and fibers is taken to be 20 MPa, low but within the range found in CMCs.

When the axial fiber load first exceeds the strength of a particular element, that element fails and the program simulates the debonded, slipping fiber elements on either side of the break. Since the stress in the broken fiber element and the slipping fiber elements will no longer change as the strain is increased, these elements are eliminated from the finite element model (i.e. their stiffness contributions are removed). The effect of the missing fiber segments on the matrix and on the remaining adjacent fiber segments is then introduced by the imposition of equivalent nodal forces to represent the traction τ of the fiber acting on the matrix and the presence of the stressed fiber termination at the end of the missing zone of elements. These forces are transmitted to the remaining intact fibers by the shear stiffness of the effective medium elements, simulating the role of the matrix.

As a slip zone grows due to increasing strain, further fiber elements are removed and additional nodal forces are added. If a slip zone shrinks, the procedure is reversed. If a slip zone is calculated to project beyond the end of the model at any time, it is introduced in a periodic fashion into the other end of the model. In this way, a periodic system in the x -direction is simulated. In some cases, the slip zones of 2 nearby breaks in a single fiber can meet each other either through growth or when a new break occurs just outside the slip zone of a previous break. In this case, the fiber segments of both slip zones are removed and replaced with equivalent nodal forces pointing away from the break to which they are nearest, since the intersection of the slip zones will be half way between the 2 cracks.

Until all of the fibers in the model have broken, it is possible for increasing strain to elevate the load in an intact fiber element. However, the equilibrium load on a plane cut through the model can no longer increase when all of the fibers have broken and the slip lengths from fiber breaks in *all* fibers overlap on that plane. This condition is used in the finite element model to determine when

pullout is possible and to determine the location of the cross-section which supports the lowest load. The latter cross-section will become the fracture plane for ultimate failure.

During failure of the composite, fiber breaks move past the location of effective medium element nodes, reducing the load on the effective medium nodes. As fiber pullout occurs, the axial load on the finite element model will therefore generally diminish and the lengths of slip zones at fiber breaks diminish in concert. However it is assumed for simplicity that this is accomplished without the formation of reverse slip zones (McMeeking and Evans, 1990). Instead, the length of the slip zone is simply reduced to the value it had after monotonic loading to the current stress level. Any potential effects of load cycling are ignored. In the pullout zone, this simple approach is probably correct because reverse slip will usually be overcome by the pullout process. Hysteresis associated with reversal effects at breaks not in the pullout zone are believed to have a negligible effect on the overall composite behavior.

Pullout is ultimately achieved in the code after a plane with all fibers slipping across it has been created due to all fiber failing. This cross-section is assumed to be a matrix crack which opens to form the ultimate failure plane and therefore transmits no axial or shear tractions between the pieces of the finite element model on either side of the failure plane. When a fiber end has passed this plane, it is considered to have pulled out and is no longer connecting together the two pieces of the finite element model. Failure will finally occur when all fibers have pulled out.

Increments of the imposed strain are chosen to produce an increment for the composite which causes the failure of no more than 1 fiber element during that strain increment. After each increment of the strain, the code uses the new stresses in the fiber elements to update the slip zones of all broken elements and then seeks the fiber element which has exceeded its strength by the largest margin. A new break and slip zones are created in this location. The finite element equations are solved again without any increase in the applied load or strain. The process is repeated of seeking the fiber element which has a stress exceeding its strength by the greatest amount. This fiber element is failed and new slip zones for it created. The finite element equations are re-solved and the procedure repeated again without increase of applied load or strain. This sequence of load redistributions from fiber breaks and re-solution of the equations continues until no more fiber elements are overstressed compared to strength. Only then is the applied load or strain increased to cause more breaks.

RESULTS

A simulated stress-strain curve for a composite material with $\tau = 20$ MPa, a fiber volume fraction f of 0.3 and a fiber strength distribution consistent with a Weibull modulus $m = 2$ is shown in Fig. 2. The fiber elements therefore have a wide distribution of strengths. The stress S in Fig. 2 is defined as the total load applied to the material divided by the composite cross-sectional area. The strain e is defined to be the difference between the end plane axial displacements (imposed as boundary conditions) divided by the length of the model. The response is at first linear with composite Young's modulus equal to fE , as expected for a material with a strengthless matrix. The first fiber fracture occurs at $e = 0.14\%$. Above a strain of 0.14%, fiber segments break randomly. The fraction of fibers which have at least 1 break is marked at various strains in Fig. 2. Even when 40% of the fibers are broken, there is little effect on the elastic stiffness of the composite. However, at strains greater than 1%, fiber damage accumulates rapidly and ultimate strength is reached at about 1.3% strain when 64% of the fibers have breaks. The ultimate strength is 1.1 GPa.

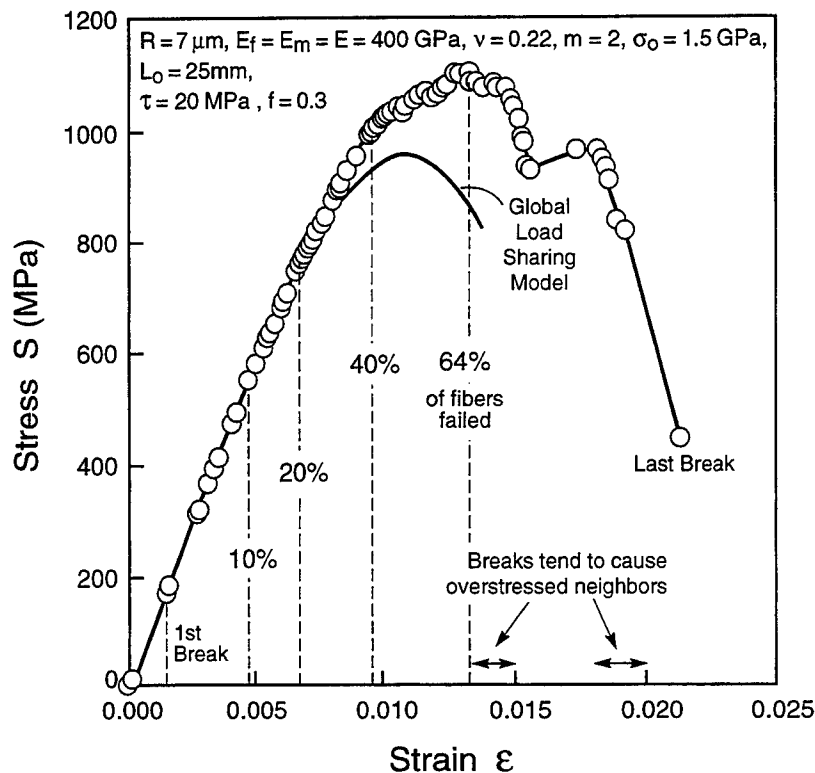


Fig. 2 Simulated stress-strain curve for a material with fibers having a low Weibull modulus.

It is only beyond ultimate strength that the failure of one fiber segment causes a nearby neighbor to fail without any increase required in the imposed strain. Even then, this effect is limited to no more than 2 consequent failures before the strain has to be increased again to cause more fractures. However, the 2 occasions upon which this clustering of breaks occurs at strains of about 1.3% and 1.8% are significant. They lead to steep falls in the stress, in the composite, as can be seen in Fig. 2.

Finally the last break occurs at 2.2% strain and the calculation is terminated then. After the last break has occurred, deformation localizes near a single layer of elements and is accommodated by fiber pullout. This occurs while the nominal strain in the model increases to about 15% and the stress gradually declines as dictated by the friction stress at the fiber-matrix interface. The last process is omitted because of the lengthy computation required for a phenomenon which can be understood instead with a simple model of broken fibers pulling out of the matrix and being resisted by friction.

The stress-strain curve shown in Fig. 2 is quite similar to that expected from the global load sharing model of Curtin (1991), which is also plotted on Fig. 2. However, the global load sharing model gives an ultimate strength of 970 MPa and a strain at ultimate strength of 1.08%. It can be seen in Fig. 3 that the computational simulation is stronger and tougher than the prediction of the global load sharing model.

A simulated stress-strain curve for a composite with $\tau = 20$ MPa, a volume fraction $f = 0.3$ and a fiber strength distribution consistent with a Weibull modulus $m = 10$ is shown in Fig. 3. The fiber elements therefore have a narrow distribution of strengths. In this case, the response is essentially

linear with an abrupt brittle transition to failure at a relatively low strain and stress. The first fiber break occurs at 0.33% strain. Ultimate strength is reached when only 14% of the fibers have one break or more and occurs at a strain of only 0.46%. The narrow strength distribution in the fiber elements means that many become overstressed together even though the stress concentrations are very modest. Initially, 3 to 4 neighbors become overstressed starting at about 0.45% strain. However, very quickly up to about 30 fibers at a time are overstressed when a single break occurs and the stress drops very rapidly for extremely small increments of strain. When the last break occurs, the composite stress is quite modest.

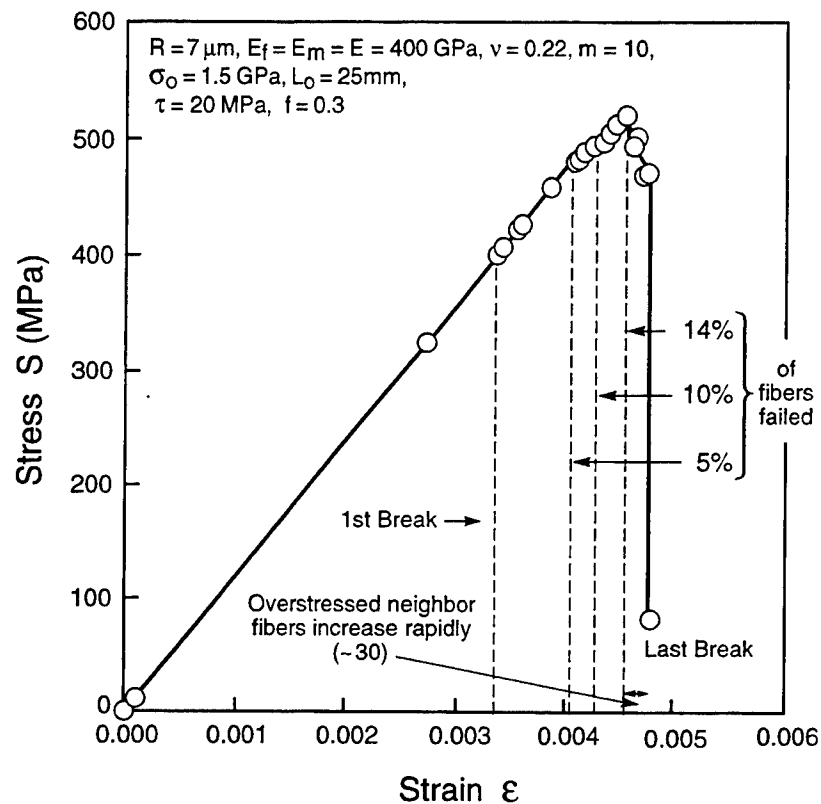


Fig. 3 Simulated stress-strain curve for a material with fibers having a high Weibull modulus.

DISCUSSION

The 2 simulated stress-strain curves contrast the effect of the strength distribution within the fibers for a narrow and a wide spread. Other parameters such as the interface shear strength were not varied. However, the strong effect of the Weibull modulus causes a transition from a fairly ductile failure when $m = 2$ with good energy dissipation to a brittle response when $m = 10$. The wide distributions of strengths within the fibers can therefore provide damage tolerance in a CMC. Other aspects of the influence of material parameters are discussed more fully in by McGlockton et al., (1996).

ACKNOWLEDGMENT

This research was supported by the Defense Advanced Research Projects Agency through the University Research Initiative, ONR Contract N00014-92-J-1808. BNC was supported under AFOSR Contract No. F49620-94-C-0030.

REFERENCES

- Cox, B.N., W.C. Carter and N.A. Fleck, (1994), "A Binary Model of Textile Composites- I. Formulation," *Acta Metallurgica et Materialia*, **42**, p. 3463.
- Curtin, W.A., (1991), "Theory of Mechanical Properties of Ceramic Matrix Composites," *Journal of the American Ceramic Society*, **74**, p. 2837.
- Evans, A.G. and F.W. Zok, (1994), "The Physics and Mechanics of Fibre-reinforced Brittle Matrix Composites," *Journal of Materials Science*, **29**, p. 3857.
- McGlockton, M.A., R.M. McMeeking and B.N. Cox, 1996, "A Model for the Axial Strength of Unidirectional Ceramic Matrix Fiber Composites," to be published.
- McMeeking, R.M. and A.G. Evans, (1990), "Matrix Fatigue Cracking in Fiber Composites," *Mechanics of Materials*, **9**, p. 217.
- Xu, J., B.N. Cox, M.A. McGlockton and W.C. Carter, (1995), "A Binary Model of Textile Composites- II. The Elastic Regime," *Acta Metallurgica et Materialia*, **43**, p. 3511.

Application of Weakest-Link Fracture Statistics to Fiber-Reinforced Ceramic-Matrix Composites

John C. McNulty* and Frank W. Zok*

Materials Department, University of California, Santa Barbara, California 93106

The strength and reliability of fiber-reinforced ceramic-matrix composites (CMCs) are dependent on whether conditions of local or global load sharing prevail. Global load sharing is promoted by a low interfacial sliding stress and is manifested in a zero-tangent modulus at the point of tensile failure along with random fiber failures and extensive fiber pullout. In this paper, it is demonstrated that conditions of global load sharing are not present in two commonly studied CMCs, despite the fibrous appearance of their fracture surfaces. This behavior is manifested in a volume-dependent strength, as evidenced by strength differences measured in tension and flexure (accounting for the nonlinear stress distribution in flexure). Methods of weakest-link statistics are used to relate the strengths measured in the two test configurations. Estimates for the Weibull moduli of the two systems are obtained from the experiments and compared with values obtained through Monte Carlo simulations based on a three-dimensional-lattice Green's function method. The implications of these results on the strength of large components and of small regions of high stress concentration are discussed briefly.

I. Introduction

A TENSILE stress-strain curve for a fiber-reinforced ceramic-matrix composite (CMC) is illustrated in Fig. 1. Typically, such curves exhibit three characteristic features: linear elastic response at small stresses; nonlinear behavior associated with progressive matrix cracking at intermediate stresses; and a second linear regime in which essentially all the applied stress is supported by the fibers and the tangent modulus, $d\sigma/d\varepsilon$ (where σ is stress and ε is tensile strain), is $\sim f_1 E_f$, where f_1 is the volume fraction of fibers aligned with the loading direction and E_f is the Young's modulus of the fiber. In some instances, fiber failure at high stresses leads to a further reduction in the tangent modulus (below $f_1 E_f$). The ultimate strength is dictated by the strength distribution of the individual fibers and the load-transfer characteristics between neighboring fibers.¹

The extent of load transfer is governed mainly by the interfacial sliding stress, τ . When τ is sufficiently low, global load sharing (GLS) conditions are obtained. In this regime, the load that is carried by a broken fiber is distributed equally to all fibers in the plane of the break, with no attendant stress concentration. The GLS fiber bundle strength is dictated by a characteristic slip length, δ_c .^{2,3}

$$\delta_c = \left(\frac{S_o R L_o^{1/m}}{\tau} \right)^{m/(m+1)} \quad (1)$$

where R is the fiber radius, m the Weibull modulus of the fibers,

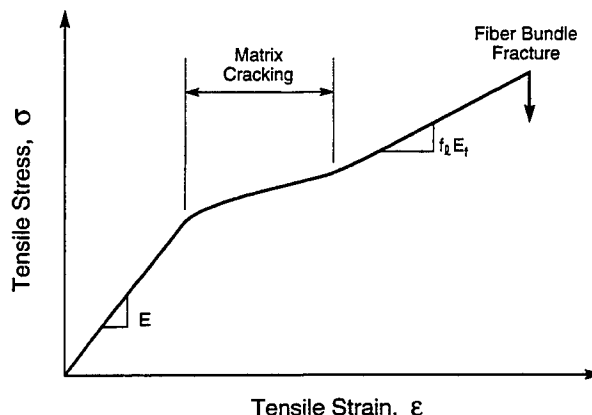


Fig. 1. Schematic showing the tensile stress-strain response of a fiber-reinforced CMC.

and S_o the reference strength corresponding to a reference length L_o . Provided the length of the composite is greater than $\sim 2\delta_c$ and the number of fibers is large, the stress-strain response of the fiber bundle is essentially deterministic (Fig. 2(a)) and given, approximately, by²

$$\frac{\sigma_f(\varepsilon)}{\sigma^*} = \left(\frac{\varepsilon E_f}{\sigma^*} \right) \left[1 - 0.5 \left(\frac{\varepsilon E_f}{\sigma^*} \right)^{m+1} \right] \quad (2)$$

where σ^* is a characteristic strength defined by

$$\sigma^* = \left(\frac{S_o^m \tau L_o}{R} \right)^{1/(m+1)} \quad (3)$$

Fiber bundle failure occurs when $d\sigma_f/d\varepsilon = 0$ (Fig. 2(b)); the corresponding strength is

$$\frac{\bar{\sigma}_f}{\sigma^*} = \left(\frac{2}{2+m} \right)^{1/(m+1)} \left(\frac{m+1}{m+2} \right) \quad (4)$$

When the sliding stress is large, the load from a broken fiber is distributed preferentially to its neighbors—the so-called local load sharing (LLS) condition. In this regime, the stress-strain response initially follows Eq. (2); however, the fiber bundle strength falls below the value predicted by Eq. (4). Moreover, the bundle strength becomes intrinsically stochastic in nature. One of the important implications is that the strength follows weakest-link statistics and, hence, exhibits a volume dependence. This volume dependence has been reported for a number of fiber composites with well-bonded interfaces, including epoxy/graphite⁴⁻⁷ and aluminum/ Al_2O_3 .⁸

Curtin and coworkers^{9,10} developed a three-dimensional lattice Green's function method to study the evolution of fiber damage and ultimate fracture under extreme LLS conditions. They identified an intrinsic link size, comparable to the critical cluster of fiber breaks at ultimate fracture, which dictates the stochasticity of composite fracture. Knowing the strength distribution of the intrinsic link, weakest-link scaling is used to

B. N. Cox—contributing editor

Manuscript No. 191578. Received August 21, 1996; approved December 2, 1996. Supported by the ARPA University Research Initiative Program at UCSB under U.S. Office of Naval Research Contract No. N00014-92-J-1808.
*Member, American Ceramic Society.

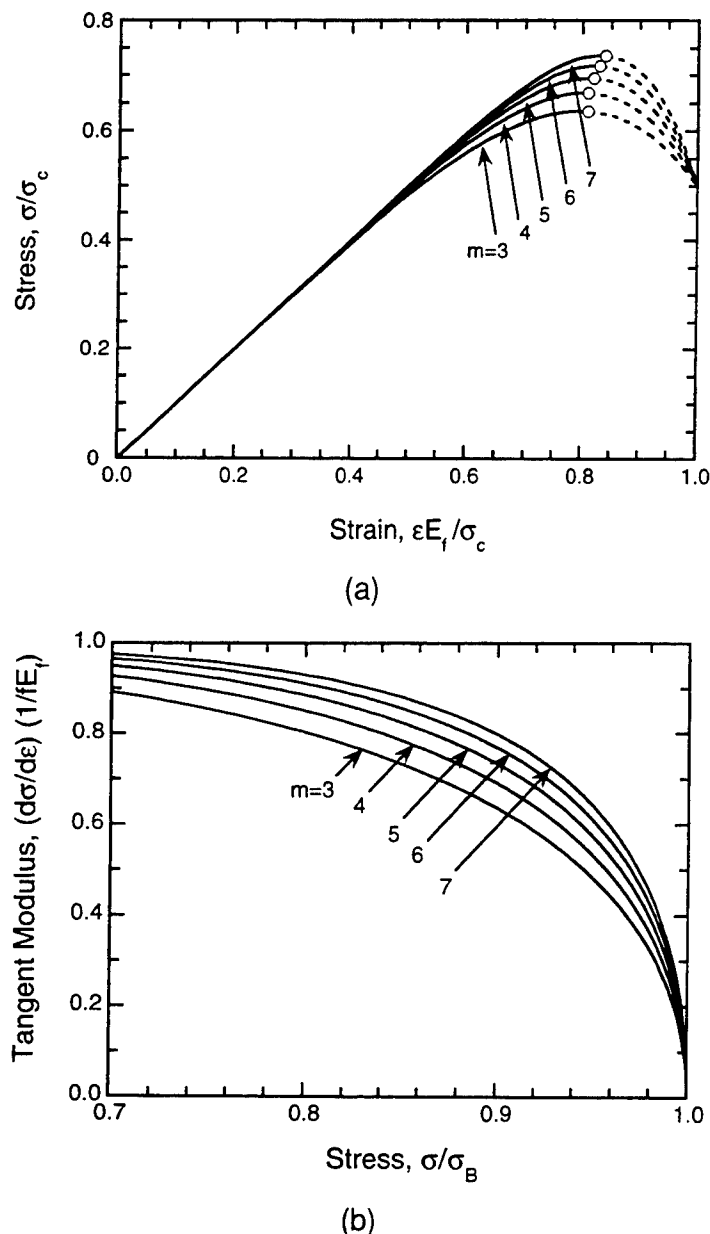


Fig. 2. Predicted fiber bundle behavior for GLS materials ((a) stress-strain response and (b) variation in tangent modulus with applied stress). Open circles in Fig. 2(a) represent the points of tensile instability.

calculate the strength distribution of a composite that is composed of a collection of such links. The simulations indicate that the strength distribution can be approximated by the Weibull function, although the apparent Weibull modulus of the composite, m_c , is larger than that of the fibers. Consequently, the composite strength distribution is predicted to be narrower than that of the fibers alone.

Although the existing models provide some insight into the stochasticity of composite fracture in the two limiting load-sharing regimes, it is not clear when GLS and LLS conditions are present. Moreover, the connections between the strength distributions for the fibers and the composite for LLS materials are not well established. Examinations of stress-strain curves and fracture surfaces provide some indications. Under GLS conditions, the fracture surface is expected to be fibrous, with random fiber breaks and extensive fiber pullout, indicating little correlation between the locations of fiber breaks. Moreover, the stress-strain curves are expected to exhibit a gradual reduction in $d\sigma/d\epsilon$ as the fibers break, ultimately attaining $d\sigma/d\epsilon = 0$ at

fracture. The predicted mechanical response of the fiber bundle for GLS materials is shown in Fig. 2. As a general rule, if $d\sigma/d\epsilon$ decreases to a value of $\sim f_f E_f/2$ at fracture, then the bundle strength is $\leq 5\%$ of the GLS value (for $m \geq 3$).¹

The objective of the present article is to ascertain experimentally whether GLS conditions are obtained in two commonly studied CMCs and to examine the effects of volume on composite strength. It is demonstrated that, despite the fibrous appearance of the fracture surfaces, GLS conditions are not obtained. This condition is manifested in the manner in which $d\sigma/d\epsilon$ develops with stress and, more importantly, in a volume-dependent strength. The volume dependence is examined by comparing the behavior of the CMCs in tension and in flexure, taking into account the nonlinear stress distribution in the flexure specimens. Weakest-link statistics are used to relate the strengths that are measured in the two test configurations. Estimates for the composite Weibull moduli are obtained and compared to the values that were obtained from Curtin's simulations. The effects of the volume-dependent strength on the notched tensile properties are detailed elsewhere.¹¹

II. Materials and Test Procedures

Two CMC systems were studied. The first[†] was a borosilicate-glass-doped magnesium aluminosilicate (MAS) glass-ceramic matrix reinforced with Nicalon[‡] fibers in a [0/90]_{3s} (crossply) configuration. A thin, boron-modified carbon layer, ~100 nm thick, was obtained on the fibers by an *in-situ* reaction. The volume fraction of fibers, f , was ~40%. The MAS matrix was fully dense. The second[§] was a SiC matrix, produced by chemical vapor infiltration, reinforced with ~32% of Nicalon fibers in a plain-weave configuration. In this case, the fibers had been coated with a relatively thick (~1 μ m) carbon layer. The SiC matrix contained porosity at two levels: large pores between the tows and fine-scale porosity within the tows. The volume fractions of the two were 3.0% and 5.6%, respectively (determined from quantitative metallography of polished cross sections). The microstructures of the two materials are shown in Fig. 3.

Uniaxial tension tests were performed on straight bars of the MAS/Nicalon composite, with a gauge length of 75 mm and width of 5.0 mm. Fiberglass tabs were affixed to the specimen ends using epoxy. The specimens were loaded using hydraulic wedge grips mounted on a servohydraulic testing machine. The axial strains were measured with a clip-on extensometer over a 10 mm gauge length. Similar tests were performed on the SiC/Nicalon composite, although the specimens had a dogbone-shaped geometry, with a gauge length of 55 mm and a width of 10.5 mm. All the reported test results corresponded to gauge failures.

Four-point flexure tests were performed on the two composites, with the loading direction parallel to the laminae or fiber weaves ("edge-on" orientation). The cross-sectional areas of the flexural specimens were the same as those of the corresponding tensile specimens. The inner and outer spans were 24 and 68 mm for the MAS/Nicalon composite and 39 and 95 mm for the SiC/Nicalon composite. Strains were measured on the compressive and tensile faces using strain gauges that were 1 mm wide and 3 mm long. Fracture consistently occurred within the inner span. Either two or three tests were performed on each material in both tension and flexure. Following testing, the fracture surfaces of the specimens were examined using scanning electron microscopy (SEM).

[†]Produced by Corning, Inc., Corning, NY.

[‡]Ceramic grade, produced by Nippon Carbon, Tokyo, Japan.

[§]Produced by DuPont Lanxide Composites, Newark, DE.

III. Results and Analysis

Figure 4 shows typical tensile test results, presented in terms of the stress-strain response and the variation in tangent modulus with stress. The strength results from all tests are summarized in Table I. Both materials exhibit the characteristics shown schematically in Fig. 1, which are, notably, a linear elastic regime, a nonlinear regime that is associated with cracking, and a second almost linear regime that is associated with fiber loading. These trends are demonstrated more vividly in the tangent modulus plots (Fig. 4(b)). One of the key features in these plots is the absence of a large reduction in the tangent modulus as the stress approaches the ultimate tensile strength, suggesting that the strength lies below the expected GLS value and that some degree of LLS must exist between the fibers.¹

SEM micrographs of the fracture surfaces are shown in Fig. 5. In the SiC/Nicalon composite, there is only a modest amount of fiber pullout. Moreover, there are regions in all the bundles in which the fiber-fracture locations are essentially coplanar with one another, indicating a strong correlation

¹In the Nicalon/SiC composite, the terminal value of the tangent modulus is essentially equivalent to the value expected based on fiber loading: $fE_f/2 \approx 29$ –32 GPa (based on a fiber modulus $E_f = 180$ –200 GPa). In the Nicalon/MAS composite, the tangent modulus attains a saturation value of ~20–25 GPa at a strain of ~0.2%–0.3% and remains at that level up to the fracture strain (~0.9%). This level is somewhat lower than the expected value of $fE_f/2 \approx 36$ –40 GPa. The discrepancy can be attributed to the progressive development of matrix cracks over the entire range of nonlinear straining. This result was obtained by replicating the tensile surface with acetate tape at various stress levels and subsequently measuring the spacing between the cracks on the replicas using optical microscopy. Evidently, the crack density in the axial plies increases linearly as strain increases and never attains a saturation level prior to tensile fracture.

Table I. Summary of Ultimate Strengths and Failure Strains

Loading	Ultimate strength (MPa)	Failure strain (%)
Nicalon/MAS		
Tension	324	0.93
Tension	299	0.86
Flexure	381	1.40
Flexure	360	1.30
Flexure	359	1.34
Nicalon/SiC		
Tension	169	*†
Tension	176	0.37
Flexure	213	0.57
Flexure	187	0.52

†The symbol "" represents extensometer failure.

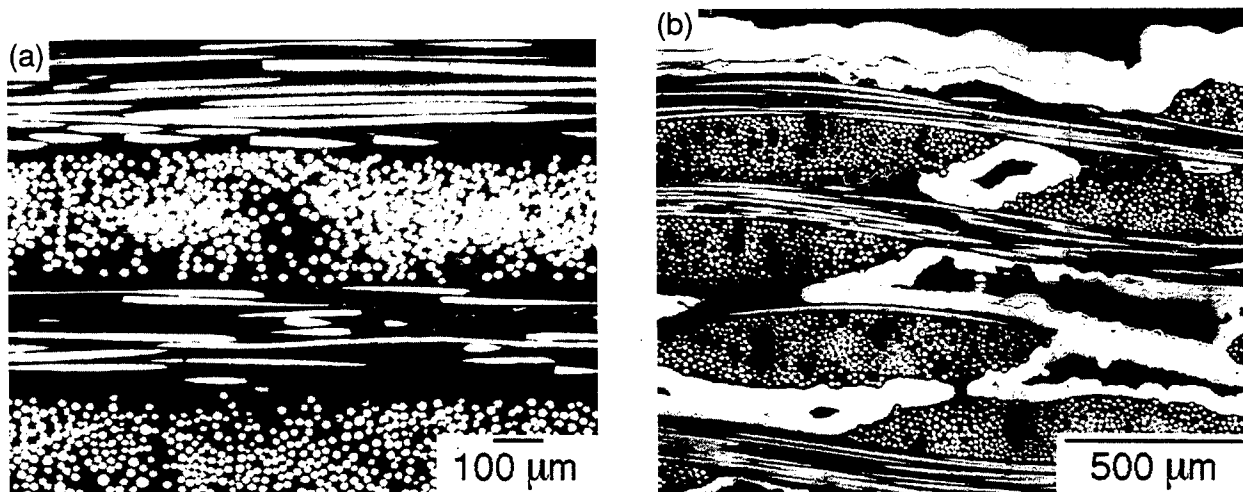


Fig. 3. Micrographs of the (a) Nicalon/MAS and (b) Nicalon/SiC composites.

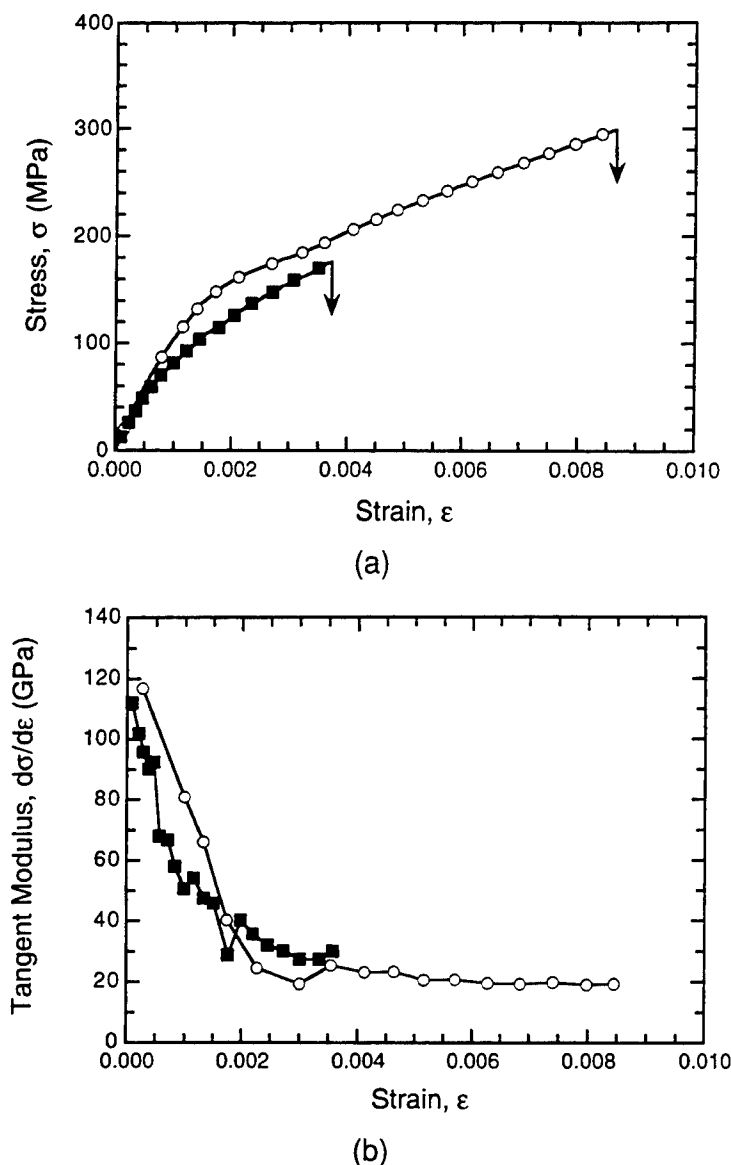


Fig. 4. Tensile response of the (■) Nicalon/SiC and (○) Nicalon/MAS composites ((a) stress-strain behavior and (b) evolution of tangent modulus with stress).

between breaks and, again, suggesting the existence of LLS conditions. In the MAS/Nicalon composite, the extent of fiber pullout is considerably greater, although there are small regions where the breaks seem somewhat correlated with one another (see, for example, the broken fibers near the bottom right corner of Fig. 5(d)). In addition, the failure strain of the MAS/Nicalon composite is almost twice that of the Nicalon/SiC composite. It is speculated that this difference may be ascribed to fiber degradation during weaving of the fiber cloths for the SiC/Nicalon material.

The results of typical flexural tests are shown in Fig. 6. In both materials, the tensile and compressive strains, ϵ_T and ϵ_C , are initially of the same magnitude (as expected in a linear elastic beam). Once matrix cracking occurs, the value of ϵ_T exceeds the value of ϵ_C . Moreover, the value of ϵ_T at fracture invariably exceeds the value measured in the uniaxial tensile tests. Evidently, the failure strains are not deterministic, again indicating that GLS conditions are not obtained in the two composites.

The true values of tensile strength in the flexure specimens were obtained in the following manner. In general, the bending moment, M , is related to the uniaxial stress-strain response, $\sigma(\epsilon)$, through the relation

$$M = \frac{BD^2}{(\epsilon_T - \epsilon_C)^2} \int_{\epsilon_C}^{\epsilon_T} \sigma(\epsilon) \epsilon d\epsilon \quad (5)$$

where B and D are the specimen thickness and height, respectively. Rearranging Eq. (5) and differentiating it yields the following result:

$$\frac{d}{d\epsilon_T} \left[\frac{(\epsilon_T - \epsilon_C)^2 M}{BD^2} \right] = \sigma(\epsilon_T) \epsilon_T - \sigma(\epsilon_C) \epsilon_C \frac{d\epsilon_C}{d\epsilon_T} \quad (6)$$

For mechanical equilibrium, the forces acting on any plane through the specimen must be zero, yielding the additional requirement of

$$\int_{\epsilon_T}^{\epsilon_C} \sigma(\epsilon) d\epsilon = 0 \quad (7)$$

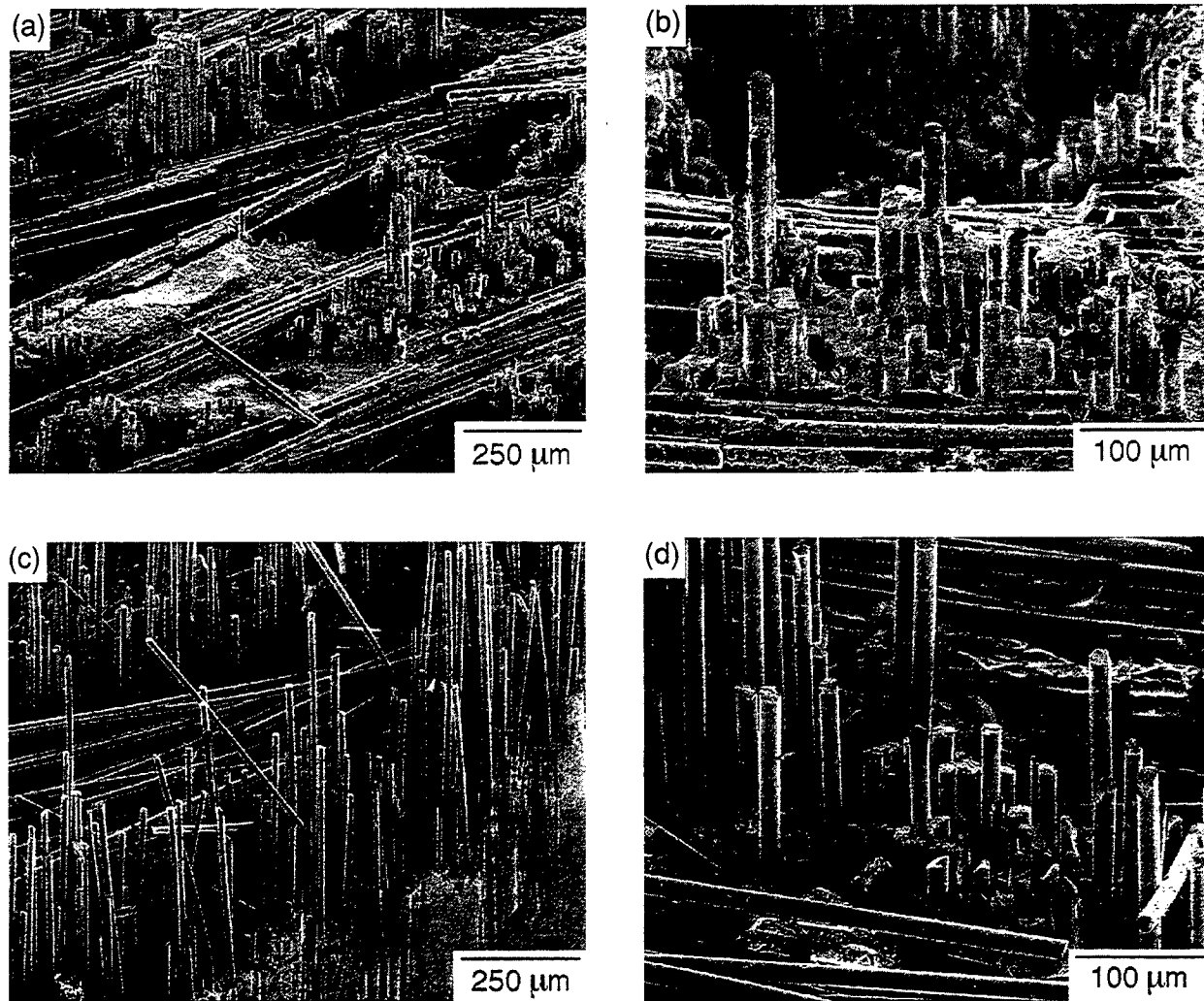


Fig. 5. Fracture surfaces of (a and b) Nicalon/SiC and (c and d) Nicalon/MAS, at low and high magnifications.

which, when differentiated, becomes

$$\sigma(\epsilon_c) \frac{d\epsilon_c}{d\epsilon_T} = \sigma(\epsilon_T) \quad (8)$$

Combining Eqs. (6) and (8) gives the tensile stress-strain relation

$$\sigma(\epsilon_T) = \frac{1}{(\epsilon_T - \epsilon_c)} \frac{d}{d\epsilon_T} \left[\frac{(\epsilon_T - \epsilon_c)^2 M}{BD^2} \right] \quad (9)$$

The derivative on the right-hand side of Eq. (9) is evaluated by fitting the function to a smooth, monotonically increasing function and subsequently differentiating the function. The true tensile strength is evaluated from Eq. (9) at the load maximum. (Similar methodologies for relating the flexural to tensile strengths are found in the literature but are either numerical^{12,13} or expressed in a different analytical form.¹⁴)

Comparisons of the tensile stress-strain curves obtained from the flexure and tensile specimens are shown in Fig. 7. Over most of the loading, the two tests yield similar results. The main difference is that the strengths and failure strains that are obtained in flexure exceed the corresponding values that are obtained in uniaxial tension. The slight differences in stress-strain response can probably be ascribed to the intrinsic variability in material properties. The ratio of mean strengths (bending/tension) are indicated on Fig. 8. The ratios are in the range of 1.10–1.20 for both systems. Previous studies on glass-

fiber-reinforced polymers^{5,6} yielded strength ratios of 1.4–1.5. The differences are most likely due to differences in interfacial bonding and fiber strength distributions.

IV. Weakest-Link Statistics

The experimental results demonstrate that the tensile strengths of the composites are dependent on the volume under stress and, therefore, are expected to follow weakest-link scaling, in accordance with¹⁵

$$P_f = 1 - \exp \left(- \int_V g(\sigma) dV \right) \quad (10)$$

where P_f is the cumulative failure probability at a stress σ ; V is volume, and $g(\sigma)$ is a positive, monotonically increasing function of σ . If the strength follows a Weibull distribution, then

$$g(\sigma) = \frac{1}{V_0} \left(\frac{\sigma}{\sigma_0} \right)^m \quad (11)$$

where σ_0 is the reference stress corresponding to a reference volume, V_0 , and m is the Weibull modulus. Substituting Eq. (11) into Eq. (10) yields

$$P_f = 1 - \exp \left[-k \left(\frac{V}{V_0} \right) \left(\frac{\sigma_{\max}}{\sigma_0} \right)^m \right] \quad (12)$$

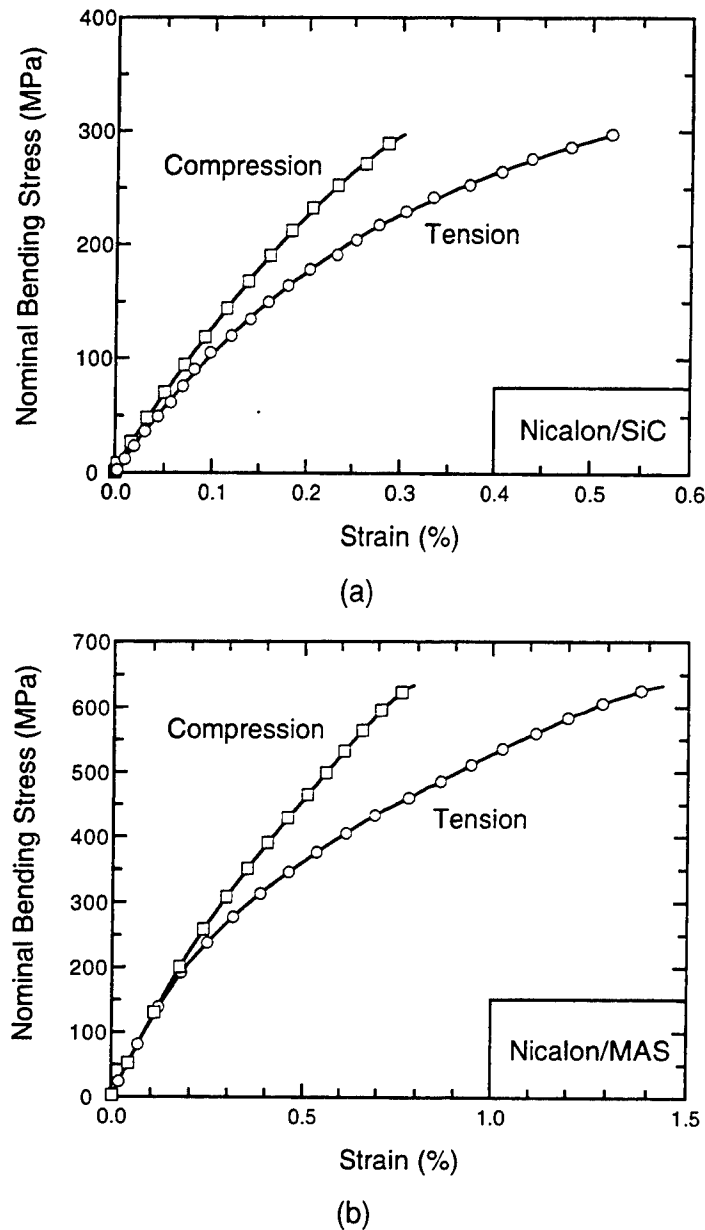


Fig. 6. Flexural response of (a) Nicalon/SiC and (b) Nicalon/MAS.

where k is a dimensionless coefficient that is defined by

$$k = \frac{1}{V(\sigma_{\max})^m} \int_V \sigma^m dV \quad (13)$$

and σ_{\max} is the maximum tensile stress. For uniaxial tension, $k = k_T = 1$, and, for pure bending of an elastic body, $k = k_B = 0.5/(m + 1)$. Solutions exist for k in other loading configurations; for linear elastic materials, k is a function of m and specimen geometry only.¹⁵ From Eq. (12), it follows that the ratio of the median strengths,¹⁶ $\bar{\sigma}_1/\bar{\sigma}_2$, obtained from two different loading configurations with k factors of k_1 and k_2 is

$$\frac{\bar{\sigma}_1}{\bar{\sigma}_2} = \left(\frac{k_2 V_2}{k_1 V_1} \right)^{1/m} \quad (14)$$

Thus, the strength ratio in bending to that in tension is given by

$$\frac{\sigma_B}{\sigma_T} = \left(\frac{V_T}{V_B k_B} \right)^{1/m} = \left[2(m + 1) \left(\frac{V_T}{V_B} \right) \right]^{1/m} \quad (15)$$

where B and T refer to bending and tension, respectively. (In this case, V_B is taken as the specimen volume within the inner loading spans of the flexural specimens.)

Inelastic deformation changes the bending solution. However, because the stress within the inner span varies only along the loading direction, Eq. (13) can be rewritten as

$$k_B = \frac{1}{D \sigma_T^m} \int_0^{y^*} (\sigma(y_T))^m dy \quad (16)$$

where y^* is the distance from the neutral axis to the tensile face. Because the strain distribution is linear across the specimen, the neutral axis is at

$$y^* = \left(\frac{\epsilon_T}{\epsilon_T - \epsilon_C} \right) D \quad (17)$$

¹⁶The same result pertains to the ratio of mean strengths.

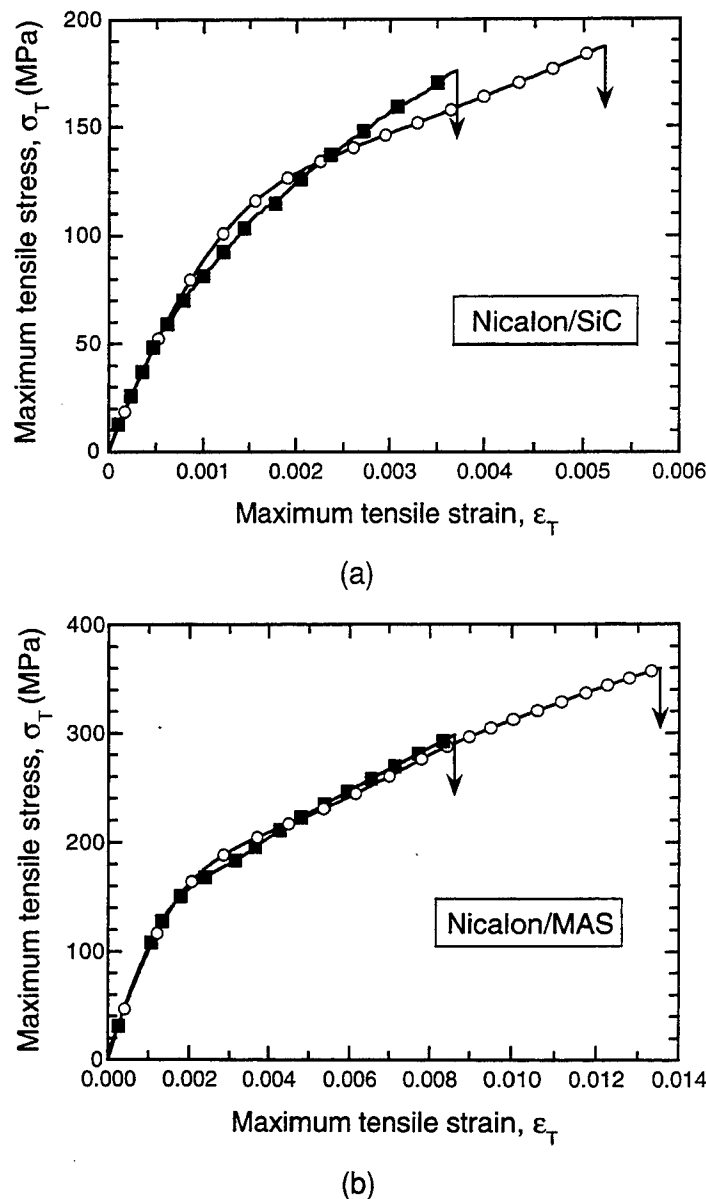


Fig. 7. Comparison of the true tensile stress-strain response obtained from (○) flexure tests with (■) those measured in uniaxial tension tests ((a) Nicalon/SiC and (b) Nicalon/MAS).

and the strain ϵ is related to position y through

$$y = \left(\frac{\epsilon}{\epsilon_T - \epsilon_C} \right) D \quad (18)$$

The value of k_b is obtained by combining Eqs. (16)–(18) with the measured tensile stress-strain response and numerically integrating the result, using various assumed values of m .

The calculated mean strength ratios (bending/tension) are plotted against m in Fig. 8. The strength ratios determined from the experiments are indicated by the horizontal dashed lines. The Weibull moduli, m , obtained from the intersections of the calculated and measured curves are ~ 24 for the MAS/Nicalon composite and ~ 28 for the SiC/Nicalon composite. These values are very much higher than those of the Nicalon fibers alone ($m_f \approx 3$ –5).

It is recognized that a larger number of tests is needed to ascertain m accurately, because of its strong sensitivity to the strength ratio. The degree of this sensitivity can be demonstrated by combining the higher bend strength (213 MPa) with

the lower tensile strength (169 MPa) for the SiC/Nicalon composite, yielding a strength ratio of ~ 1.26 and an m value of ~ 15 . Consequently, these values are to be considered as preliminary estimates only. Nevertheless, the experiments clearly demonstrate the volume dependence of the tensile strength and show that the Weibull moduli of the composites exceed those of the fibers by a substantial amount.

The computer simulations for strongly LLS materials yield qualitatively similar results.¹⁰ The predicted strength distributions for composites are in approximate accordance with the Weibull function, with a modulus that exceeds that of the fibers. For example, for a fiber Weibull modulus that is typical of Nicalon fibers (i.e., $m_f = 5$), the predicted composite modulus is in the range of ~ 70 –80 (depending weakly on composite volume). Despite the strongly LLS conditions used in the simulations, the predicted strength distribution is narrower than one inferred from the present experiments. Nevertheless, both predict a distribution that is considerably narrower than that of the fibers alone. The corresponding coefficients of variation, μ (taken as $\sim 1.2/m$), are $\sim 1.6\%$ and $\sim 5\%$ for the simulations

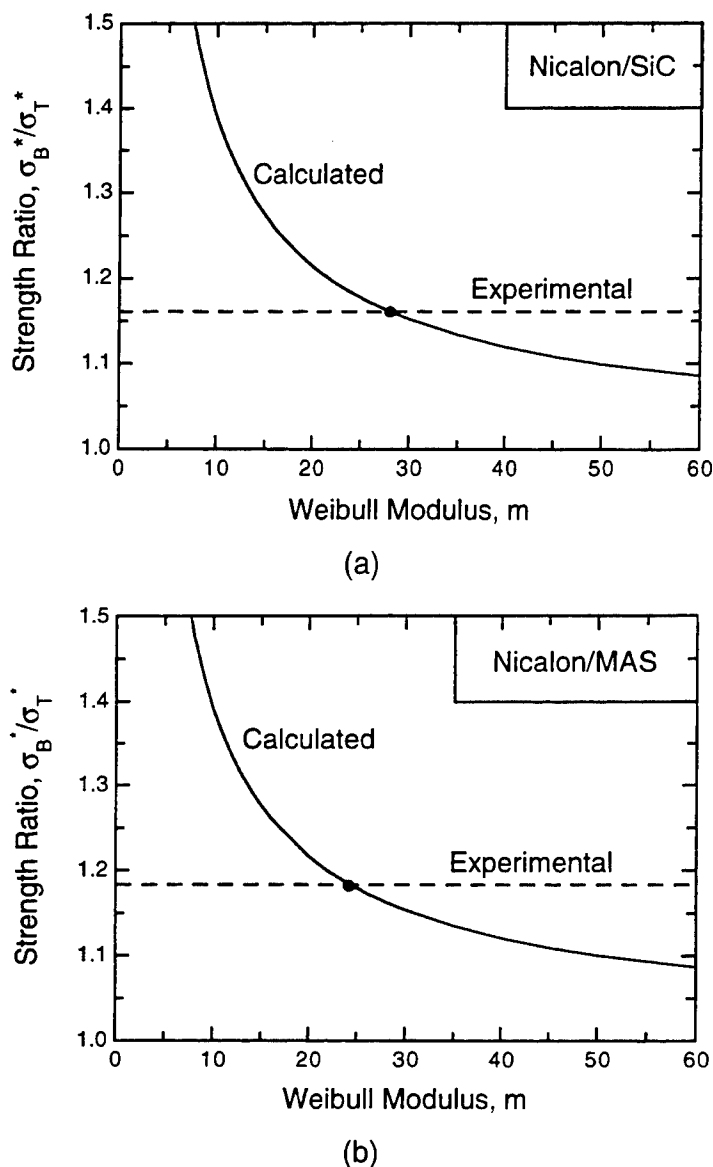


Fig. 8. Variation in the strength ratio (flexure/tension) as a function of the composite Weibull modulus ((a) Nicalon/SiC and (b) Nicalon/MAS). Dashed lines indicate the average values obtained from the experiments.

and the experiments on the composites, respectively, and $\sim 25\%$ for the fibers. It is surmised that the discrepancies between the simulations and the experiments may be attributed to other factors that cause strength variability, including variations in fiber content and experimental errors that are associated with the measurements. In addition, the measured strengths may be influenced by the unbridged cracks in the off-axis (90°) plies or fiber tows or by the presence of matrix porosity, resulting in additional stochastic effects. Such effects would not be expected to be significant in GLS materials.

V. Concluding Remarks

The present results have important implications regarding failure prediction in CMCs. First, the strengths that are measured on small laboratory coupons are expected to be somewhat higher than those that are representative of larger structures. However, the estimates of m that are obtained from the experiments suggest that this volume dependence is relatively small. For example, for $m = 25$, the volume must increase by a factor of >1000 to effect a strength reduction of 25%. Conversely,

regions of high stress concentration, such as those found ahead of notches or manufacturing flaws, are expected to sustain higher stress levels at failure because of the relatively small volumes that have been subjected to the stress elevation. Indeed, previous experiments on notched strength have indicated that the average net-section stress at failure can be comparable to or even greater than the unnotched strength, despite the presence of stress concentrations at the notch tip.¹⁶ The inference from this observation is that the strength exhibits a volume dependence, in accordance with weakest-link scaling laws. The effects of notches on the tensile strength of CMCs are addressed in further detail in a companion paper.¹¹

One of the key outstanding issues relates to the *degree* of local load transfer that occurs in these and other CMCs and its effect on strength variability. No quantitative information about such effects is obtained from the present experiments. Intuitively, the extent of fiber pullout (particularly in the Nicalon/MAS composite) suggests that the degree of local load transfer is probably small, although apparently it is sufficiently large to cause the reported strength variability. Conclusions regarding load sharing that are based solely on fracture surface observations alone therefore may be somewhat misleading.

Acknowledgment: The authors gratefully acknowledge Z. Suo for suggesting the procedure used to evaluate the stress distribution in bending.

References

- ¹A. G. Evans and F. W. Zok, "The Physics and Mechanics of Fibre-Reinforced Brittle Matrix Composites," *J. Mater. Sci.*, **29** [15] 3857-96 (1994).
- ²W. A. Curtin, "Theory of Mechanical Properties of Ceramic-Matrix Composites," *J. Am. Ceram. Soc.*, **74** [11] 2837-45 (1991).
- ³M. Y. He, A. G. Evans, and W. A. Curtin, "The Ultimate Tensile Strength of Metal and Ceramic Matrix Composites," *Acta Metall. Mater.*, **41**, 871-78 (1993).
- ⁴R. E. Bullock, "Strength Ratios of Composite Materials in Tension and Flexure," *J. Compos. Mater.*, **8**, 200-206 (1974).
- ⁵M. R. Wisnom, "The Effect of Specimen Size on the Bending Strength of Unidirectional Carbon Fiber-Epoxy," *Compos. Struct.*, **18** [1] 47-63 (1991).
- ⁶M. R. Wisnom, "Relationship Between Strength Variability and Size Effect in Unidirectional Carbon Fibre/Epoxy," *Composites*, **22** [1] 47-52 (1991).
- ⁷M. T. Kortschot and P. W. R. Beaumont, "Damage Mechanics of Composite Materials: II—A Damaged-Based Notch Strength Model," *Compos. Sci. Technol.*, **39**, 303-26 (1990).
- ⁸U. Ramamurty, F. W. Zok, F. A. Leckie, and H. Dève, "Strength Variability in Alumina Fiber-Reinforced Aluminum Matrix Composites," *Acta Mater.*, in press.
- ⁹S. J. Zhou and W. A. Curtin, "Failure of Fiber Composites: A Lattice Green Function Model," *Acta Metall. Mater.*, **43** [8] 3093-104 (1995).
- ¹⁰M. Iznabdeljalil and W. A. Curtin, "Size Effects on the Strength of Fiber-Reinforced Composite," *Int. J. Solids Struct.*, in press.
- ¹¹J. C. McNulty, G. M. Genin, F. W. Zok, J. W. Hutchinson, and A. G. Evans, "Notched Tensile Strength of Fiber-Reinforced Ceramic Composites: Effects of Nonlinear Deformation and Weakest-Link Statistics," to be submitted to *J. Am. Ceram. Soc.*
- ¹²P. S. Steif and A. Trojnecki, "Bend Strength versus Tensile Strength of Fiber-Reinforced Ceramics," *J. Am. Ceram. Soc.*, **77** [1] 221-29 (1994).
- ¹³T.-J. Chuang and Y.-W. Mai, "Flexural Behavior of Strain-Softening Solids," *Int. J. Solids Struct.*, **25** [12] 1427-43 (1989).
- ¹⁴V. Laws, "Derivation of the Tensile Stress-Strain Curve from Bending Data," *J. Mater. Sci.*, **16**, 1299-304 (1981).
- ¹⁵G. J. DeSalvo, "Theory and Structural Design Applications of Weibull Statistics," Westinghouse Electric Corporation, Astronuclear Laboratory, Pittsburgh, PA, Document WANL-TME-2688, May 1970.
- ¹⁶T. J. Mackin, T. E. Purcell, M. Y. He, and A. G. Evans, "Notch Sensitivity and Stress Redistribution in Three Ceramic-Matrix Composites," *J. Am. Ceram. Soc.*, **78**, 1719-28 (1995). □



NOTCH-SENSITIVITY OF FIBER-REINFORCED CERAMIC MATRIX COMPOSITES: EFFECTS OF INELASTIC STRAINING AND VOLUME-DEPENDENT STRENGTH

J. C. McNulty*, F. W. Zok*, G. M. Genin[‡], and A. G. Evans^{*‡}

*Materials Department
University of California
Santa Barbara, California 93106

[‡]Division of Applied Sciences
Harvard University
Cambridge, Massachusetts 02138

[#]Currently with Engineering Department
Cambridge University
Cambridge, England CB2 1PZ

Submitted to the *Journal of the American Ceramic Society*

October, 1997

ABSTRACT

The effects of circular holes and sharp notches on the tensile strength of two Nicalon-reinforced ceramic composites have been investigated. The influence of inelastic straining on the re-distribution of stress has been elucidated through measurements of the local strains in the regions of high stress concentration, coupled with finite element simulations of the test geometries, using a non-linear constitutive law appropriate to ceramic composites. The scale-dependence of strength has been inferred from tests performed on specimens of varying size. The utility of two failure models that incorporate both the inelastic straining and the scale-dependence have been assessed: one based on the point stress failure criterion and the other on weakest-link fracture statistics. Both approaches provide a reasonably consistent description of the experimental measurements. Some of the implications and limitations associated with the failure models are discussed.

1. INTRODUCTION

One of the attractive characteristics of fiber-reinforced ceramic matrix composites (CMCs) is their ability to undergo inelastic straining. The straining is effected through the formation of matrix cracks and the associated debonding and sliding along the fiber-matrix interfaces. A key role of the inelastic straining is to mitigate stress concentrations that occur around geometric discontinuities in CMC components, rendering them relatively notch-insensitive [1-8]. Measurements of strains (using Moiré interferometry [7]) and stresses (using SPATE [1]) in notched specimens have clearly demonstrated these effects. One of the main objectives of the present work is to develop and critically assess models of notched strength, taking into account this inelastic behavior.

Broadly, the process of fracture in notched geometries involves two steps. (i) Strain localization at the notch tip through failure of the fiber bundle and the formation of a macroscopic crack, with bridging occurring subsequently through pullout of the broken fibers. At the simplest level, this event is expected to occur when the maximum local stress reaches the fiber bundle strength. (ii) The localized band then propagates across the remaining section. The band may propagate stably under increasing applied stress, provided that the bridging tractions acting across the crack are sufficiently high. Among these two steps, that requiring the higher stress dictates the notched-strength. Modeling approaches for both processes have been developed: the former based on stress analysis [9, 10] and the latter on the mechanics of bridged cracks [11-20]. However, the utility of these models in predicting notched-strength of fiber-reinforced CMCs has not been verified.

Some insight into the local failure conditions can be gained from the extensive experience with polymer matrix composites (PMCs) [21-25]. A key result is that strain localization does *not* occur when the maximum stress at the tip of a notch reaches the unnotched strength (as suggested by a simple maximum stress approach), but rather at substantially higher stresses. The maximum stress approach also yields strength predictions that are independent of specimen size for self-similar geometries: a result inconsistent with experimental measurements [21, 23, 24], which reveal that the strength decreases with increasing notch size. One approach having utility in rationalizing the size effect comprises the point stress failure criterion [21-25]. Here, localization is postulated to occur when a critical stress (usually taken to be the unnotched tensile strength) is attained over a characteristic length, d , ahead of the notch. This approach is readily implemented in PMCs, through the use of well-established solutions for the stress fields in elastic, anisotropic bodies. Interestingly, the values of the characteristic length inferred from tensile tests on center-hole panels in a variety of PMCs fall in the rather narrow range, $d \sim 0.7\text{--}1.1$ mm [21, 23, 24].

An alternate approach to failure prediction is based on the premise that the composite strength is probabilistic and hence follows weakest-link fracture statistics. It has found utility in describing the strength of open-hole tensile panels of some PMCs, including the trend in strength with hole size [26]. This approach has not been pursued within the context of CMCs, in part because of the perception that their strength is scale independent. However, recent work on both a laminated glass-ceramic CMC and a woven CVI material [27] has indicated significant scale dependence. That is, comparisons of strengths and failure strains measured in uniaxial tension and four-point flexure have demonstrated effects of size and stress gradients on the failure condition, upon taking into account the non-linearities in the stress distributions present in the flexure specimens. These results have been interpreted in the context of weakest-link fracture statistics, with the failure probability taken to follow the Weibull function. The comparisons yield Weibull moduli in the range ~ 20 -30: much higher than the values associated with the fibers alone (~ 3 -5). An additional inference is that, during tensile straining, the load from a broken fiber is not shed globally to all other fibers in the plane of the break, but rather, preferentially to neighboring fibers. This local load sharing behavior gives rise to intrinsic stochastic behavior in the fiber bundle strength, including the scale dependence associated with weakest-link statistics. One of the goals of the present work is to assess the utility of both the probabilistic model and the point stress criterion for notched strength prediction of CMCs.

Application of either approach to CMCs must account for the inelastic straining that precedes localization. For this purpose, non-linear constitutive laws appropriate to CMCs are needed to compute stress distributions in notched geometries. Two such constitutive laws have been developed recently, both applicable to biaxial (in-plane) stressing. The first is based on continuum damage mechanics, with thermodynamic potentials derived from the micromechanics of matrix cracking and fiber-matrix sliding [10]. The second is more phenomenological and based upon an interpolation procedure

for evaluating the in-plane stresses at a prescribed state of biaxial strain, using experimental measurements of the uniaxial response [9]. The latter approach is utilized here. The constitutive law is validated through comparisons of measured and predicted strains around notches and subsequently used in failure prediction. Comparisons between the nature of the two constitutive laws and their predictive capabilities are presented elsewhere [28].

The post-localization response of composites has been addressed through crack bridging models within the context of fracture mechanics [11-20]. The material response within the band is characterized by a bridging traction law, with a characteristic strength, σ_0 , and a fracture energy, Γ . The effectiveness of the bridging is dictated by a bridging length scale, given by $\Gamma E / \sigma_0^2$, where E is the elastic modulus [17-19]. The shape of the traction law plays a secondary role. The notched-strength (corresponding to the stress at the point of instability of the localized band), is governed by the ratio, α , of the notch size, a_0 , to the characteristic length: $\alpha = a_0 / (\Gamma E / \sigma_0^2)$. As $\alpha \rightarrow 0$, the material exhibits notch-insensitive behavior, with a strength $\sigma / \sigma_0 = 1$, independent of notch shape. Conversely, as $\alpha \rightarrow \infty$, notch-sensitivity is obtained. The notch shape plays a key role in the latter regime: sharp notches giving rise to classic Griffith behavior and circular holes yielding a limiting strength of $\sigma / \sigma_0 = 1 / k_\sigma$, where k_σ is the stress concentration factor. Relatively comprehensive notched strength solutions for a wide range of notch sizes and shapes and bridging traction laws have been developed [13-20]. The bridging approach has found utility in the prediction of crack stability in whisker-reinforced ceramics [20], as well as fiber-reinforced titanium composites [19], but has not been applied to fiber-reinforced ceramics. The present work indicates that this approach may be applicable to the latter class of composites in the regime of long, sharp notches.

The main objective of this study is to develop mechanism-based models for the tensile strength of CMC components containing stress concentrating features, including

sharp notches and circular holes. This is accomplished through a series of experiments on two prototypical CMCs (a laminated cross-ply Nicalon/MAS and a plain weave Nicalon/SiC), identical to those used in the recent study comparing tensile and flexure properties [27]. *In-situ* observations of the notched specimens are used to establish the loading conditions at the onset of localization and hence identify an appropriate approach to strength prediction. In addition, simulations of the stress fields in the notched geometries are performed using a non-linear constitutive law. The computed stress fields are combined with several proposed failure criteria to predict notched-strength and the validity of the criteria assessed by comparison with the experimental measurements. An approach for predicting transitions in the strength-limiting process (initiation vs. propagation of the localization) is outlined and implemented for one of the two systems.

2. MATERIALS AND TESTING PROCEDURES

Two CMC systems were studied. The first[§] was a borosilicate-glass-doped magnesium aluminosilicate (MAS) glass-ceramic matrix reinforced with Nicalon[¥] fibers in a $[0/90]_{3s}$ (crossply) configuration (Figure 1(a)). The volume fraction of fibers, f , was ~40%. The MAS matrix was fully dense. The second[¶] was a SiC matrix, produced by chemical vapor infiltration, reinforced with ~32% of Nicalon fibers in a plain-weave configuration (Figure 1(b)). The SiC matrix contained porosity at two levels: large pores between the tows and fine-scale porosity within the tows. The volume fractions of the two were 3.0% and 5.6%, respectively (determined from quantitative metallography of polished cross-sections). Following specimen fabrication, a SiC overcoat was applied, also by CVI, resulting in the external surface shown in Figure 1(c). It is comprised of

[§] Produced by Corning, Inc., Corning, NY.

[¥] Ceramic grade, produced by Nippon Carbon, Tokyo, Japan.

[¶] Produced by DuPont Lanxide Composites, Newark, DE.

relatively coarse SiC nodules ($\sim 100\ \mu\text{m}$). It also exhibits undulations that reflect the morphology of the underlying fiber tows.

Uniaxial tension tests were performed on the Nicalon/SiC composite using standard (unnotched) dog-bone specimens in both $0^\circ/90^\circ$ and $\pm 45^\circ$ orientations, with a cross-section of $2.6\ \text{mm} \times 10.3\ \text{mm}$ and gauge length of $55\ \text{mm}$. Similar tests were performed on the Nicalon/MAS composite in the $0^\circ/90^\circ$ orientation using straight bars with a cross-section of $2.6\ \text{mm} \times 4.0\ \text{mm}$ and gauge length of $75\ \text{mm}$. The tensile strains were measured using a $10\ \text{mm}$ clip-on extensometer as well as with two strain gauges ($2\ \text{mm} \times 2\ \text{mm}$) oriented parallel and perpendicular to the fiber direction. The off-axis properties of the Nicalon/MAS were determined using the Iosipescu shear test. The specimen dimensions and test procedures were similar to those described in [29]. Strain gauges ($2\ \text{mm} \times 2\ \text{mm}$) were affixed to the Iosipescu samples at both $+45^\circ$ and -45° to the loading axis.

Tensile tests were also performed on a series of specimens containing circular through-thickness holes at the specimen center. For the Nicalon/SiC material, the hole diameter, $2a$, ranged from 2.3 to $7.6\ \text{mm}$, and the specimen width, $2w$, from 12.7 to $38.1\ \text{mm}$. In six of the specimens, the normalized hole size, a/w , was 0.2 ; in the remaining two, it was 0.067 . For the Nicalon/MAS material, $2a$ ranged from 2.5 to $5.1\ \text{mm}$, with $a/w=0.2$ for all specimens. A parallel set of experiments was conducted on double-edge notched tensile specimens of the Nicalon/MAS. The notch size, $2a$, ranged from 2.5 to $7.6\ \text{mm}$, with $a/w=0.2$. The notch width was $0.3\ \text{mm}$ and the notch tip radius was $\approx 0.15\ \text{mm}$.

The center-hole Nicalon/MAS specimens were instrumented with strain gauges, shown schematically in Figure 2(a). Small ($1\ \text{mm} \times 1\ \text{mm}$) gauges were placed at three locations around the hole perimeter: (i) along the equatorial plane at the location of maximum strain (gauge #1 in Figure 2(a)); (ii) at 45° to the equatorial plane (#2), and (iii) in the polar region, at 90° to the equatorial plane (#3). Each of these was oriented to

measure the normal strain in the tangential direction. In addition, small gauges were placed along the equatorial plane at the mid-point between the hole edge and specimen edge (#4), and a location remote from the hole (#5). Finally, a larger gauge (2 mm x 3 mm) was placed at a remote location (#6), for comparison with the corresponding small gauge. The Nicalon/SiC specimens were instrumented with small gauges at locations #1 and #4 (along the equatorial plane) and two remote gauges, one small (#5) and one large (#6). Each of the small gauges was placed directly over a longitudinal fiber tow. The gauge configuration for the double-edge notched Nicalon/MAS specimens is shown in Figure 2(b). Four small gauges were placed along the reduced section: at each notch tip (#1 and 2), at the quarter section (#3), and at the midsection (#4). One purpose of the gauges located at the hole or notch edge was to ascertain the local (peak) strain at the onset of composite failure. Moreover, comparisons of all strain measurements with the values predicted by the finite element simulations were used to critically assess the predictive capability of the non-linear constitutive law (described below).

Beveled fiberglass tabs were bonded to the specimen ends with a cyano-acrylate adhesive. The tests were conducted in a servo-hydraulic testing machine with hydraulic wedge grips, at a displacement rate of $\sim 0.002 \mu\text{m}/\text{min}$. The evolution of damage around the holes was monitored continuously using a stereo microscope attached to a CCD camera and video recorder. Following fracture, the specimens were examined in a scanning electron microscope (SEM).

3. MEASUREMENTS AND OBSERVATIONS

The unnotched stress-strain behavior of the two composites is shown in Figure 3. While both materials develop inelastic strain and exhibit similar stress-strain characteristics, their fracture properties are markedly different. Notably, the tensile

strength and failure strain of the Nicalon/MAS in the $0^\circ/90^\circ$ orientation are roughly twice the corresponding values for the Nicalon/SiC. These differences are likely due to a degradation of the fibers upon weaving of the fiber cloths and upon composite processing.

The trends in strength with notch size for both circular holes and sharp notches are plotted in Figure 4. The results are presented in terms of the net section stresses, σ_N , as well as the stresses normalized by the respective unnotched strength, σ_0 . Also shown in the figure are the expected results for two limiting cases: (i) completely notch-insensitive ($\sigma_N/\sigma_0 = 1$), and (ii) strongly notch-sensitive ($\sigma_N/\sigma_0 = 1/k_\sigma$). For a circular hole with $a/w = 0.2$, $k_\sigma = 2.5$ [30]. Despite the differences in the unnotched properties, the two materials exhibit similar notch strength characteristics. For both, the strength decreases gradually with increasing hole size, by $\sim 25\text{-}30\%$ over the entire range of notch sizes. Similar reductions were obtained for the double-edge notched Nicalon/MAS specimens. For the Nicalon/SiC, the strength also decreases with increasing specimen width. These trends suggest that the strengths of these materials are not deterministic and exhibit a volume-dependence. Similar conclusions have been reached previously, based on comparisons of the tensile and flexural strengths of the same two CMCs [27].

The variations in the local strains on a center-hole Nicalon/MAS specimen are plotted in Figure 5(a). As expected, the tensile strain develops more rapidly at the edge of the hole than at locations remote from the hole. The strain concentration obtained from the gauge placed at the hole edge (#1) was consistent with the value predicted from an elastic calculation: $\bar{k}_\epsilon = \bar{\epsilon}_1/\epsilon_\infty \approx 1.6$ where \bar{k}_ϵ is the strain concentration averaged over the gauge area, $\bar{\epsilon}_1$ is the average local axial strain and ϵ_∞ is the remote tensile strain (see [30] for equations). Moreover, both the small and large remote gauges were in excellent agreement with the extensometer output in the unnotched test (compare with Figure 3(b)).

There are two additional significant features. (i) Direct optical observations indicate that the load maximum is coincident with the localization of deformation, as manifested by the formation of a large crack at the edge of the hole. A sequence of micrographs showing the development of such a crack *at* the load maximum are presented in Figure 6. These cracks were observed to propagate stably for a brief period, subject to a decreasing load, prior to catastrophic fracture. The increased crack opening is associated with fiber failure, subject to substantial bridging by the broken fibers. The propagation of the localized band coincides with a rapid increase in the strains measured on the gauges situated along the equatorial plane. Clearly, the gauge measurements following the load maximum are associated with the local crack opening displacements and are not representative of the true local strains. (ii) The peak strains at the hole edge were substantially higher than the unnotched failure strain ($\approx 1.6\%$ compared with $\approx 0.96\%$). This result corroborates the hypothesis that the strength is not deterministic and may follow weakest-link scaling laws. Similar differences in failure strains were reported previously for tests performed in flexure and tension, with the flexural failure strains reaching $\approx 1.3\text{--}1.4\%$ [27].

Analogous results were obtained for the Nicalon/MAS specimens with double-edge notches (Figure 5(c)). Notably, the peak strain within the gauge at the notch tip (at the load maximum) was similar to that obtained for holes. In addition, the load maximum was associated with the development of a large macroscopic crack, which again propagated stably for a short period under decreasing load.

An implication of the strain measurements and the *in-situ* observations is that the notched strength is dictated by the *onset* of strain localization, with no additional load bearing capacity obtained upon growth of the localized band. This conclusion is vital to the development of an appropriate failure criterion, as described in the Introduction and detailed further in Section 5. Notwithstanding these observations, there remains the

possibility that the strength may be dictated by the *propagation* of the localized band for larger notch sizes. Calculations that address this issue are presented in Section 6.4.

The strain gauge measurements for a typical notched Nicalon/SiC specimen is presented in Figure 5(a). In this case, the remote strains measured with the small gauges (each mounted on a single longitudinal tow) were considerably lower than the strains obtained from the extensometer in the unnotched tension test (by ~20-60%). The discrepancy is surmised to result from bending of the longitudinal tows upon tensile loading. Such bending induces a compressive strain on the external surface of the tows. Finite element analyses using a cell model representative of the plain-weave fiber architecture and matrix porosity affirm that such bending occurs and that the surface strains on the longitudinal tows are lower than the applied strains [31]. There was also considerable scatter in the strains obtained with the small gauges: a consequence of the inhomogeneity of the underlying microstructure, particularly the large-scale porosity (Figure 1(b)). The surface roughness associated with the SiC nodules (Figure 1(c)) may also contribute to this scatter. Once cracks formed in the SiC overcoat, the local strains exhibited either positive or negative "bursts", depending on the crack locations. When they occurred directly beneath the gauges, the strains increased; when they occurred adjacent to the gauges, the strains decreased. The output from the large gauges was in somewhat better agreement with the extensometer output, though there was still considerable scatter and pronounced bursts upon matrix cracking. In light of these problems, the strain gauge data are not deemed to be representative of the true bulk strains in this material; consequently, no further analysis was performed with these data.

The *in-situ* observations on the Nicalon/SiC did not reveal the development of a localized band prior to fracture. Moreover, there was no stable post-maximum region of loading. The inference is that fracture occurs catastrophically at the *onset* of localization. This result, in combination with the low pullout lengths (described below), indicate that

bridging within the localized band is ineffective in stabilizing the band. Indeed, the bridging in this CMC is even less effective than in the Nicalon/MAS system.

Prior to failure, both materials exhibited multiple matrix cracking along the entire specimen length. For the Nicalon/SiC, the density of cracks was relatively low ($\sim 1\text{-}2/\text{mm}$). For the Nicalon/MAS, it was considerably higher (~ 20 to $30/\text{mm}$). The notched Nicalon/MAS specimens also exhibited shear bands within the outer ply. These bands had initiated at an angle of $\sim 45^\circ$ to the equatorial plane and were $\sim 1\text{-}2$ mm in length (Figure 7(c)). Such bands were not seen in the bulk (based on fracture surface examinations) and are believed to be a surface phenomenon only. Moreover, there was no evidence of splitting between the plies or cloths in either material, in contrast to earlier observations on a Nicalon/CAS composite [6].

The fracture surfaces of both materials were planar and oriented perpendicular to the loading direction. The location of the fracture planes with respect to the holes and notches was within $\sim 30^\circ$ of the equatorial plane. In the Nicalon/SiC (Figure 7(a)), the fracture surfaces exhibited minimal fiber pullout (≤ 0.1 mm), and the fibers tended to pullout as bundles rather than individual filaments. The fiber fracture locations within the bundles appeared to be highly correlated, consistent with results obtained in unnotched tension and flexure [27]. In the Nicalon/MAS (Figure 7(b)), fiber pullout was more extensive (≈ 0.3 to 0.4 mm), and the correlations in the fiber failure locations appeared to be weak.

4. SIMULATIONS OF STRAIN DISTRIBUTIONS

The effects of inelastic deformation on the stress and strain distributions around the notches and holes was assessed through finite element simulations of the specimen geometries used in the experiments. The calculations are based on the non-linear constitutive law developed by Genin and Hutchinson [9]. The law implicitly accounts

for the inelastic strains associated with matrix cracking and interface debonding and sliding. It was calibrated for the two materials using the unnotched tensile and shear data. The response in other orientations, subject to arbitrary biaxial loads, is predicted by the model [9]. The constitutive law was implemented in a commercial finite element code (ABAQUS). The outputs from the analysis are the distributions of the in-plane stresses and strains throughout the notched specimens. To simulate loadings for which the local stresses exceed the critical values obtained in the unnotched tensile tests, the stress-strain data used for the calibration were extrapolated linearly beyond the failure point, with a tangent modulus equal to that at failure.

Comparisons of the simulated and measured strains on the Nicalon/MAS specimens with center holes are shown in Figure 8. (Such comparisons were not made for the Nicalon/SiC specimens because of the irregularities in the surface strain measurements.) Excellent agreement was obtained for all strain gauge locations around the hole (#1-4); the only exception was the deviation in the gauge at the 45° location at high strain levels (#2, Figure 8(b)), due to the proximity of the shear bands on the specimen surface and the associated relaxation of the strains in the surrounding regions. The strong correlations between the measured and predicted strains provide a validation of the proposed constitutive law and justify its use for failure prediction.

5. FAILURE PREDICTION

The stress distributions calculated using the non-linear constitutive law have been used to predict the onset of failure, subject to three failure criteria.

(i) At the simplest level, failure is assumed to occur when the maximum tensile stress (at the notch tip) reaches a critical value, equal to the unnotched ultimate tensile strength (UTS). The predicted trends in notched strength are shown in Figure 9 as the solid lines labeled $d = 0$. These predictions lie above those based on the elastic

calculations, by $\sim 25\%$ for the Nicalon/SiC and $\sim 50\text{-}80\%$ for the Nicalon/MAS, but well below the measured values. More importantly, the strength is predicted to be independent of hole diameter for fixed a/w , because of the absence of a length scale in the failure criterion. This, too, is inconsistent with the experimental data.

(ii) To account for the size effect, the point stress criterion has been utilized. As noted earlier, this criterion is based on the attainment of a critical stress over a characteristic distance, d , from the edge of the hole or notch. The critical stress was taken to be the unnotched UTS and the characteristic distance was inferred from comparisons between the measured strengths and those predicted using the non-linear constitutive law, assuming a range of values for d . (The limiting case of $d = 0$ corresponds to a deterministic strength, equal to the unnotched UTS, as described in the preceding paragraph.) The utility of the approach was further assessed by comparing the values of the characteristic distance obtained from different test geometries. The comparisons are shown in Figures 9. For the Nicalon/SiC material, the predicted trends in the strength with both hole diameter (for fixed a/w) and panel width (for fixed hole size) yield the same characteristic distance: $d \approx 0.75$ mm. For the Nicalon/MAS, the trends in strength with both hole diameter and notch length (for fixed a/w) yield similar values: $d \approx 0.5\text{-}0.75$ mm.

(iii) The third approach to failure prediction is probabilistic. It assumes that the composite strength follows weakest-link scaling laws such that the survival probability is given by the product of the survival probabilities of the individual volume elements that comprise the body. The strength distribution of the volume elements was assumed to follow the Weibull function with a reference strength, S_0 , a reference volume, V_0 , and a dispersion index, m . The failure probabilities of the notched specimens were calculated on the basis of the stress component acting along the fiber direction. Calculations were performed for a range of values of m (10-40), with the corresponding values of S_0 selected to be consistent with the average unnotched UTS (Table I).

The calculated mean strengths are compared with the experimental measurements for the two materials in Figure 10. For the Nicalon/SiC, the calculations based on $m \approx 15 \pm 5$ correlate best with the experimental data. The inferred value of m is somewhat lower than the one obtained upon comparing flexural to tensile strengths (~ 28). The discrepancy may be attributed to the small number of tests and hence the uncertainty in m . A value of ~ 25 -40 correlates best for the Nicalon/MAS with the center holes (Figure 10(c)). This range is consistent with the value obtained from the flexure and tension test results ($m \approx 24$). The inferred value from the double-edge notched specimens is considerably lower (Figure 10(d)). However, the applicability of the probabilistic model to the latter specimen geometry is considered to be suspect, because of the large stress gradients present at the notch tip, as described below.

6. DISCUSSION

6.1 General Remarks

Both the Nicalon/SiC and Nicalon/MAS materials exhibit a modest degree of notch-sensitivity. This behavior is attributable to both the redistribution of stress due to inelastic straining and the volume-dependence of strength. The effects of size on strength can be predicted either through the use of a characteristic distance in conjunction with a deterministic strength, or through the use of weakest-link statistics. It is emphasized that the trends cannot be rationalized solely on the basis of the stress redistribution due to inelastic straining subject to a deterministic strength.

Previous studies of the notched strength of a Nicalon/CAS composite had focused on the contribution from inelastic straining alone [1]. Stress measurements made around notches at progressively increasing applied stress showed a reduction in the stress concentration following non-linear straining. A significant level of stress concentration (~ 2.1) was present at the point of fracture, yet the notched strength

remained essentially at the same level as the unnotched strength. This seeming discrepancy can be rationalized on the basis of a volume-dependent strength, as illustrated through the present work.

6.2 Point Stress Failure Criterion

The physical significance of the characteristic distance in the point stress failure criterion can be rationalized on the basis of the size of the critical flaw at which failure initiates. In monolithic ceramics, the strength-limiting flaws are typically $\sim 1\text{-}10\text{ }\mu\text{m}$ in diameter, as inferred from their tensile strength and fracture toughness. The consequence is an extreme sensitivity to stress concentrations. The corresponding flaws in CMCs are much larger because of the nature of the damage that leads to failure. Upon straining, flaws within the fibers are initially activated in a stable manner, leading to progressive fiber breakage. Moreover, in LLS materials, the fiber failure events are correlated because of the stress concentrations produced by the breaks. Catastrophic failure occurs when a cluster of broken fibers reaches a critical size. This cluster can be viewed as the critical flaw. Monte Carlo simulations of fiber damage in LLS composites indicate that the length of the flaw is of the order $\sqrt{n_c} \lambda$, where n_c is the number of breaks in the critical cluster and λ is the fiber spacing ($\lambda \approx 25\text{ }\mu\text{m}$ in the Nicalon-reinforced CMCs). For a fiber Weibull modulus of 5, the critical cluster comprises ~ 60 fibers [32], such that the flaw size is $\sqrt{n_c} \lambda \approx 200\text{ }\mu\text{m}$. It is surmised that the characteristic distance inferred in the present study is a multiple of the critical cluster size: the ratio being $d/\sqrt{n_c} \lambda \approx 3$. A related approach has been used to rationalize cleavage fracture of steels in the presence of notches. Specifically, fracture is predicted to occur when the tensile stress ahead of the notch exceeds the fracture stress of the cementite particles over a distance of ~ 2 times the particle spacing [33].

The characteristic distance in the point stress criterion for both CMCs used in this study is about 0.5-0.75 mm. A concurrent study on a porous all-oxide CMC has yielded

a similar value ($d = 0.7$ mm) [34]. Moreover, previous studies on fiber-reinforced polymer matrix composites (PMCs), including glass/epoxy [21, 23], glass/polyester [23], and graphite/epoxy [24], have also yielded values in the same range, from 0.7 to 1.1 mm. In light of the diversity of these composites, the strong similarities in the values of d are striking. The only apparent microstructural feature common to all systems is the fiber diameter, which spans the rather narrow range of ~ 8 to 15 μm . Consequently, the characteristic distance represents roughly the same number of fibers in each system, consistent with the assertion that the distance is dictated by the critical cluster of fiber breaks.

6.3 Assessment of Weakest-Link Scaling

The concept of a critical cluster of fiber breaks has implications in the assessment of the probabilistic failure model. In implementing the model, the structure or component is discretized into an array of representative volume elements and the stresses in these elements are used to determine the overall failure probability. Weakest link scaling laws are violated when the critical flaw size becomes comparable to the dimensions of the structure. The relevant dimension in the notched tensile specimens is the notch radius.

For the open-hole specimens, the key dimension is the hole radius, which ranges from ~ 1 to 4 mm. In this case, the probabilistic failure model is expected to be valid, particularly at the high end of this size range. By contrast, in the double-edge notched specimens, the relevant dimension is the notch root radius (150 μm), which is comparable to the critical flaw size ($\sqrt{n_c} \lambda \approx 200$ μm). Consequently, the weakest link scaling model cannot be used in accordance with its usual formulation. An alternative probabilistic methodology would be needed to address the notch behavior, consistent with a considerably enhanced notch tolerance.

6.4 Transitions in the Strength-Limiting Process

The onset of localization controls the tensile strength of the Nicalon-reinforced CMCs for both the center-hole and double-edge notched geometries for notch sizes $2a \leq 10$ mm. Recognizing that this range of notch sizes is rather small, it is suggested that a transition to propagation-controlled fracture might occur at larger notch sizes. To assess this hypothesis, the stresses associated with each process were calculated over a broad range of notch sizes for both geometries, with $a/w = 0.2$. The results are plotted on Figure 12. The calculations were performed for the Nicalon/MAS, in part because of the expectation that bridging plays a greater role in this system than in the Nicalon/SiC.

The stress required for *initiation* of the localized band was calculated using the point stress failure criterion, with the characteristic distance, d , assumed to range from 0 to 0.75 mm. As $a \rightarrow \infty$, all of the curves for the center-hole specimen asymptotically converge to $1/k_p$ where k_p is the stress concentration evaluated at a net section stress equal to the unnotched UTS. (Naturally, the limiting stress is substantially higher than the elastic prediction, $1/k_\sigma$, because of the contribution associated with inelastic straining). In contrast, for sharp notches, the strength decreases monotonically with increasing notch size and the curves for different values of d never converge.

The stress required for *propagation* of the band was calculated using a standard crack bridging model, implemented in the ABAQUS finite element code. The zone of localization was modeled as a sheet of springs connecting two elastic blocks, with an exponentially-softening traction law used to describe the response of the springs. This traction law was selected because it most closely approximates the pullout behavior of Nicalon/MAS once all of the fibers have failed [35]. The form of the pullout curve is a manifestation of the exponential distribution of pullout lengths coupled with a constant sliding stress. The bridging parameters were obtained from a fiber bundle pullout test, performed on a deeply-notched tensile bar of the Nicalon/MAS composite, as described

in [35]. The values used in the calculations are $\sigma_o = 100$ MPa, $\Gamma = 40$ kJ/m², and $E = 130$ GPa. Similar pullout characteristics have been reported independently for a comparable laminated CMC [36].

The results are presented in Figure 12. For the center-hole geometry (Figure 12(a)), the limiting stress for the onset of localization (corresponding to $d = 0.0$ mm) is nearly twice that required for propagation, and the difference between the two increases with increasing hole diameter. A key conclusion is that the initiation event is expected to control the notched strength of the center-hole specimens *for all hole sizes*. For sharp notches (Figure 12(b)), the stress required for the onset of localization drops rapidly with increasing notch size. As in the case of circular holes, the stress required for propagation decreases only slightly with increasing notch size. Consequently, a transition from initiation-controlled to propagation-controlled fracture is predicted to occur, at a critical notch size that depends rather sensitively on the characteristic length associated with initiation. For $d = 0.5$ mm, the transition occurs for a notch size of ~ 80 mm: an order of magnitude larger than the notch sizes used in the present experiments. The transition shifts rapidly to larger values of notch size as the characteristic length increases.

For the Nicalon/SiC, the strength of center-hole specimens is also dictated by the onset of localization. Moreover, for sharply-notched geometries, the transition to propagation-control would occur for even larger notch lengths, outside the range relevant to realistic CMC components.

7. SUMMARY

The Nicalon-reinforced CMCs exhibit modest notch-sensitivity. Two factors govern this behavior: (i) stress redistribution arising from inelastic straining, mitigating

stress concentrations at the notch tip, and (ii) the volume-dependence of strength, manifested in higher failure stresses and strains at the notch tip.

The onset of localization, marked by the formation of a bridged macroscopic crack, coincides with the load maximum. The implication is that the onset of localization is the critical event that governs strength (at least over the range of notch sizes and shapes investigated here). Calculations for both initiation and propagation of the localized band indicate that fracture of the center-hole geometries is expected to be initiation-controlled for all hole sizes; in contrast, a transition to propagation-controlled fracture is predicted for the sharply-notched geometries, at notch sizes of several 10's or 100's of mm.

The point stress criterion in combination with the computed stress distribution (using the non-linear constitutive law) provides an accurate description of failure initiation. The inferred characteristic length (~ 0.50 to 0.75 mm) is consistent with the experimental data for all specimen sizes and notch shapes, and appears to be the same for the two Nicalon-reinforced CMCs as well as other polymer- and ceramic-matrix systems. This approach to failure prediction has the advantage of being relatively easy to implement and calibrate. The characteristic length is believed to be associated with the critical cluster of fiber breaks needed to initiate fiber bundle failure.

The probabilistic failure model is consistent with the experimental data on specimens containing circular holes. The inferred Weibull moduli fall in the range ~ 15 -40, comparable to values obtained from comparisons of tensile and flexural strengths [27]. However, implementation of the model is more computationally-intensive, requiring calculation of the full stress field in the structure along with numerical integration over all volume elements to obtain the failure probability. Moreover, in geometries containing sharp notches, the assumptions underlying weakest-link scaling laws appear to be violated, because of the relatively large size of the fundamental volume element. This causes the diminution in strength with notch

sharpness to be much less than that expected from standard weakest link approaches. The direct consequence is robust damage tolerance relative to monolithic ceramics.

ACKNOWLEDGMENTS

Funding for this work was provided by the ARPA University Research Initiative Program at UCSB under ONR contract No. N00014-92-J-1808. The authors acknowledge the assistance of X.-Y. Gong with some of the simulations.

REFERENCES

1. T.J. Mackin, T.E. Purcell, M.Y. He, and A.G. Evans, "Notch sensitivity and stress redistribution in three ceramic-matrix composites," *J. Am. Ceram. Soc.*, **78** [7] 1719-28 (1995).
2. S. Mall, D.E. Bullock, and J.J. Pernot, "Tensile fracture behaviour of fibre-reinforced ceramic-matrix composite with hole," *Composites*, **25** [3] 237-242 (1994).
3. S. Mall, W.R. Moschelle, and J.J. Pernot, "Fatigue behavior of a fiber-reinforced ceramic-matrix composite with a circular hole," *Comp. Sci. and Tech.*, **49**, 173-182 (1993).
4. S. Mall and W.A. Weidenar, "Tension-compression fatigue behaviour of fibre-reinforced ceramic matrix composite with hole," *Composites*, **26**, 631-36 (1995).
5. H.R. Shercliff, P.W.R. Beaumont, and G. Vekinis, "Direct observation of the fracture of CAS-glass/SiC composites. Part I - Delamination," *J. Mat. Sci.*, **29** [14] 3643-52 (1994).
6. H.R. Shercliff, P.W.R. Beaumont, and G. Vekinis, "Direct observation of the fracture of CAS-glass/SiC composites. Part II - Notched tension," *J. Mat. Sci.*, **29** [16] 4184-90 (1994).
7. T.J. Mackin, K.E. Perry, J.S. Epstein, C. Cady, and A.G. Evans, "Strain fields and damage around notches in ceramic-matrix composites," *J. Am. Ceram. Soc.*, **79** [1] 65-73 (1996).
8. F.E. Heredia, S.M. Spearing, T.J. Mackin, M.Y. He, A.G. Evans, P. Mosher, and P. Bronsted, "Notch effects in carbon matrix composites," *J. Am. Ceram. Soc.*, **77** [11] 2817-27 (1994).
9. G.M. Genin and J.W. Hutchinson, "Composite laminates in plane stress: constitutive modeling and stress redistribution due to matrix cracking," *J. Am. Ceram. Soc.*, **80** [5] 1245-55 (1997).

10. F. Hild, A. Burr, and F.A. Leckie, "Fiber breakage and fiber pull-out of fiber-reinforced ceramic-matrix composites," *Euro. J. Mech. A/Solids*, **13** [6] 731-749 (1994).
11. M.E. Waddoups, J.R. Eisenmann, and B.E. Kaminski, "Macroscopic fracture mechanics of advanced composite materials," *J. Comp. Mat.*, **5**, 446-54 (1971).
12. W.P. Keith and K.T. Kedward, "Notched strength of ceramic-matrix composites," to be published in *Comp. Sci. and Tech.*, **57** (1997).
13. D.B. Marshall and B.N. Cox, "Tensile fracture of brittle matrix composites: influence of fiber strength," *Acta Metall. mater.*, **35** [11] 2607-19 (1987).
14. B.N. Cox and C.S. Lo, "Load ratio, notch, and scale effects for bridged cracks in fibrous composites," *Acta Metall. mater.*, **40** [1] 69-80 (1992).
15. B.N. Cox and C.S. Lo, "Simple approximations for bridged cracks in fibrous composites," *Acta Metall. mater.*, **40** [7] 1487-96 (1992).
16. B. Budiansky and Y.L. Cui, "On the tensile strength of a fiber-reinforced ceramic composite containing a crack-like flaw," *J. Mech. Phys. Solids*, **42** [1] 1-19 (1994).
17. Z. Suo, S. Ho, and X. Gong, "Notch ductile-to-brittle transition due to localized inelastic band," *J. Eng. Mat. and Tech.*, **115**, 319-26 (1993).
18. G. Bao and Z. Suo, "Remarks on crack-bridging concepts," *Appl. Mech. Rev.*, **24**, 355-66 (1992).
19. S.J. Connell, F.W. Zok, Z.Z. Du, and Z. Suo, "On the tensile properties of a fiber reinforced titanium matrix composite - II. Influence of notches and holes," *Acta Metall. mater.*, **42** [10] 3451-61 (1994).
20. P.F. Becher, "Microstructural design of toughened ceramics," *J. Am. Ceram. Soc.*, **74** [2] 255-69 (1991).
21. J.M. Whitney and R.J. Nuismer, "Stress fracture criteria for laminated composites containing stress concentrations," *J. Comp. Mat.*, **8**, 252-65 (1974).
22. J. Auerbuch and M.S. Madhukar, "Notched strength of composite laminates: predictions and experiments - A Review," *J. Rein. Plas. and Comp.*, **4**, 3-159 (1985).

23. J-K. Kim, D-S. Kim, and N. Takeda, "Notched strength and fracture criterion in fabric composite plates containing a circular hole," *J. Comp. Mat.*, **29** [7] 982-998 (1995).
24. S.C. Tan, "Effective stress fracture models for unnotched and notched multidirectional laminates," *J. Comp. Mat.*, **22**, 322-40 (1988).
25. H.G. Kim, W. Hwang, and K.S. Han, "Notched strength of woven laminate composites containing circular holes," *Key Engineering Materials*, **51-52**, 125-30 (1990).
26. M.T. Kortschot and P.W.R. Beaumont, "Damage mechanics of composite materials. II. A damaged-based notched strength model," *Comp. Sci. and Tech.*, **39** [4] 303-26 (1990).
27. J.C. McNulty and F.W. Zok, "Application of weakest-link fracture statistics to fiber-reinforced ceramic matrix composites," *J. Am. Ceram. Soc.*, **80** [6] 1327-32 (1997).
28. X-Y. Gong, J.C. McNulty, F.W. Zok, and F.A. Leckie, "Strength-limited design of ceramic composite panels containing open holes," in preparation.
29. D.E. Walrath and D.F. Adams, "Current status of the Iosipescu shear test method," *J. Comp. Mat.*, **21** [6] 494-507 (1987).
30. G.N. Savin, Stress Concentration Around Holes, pp. 105-13, International Series of Monographs in Aeronautics and Astronautics, Pergamon Press, London (1961).
31. J.L. Kuhn and P.G. Charalambides, "Elastic response of porous matrix plain weave fabric composites: Part II - Results," submitted to *J. Am. Ceram. Soc.*, (1996).
32. M. Ibnabdeljalil and W.A. Curtin, "Strength and Reliability of Fiber-reinforced Composites: Localized Load-sharing and Associated Size Effects," *Int. J. Solids Struct.* **34**, 2649-2668 (1997).
33. R.O. Ritchie, R.F. Knott and J.R. Rice, "On the Relationship Between Critical Tensile Stress and Fracture Toughness in Mild Steel," *J. Mech. Phys. Solids*, **21**, 395-410 (1973).

34. J.A. Heathcote, F.W. Zok, X-Y. Gong, U. Ramamurty, and F.A. Leckie, "Notched and unnotched mechanical behavior of an all-oxide composite," in preparation.
35. J.C. McNulty and F. W. Zok, "Monotonic and cyclic strength of Nicalon-reinforced ceramic composites", in preparation.
36. P. Brenet, F. Conchin, G. Fantozzi, P. Reynaud and C. Tallaron, "Direct measurement of crack bridging tractions: a new approach to the fracture of ceramic composites," *Comp. Sci. Tech.*, **56**, 817-23 (1996).

Table 1 Summary of the statistical parameters used in the probabilistic model.

Material	Shape Parameter, m	Reference Strength, S_o (MPa) for $V_o=1\text{m}^3$
Nicalon/SiC	10	94
	15	115
	20	128
Nicalon/MAS	20	224
	26	241
	40	264

FIGURES

- Figure 1 Microstructures of (a) Nicalon/MAS and (b) Nicalon/SiC, and (c) the external surface of the Nicalon/SiC.
- Figure 2 Schematic of the strain gauge configurations for specimens with (a) holes, and (b) notches. The lines within the gauges indicate the direction of strain measurement.
- Figure 3 Unnotched tensile and shear behavior of (a) Nicalon/SiC and (b) Nicalon/MAS.
- Figure 4 (a) Effects of notch size, $2a$, on strength. (b) Normalized strength for center-hole specimens with $a/w=0.2$.
- Figure 5 Strain distributions for (a) center-hole Nicalon/MAS ($a/w = 0.2$, $2w = 12.7$ mm), (b) double-edge notched Nicalon/MAS ($a/w=0.2$, $2w=38.1$ mm) and (c) center-hole Nicalon/SiC ($a/w = 0.2$, $2w = 25.4$ mm). The solid circles in (a) and (b) indicate the load maximum and attendant formation of a large macroscopic crack.
- Figure 6 Optical micrographs of a center-hole Nicalon/MAS specimen, illustrating the formation of a macroscopic crack at remote stresses of (a) 208 MPa, (b) 209 MPa, and (c) 199 MPa (beyond the load maximum) ($a/w = 0.2$, $2w = 12.7$ mm).
- Figure 7 SEM micrographs of the fracture surfaces of (a) Nicalon/SiC ($a/w = 0.2$, $2w = 25.4$ mm) and (b) Nicalon/MAS ($a/w = 0.2$, $2w = 12.7$ mm). (c) Shear cracking in outer ply of Nicalon/MAS.
- Figure 8 Comparison of calculated stress-strain distributions with experimental data for center-hole Nicalon/MAS specimens: (a) $a/w = 0.2$, $2w = 12.7$ mm, and (b) $a/w = 0.2$, $2w = 25.4$ mm. The solid lines are the predictions.
- Figure 9 Comparisons of predicted strengths with experimental data, using the point stress failure criterion: (a, b) Nicalon/SiC and (c, d) Nicalon/MAS. The solid lines are the predictions.

Figure 10 Comparisons of predicted strengths with experimental data, using the probabilistic model: (a, b) Nicalon/SiC and (c, d) Nicalon/MAS. The solid lines are the predictions.

Figure 11 Stresses required for initiation and propagation of the localized band in Nicalon/MAS, for (a) circular holes and (b) sharp notches.

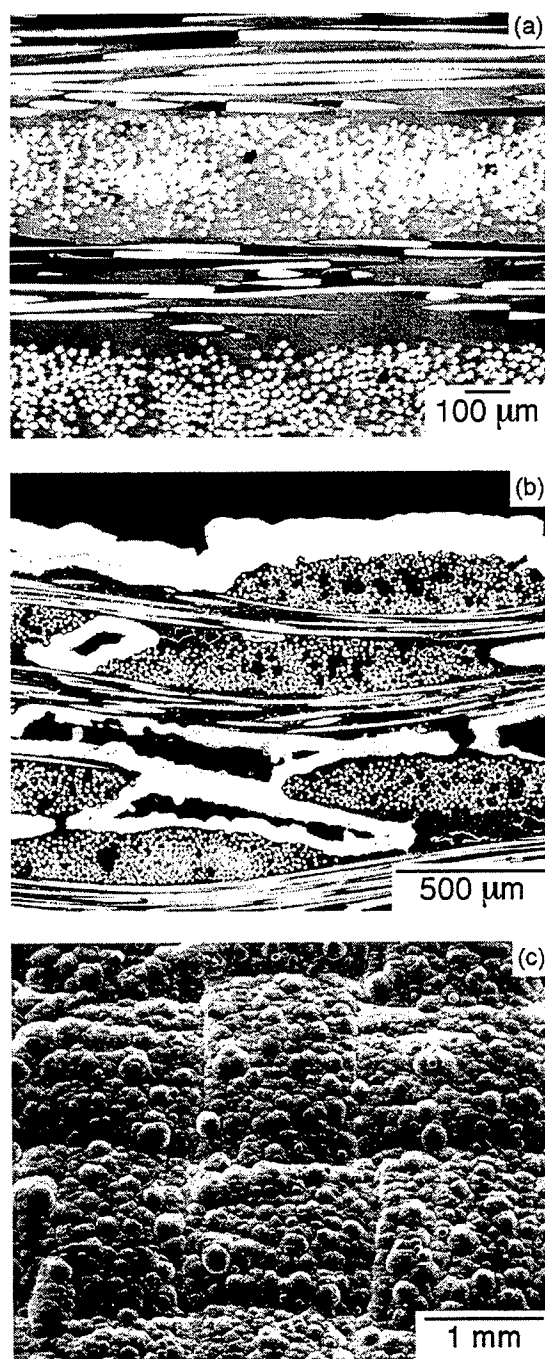


Figure 1 Microstructures of (a) Nicalon/MAS and (b) Nicalon/SiC, and (c) the external surface of the Nicalon/SiC.

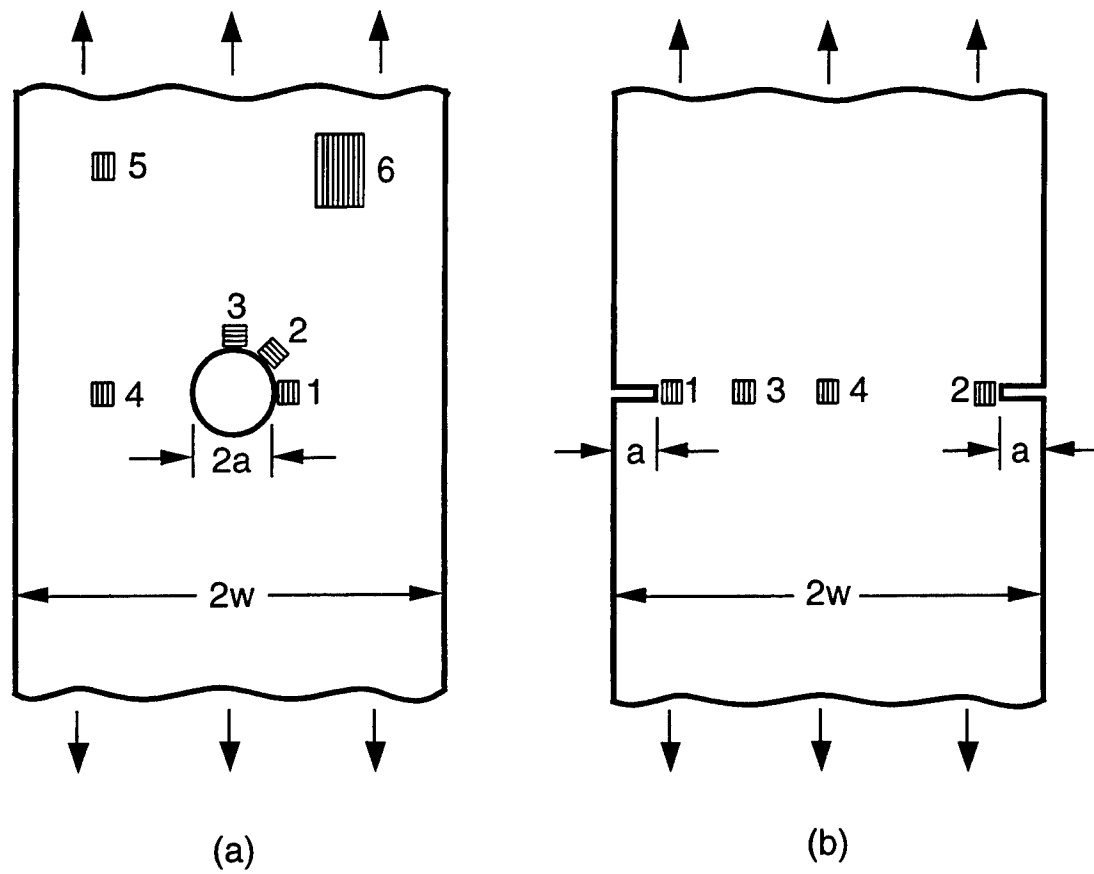
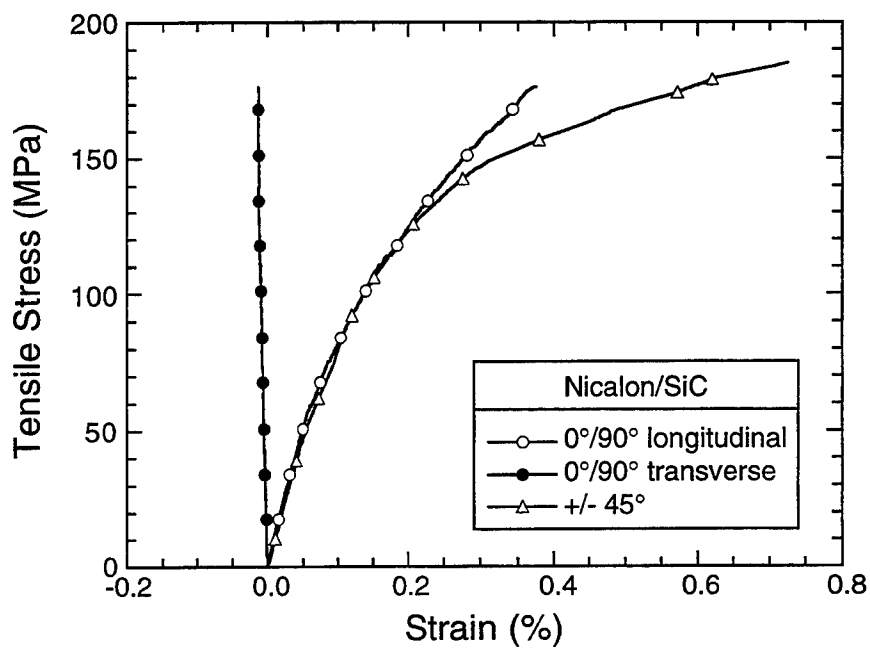
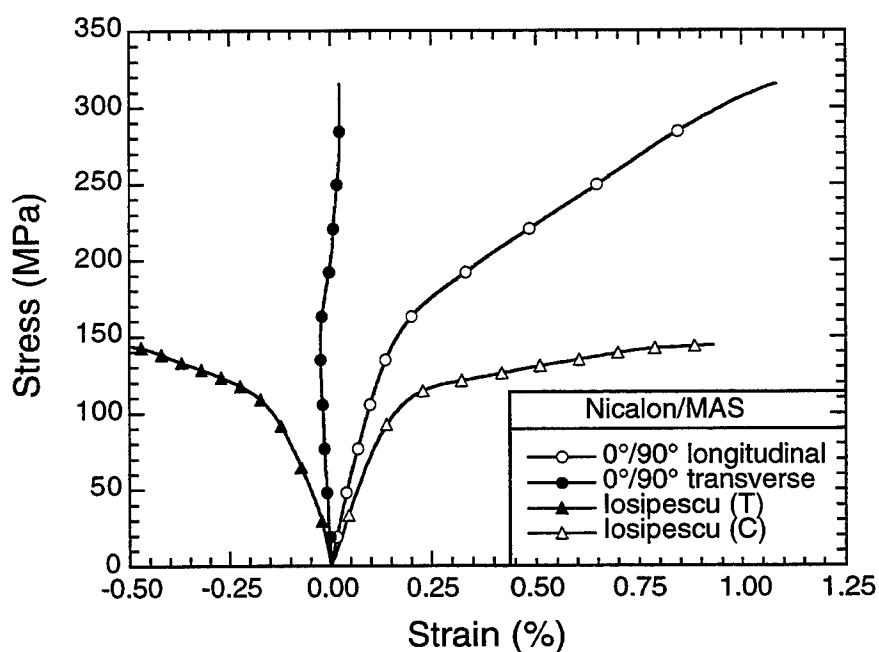


Figure 2 Schematic of the strain gauge configurations for specimens with (a) holes, and (b) notches. The lines within the gauges indicate the direction of strain measurement.

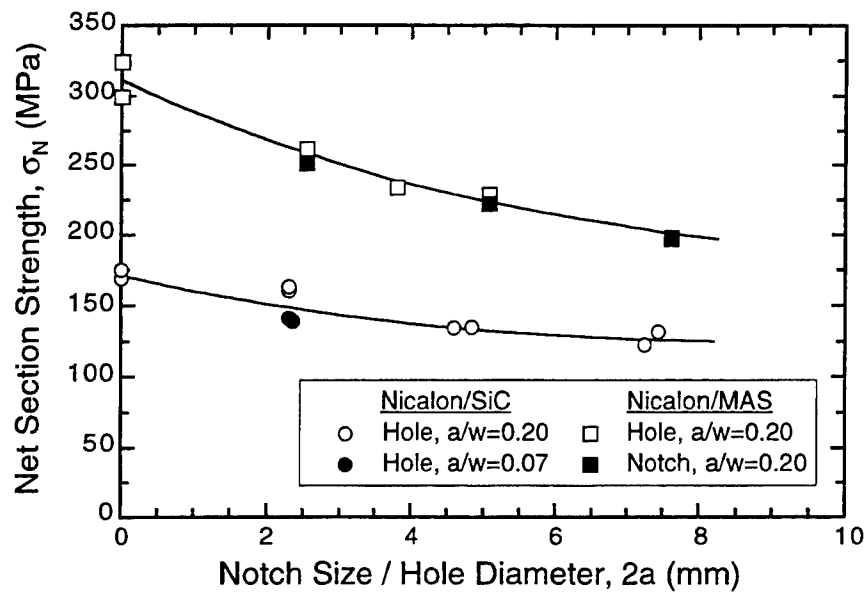


(a)

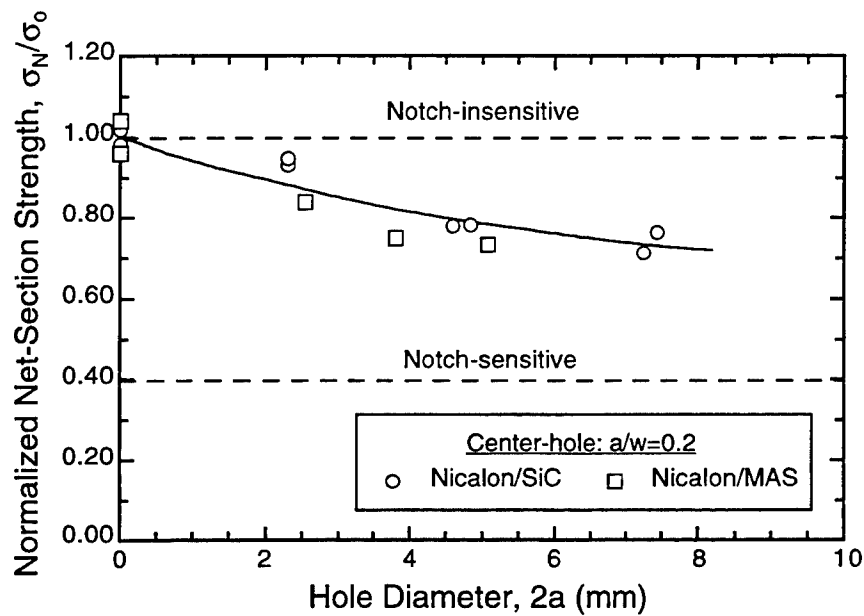


(b)

Figure 3 Unnotched tensile and shear behavior of (a) Nicalon/SiC and (b) Nicalon/MAS.

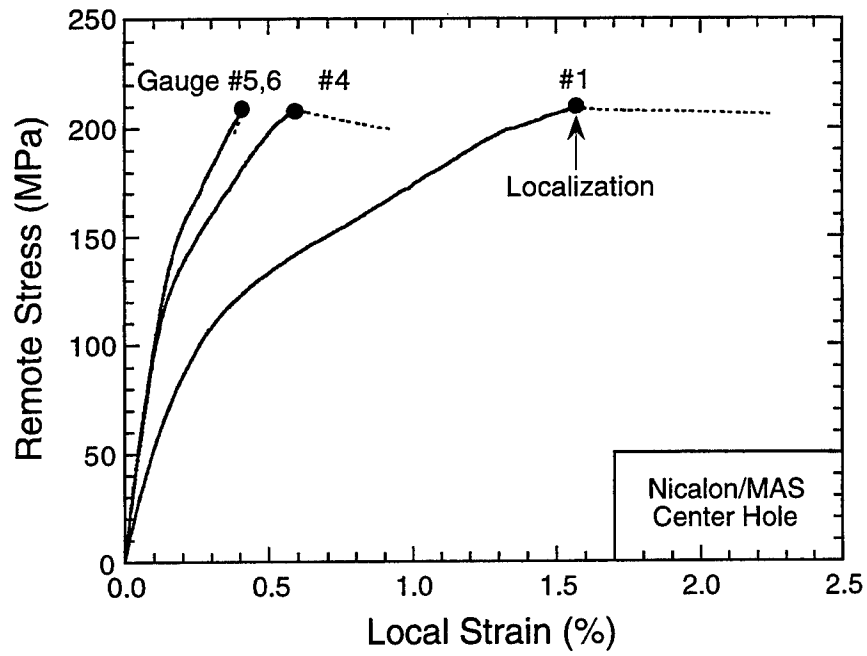


(a)

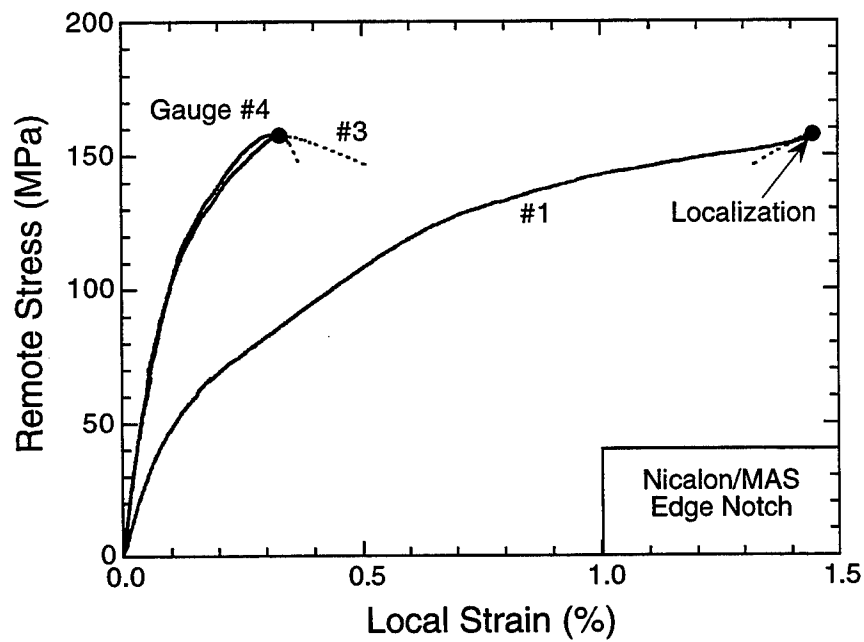


(b)

Figure 4 (a) Effects of notch size, $2a$, on strength. (b) Normalized strength for center-hole specimens with $a/w=0.2$.



(a)



(b)

Figure 5

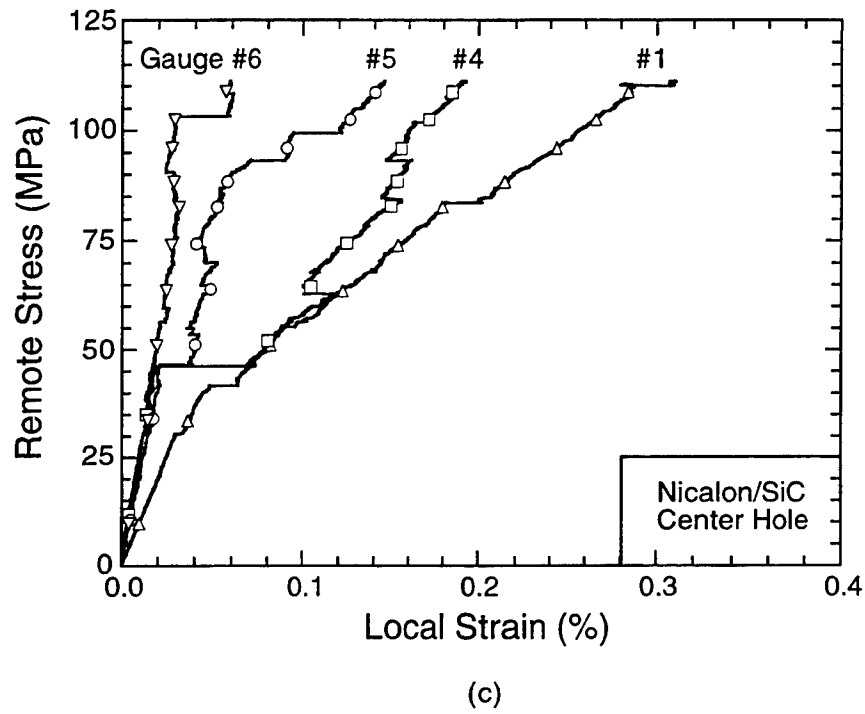


Figure 5 Strain distributions for (a) center-hole Nicalon/MAS ($a/w = 0.2$, $2w = 12.7$ mm), (b) double-edge notched Nicalon/MAS ($a/w = 0.2$, $2w = 38.1$ mm) and (c) center-hole Nicalon/SiC ($a/w = 0.2$, $2w = 25.4$ mm). The solid circles in (a) and (b) indicate the load maximum and attendant formation of a large macroscopic crack.

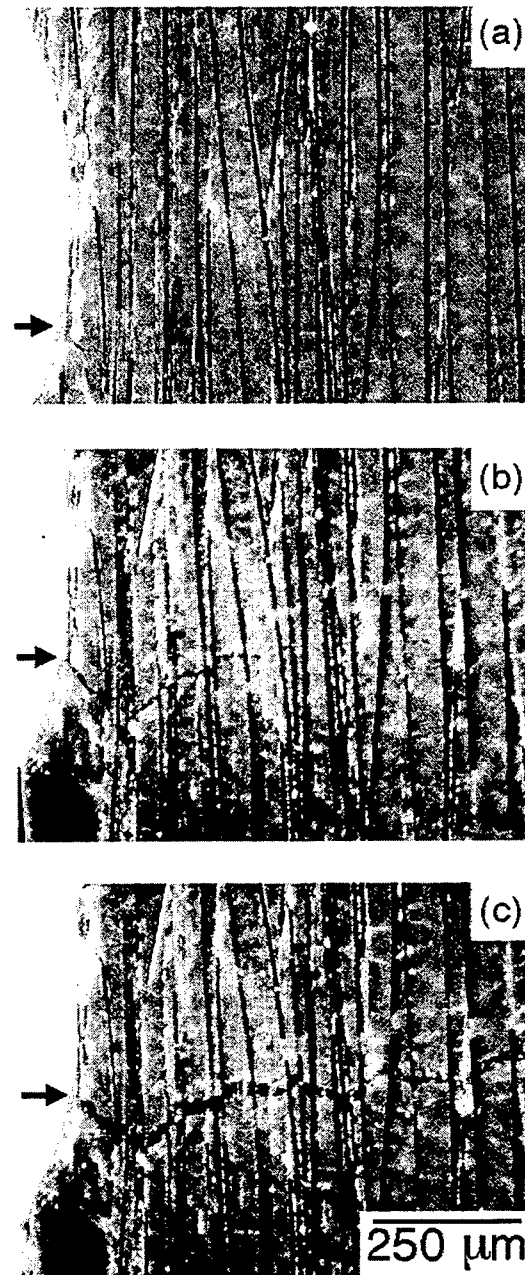


Figure 6 Optical micrographs of a center-hole Nicalon/MAS specimen, illustrating the formation of a macroscopic crack at remote stresses of (a) 208 MPa, (b) 209 MPa, and (c) 199 MPa (beyond the load maximum) ($a/w = 0.2$, $2w = 12.7$ mm).

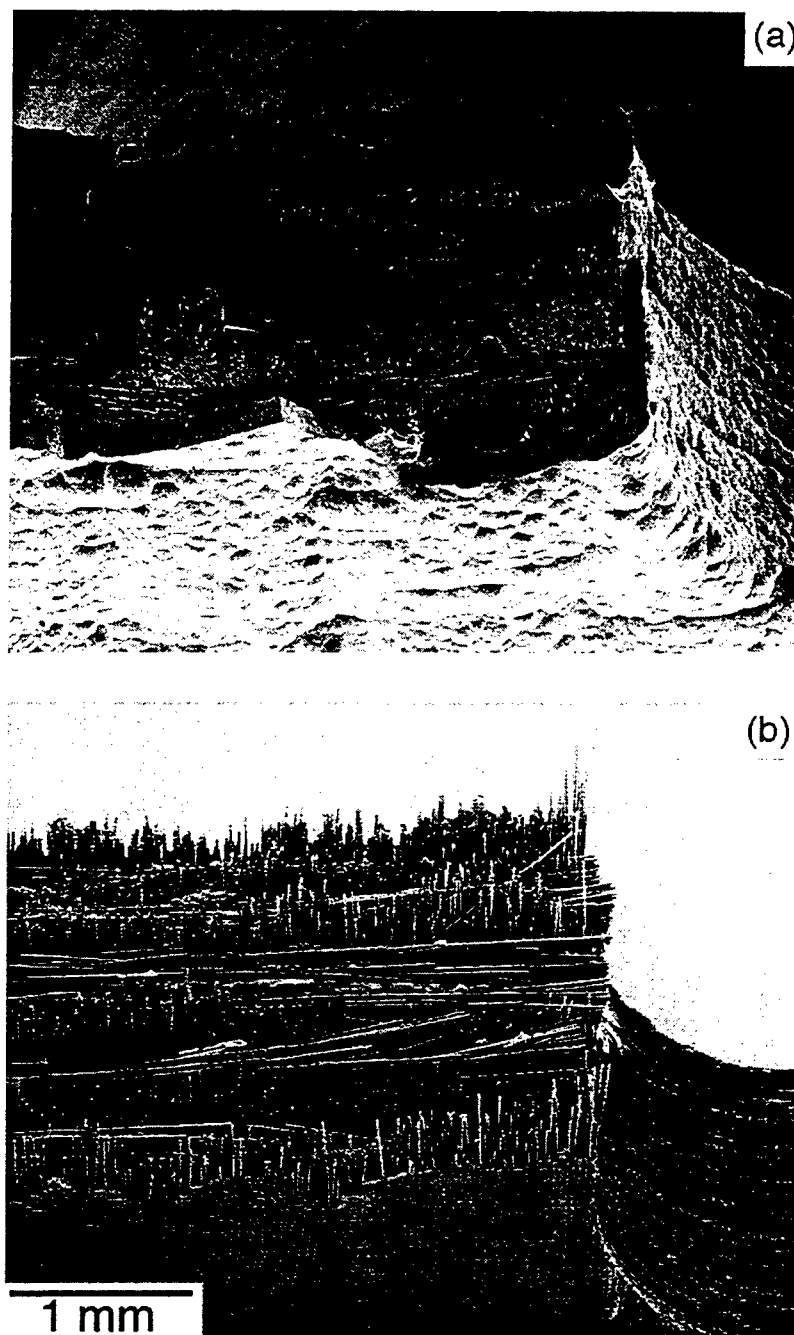


Figure 7

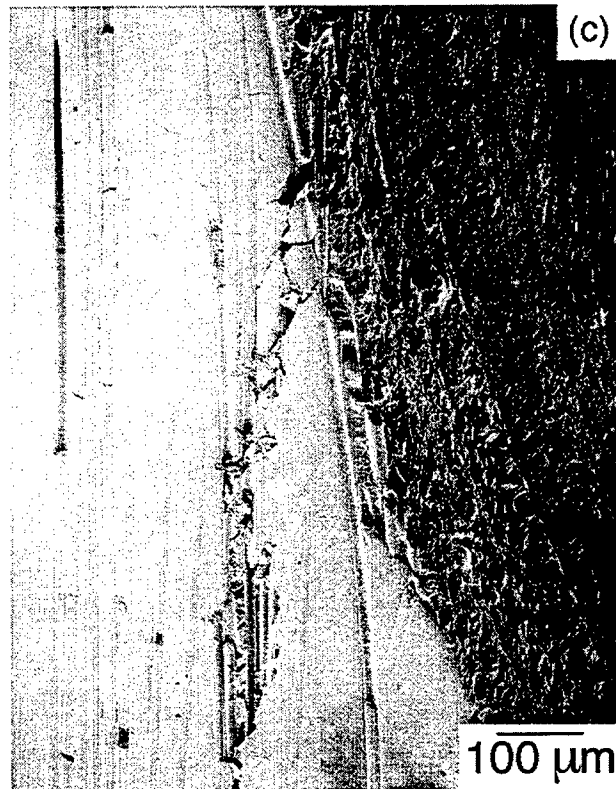
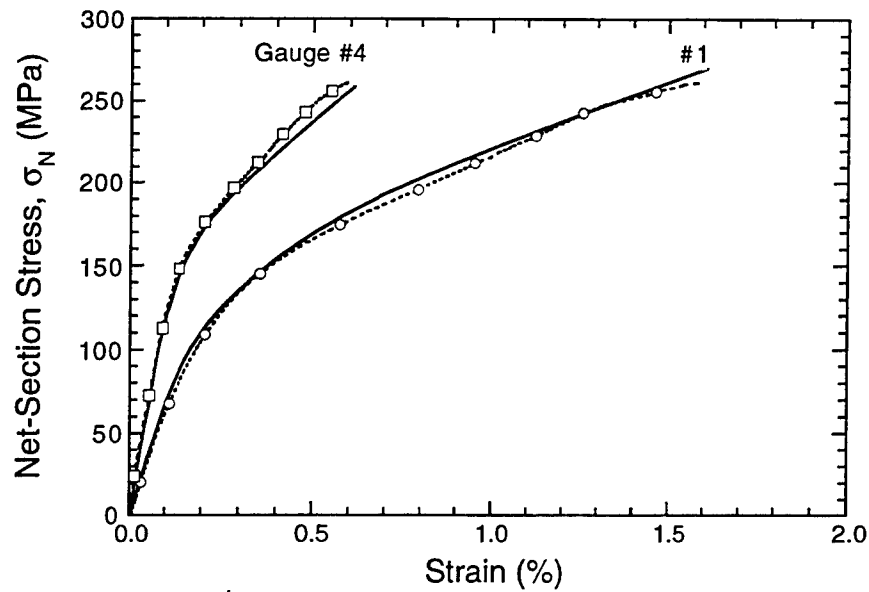
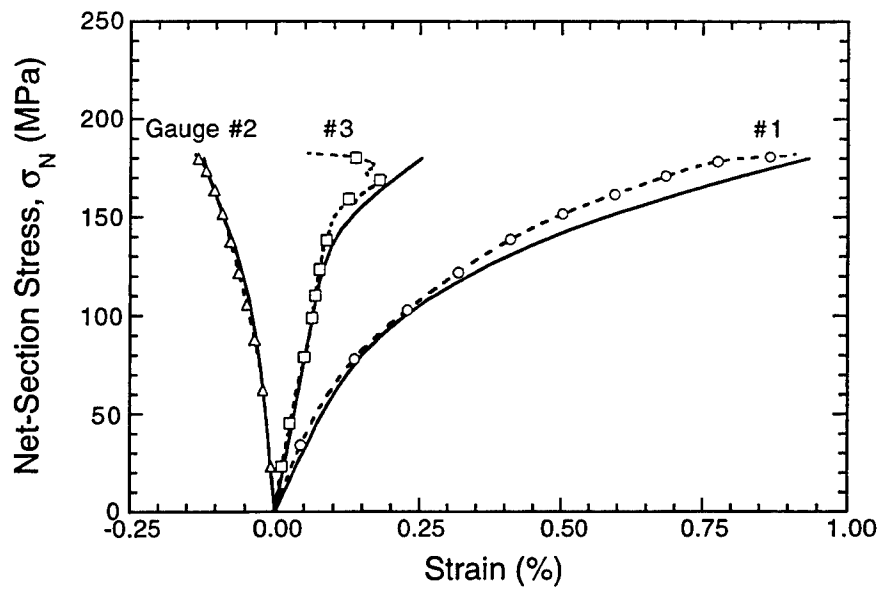


Figure 7 SEM micrographs of the fracture surfaces of (a) Nicalon/SiC ($a/w = 0.2$, $2w = 25.4$ mm) and (b) Nicalon/MAS ($a/w = 0.2$, $2w = 12.7$ mm). (c) Shear cracking in outer ply of Nicalon/MAS.

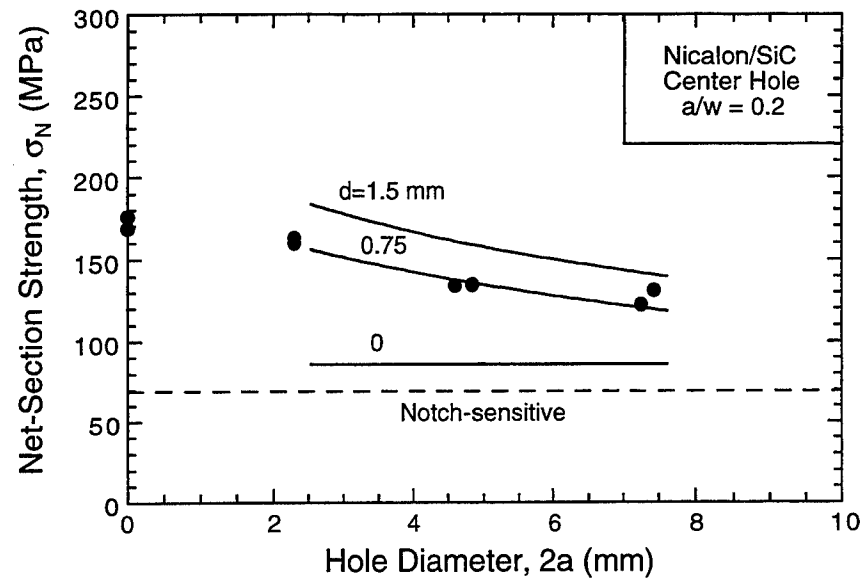


(a)

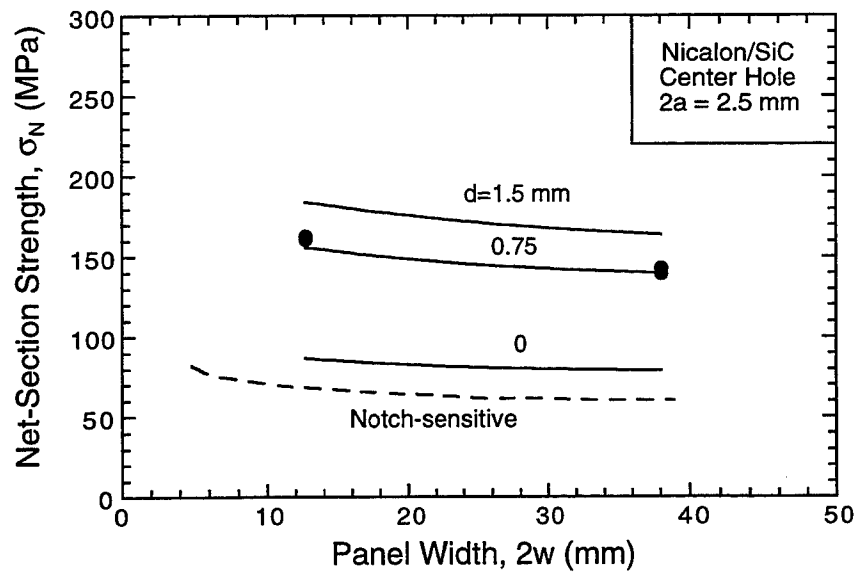


(b)

Figure 8 Comparison of calculated stress-strain distributions with experimental data for center-hole Nicalon/MAS specimens: (a) $a/w = 0.2$, $2w = 12.7$ mm, and (b) $a/w = 0.2$, $2w = 25.4$ mm. The solid lines are the predictions.

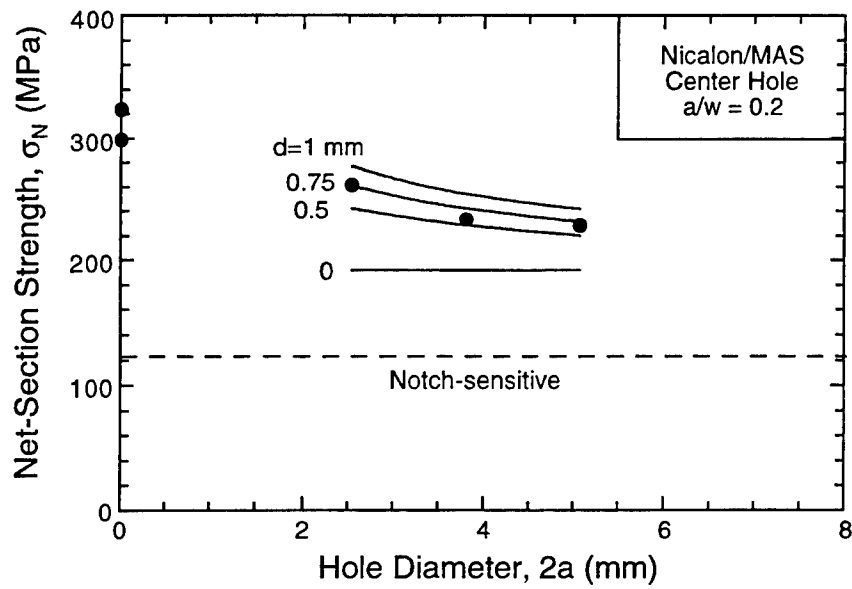


(a)

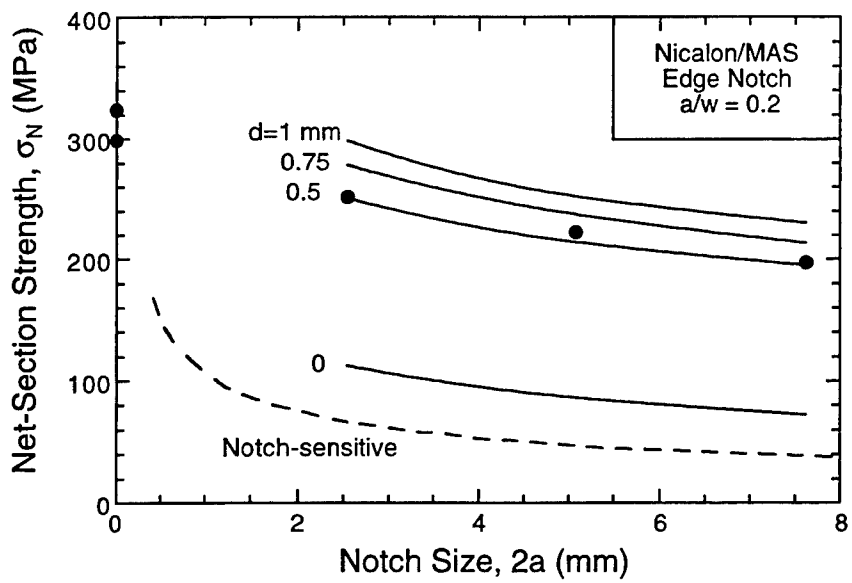


(b)

Figure 9

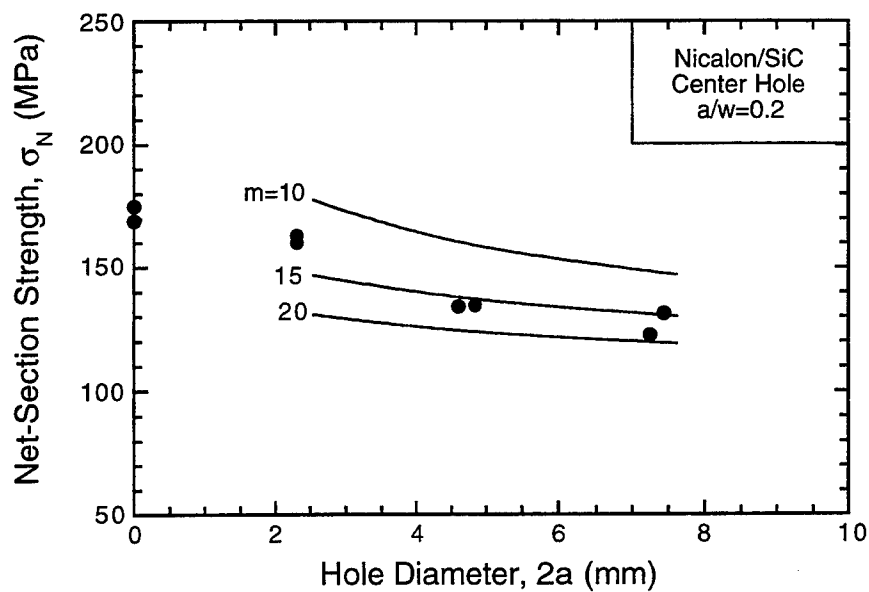


(c)

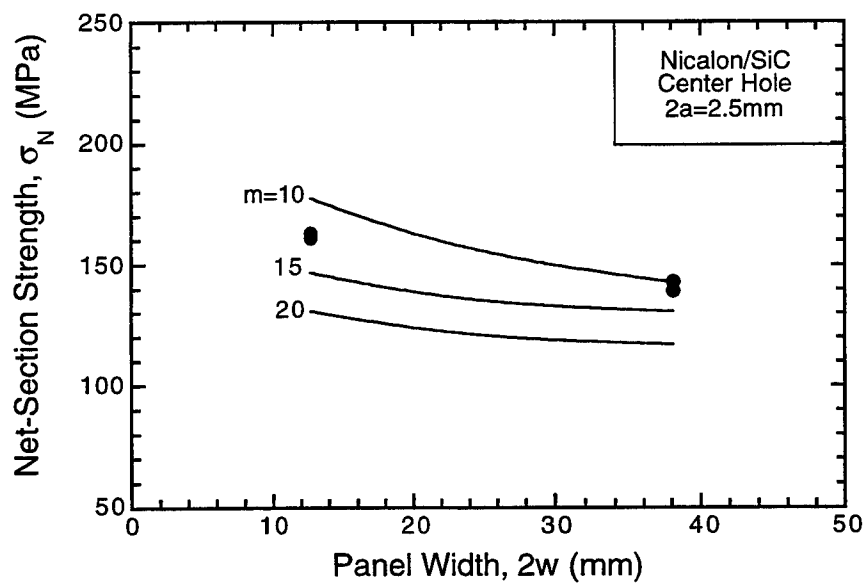


(d)

Figure 9 Comparisons of predicted strengths with experimental data, using the point stress failure criterion: (a, b) Nicalon/SiC and (c, d) Nicalon/MAS. The solid lines are the predictions.

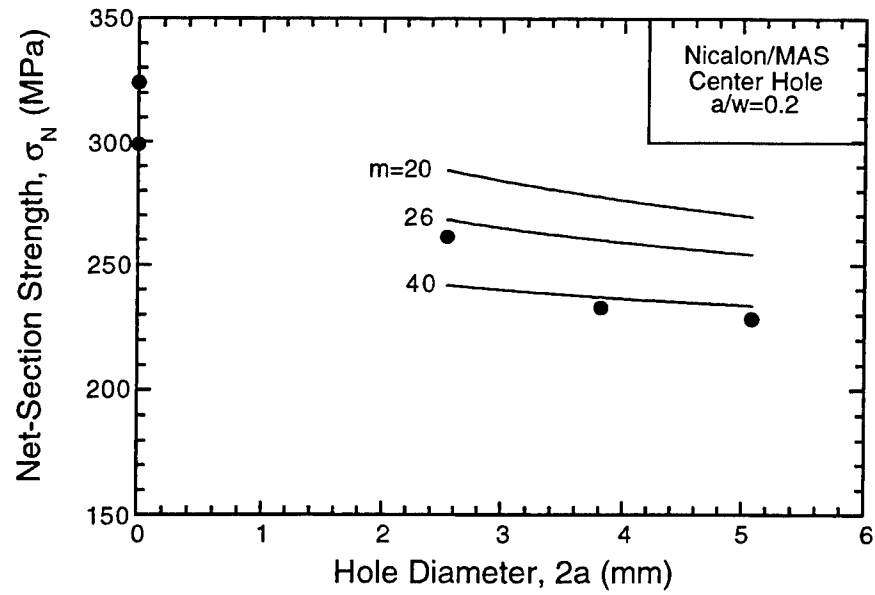


(a)

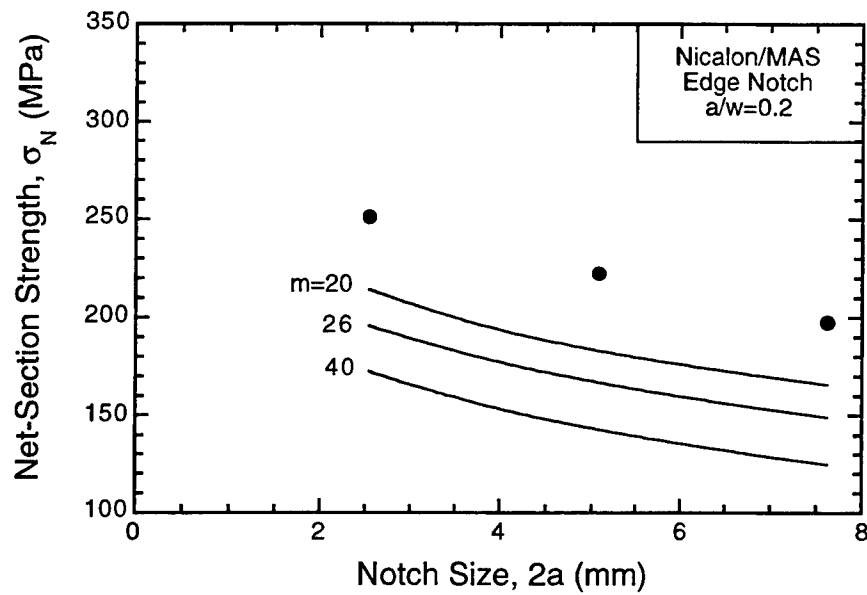


(b)

Figure 10

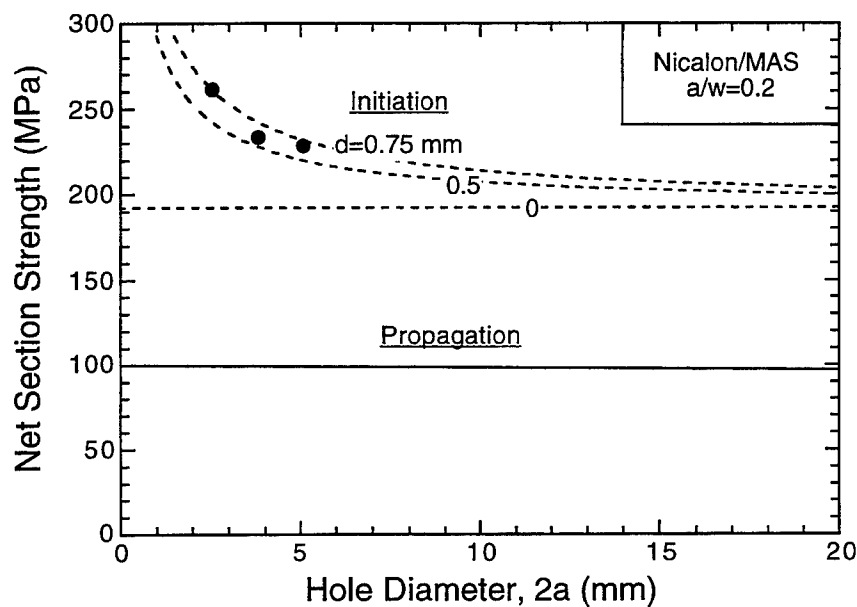


(c)

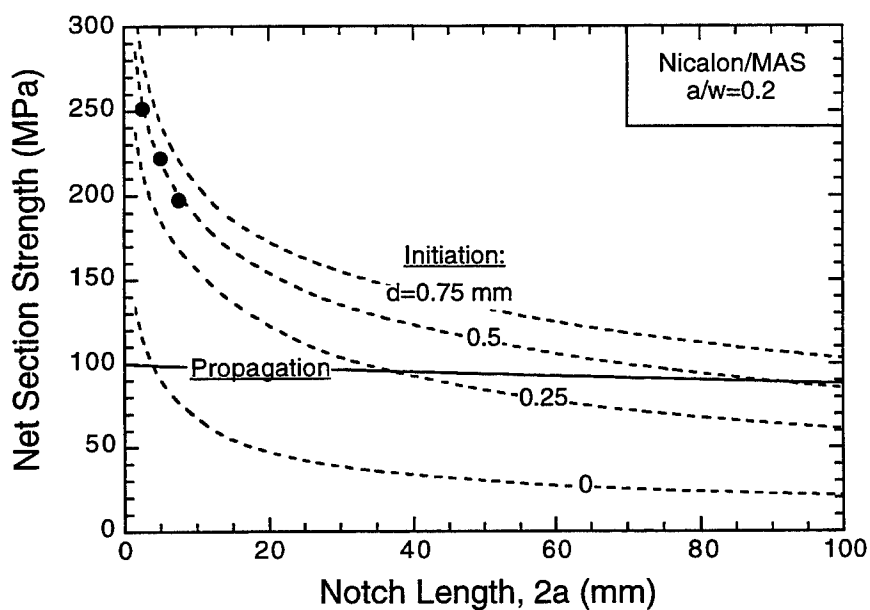


(d)

Figure 10 Comparisons of predicted strengths with experimental data, using the probabilistic model: (a, b) Nicalon/SiC and (c, d) Nicalon/MAS. The solid lines are the predictions.



(a)



(b)

Figure 11 Stresses required for initiation and propagation of the localized band in Nicalon/MAS, for (a) circular holes and (b) sharp notches.

Failure of a porous solid from a deep notch

P. Redanz

*Department of Solid Mechanics, Technical University of Denmark, DK-2800
Lyngby, Denmark*

N. A. Fleck and R. M. McMeeking *

*Cambridge University Engineering Department, Trumpington St, Cambridge CB2
1PZ, U.K.*

(Received ; Accepted in final form)

Abstract. A finite strain finite element method is used to examine the stress state near the tip of a deep notch in an elastic-plastic porous solid. The notch is loaded in mode I plane strain tension and small scale yielding is assumed. Two rate independent strain hardening material models are used: a version of the Gurson model [1] and the more recent FKM model developed by Fleck, Kuhn and McMeeking [2]. Under increasing K_I , void growth is initially stable and independent of mesh dimension. Localization of plastic flow sets in at a finite value K_i , and the deformation field is mesh-size dependent thereafter. The initiation of crack growth at the notch root is assumed to occur when a critical level of porosity is attained. The results show that the shape of the plastic zone for both the Gurson and the FKM material is highly dependent on the initial porosity. In the case of low initial porosity, the plastic zone shape is similar to that of a fully dense material; at higher initial porosities the plastic zone is concentrated ahead of the notch tip. The effect of the initial void volume fraction on the porosity field and the critical stress intensity factor is studied, and the mesh-size dependence of the results is discussed. The analysis is useful for prediction of the notched strength of porous metals.

1. Introduction

Sintered metals are used increasingly in the production of engineering components due to the advantages which they offer in terms of the ease of processing and mechanical properties. Complex shaped components such as gears and cams can be made to near net final shape from metallic powders. A characteristic feature of sintered materials is their porosity, which ranges from zero up to 0.5. The porosity may be used to advantage in gears and bearings by permitting the impregnation of the material with a liquid or solid lubricant. When the part contains a deep notch, failure may be by void growth from the notch root. Tensile stresses at the notch root lead to void growth and coalescence: a crack is nucleated. The main aim of the current paper is to develop a failure criterion for the nucleation of cracking from a notch root. The finite

* On leave from Department of Mechanical Engineering, University of California, Santa Barbara, CA 93106, U.S.A.

element method is used to examine the notch tip stress and deformation state in a porous solid.

The geometry of interest is shown in Fig.1. We consider a long notch of initial tip radius $\delta_0/2$ in a ductile porous solid. Mode I small scale yielding conditions are assumed, whereby the remote elastic field is characterised by the mode I stress intensity factor K_I . We shall show that under increasing K_I void growth is initially stable and independent of mesh dimension. Localization of plastic flow sets in at a finite value K_i , and the deformation field is mesh-size dependent thereafter. The criterion for the initiation of ductile crack growth is assumed to be the attainment of a critical void volume fraction, f_c . The results lead to the prediction of a critical stress intensity factor K_c as a function of initial porosity.

In the present work two porous material models are studied: the Gurson model [1] and the more recent FKM model developed by Fleck, Kuhn and McMeeking [2]. The Gurson material model, which is appropriate for low porosities, considers the porous material as a plastic matrix containing separated, spherical voids. In the limit of zero porosity, the Gurson model reduces to J_2 -flow theory. The FKM model assumes that a porous material consists of spherical particles bonded perfectly at isolated contacts. The FKM model is applicable at higher porosities from about 0.10 up to the limit of dense random packing for equi-sized spheres; at dense random packing the void volume fraction f is 0.36.

The Gurson model has been used widely in the study of ductile fracture. For example, Drugan & Miao [3]-[5] performed analytical analyses of the stress distribution around both a stationary and a growing crack tip for the case of a Gurson solid at fixed porosity. Other work on the effects of porosity on crack fields in ductile metals has consisted mainly of numerical studies, see for example Jagota *et al.* [6]; Aoki *et al.* [7] and [8]; Needleman & Tvergaard [9]; and Aravas & McMeeking [10], all using the Gurson model. Pan and co-workers [11]-[13] have studied the crack tip stress fields and the plastic zones in pressure-sensitive materials using both asymptotic methods and the finite element method. They use a linear combination of the effective stress and the mean stress as the yield criterion; no porosity parameter is involved explicitly in their work in contrast to the treatment given below.

It is well-known that void growth leads to material softening and to the phenomenon of strain localization. The localization is associated with local unloading of material elements and to a switch of the governing field equations from elliptic to hyperbolic in nature. Post-localization, the response is sensitive to mesh size with a coarser mesh giving the stiffer response. In the current study, void growth is con-

sidered to well past localization and the role of mesh size is explored. We consider the geometry of a deep notch of initial opening δ_0 and root radius $\delta_0/2$ in order to set a length scale to the problem and to introduce a finite stress concentration at the notch root. Localization is expected to initiate at a finite value of K_I , independent of mesh size provided the mesh is sufficiently fine in relation to δ_0 . Subsequently, deformation is localized within a band of thickness equal to the mesh size, and the post-localization response is mesh-size dependent. In the limit of a vanishing root radius, the notch becomes a crack and the strain state at the crack tip is unbounded. Then, the smaller the mesh the lower is the critical value of K_I corresponding to the onset of localization.

2. Constitutive relations

The analysis is based on a convected co-ordinate Lagrangian formulation of the field equations, in which g_{ij} and G_{ij} are the metric tensors in the reference configuration and the current configuration, respectively, with determinants g and G . The Lagrangian strain tensor is $\eta_{ij} = \frac{1}{2}(G_{ij} - g_{ij}) = \frac{1}{2}(u_{i,j} + u_{j,i} + u_{,i}^k u_{k,j})$ where u^i are the displacement components on the reference base vectors, and $(\cdot)_{,i}$ denotes the covariant derivatives in the reference frame. The contravariant components of the Kirchhoff stress tensor, τ^{ij} , on the current base vectors are related to the contravariant components of the Cauchy or true stress tensor by $\tau^{ij} = \sqrt{G/g} \sigma^{ij}$. The initial state is taken as the reference configuration.

The strain increment is assumed to be the sum of the elastic and plastic parts, $\dot{\eta}_{ij} = \dot{\eta}_{ij}^E + \dot{\eta}_{ij}^P$, where (\cdot) denotes differentiation with respect to a loading parameter. The elastic part of the strain is taken to be small and therefore the elastic constitutive response is approximately given by the hypoelastic relation

$$\overset{\nabla}{\sigma}{}^{ij} = \mathcal{R}^{ijkl} \dot{\eta}_{kl}^E = \mathcal{R}^{ijkl} (\dot{\eta}_{kl} - \dot{\eta}_{kl}^P) \quad (1)$$

where the Jaumann (co-rotational) rate of the Cauchy stress tensor, $\overset{\nabla}{\sigma}{}^{ij}$, is related to the convected rate by

$$\overset{\nabla}{\sigma}{}^{ij} = \dot{\sigma}^{kl} + \frac{1}{2} \{ G^{ik} \sigma^{jl} + G^{jk} \sigma^{il} + G^{il} \sigma^{jk} + G^{jl} \sigma^{ik} \} \dot{\eta}_{kl} \quad (2)$$

The finite strain generalization of Budiansky (see Hutchinson, [14]) is used

$$\mathcal{R}^{ijkl} = \frac{E}{1+\nu} \left\{ \frac{1}{2} (G^{ik} G^{jl} + G^{il} G^{jk}) + \frac{\nu}{1-2\nu} G^{ij} G^{kl} \right\} \quad (3)$$

where E and ν are Young's modulus and Poisson's ratio, respectively. Equilibrium is enforced via the principle of virtual work

$$\int_V \tau^{ij} \delta \eta_{ij} dV = \int_S T^i \delta u_i dS \quad (4)$$

with body forces neglected. Here V and S are the volume and the surface of the body in the reference state. The components of the surface tractions per unit area in the reference configuration on the reference base vectors are given by

$$T^i = (\tau^{ij} + \tau^{kj} u_{,k}^i) n_j \quad (5)$$

with n_j as the components of the surface normal in the reference state.

For time independent plasticity the resulting incremental constitutive relations are of the form

$$\dot{\tau}^{ij} = L^{ijkl} \dot{\eta}_{kl} \quad (6)$$

The uniaxial true stress-logarithmic strain curve for the matrix material in tension is represented by the piecewise power law

$$\epsilon = \begin{cases} \sigma/E & \sigma \leq \sigma_y \\ \frac{\sigma_y}{E} \left(\frac{\sigma}{\sigma_y} \right)^n & \sigma > \sigma_y \end{cases} \quad (7)$$

where σ_y is the uniaxial yield stress and n is the strain hardening exponent.

3. Porous material models

The yield surface for a porous material depends upon the stress state σ^{ij} , the yield strength of the matrix σ_M and the void volume fraction f ; the yield function Φ can be written in the form

$$\Phi(\sigma^{ij}, \sigma_M, f) = 0 \quad (8)$$

3.1. GURSON MODEL

The Gurson model [1] assumes that porosity exists in the form of isolated, spherical voids. In this study, an elastic-strain hardening plastic version of the model is used. The yield surface is given by

$$\Phi = \frac{\sigma_e^2}{\sigma_M^2} + 2q_1 f \cosh \left\{ \frac{q_2}{2} \frac{\sigma_k^k}{\sigma_M} \right\} - (1 + (q_1 f)^2) = 0 \quad (9)$$

with the macroscopic effective Mises stress given by $\sigma_e = (3s_{ij}s^{ij}/2)^{1/2}$ in which $s^{ij} = \sigma^{ij} - G^{ij}\sigma_k^k/3$ is the stress deviator. The constants q_1 and q_2 are the Tvergaard adjustment factors [15]-[16] set to 1.5 and 1.0, respectively, in the present study. In the limit of zero porosity the Gurson model reduces to J_2 -flow theory.

3.2. FKM MODEL

The more recent FKM porous material model suggested by Fleck, Kuhn and McMeeking [2] assumes that the material consists of spherical particles joined by discrete necks. The FKM model is applicable at higher porosities from approximately 0.10 up to the limit of dense random packing, taken to be that for equi-sized spheres, $f = \hat{f} = 0.36$. The yield surface is given by

$$\Phi = \left(\frac{5}{18} \frac{\sigma_e}{p_y} + \frac{2}{3} \right)^2 + \left(\frac{\sqrt{5}}{3} \frac{\frac{1}{3}\sigma_k^k}{p_y} \right)^2 - 1 = 0 \quad (10)$$

with

$$p_y = 2.97(1-f)^2 \frac{\hat{f}-f}{\hat{f}} \sigma_M \quad (11)$$

Fig.2 shows a comparison of the FKM yield surface and that of the Gurson model. The FKM yield surface contains a vertex on the hydrostatic stress axis in $(\sigma_e, \frac{1}{3}\sigma_k^k)$ space. For numerical computation purposes, the vertex is rounded off by a quadratic approximation to the yield surface near the vertex as done by Fleck, Otoyoy & Needleman [17].

3.3. BASIC POROUS MATERIAL EQUATIONS

A detailed discussion of the procedure for the Gurson material is given by Tvergaard [18]; here, only a brief summary is reported. Since the elastic deformations are small compared to the plastic deformations the elastic contribution to the change in f with deformation is neglected. The matrix material is plastically incompressible, and so the rate of growth of the porosity is given by

$$\dot{f} = (1-f)G^{ij}\dot{\eta}_{ij}^P \quad (12)$$

The incremental relation between the effective plastic strain in the matrix, ϵ_M^P , and the equivalent tensile yield strength of the matrix, σ_M , is given by

$$\dot{\epsilon}_M^P = \left(\frac{1}{E_t} - \frac{1}{E} \right) \dot{\sigma}_M \quad (13)$$

where E_t is the slope of the uniaxial true stress-logarithmic strain curve for the matrix material. Here, σ_M and ϵ_M^P are viewed as spatial averages of the actual microscopic fields in the matrix material.

The plastic part of the strain increment is assumed to be

$$\dot{\eta}_{ij}^P = \Lambda \frac{\partial \Phi}{\partial \sigma^{ij}} \quad (14)$$

where Λ is the plastic multiplier and $\partial \Phi / \partial \sigma^{ij}$ gives the direction of the plastic strain increment. Normality for the matrix material at the microscopic level implies macroscopic normality for the porous aggregate [19]-[20]. The macroscopic plastic work rate is equated with the plastic work rate in the matrix material, giving

$$\sigma^{ij} \dot{\eta}_{ij}^P = F(f) \sigma_M \dot{\epsilon}_M^P \quad (15)$$

where $F(f)$ is the volume fraction of deforming material. In the Gurson model $F(f) = 1 - f$ since all of the matrix material in the original model is assumed to yield. An expression for $F(f)$ in the FKM model is taken from Fleck, Otoy & Needleman [17] as

$$F = \frac{45}{\sqrt{3}} (1 - f)^2 \left(\frac{\dot{f} - f}{\dot{f}} \right)^{3/2} \quad (16)$$

Using (13) and (15), the rate of the tensile equivalent flow stress in the matrix material follows as

$$\dot{\sigma}_M = \frac{E E_t}{E - E_t} \frac{\sigma^{ij} \dot{\eta}_{ij}^P}{F(f) \sigma_M} \quad (17)$$

Initiation of plastic yielding occurs when $\dot{\Phi} = 0$ and $\dot{\Phi} > 0$. The consistency condition for continued plastic flow, $\dot{\Phi} = 0$, is used to obtain an expression for the plastic multiplier Λ , and thereby the plastic strain increment,

$$\dot{\eta}_{ij}^P = \frac{1}{H} \frac{\partial \Phi}{\partial \sigma^{ij}} \frac{\partial \Phi}{\partial \sigma^{kl}} \dot{\sigma}^{kl} \quad (18)$$

with

$$H = - \left(\frac{\partial \Phi}{\partial f} (1 - f) G^{ij} + \frac{\partial \Phi}{\partial \sigma_M} \frac{E E_t}{E - E_t} \frac{\sigma^{ij}}{F(f) \sigma_M} \right) \frac{\partial \Phi}{\partial \sigma^{ij}} \quad (19)$$

Upon substituting (18) into (1), the instantaneous moduli from (6) are determined as

$$L^{ijkl} = \mathcal{L}^{ijkl} - \mu M^{ij} M^{kl} \quad (20)$$

where

$$\mathcal{L}^{ijkl} = \sqrt{\frac{G}{g}} \left\{ \mathcal{R}^{ijkl} - \frac{1}{2} (\sigma^{ik} G^{jl} + \sigma^{jk} G^{il} + \sigma^{il} G^{jk} + \sigma^{jl} G^{ik}) + \sigma^{ij} G^{kl} \right\} \quad (21)$$

$$\mu = \begin{cases} 0 & \text{elastic unloading} \\ \sqrt{\frac{G}{g}} \left[H + \frac{\partial \Phi}{\partial \sigma^{rs}} \mathcal{R}^{rskl} \frac{\partial \Phi}{\partial \sigma^{kl}} \right]^{-1} & \text{plastic loading} \end{cases} \quad (22)$$

and M^{ij} is defined by

$$M^{ij} = \mathcal{R}^{ijkl} \frac{\partial \Phi}{\partial \sigma^{kl}} \quad (23)$$

4. Numerical method

The finite element mesh used for the calculations is shown in Fig.3a. The mesh consists of 1718 nodes and 524 isoparametric eight-noded elements. An enlargement of the near tip region is shown in Fig.3b. Due to symmetry about the crack line, only half of the body is analysed, as shown. The calculations for the porous material are carried out with 3x3 Gauss integration points in each element. The ratio between the initial notch opening, δ_0 , and the outer mesh radius, R_b , is 1/2500.

The reference state is represented by a Cartesian coordinate system x^1 - x^2 and a state of plane-strain deformation is assumed. The origin of the Cartesian frame is set at the center of the semi-circular notch tip in Fig.3b. Numerical solutions are obtained by an incrementally linear method. An approximate equilibrium state is fulfilled for the current values of the stresses, σ^{ij} , the strains, η_{ij} , etc.. By expanding the principle of virtual work (4) about this known state, the equations regarding the increments, δ^{ij} , $\dot{\eta}_{ij}$, etc. are obtained. With body forces neglected, the expansion of the principle of virtual work takes the form

$$\int_V \left\{ \dot{\tau}^{ij} \delta \eta_{ij} + \tau^{ij} \dot{u}_i^k \delta u_{k,j} \right\} dV = \int_S \dot{T}^i \delta u_i dS - \left[\int_V \tau^{ij} \delta \eta_{ij} dV - \int_S T^i \delta u_i dS \right] \quad (24)$$

The term in square brackets of (24) vanishes according to (4), if the current state satisfies equilibrium. It is included here to prevent the solution from drifting away from the true equilibrium state.

The value of the parameter μ in (20) is chosen at each material point according to the state of the material in the previous increment. This type of procedure gives good accuracy provided the increments are sufficiently small (see for example Tvergaard: [21]).

Small-scale yielding conditions are assumed and the remote field is the mode I K-field. The displacement boundary conditions imposed at the outer semi-circular boundary are of the form

$$\begin{Bmatrix} u_1 \\ u_2 \end{Bmatrix} = \frac{K_I}{E}(1+\nu)\sqrt{\frac{R_b}{2\pi}} \begin{Bmatrix} \left(1 - 2\nu + \sin^2\frac{\theta}{2}\right) \cos\frac{\theta}{2} \\ \left(2 - 2\nu + \cos^2\frac{\theta}{2}\right) \sin\frac{\theta}{2} \end{Bmatrix} \quad (25)$$

where u_1 and u_2 are the Cartesian components of the displacement vector and (r, θ) are polar co-ordinates as defined in Fig.3. K_I is the mode I stress intensity factor. The remaining boundary conditions are

$$\begin{aligned} T^i &= 0 \text{ on the crack surface} \\ T^1 &= 0, u_2 = 0 \text{ for } x^2 = 0, x^1 \geq \frac{1}{2}\delta_0 \end{aligned} \quad (26)$$

5. Results

In a typical finite element calculation, the notched porous solid is loaded with an increasing K_I , and the evolution of stress state and porosity is determined. Initially, at small values of K_I , plastic deformation and attendant void growth occur in a stable manner in the vicinity of the notch root. In this regime the response is independent of mesh size for a sufficiently refined mesh in relation to the notch opening δ_0 . At a particular value of K_I , termed K_i , localization of deformation with elastic unloading initiates at some point in the mesh. Thereafter, material loads within a narrow band near the notch root and adjacent material unloads. The width of the band of continuing localized deformation is set by the mesh size, and the post-localization response is thereby mesh-size dependent. The initiation of ductile crack growth, which may eventually lead to failure, is defined to occur when the porosity attains a critical value, $f_{max} = f_c$ at any material point. This condition defines the critical stress intensity factor, K_c , at which fracture begins by void coalescence.

Both the Gurson model and the FKM model predict softening responses which lead to mesh size dependence in the post-localization regime. Needleman and Tvergaard [22] have discussed these mesh effects for the Gurson model. Here, calculations are carried out for three different meshes, $l_0/\delta_0 = 0.131$, $l_0/\delta_0 = 0.087$ and $l_0/\delta_0 = 0.052$, where l_0 is the

initial height of the first element directly ahead of the notch tip. The median mesh, $l_0/\delta_0 = 0.0873$, is the one shown in Fig.3 and is used in all calculations unless otherwise stated. The calculations are carried out for a matrix material with $\sigma_y/E = 0.0025$, $\nu = 0.3$ and strain hardening exponent, $n = 10$.

The maximum porosity at any point within the mesh is plotted as a function of stress intensity factor, K_I , for the three different meshes. Results are given in Fig.4a for the Gurson solid (for an initial porosity $f_0 = 0.05$) and in Fig.5a for the FKM solid (for an initial porosity $f_0 = 0.14$). For both material models the R-curves are insensitive to mesh size prior to localization, but become strongly sensitive to mesh size in the post-localization regime. After localization, void growth occurs more easily in the fine mesh and the estimated fracture toughness value, K_c , corresponding to $f_{max} = f_c = 0.20$, decreases with decreasing mesh size, as shown in Figs. 4a and 5a. In the limit of vanishing mesh size we would expect $K_c = K_i$. Thus, the value K_i serves as a useful measure of the notch toughness.

For low initial porosities such as $f_0 = 0.05$, the Gurson solid is the appropriate constitutive model and stable plastic void growth occurs for a large range of K_I ; localization sets in when the void volume fraction has approximately doubled from its initial value. At higher initial porosities, such as $f_0 = 0.14$, the FKM solid is appropriate; localization occurs at a low level of K_I and the void volume fraction has increased by about 10% above its initial value.

Typical plots of the plastic zone shape are shown in Fig.4b for the Gurson solid, and in Fig.5b for the FKM solid. X_0 is the horizontal distance from the center of the semi-circular notch tip to a point of interest, such as the plastic zone boundary. It is again evident that, prior to localization, there is a negligible effect of mesh size on the response. This is illustrated for the Gurson solid in Fig. 4b: the plastic zone boundary is shown for $K_c/\sigma_y\sqrt{\delta_0} = 11$, labelled state C for the coarse mesh and state D for the fine mesh. The plastic zone shape is reminiscent of that for a plane strain mode I crack in a von Mises solid. A similar insensitivity of results to mesh size prior to localization is observed for the FKM solid, see Fig. 5b. Therein, the plastic zone boundary is shown for $K_c/\sigma_y\sqrt{\delta_0} = 1.4$, labelled state C for the coarse mesh and state D for the fine mesh. For the FKM solid the plastic zone is concentrated ahead of the notch tip; this is suggestive of a plane stress Dugdale model of notch root plasticity. The difference in shapes of plastic zone for the two material models is consistent with the difference in shape of the yield surfaces. The FKM solid has a much lower ratio of hydrostatic yield strength to deviatoric yield strength compared with the Gurson solid, and high stress triaxiality is unable

to develop ahead of the notch. Consequently, the plastic zone shape is similar to that generated in a fully dense solid under plane stress conditions. In contrast, the Gurson solid can support larger hydrostatic stresses and the plastic zone shape is similar to that at the tip of a mode I crack under plane strain conditions.

The plastic zone shapes at the onset of fracture (e.g. $f_{max} = f_c = 0.20$) are included in Figs. 4b and 5b. The critical state is labelled A for the coarse mesh ($l_0/\delta_0 = 0.131$), and labelled B for the fine mesh ($l_0/\delta_0 = 0.052$), as cross-referenced on the R-curves of Figs. 4a and 5a. For both constitutive descriptions, a larger value of K_c and a larger plastic zone size are exhibited by the coarser mesh. The localized strip of plastic deforming material directly ahead of the notch tip has the height of 2 integration points and extends a couple of notch openings ahead of the notch.

The notch opening displacements are $\delta/\delta_0 = 1.244$ and $\delta/\delta_0 = 1.178$ at points B and D in Fig. 4a, respectively, for the Gurson material with low initial porosity. When the FKM model with high initial porosity is used the notch opening displacement is $\delta/\delta_0 = 1.017$ in state B and $\delta/\delta_0 = 1.008$ in state D in Fig. 5a.

The tensile stress component σ_{22} is plotted as a function of distance directly ahead of the notch for states B and D in Fig. 4c (Gurson solid), and in Fig. 5c (FKM solid). Prior to localization (state B) the stress distribution σ_{22} is similar to that for a blunted crack in a strain hardening fully dense solid (Rice & Johnson [23], and McMeeking [24]). The stress attains a peak value at a distance ahead of the notch of approximately the notch root radius. At the later stages of loading, when $f_{max} = 0.20$ at state B, the stress peak has moved away from the notch tip. Between the notch tip and the location of the stress peak plastic deformation has localized and the stress level has decreased due to void growth. The unstable nature of the void growth within the band is clear from the highly localized contours of porosity as shown for the fine mesh at $f_{max} = f_c = 0.20$ in Figs. 4d and 5d. The highly local void growth at the notch root is consistent with the predictions of Aravas & McMeeking [10], who examined the rupture of the ligament between a blunt crack and a neighbouring void. In reality an additional material length scale is involved, in the form of the finite spacing of void-nucleating particles, such as carbide particles in steels. In order to model this feature an additional length scale is required within the constitutive description, for example by the addition of a cohesive zone ahead of the notch tip, as implemented by Tvergaard & Hutchinson [25], or by use of a non-local plasticity law, see for example Fleck & Hutchinson [26].

A comparison of the plastic zones for the two material models is given in Fig.6. In both cases, the initial porosity is $f_0 = 0.09$ and the critical porosity, $f_c = 0.20$ has been attained. The medium mesh ($l_0/\delta_0 = 0.087$) is used. The plastic zone of the FKM model is concentrated near the notch tip and the critical stress intensity factor is much lower than in the Gurson material case. When the critical porosity is attained, the Gurson model predicts a critical stress intensity factor of $K_c/\sigma_y\sqrt{\delta_0} = 9.78$ which is approximately twice that of the FKM model ($K_c/\sigma_y\sqrt{\delta_0} = 4.20$). The size of the plastic zone of the Gurson model is also much larger than that of the FKM model. These differences may be explained in broad terms as follows. For a void volume fraction in the range 0.1 to 0.2, the FKM solid has a much lower ratio of hydrostatic strength to deviatoric strength than that of the Gurson solid. Also, the FKM solid softens more rapidly with increasing porosity. Consequently, the FKM solid is unable to support significant hydrostatic stresses and the usual plane strain plastic zone is unable to develop.

The stress intensity factor for the initiation of localization K_i and the critical stress intensity factor K_c for the initiation of ductile crack growth are both highly dependent on the initial porosity as shown in Fig.7a. On the other hand, the assumed value of critical porosity has lesser effect on the magnitude of K_c : numerical experimentation revealed that an increase in f_c from 0.2 to 0.3 resulted in an increase of K_c by a few percent. We emphasize that predictions of K_i are not strongly dependent of the mesh but predictions of K_c are sensitive to the ratio of mesh size to initial notch opening. The results shown in Fig. 7 pertain to $l_0/\delta_0 = 0.087$. As mentioned above, the Gurson model is the more realistic model at low porosities and the FKM model is more appropriate at higher porosities. The lowest initial porosity used with the FKM model is 0.09. At initial porosities higher than 0.10 the values of K_i and K_c for the Gurson model lie approximately a factor of two above those for the FKM model.

6. Discussion

It is clear that the deformation response becomes mesh size dependent at the onset of localization. It is suggested that the stress intensity factor K_i at localization is a useful measure of notch toughness, since it is slightly conservative, $K_i < K_c$, and is not strongly mesh dependent.

So far, the mesh size has been considered to be a modelling artifact with no physical significance. An alternative strategy is to assume that the mesh size is an approximate measure of the particle size of a sintered solid, and that material response depends upon this internal

material length scale. Results for different mesh sizes are then ascribed a physical significance: results for a large mesh are representative of the behaviour of a sintered solid containing large particles, and results for a fine mesh apply to a sintered solid containing fine particles. The fracture toughness of a sintered solid containing a sharp crack would then scale with the particle size.

With the chosen critical porosity criterion for initiation of ductile crack growth, the Gurson and FKM constitutive laws predict quite different plastic zones and critical stress intensity factors. The plastic zones predicted by the Gurson model are much larger than those predicted by the FKM model partly due to the larger value of the stress intensity factor when the critical porosity is attained. The FKM solid is unable to support large hydrostatic stresses and thus, the usual plane strain plastic zone is unable to develop. However, the material models are based on different assumptions and are valid for different ranges of porosity. The FKM model is thought to be valid for porosity f in the range 0.1 to 0.35, and the Gurson model is realistic for $f < 0.1$.

Despite the obvious difference between the material models, it has been shown that the shape and size of the plastic zone in general is highly dependent on the initial porosity of the material. In the case of low initial porosity, the shape of the plastic zone is quite similar to that of a crack tip field in a fully dense material except directly adjacent to the notch tip where the increase in porosity causes stress relaxation. At higher initial porosities, the plastic zone is small and concentrated ahead of the notch tip.

The maximum porosity in the present study is always located on the horizontal line ahead of the notch tip, independent of the initial porosity. In the Gurson case with low initial porosity, the growth in porosity > 0.01 at $K = K_i$ is concentrated around the notch tip and occurs in a small region within a large plastic zone. On the other hand, in the case of high initial porosity using the FKM model the region over which porosity has increased by more than 0.01 at $K = K_i$ occupies about half of the plastic zone. It has been shown that the computed critical stress intensity factor is highly dependent on the initial porosity and less dependent on the choice of the magnitude of the critical porosity.

Acknowledgements

The work of Pia Redanz was financially supported by the MUP2 research programme Materials Processing, Properties and Modelling, financed by the Danish Agency for Development of Trade and Industry, the Danish Natural Science Research Council, and the Danish Techni-

cal Research Council. The contribution of Pia Redanz's Ph.D. thesis advisor, Professor Viggo Tvergaard, is gratefully acknowledged. R. M. McMeeking was supported by a Visiting Professorship at Cambridge University, and is grateful for the financial support of the Cambridge Centre for Micromechanics.

References

1. A. L. Gurson, Continuum theory of ductile rupture by void nucleation and growth: part I - Yield criteria and flow rules for porous ductile media. *J. Engng. Materials Technol.*, ASME 99 (1977) 2-15.
2. N. A. Fleck, L. T. Kuhn and R. M. McMeeking, Yielding of metal powder bonded by isolated contacts. *J. Mech. Phys. Solids* 40(5) (1992) 1139-1162.
3. W. J. Drugan and Y. Miao, Influence of porosity on plane strain tensile crack-tip stress fields in elastic-plastic materials: Part I. *J. Appl. Mech.* 59 (1992) 559-567.
4. Y. Miao and W. J. Drugan, Influence of porosity on plane strain tensile crack-tip stress fields in elastic-plastic materials: Part II. *J. Appl. Mech.* 60 (1993) 883-889.
5. Y. Miao and W. J. Drugan, Asymptotic analysis of growing crack stress/deformation fields in porous ductile metals and implications for stable crack growth. *Int. J. Fracture* 72 (1995) 69-96.
6. A. Jagota, C.-Y. Hui and P. R. Dawson, The determination of fracture toughness for a porous elastic-plastic solid. *Int. J. Fracture* 33 (1987) 111-124.
7. S. Aoki, K. Kishimoto, A. Takeya and M. Sakata, Effects of microvoids on crack blunting and initiation in ductile materials. *Int. J. Fracture* 24 (1984) 267-278.
8. S. Aoki, K. Kishimoto, T. Yoshida and M. Sakata, A finite element study of the near crack tip deformation of a ductile material under mixed mode loading. *J. Mech. Phys. Solids* 35(4) (1987) 431-455.
9. A. Needleman and V. Tvergaard, An analysis of ductile rupture modes at a crack tip. *J. Mech. Phys. Solids* 35(2) (1987) 151-183.
10. N. Aravas and R. M. McMeeking, Microvoid growth and failure in the ligament between a hole and a blunt crack. *Int. J. Fracture* 29 (1985) 21-38.
11. F. Z. Li and J. Pan, Plane-strain crack-tip fields for pressure-sensitive dilatant materials. *J. Appl. Mech.* 57 (1990) 40-49.
12. P. Dong and J. Pan, Elastic-plastic analysis of cracks in pressure-sensitive materials. *Int. J. Solids Structures* 28(9) (1991) 1113-1127.
13. M. Kim and J. Pan, Effects of non-singular stresses on crack-tip fields for pressure-sensitive materials, Part 1: Plane strain case. *Int. J. Fracture* 68 (1994) 1-34.
14. J. W. Hutchinson, Finite strain analysis of elastic-plastic solids and structures. In R. F. Hartung (ed.), *Numerical Solution of Nonlinear Structural Problems* ASME 17, New York (1973).
15. V. Tvergaard, Influence of voids on shear band instabilities under plane strain conditions. *Int. J. Fracture* 17 (1981) 389-407.
16. V. Tvergaard, On localisation in ductile materials containing spherical voids. *Int. J. Fracture* 18 (1982) 237-252.
17. N. A. Fleck, H. Ohtoyo and A. Needleman, Indentation of porous solids. *Int. J. Solids Structures* 29(13) (1992) 1613-1636.
18. V. Tvergaard, Material Failure by Void Growth to Coalescence. In J. W. Hutchinson & T. Y. Wu (eds.) *Advances in Appl. Mech.* 27 (1990) 83-151.

19. C. A. Berg, Plastic dilatation and void interaction. In M. F. Kanninen, W. F. Adler, A. R. Rosenfield and R. I. Jaffee (eds.), *Inelastic Behavior of Solids*. McGraw-Hill, New York (1970) pp. 171-210.
20. J. F. W. Bishop and R. Hill, A theory of the plastic distortion of a polycrystalline aggregate under combined stresses. *Phil. Mag.* 42 (1951) 414-427.
21. V. Tvergaard, Influence of Void Nucleation on Ductile Shear Fracture at a Free Surface. *J. Mech. Phys. Solids* 30(6) (1982) 399-425.
22. A. Needleman and V. Tvergaard, Mesh effects in the analysis of dynamic ductile crack growth. *Engineering Fracture Mechanics* 47 (1994) 75-91.
23. J. R. Rice and M. A. Johnson, The role of large crack tip geometry changes in plane strain fracture. In M. F. Kanninen, W. F. Adler, A. R. Rosenfield and R. I. Jaffee (eds.), *Inelastic Behavior of Solids*. McGraw-Hill, New York (1970) 641-672.
24. R. M. McMeeking, Finite deformation analysis of crack-tip opening in elastic-plastic materials and implications for fracture. *J. Mech. Phys. Solids* 25 (1977) 357-381.
25. V. Tvergaard and J.W. Hutchinson, The relation between crack growth resistance and fracture process parameters in elastic-plastic solids, *J. Mech. Phys. Solids*, 40(6) (1992) 1377-1397.
26. N.A. Fleck and J.W. Hutchinson, Strain Gradient Plasticity, *Advances in Applied Mechanics*, Academic Press, 33 (1997) 295-361.

Figure captions

Figure 1. The small scale yielding problem for a long blunted notch in a porous solid. The area around the notch tip is shown enlarged to show the finite notch root radius $\frac{1}{2}\delta_0$.

Figure 2. Comparison of the yield surfaces for the Gurson model and the FKM model.

Figure 3. Finite element mesh in initial configuration (medium mesh, $l_0/\delta_0 = 0.087$): (a) full mesh, and (b) enlarged near tip region of mesh.

Figure 4. Results for the Gurson model with the initial porosity $f_0 = 0.05$. (a) The stress intensity factor, K_I , as a function of the maximum porosity for three different meshes, $l_0/\delta_0 = 0.131$, $l_0/\delta_0 = 0.087$ and $l_0/\delta_0 = 0.052$. The onset of localization is marked for each mesh. (b) The plastic zone boundary at $f_{max} = 0.2$ for the coarse mesh (state A) and for the fine mesh (state B) post-localization, and at $f_{max} = 0.08$ for the coarse mesh (state C) and for the fine mesh (state D) pre-localization. (c) The tensile stress directly ahead of the notch $\hat{\sigma}_{22}$ normalised by the yield stress σ_y , as a function of the initial horizontal distance from the center of the semi-circular notch tip X_0 , for states B and D.

Figure 5. Results for the FKM model with the initial porosity $f_0 = 0.14$. (a) The stress intensity factor, K_I , as a function of the maximum porosity for three different meshes, $l_0/\delta_0 = 0.131$, $l_0/\delta_0 = 0.087$ and $l_0/\delta_0 = 0.052$. The onset of localization is marked for each mesh. (b) The plastic zone boundary at $f_{max} = 0.2$ for the coarse mesh (state A) and for the fine mesh (state B) post-localization, and at $f_{max} = 0.142$ for the coarse mesh (state C) and for the fine mesh (state D) pre-localization. (c) The tensile stress directly ahead of the notch $\hat{\sigma}_{22}$ normalised by the yield stress σ_y , as a function of the initial horizontal distance from the center of the semi-circular notch tip X_0 , for states B and D.

Figure 6. Comparison of the plastic zones from the FKM model and the Gurson model with the same initial porosity, $f_0 = 0.09$, and the same critical porosity, $f_c = 0.20$. (a) full size of both plastic zones, and (b) an enlargement of the near tip region.

Figure 7. The normalized stress intensity factor for the initiation of localization K_i and the critical stress intensity factor K_c ($f_c = 0.20$) as functions of initial porosity, f_0 .

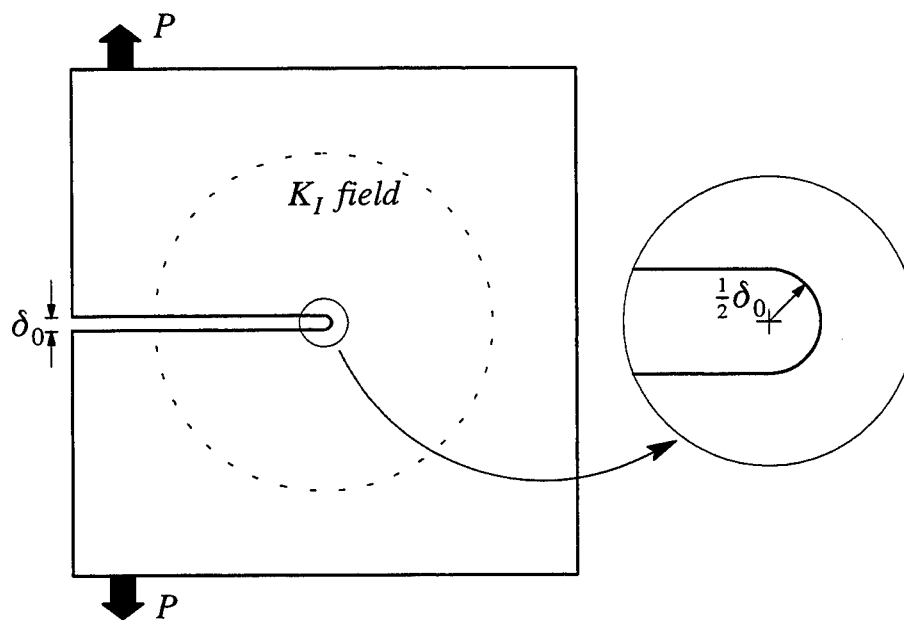


Fig.1

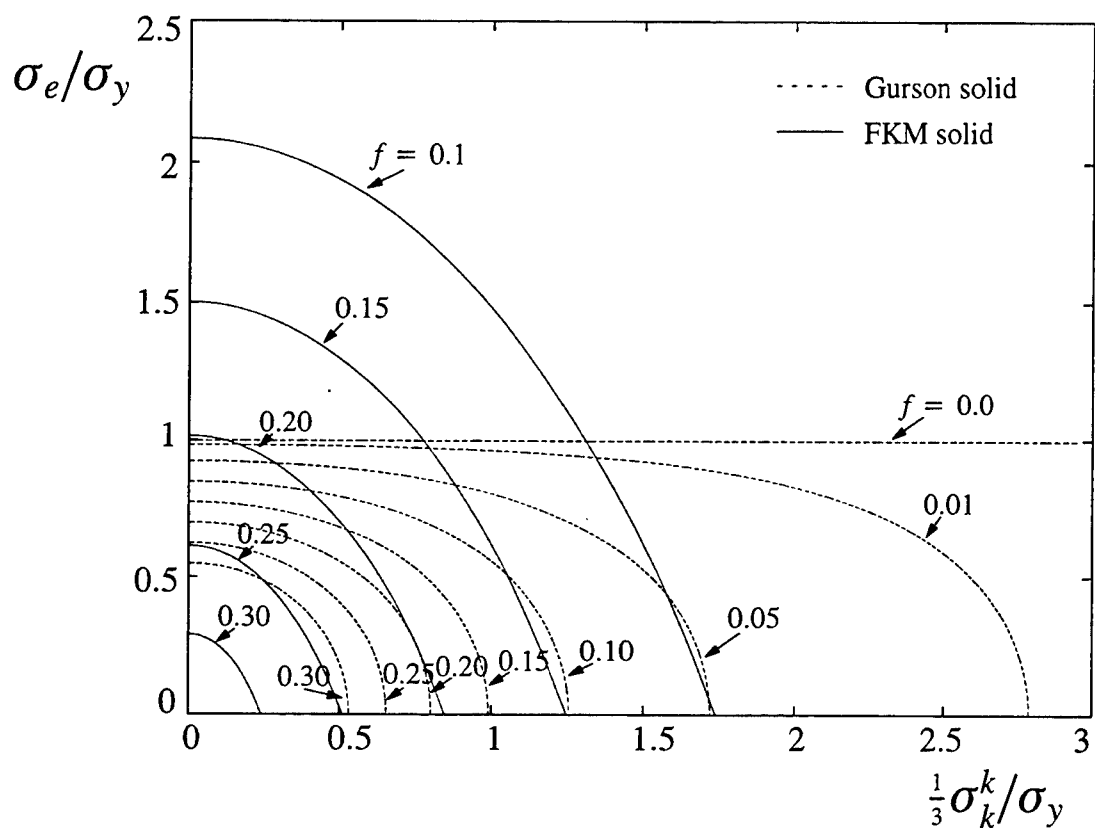


Fig.2

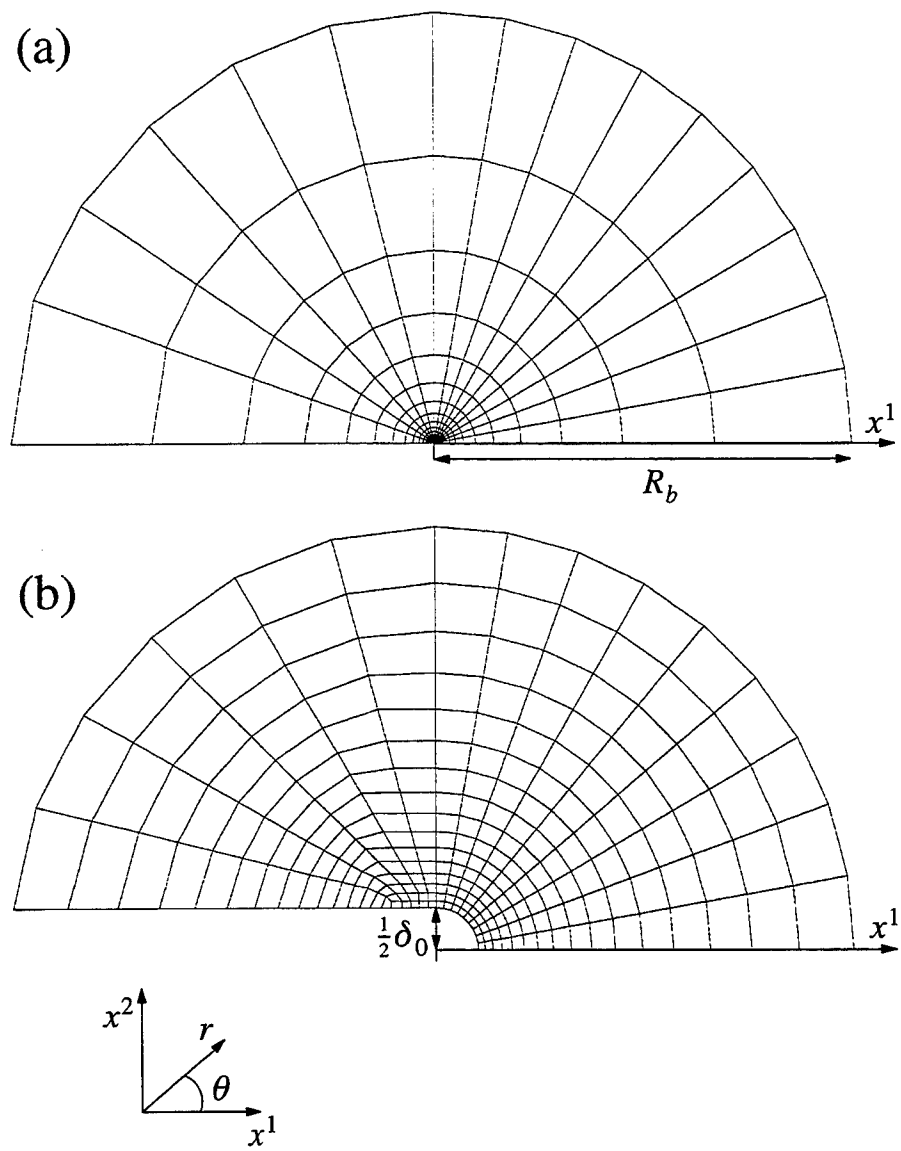


Fig.3

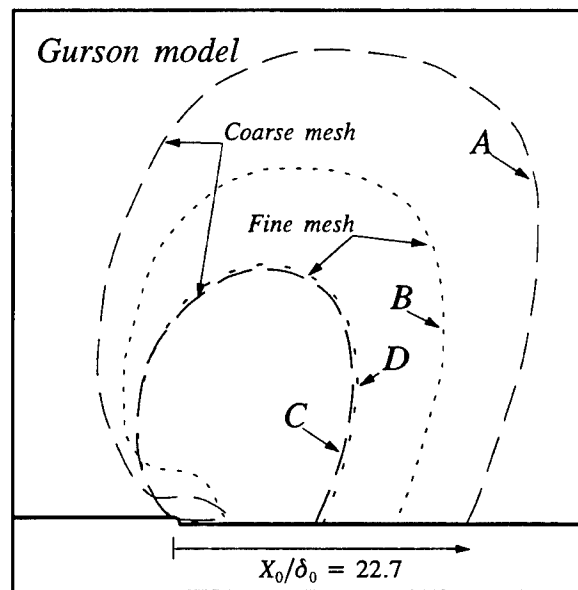
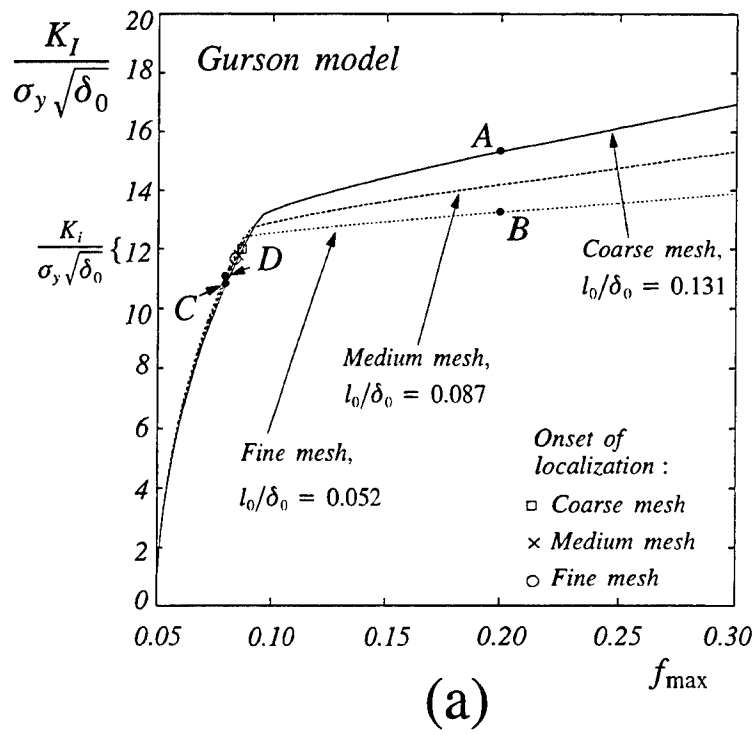


Fig.4

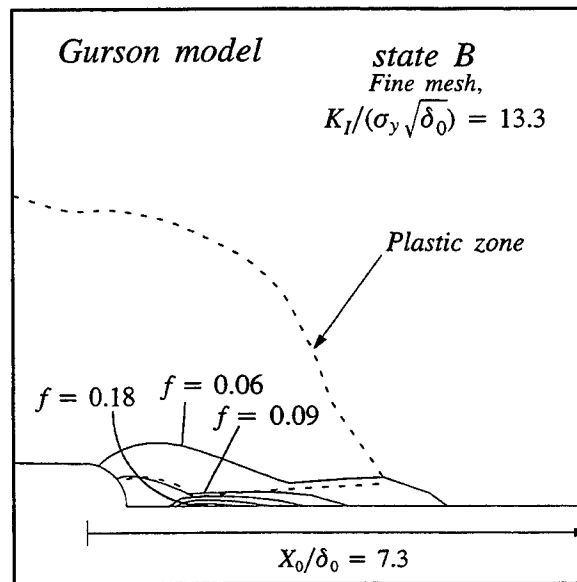
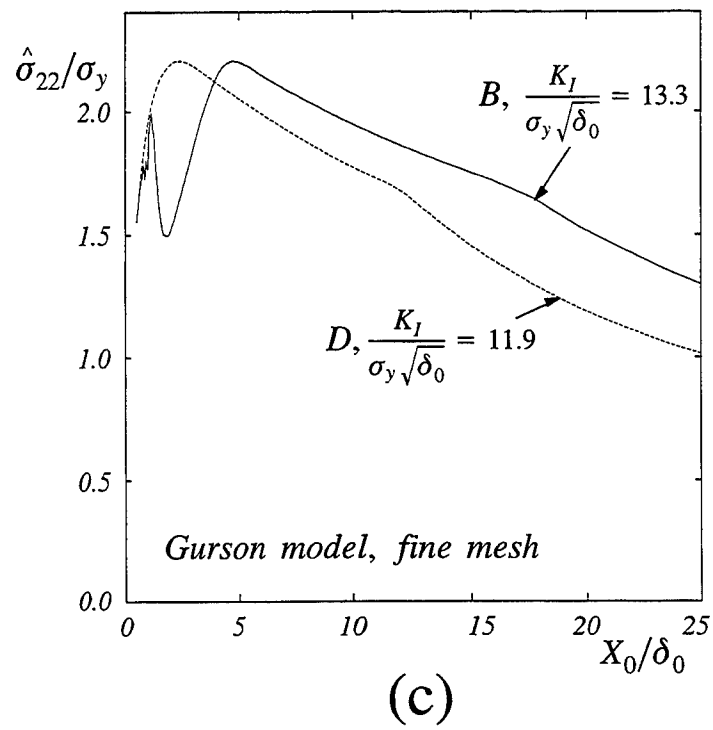
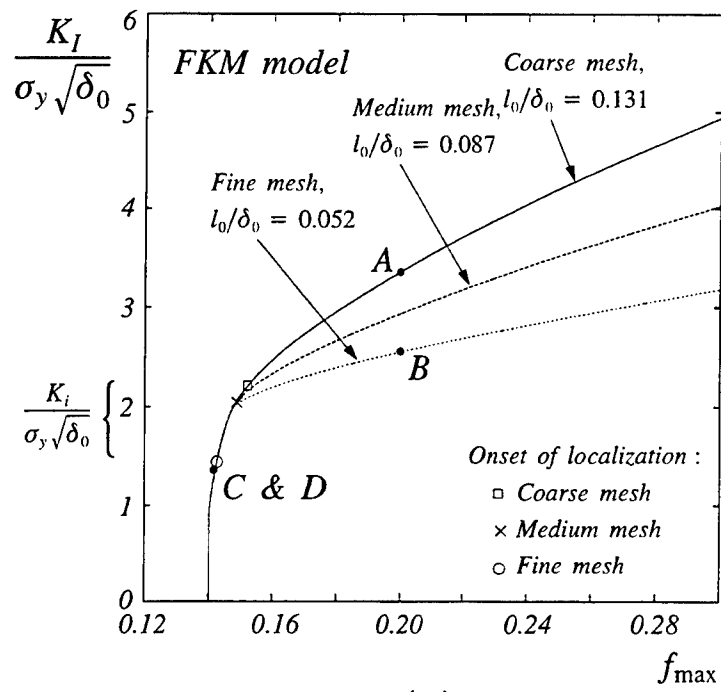
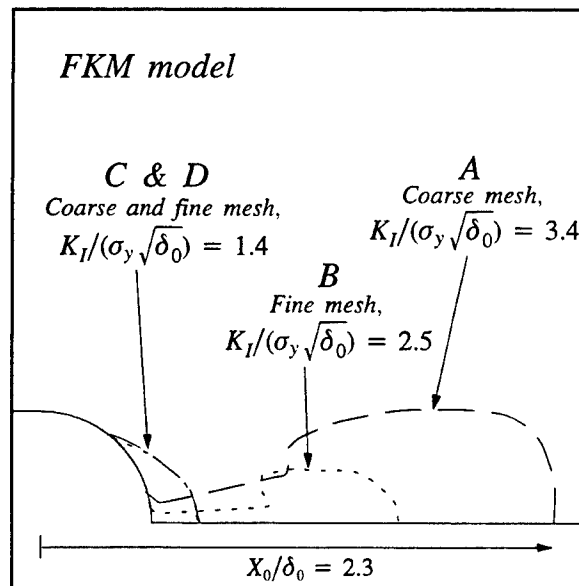


Fig.4 (continued)

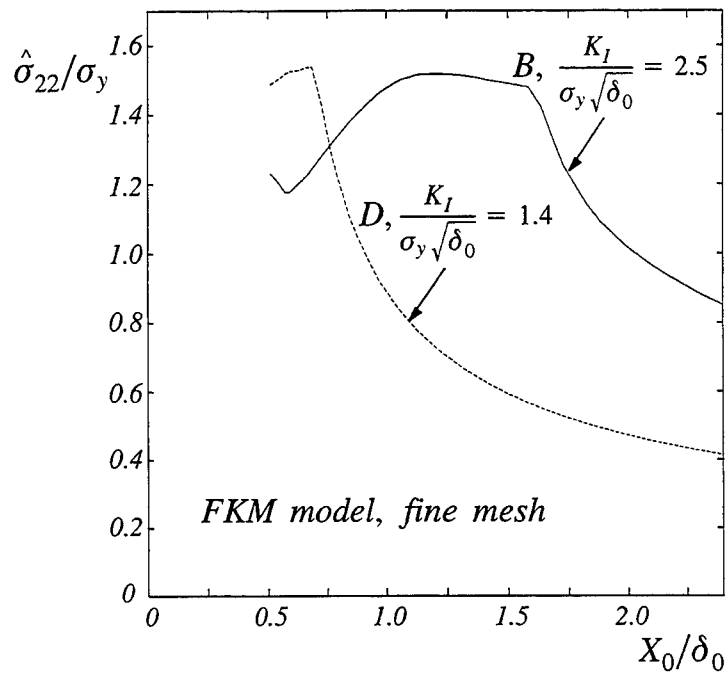


(a)

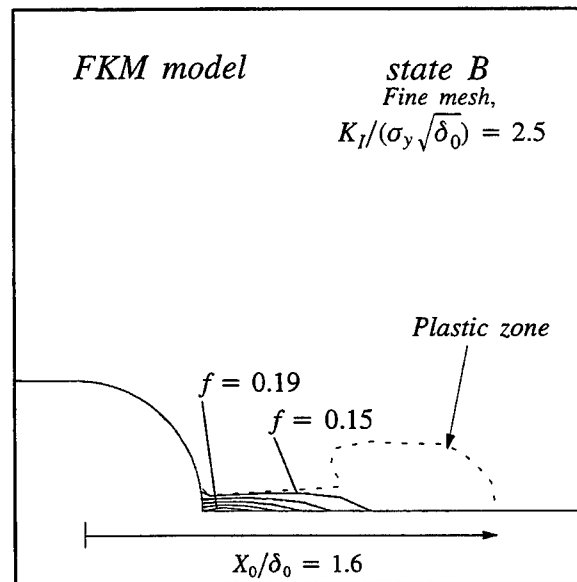


(b)

Fig.5

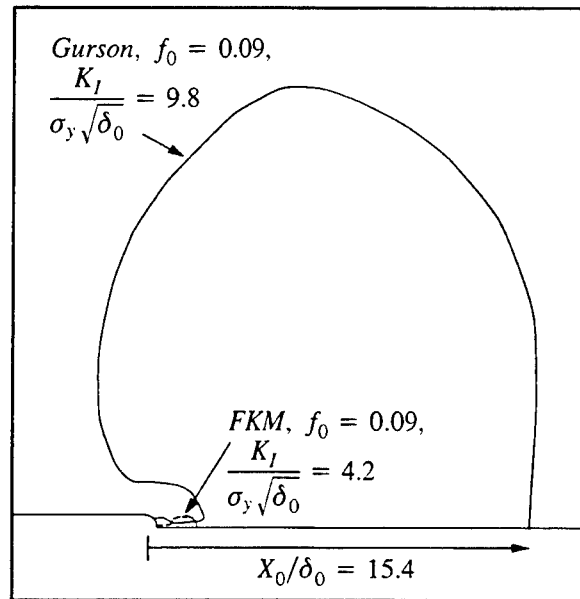


(c)

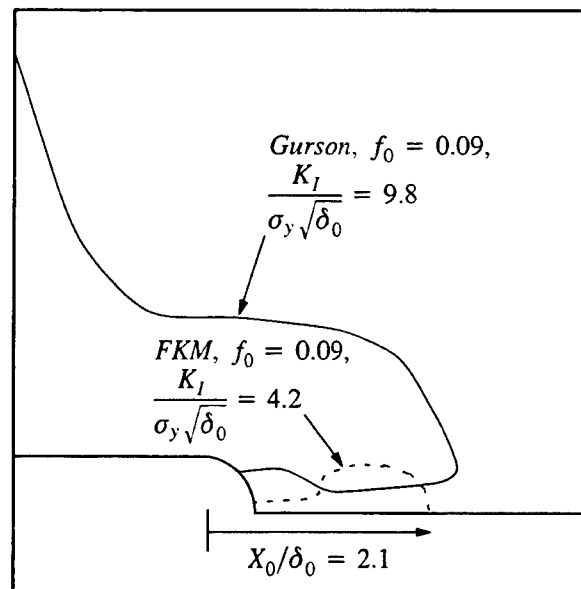


(d)

Fig.5 (continued)



(a)



(b)

Fig.6

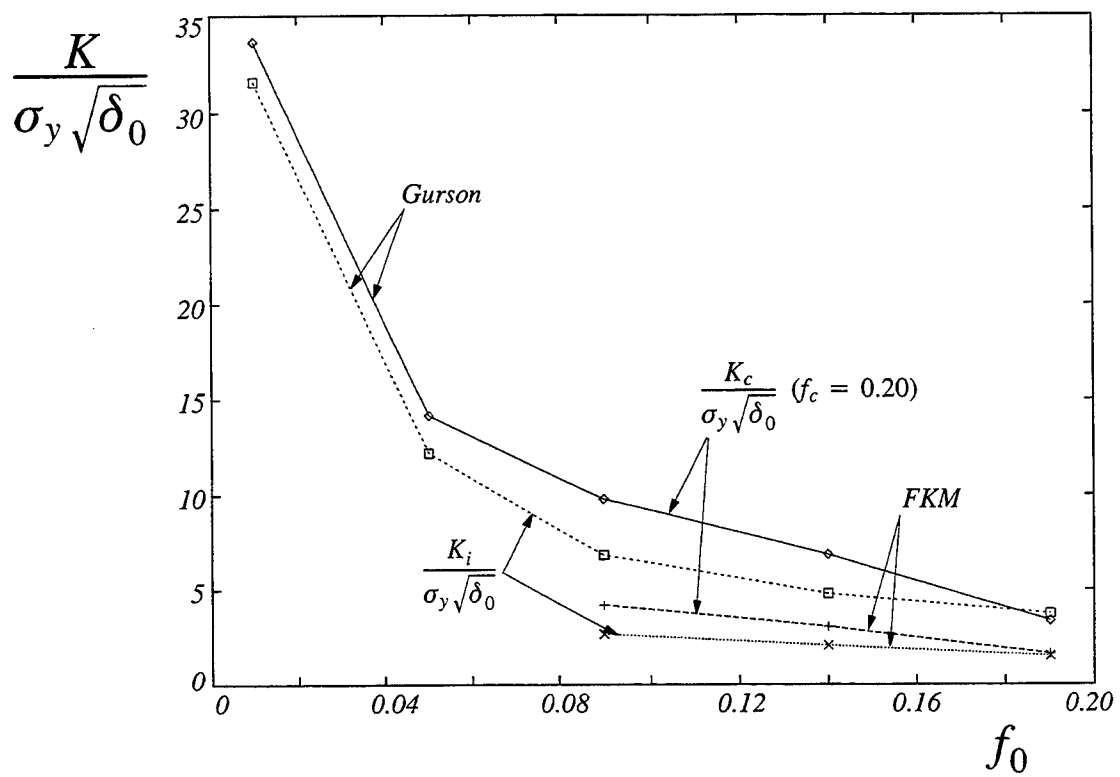


Fig.7



EFFECT OF NOTCH ROOT RADIUS ON THE INITIATION TOUGHNESS OF A C-FIBER/SiC-MATRIX COMPOSITE

J.Y. Shen and J.P. Hirth

Mechanical and Materials Engineering Department, Washington State University,
Pullman, WA 99164-2920

F.W. Zok and J.A. Heathcote

Materials Department, University of California, Santa Barbara, CA 93106

(Received August 26, 1997)

(Accepted October 6, 1997)

Introduction

Fiber-reinforced ceramic matrix composites (CMCs) have a major advantage over monolithic ceramics in that they fail in a noncatastrophic manner because of their ability to redistribute stress through inelastic straining and hence retain good strength in the presence of holes and notches [1,2]. Previous studies have addressed issues related to the tensile stress-strain characteristics [2–4] and the effects of notches on tensile strength in a variety of CMCs [5–8]. In the vast majority of experimental studies of notch strength, tests have been performed on relatively narrow specimens with correspondingly short notches (typically several mm). Consequently, the measured properties may not be fully representative of large engineering structures. A complementary approach to assessing notch-sensitivity involves the use of fracture mechanics tests to obtain the fracture resistance. Arguably, this approach is more relevant to failure prediction of structures containing either large notches or cracks.

The specific objective of the present study was to evaluate the effect of notch root radius on the initiation toughness of a commercial C-fiber/SiC-matrix composite. Previous studies on monolithic metallic materials and metal matrix composites have shown that the initiation toughness is independent of the notch root radius, ρ , below a critical value of ρ , because of the blunting that occurs before the crack extends. Beyond this critical value, the initiation toughness increases approximately linearly with ρ [9–12]. The latter trend can be rationalized on the basis of the increasing volume of material that participates in the plastic deformation ahead of the notch. The critical radius, ρ_0 , provides insight into both the intrinsic fracture and deformation characteristics of the material as well as guidance in selecting notch geometries for subsequent evaluation of fracture resistance.

Experimental Procedure

The material used in the present study was a commercial C-fiber/SiC-matrix composite, made by a chemical vapor infiltration. The fibers were in a 0°/90° plain weave architecture. The fibers were 8 μm in diameter, with a fiber volume fraction of 0.40. The composite was in the form of a plate with 0.3 cm thickness.

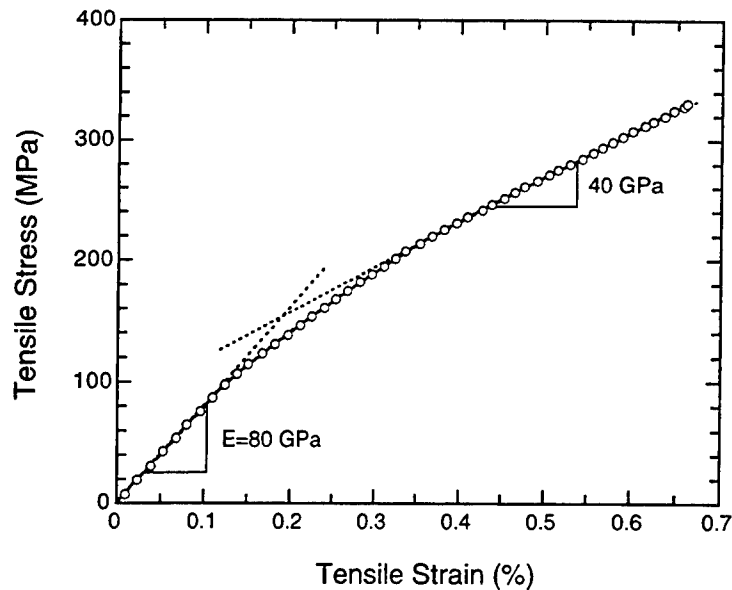


Figure 1. Tensile stress-strain response of the C/SiC composite. The effective yield stress was determined from the intersection of the two dotted lines.

A J-integral approach was used to characterize the crack initiation toughness. Measurements were made using standard compact tension specimens, with the notch oriented perpendicular to one of the fiber axes. The root radius was varied from 50–900 μm . At each loading point, the instantaneous J and crack extension, Δa , were calculated, in accordance with ASTM Standard E-813. In some instances, the cracked specimens were examined in a scanning electron microscope (SEM). Additionally, a uniaxial tension test was performed using a standard dog-bone geometry in order to determine the Young's modulus and the extent of inelastic deformation.

Results

The tensile stress-strain curve is shown in Fig. 1. The curve exhibits nonlinearity at a stress of about 100 MPa and, upon further loading, becomes linear with a reduced tangent modulus. For the purpose of subsequent analysis of the J-R curve, the effective “yield stress” of the material is taken as the stress at which the two linear portions of the curve intersect, as shown in Fig. 1. Following this approach, the yield stress is found to be $\sigma_y \approx 150$ MPa.

The J- Δa curve exhibits characteristics similar to those of metal alloys, including an initial linear portion (associated with crack tip blunting due to inelastic straining), followed by a nonlinear portion at higher values of Δa (Fig. 2). In view of the fact that the inelastic straining process involves matrix cracking and fiber pullout (not dislocation plasticity), the blunting line was constructed by performing a linear regression analysis of the linear portion of the J- Δa curve (as opposed to the usual line of slope $2\sigma_y$). The slope of this line was 33 MPa: about an order of magnitude lower than the value expected on the basis of dislocation plasticity ($2\sigma_y \approx 300$ MPa). The exclusion lines were plotted parallel to the blunting line, in accordance with the standard procedures. The candidate initiation toughness, J_Q , was then evaluated from the intersection of the 0.2 mm offset line with the curve that had been obtained by fitting the J- Δa data contained within the relevant exclusion lines. It is recognized that the standards do not strictly apply to ceramic composites and thus the J_Q values do not necessarily constitute valid J_{IC}

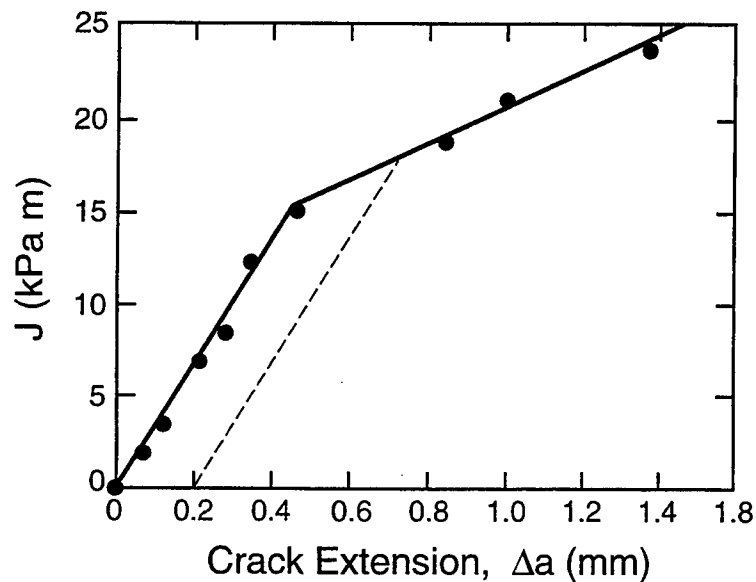


Figure 2. Typical J- Δa curve, showing the onset of non-linearity and the construction of the 0.2 mm offset line.

measurements. Nevertheless, since the values were obtained in the same manner on each of the test specimens, the results are expected to provide a useful characterization of the effects of notch root radius on the initiation toughness.

The trend in the initiation toughness with notch root radius, ρ , is plotted in Fig. 3. The toughness appears to be independent of the radius for $\rho \leq 200 \mu\text{m}$, but subsequently increases linearly with ρ . This behavior closely resembles that seen in monolithic metals [9], particulate metal-matrix composites [10] and fiber-reinforced metals [12]. Previously, it has been rationalized on the basis that crack blunting

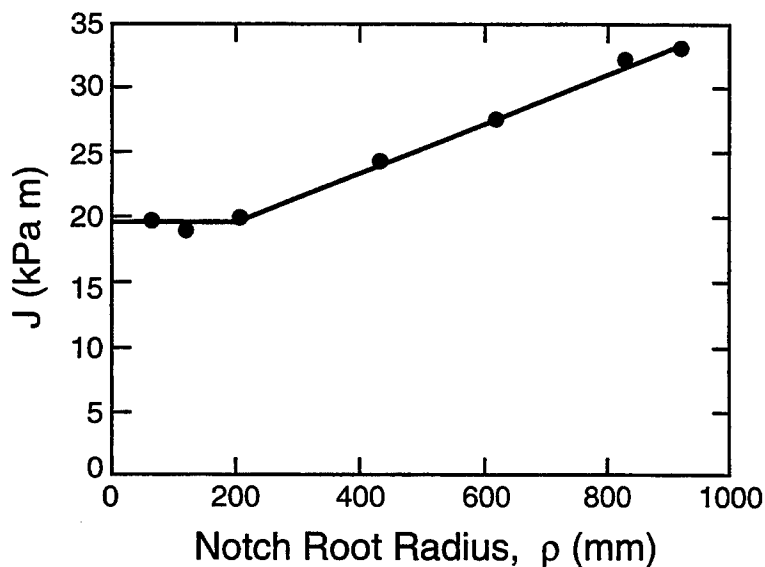


Figure 3. Effects of notch root radius on the initiation toughness.



Figure 4. SEM micrograph showing fiber pullout on the fracture surface.

occurs prior to crack extension and, for sharp notches ($\rho < \rho_o$), the critical amount of blunting corresponds to $\rho = \rho_o$.

SEM examinations of the fracture surfaces revealed the prototypical characteristics of "tough" fiber-reinforced CMCs, notably, extensive fiber pullout in the longitudinal fiber bundles (Fig. 4). The average pullout length has been estimated to be roughly 200 μm .

Discussion

Although the J - Δa curve for the C/SiC composite exhibits features similar to those for monolithic metals, there appears to be a large discrepancy between the initial measured slope and the one predicted on the basis of dislocation plasticity. Notably, in metals, crack blunting gives rise to an effective increase in crack extension, given by $\Delta a \approx \rho_o/2$, as illustrated in Figs. 5(a) and (b). Recognizing that $J \approx \rho_o \sigma_y$ for $\rho < \rho_o$, the slope of the J - Δa curve is predicted to be $2\sigma_y$. In contrast, in the C/SiC composite, the apparent crack extension that is inferred from the compliance measurements is associated with the development of a bridged crack, as illustrated schematically in Fig. 5(c). In this case, the crack extension is expected to vary as $\Delta a \approx \alpha \rho_o$, where α is a numerical coefficient ($> 1/2$), and consequently the slope of the J - Δa curve is predicted to be σ_y/α . Comparison with the measured slope yields $\alpha \approx 5$: an order of magnitude larger than the value associated with metals. This difference is plausible since

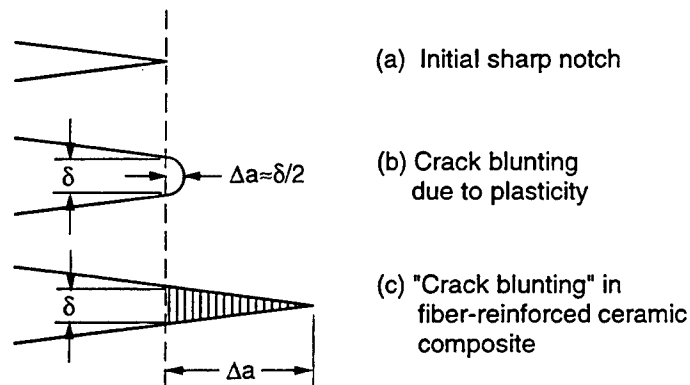


Figure 5. Schematic showing the differences in the crack blunting processes in metals and in fiber-reinforced ceramic composites and their manifestations in terms of the connections between the crack extension, Δa , and the crack tip opening displacement, δ .

the requirements of compatibility and multiple slip in metals restrict the COD for a given energy dissipation, whereas no such constraints exist in the CMCs.

At the most rudimentary level, the magnitude of the initiation toughness in the regime $\rho < \rho_0$ can be rationalized in the following way. Crack extension is envisaged to occur in two steps. In the first, a diffuse array of matrix cracks is formed ahead of the notch. These cracks dissipate energy and allow for some blunting of the crack tip. At a critical level of local strain or stress, the longitudinal fiber bundles fail along or near one of the matrix cracks, leading to the formation of a macroscopic crack that is bridged by broken fibers. Accordingly, the energy dissipation can be partitioned into two components: (i) the energy due to the formation of multiple matrix cracks around the notch tip and the associated interfacial debonding and sliding, and (ii) frictional energy associated with fiber pullout following fiber bundle failure. The former contribution is expected to be $\approx 2 \rho_0 \sigma_f \epsilon_f$, where σ_f is the tensile fracture stress (~ 300 MPa) and ϵ_f is the fracture strain ($\sim 0.6\%$). The estimated value is $J \approx 700$ J/m²: only 1/30 of the measured value (≈ 20 kJ/m²). The latter contribution is calculated from a shear lag analysis of a single broken fiber. Following complete pullout of the fiber, the dissipated energy is predicted to be $\pi \tau l^2/R$, where τ is the interface sliding stress and l is the average pullout length. Taking $l \approx 200$ μ m and estimating the sliding stress to be in the range of ≈ 5 – 10 MPa yields a fracture energy of ≈ 20 – 40 kJ/m²: comparable to the measured value. These estimates indicate that the dominant energy absorption mechanism is the one involving pullout of broken fibers following fiber bundle failure.

Interestingly, the critical notch tip radius, $\rho_0 \approx 200$ μ m, is of the same order as the average fiber pullout length. This correlation suggests that the apparent crack tip blunting obtained from the J tests is accommodated by the formation and opening of the macroscopic crack, not by the inelastic strain associated with multiple matrix cracking prior to the formation of the macroscopic crack. In metals, the critical notch root radius is associated with a process zone size connected to the extent of the plastic zone for small-scale yielding, ie. J-dominant behavior. The present results suggest that, for ceramic matrix composites, an analogous process zone size can be associated with the extent of the crack-bridging zone for small-scale bridging. Evidently, for large-scale bridging, the methodology would be inapplicable.

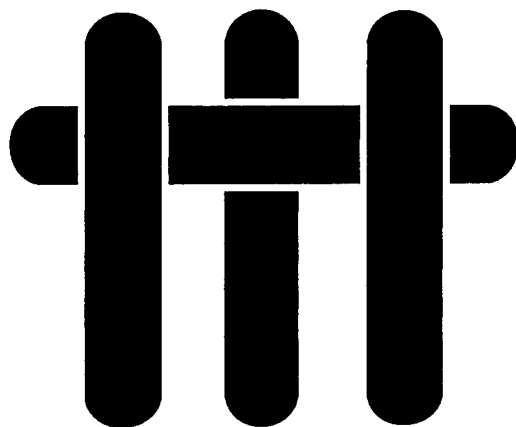
Acknowledgments

The authors are grateful for the support of this work under the Advanced Research Project Agency, University Research Initiative, under Office of Naval Research Contract NO. 00014-93-0213. They are also grateful to F.R. Frasier for help with the experiments.

References

1. N. Miriyala and P. K. Liaw, *Journal of Metals*, 9, 44 (1996).
2. C. Cady, F. E. Heredia, and A. G. Evans, *J. Am. Ceram.* 78, 2065 (1995).
3. F. E. Heredia, S. M. Spearing, and A. G. Evans, *J. Am. Ceram. Soc.* 75, 3017 (1992).
4. R. Turner, J. S. Speck, and A. G. Evans, *J. Am. Ceram. Soc.* 78, 1841 (1995).
5. T. J. Mackin, T. E. Purcell, M. Y. He, and A. G. Evans, *J. Am. Ceram. Soc.* 8, 1719 (1995).
6. C. M. Cady, T. J. Mackin, and A. G. Evans, *J. Am. Ceram. Soc.* 78, 77 (1995).
7. F. E. Heredia, S. M. Spearing, T. J. Mackin, M. Y. He, and A. G. Evans, *J. Am. Ceram. Soc.* 77, 2817 (1995).
8. A. G. Evans and F. W. Zok, *Solid State Physics*, 47, 177 (1994).
9. J. A. Begley and J. D. Landes, ASTM STP 514, p. 1, American Society For Testing and Materials, Philadelphia, PA (1972).
10. M. Manoharan and J. Lewandowski, *Int. J. Fract.* 40, R31 (1989).
11. S. V. Kamat and N. E. Prasad, *Scripta Metall. Mater.* 25, 1519 (1991).
12. S. V. Kamat, J. P. Hirth, and F. W. Zok, *J. Composite Mater.* 30, 1858 (1996).

M A T E R I A L S



STRESS RUPTURE OF AN ENHANCED NICALON™/SiC COMPOSITE AT INTERMEDIATE TEMPERATURES

T.E. Steyer and F.W. Zok

Materials Department
University of California
Santa Barbara, California 93106-5050

and

D.P. Walls

United Technologies, Pratt & Whitney
West Palm Beach, FL 33410

Submitted to *Journal of the American Ceramic Society*
Revised November, 1997

ABSTRACT

The stress rupture characteristics of an enhanced Nicalon™/SiC composite at 900°C have been examined. This temperature has been identified as being in the regime wherein oxidation embrittlement is operative. The enhancement of the composite involves the use of a coating around the fiber tows, comprising a C rich matrix and B-containing particulates. The efficacy of this oxidation protection scheme has been evaluated by comparing the stress rupture characteristics with those of both Nicalon™/SiC composites without the enhancement and the fibers alone. Such comparisons indicate that a substantial portion of the strength loss is attributable to a degradation of the fibers, and that the performance of the enhanced material is marginally better than that of the reference (non-enhanced) composite. Moreover at stress levels greater than the matrix cracking limit, oxidation embrittlement occurs rapidly and the rupture times (several hours) are short in relation to the targeted service lives of most ceramic composite components. The mechanisms associated with the embrittlement have been identified using scanning electron microscopy and Auger spectroscopy.

1. INTRODUCTION

Oxidation embrittlement represents one of the most crucial problems limiting the long term performance of SiC-based ceramic matrix composites (CMCs). The embrittlement involves oxygen ingress through matrix cracks and the subsequent reaction of the oxygen with the fiber coatings, the fibers and the matrix. It occurs as a pest phenomenon, being worst at intermediate temperatures. At higher temperatures, oxidation products that form near the external surfaces seal the matrix cracks and inhibit further oxygen ingress; at lower temperatures, the rate of embrittlement is limited by the kinetics of the oxidation reactions [1-3]. The pest phenomenon has been reported to occur in a number of SiC-based CMCs in the temperature range ~ 500 - 900°C [1-14]: considerably lower than the targeted service temperatures of ~ 1100 - 1200°C .

Two strategies for inhibiting the rate of embrittlement have been pursued. The first deals with the development of fiber coatings that oxidize to form a protective layer and inhibit further oxidation of either the fiber coatings or the fibers. One such coating is BN, which oxidizes to form B_2O_3 [15-19]. The second involves the use of surface coatings and matrix additives, typically made from various combinations of C, Si and B, which oxidize to form a glass that subsequently seals the cracks. This approach has been used extensively in C/C composites [20-23]. A similar approach is being employed in the SiC-based CMCs, using a C-B coating on the fiber tows, in an effort to mitigate the pesting phenomenon.

The present article focuses on a commercial SiC-based CMC which utilizes the latter approach to oxidation protection. Notably, it utilizes a C-B mixture that reacts to form a glass at elevated temperatures. To assess the efficacy of this approach, experiments are performed to evaluate the stress rupture characteristics at an intermediate (pesting) temperature. Comparisons are made with the embrittlement

characteristics of other SiC-based CMCs as well as the strength degradation of the fibers alone. Changes in microstructure are characterized through a combination of scanning electron microscopy and Auger spectroscopy. The observations and measurements are used to infer qualitatively the extent of degradation associated with the various embrittlement mechanisms.

2. MATERIAL

The material used in this study was a commercially-available "enhanced" SiC/NicalonTM composite*, shown in Fig. 1. The enhancement involves the addition of a C-B mixture that reacts with the oxygen and silicon to form a low melting point glass. The composite was reinforced with ceramic grade NicalonTM fibers# in a plain weave architecture. The "matrix" constituents were determined using scanning Auger microscopy (SAM)†, detailed below.

The SAM analyses were performed under ultra-high vacuum conditions with a base pressure of $< 1 \times 10^{-9}$ torr. The samples were sputtered with Ar ions incident at an accelerating voltage, $V = 3$ keV, and a probe current, $I \geq 20$ nA, over a nominal area of $100 \mu\text{m} \times 100 \mu\text{m}$. The Auger spectra were collected at an accelerating voltage of either 3 or 10 keV and a current of 100nA. The system had a 0.6% resolution, calibrated to the Cu LMM transition at 914 eV, $V = 10$ keV and $I = 10$ nA. Survey scans were performed for kinetic energies ranging from 50 to 700 eV. Atomic concentrations, C_x , were determined for each of N constituents from [24].

* Produced by DuPont Lanxide Composites, Inc., Newark, DE

Produced by Nippon Carbon Company, Ltd., Tokyo, Japan

† PHI Instruments, Model 660

$$C_x = \frac{I_x}{S_x d_x} / \sum_{\alpha=1}^N \frac{I_{\alpha}}{S_{\alpha} d_{\alpha}} \quad (1)$$

where I_x is the peak-to-peak Auger amplitude for element x , S_x is the relative sensitivity factor referenced to the Ag MNN transition at 351 eV, and d_x is a relative scale factor to account for the primary beam current, modulation energy, and lock-in amplifier sensitivity. No corrections were made to account for chemical effects on peak shapes and interactions of chemical species. Qualitative information relating to chemical bonding was determined by examining the Auger fine structure, wherein peak shifts and changes in peak shape are related to changes in valence state or density-of-states information [8, 25-29].

The matrix consists of four distinct phases. The regions surrounding the fiber tows are comprised of a C-rich matrix (> 98%) with a dispersion of fine particulates, determined from SAM analysis to be rich in B (Fig. 2). Based on the distribution of this mixture, it was evident that the individual Nicalon™ cloths had been coated with the C-B mixture prior to consolidation. The coated cloths were subsequently stacked and coated with a C layer, ~ 0.7 μm thick, by chemical vapor infiltration (CVI). The C is present both around the C-B mixture as well as on the fibers embedded within the tows, but not on the fibers situated at the periphery of the tows. This was followed by deposition of SiC, also by CVI, to produce the remainder of the matrix. The SiC is present within the tows as relatively thin layers, ~0.5-1 μm, around the fibers and around the cloths as a thicker layer, ~ 50 μm. The pathways for the ingress of the CVI gas into the tows are pinched off by the surrounding SiC, precluding the full densification of the SiC within the tows. Large pores also exist between the fiber tows, a result of the plain weave layup. The composition of the Nicalon™ fibers was determined by Auger spectroscopy to be 35.5% Si, 55% C and 9.5% O, in accord with previous measurements [28-30].

3. TESTING PROCEDURES

Mechanical tests were performed on flat dog-bone shaped tensile coupons, with a gauge section 75 mm long and 10 mm wide. Following machining, the coupons were coated with an additional SiC sealcoat by CVI, ostensibly to protect the fibers that had been exposed by cutting. The sealcoat is evident on the left side of Fig. 1(a).

Two types of tests were performed. The first was a monotonic tension test in which the specimen was subjected to a temperature gradient along its length. Such tests have been shown to clearly demonstrate the pesting phenomenon in other CMCs as well as to identify the pest regime [4]. Strictly, the pest temperature obtained from such a test is expected to depend upon the loading rate, because of the kinetic nature of the embrittling phenomenon. However, loading rate effects were not examined in the present study. The peak temperature was targeted at 900-950°C, and the minimum temperature at ~600°C. The peak temperature exceeds the temperatures associated with pesting in other SiC-based CMCs (500-850°C), but lower than that required to cause substantial creep deformation of the fibers (~ 1000-1100°C) [31-32]. The tests were performed at a rate of 0.074 MPa min⁻¹. The temperature at the location of fracture from two such tests was determined to be 900 ± 20°C (comparable to the peak temperature). Subsequent tests were performed with a uniform temperature of 900°C under fixed loading conditions until fracture. Several stress levels were employed in order to construct a stress rupture curve. For comparison, tension tests were also performed at ambient temperature, with periodic unloadings to measure hysteresis.

Following testing, the fractured specimens were examined in a scanning electron microscope. In some instances, the specimens were split longitudinally and

examined in the SAM. Upon splitting, the specimens failed along or near the fiber surfaces, exposing the oxidation products formed during testing.

4. MEASUREMENTS AND OBSERVATIONS

Figure 3 shows the tensile stress-strain response of the composite at ambient temperature. Matrix cracking initiates at a stress of ~ 60 -70 MPa. The cracking leads to a reduction in modulus, as manifested in the slopes of the hysteresis loops, and the development of a small amount of permanent strain (up to $\sim 0.05\%$). However, the loops appear narrow in relation to those measured on other CMCs [33], implying that minimal interfacial debonding and sliding occurs during loading. Indeed, examination of a fractured specimen reveals that the SiC sealcoat and the thick SiC layers around the bundles are cracked, though the cracks do not appear to penetrate past the C/particulate coating into the fiber tows (Fig. 4). In the absence of cracks within the bundles, sliding does not occur along the fiber-matrix interfaces within the tows, though it may occur to some extent along the C-B coating. This observation is consistent with the narrow hysteresis loops. The progressive reduction in elastic modulus with increasing stress is presumably a result of an increasing density of cracks within the SiC matrix.

Typical fracture surfaces from a room temperature test are shown in Fig. 5. Fracture of the longitudinal tows is characterized by relatively large amounts of pullout along with fragmentation and spalling of both the C and SiC layers within the tows (Fig. 5(a)). The fiber fracture surfaces exhibit the classical mirror-mist-hackle appearance. The transverse tows generally fail through the C coating, with extensive fragmentation of the coatings and some fiber fracture (Fig. 5(b)).

The stress rupture curve for 900°C is shown in Fig. 6. There appears to be a threshold, corresponding to the matrix cracking stress, below which the failure time is long (> 100h). Above this stress, the failure time diminishes rapidly with increasing stress. Evidently the degradation is suppressed if the oxygen is not allowed to diffuse into the composite along easy paths such as matrix cracks, but occurs rapidly once the cracks are formed.

Typical fracture surfaces of specimens that failed at times in the range ~ 4-77h are shown in Figs. 7 and 8. Over this range, the fracture surfaces were similar to one another, with the exceptions noted below. Within the fiber bundles, the C coating had been eliminated, presumably through its reaction with oxygen to form CO/CO₂ gas, creating gaps between the fibers and the surrounding SiC (Fig. 7(b)). There was also evidence of the formation of SiO₂ on the fibers. In some instances, neighboring fibers had been bonded together by the SiO₂; in others, the fibers had bonded to the surrounding SiC. The fiber fracture surfaces were generally very flat and featureless, suggesting a low fracture stress. In addition, the pullout lengths were considerably smaller than those at room temperature. The latter result is somewhat unexpected, since the absence of the C coating and the attendant loss in frictional coupling between the fibers and the matrix would suggest that the pullout lengths should increase. This seeming discrepancy is attributed to the bonding produced by the SiO₂, promoting the formation of contiguous cracks comprising several fibers. Clearly, this form of degradation can only occur within a composite and would not be manifested in the strength reduction of the fibers alone. Similar observations were made on both the tows situated near the external surfaces and those situated near the specimen center.

The regions at the periphery of the tows exhibited different characteristics. Once matrix cracks had formed, the C-B mixture reacted with both the available oxygen and Si (from either SiO₂ or SiO gas) to form a low melting point glass (Fig. 8).

Based on the constituents present, this is probably a borosilicate glass. The glass was evident along the fracture surface of the SiC. It is expected that the glass inhibits oxygen ingress into the tows along matrix cracks, though the loss of C within the bundles indicates that it is not suppressed altogether. For long exposure times, the entire C-B mixture was consumed and replaced by a relatively thick glass layer. Fig. 8(b) shows an example of fibers at the tow periphery that had been completely covered by the glass. In other regions of the periphery, fiber failure occurred in a brittle, co-planar fashion with *no* pullout and the surfaces of the fractured fibers were covered with a thin layer of the glass (Fig. 9(c)). The extent of glass formation appeared to be somewhat greater around the tows situated near the external surfaces, where the oxygen could penetrate more readily, and in specimens tested to longer failure times. However, the extent of oxidation appeared to be inhomogeneous, varying from one tow to the next. This may be due to the inhomogeneity in the distribution and thickness of the C-B mixture.

The co-planar fiber breaks at the bundle periphery may be attributed to a deleterious reaction of the fibers with the glass. Previous studies on SiC have shown that oxidation rates can be increased substantially in the presence of silicate glass relative to that in air [34]. The increase is due to the reduction in the viscosity of the silicate passivation layer and the corresponding reduction in its effectiveness as a diffusion barrier.

Additional evidence of oxide formation was obtained from Auger analysis performed on fiber surfaces that had been exposed by splitting the specimens longitudinally. The evolution of the Auger fine structures near the Si and O peaks during depth profiling are shown in Fig. 9. The Auger transition signal for Si bonded in SiO₂ occurs at a substantially lower kinetic energy than that of unoxidized Si or of Si in SiC, thereby allowing SiO₂ to be distinguished from SiC. The Si peak associated with SiO₂ (at ~ 62 eV) also contributes to a broadening of the Si-LMM

transition at ~ 92 eV. Figure 9(a) shows that the SiO_2 content decreases with increasing sputtering time, as manifested in a reduction in the SiO_2 peak and a more pronounced Si-LMM peak. The Auger fine structure for oxygen (Fig. 10(b)) provides corroborating evidence, as the O-KLL transition at ~ 510 eV is most prominent at lower sputtering times, indicating a higher oxygen concentration near the surface. After five minutes of sputtering, the Auger spectrum was essentially the same as that of bulk NicalonTM.

5. DISCUSSION

Numerous oxidation and degradation processes occur concurrently during stress rupture of the enhanced NicalonTM/SiC composite. The processes include: (i) cracking of the SiC sealcoat and the SiC around the fiber tows, leading to ingress of oxygen; (ii) oxidation of the C-B mixture in the presence of oxygen and Si to form a borosilicate glass, possibly sealing cracks and thus inhibiting (but not preventing) further oxygen ingress into the tows; (iii) penetration of oxygen into the fiber tows through the matrix cracks and the internal pores, leading to oxidation of the C coatings and the formation of gaps between the fibers and the surrounding SiC matrix; (iv) the formation of SiO_2 on the fibers, in some instances causing the fibers to bond to one another or to the SiC matrix; and (v) the interaction of the borosilicate glass with the fibers at the tow periphery, leading to an acceleration in the oxidation rate of the fibers and a degradation in their strength.

An attempt to assess the efficacy of the C/particulate coating in inhibiting oxidation embrittlement was made by comparing the measured stress rupture behavior with previous results both on NicalonTM/SiC composites without the B-C mixture and on the fibers alone. NicalonTM fibers are known to degrade at elevated temperature, reportedly because of grain growth and the formation of a surface

oxide scale, and, at sufficiently high temperatures ($\geq 1200^{\circ}\text{C}$), the formation of CO and SiO bubbles near the fiber surface. Kim and Moorhead [35] measured the strength degradation by heating the fibers in air in the absence of stress and subsequently measuring the fiber strengths at room temperature. Interestingly, the results for exposure temperatures of 800 and 1000°C (spanning the test temperature of 900°C used in the present study) were essentially the same at both temperatures.

Figure 10 shows a comparison between the strength degradation of the fibers and the present composite. For the purpose of this comparison, the stresses have been normalized by the respective pristine tensile strengths at ambient temperature. Evidently the composite degrades more rapidly than the fibers alone. Moreover, it appears that roughly half of the composite strength degradation can be attributed to the degradation of the fibers alone in the presence of air.

Figure 10 also shows comparisons with the reported stress rupture behavior of a unidirectional NicalonTM/SiC minicomposite containing similar C coatings on the fibers, measured at 700°C [14]. These results also have been normalized by the respective tensile strength at room temperature. The minicomposites exhibit a comparable reduction in strength to that of the enhanced CMC, despite the substantially lower test temperature (700 vs. 900°C). A similar trend in degradation has been observed in a woven NicalonTM/SiC CMC (without the C-B mixture) at a temperature of 800°C [10].

Several inferences can be drawn from these comparisons. First, the degradation of the fibers represents a significant fraction of the strength loss of the composites. Second, the composites degrade more rapidly than the fibers alone, indicating that additional degradation mechanisms are operative. Finally, the enhanced material exhibits a higher temperature capability than NicalonTM/SiC CMCs with C coatings alone (at least in terms of the temperature regime in which

the pesting phenomenon is most acute), possibly because of the presence of the additional C-B mixture.

6. CONCLUDING REMARKS

Stress rupture of the enhanced NicalonTM/SiC composite at 900°C involves numerous oxidation and degradation processes that operate concurrently. The presence of the C-B mixture around the fiber bundles appears to inhibit oxygen ingress into the tows along mixture cracks. However, once the glass comes into contact with the fibers, it compromises the efficacy of the SiO₂ passivation layer on the fibers.

At stresses above the matrix cracking limit, the rupture times are extremely short in relation to the targeted service lives of most CMC components ($\sim 10^3$ - 10^4 h). This deficiency may preclude the use of these materials for long-term applications. Alternatively, it may require the design stresses to be maintained below the matrix cracking limit. The latter approach is expected to yield very conservative designs with currently available CMCs, not fully exploiting their inelastic deformation capabilities. If such an approach were adopted, it would require materials with a high matrix cracking stress. The CVI CMCs are not optimal in this regard, because of the presence of large irregular pores that concentrate stress and promote matrix cracking at low levels of stress. Materials with nearly fully dense matrices, made, for example, by melt infiltration, would be preferred.

ACKNOWLEDGMENTS

Funding for this work was provided by the ARPA University Research Initiative Program at UCSB under ONR contract No. N00014-92-J-1808. The authors

gratefully acknowledge useful comments on the manuscript provided by Joseph Halada of DuPont Lanxide Composites, Inc..

REFERENCES

1. Brennan, J.J., "Interfacial Studies of Chemical Vapor Infiltrated Ceramic Matrix Composites," *Mat. Sci. Eng.*, **A126** 203-23 (1987).
2. Luh, E.Y. and A.G. Evans, "High Temperature Mechanical Properties of a Ceramic Matrix Composite," *J. Am. Ceram. Soc.*, **70** [7] 466-69 (1987).
3. Brennan, J.J., "Interfacial Chemistry and Bonding in Fiber Reinforced Glass-Ceramic Matrix Composites", pp. in Ceramic Microstructures: The Role of Interfaces, J.A. Pask and A.G. Evans, Editors. Plenum Press, New York, 1988.
4. Bischoff, E., M. Rühle, O. Sbaizero and A.G. Evans, "Microstructural Studies of the Interfacial Zone of a SiC-Fiber-Reinforced Lithium Aluminum Silicate Glass-Ceramic," *J. Am. Ceram. Soc.*, **72** [5] 741-45 (1989).
5. Prewo, K.M., B. Johnson and S. Starrett, "Silicon Carbide Fiber Reinforced Glass Ceramic Composite Tensile Behavior at Elevated Temperature," *J. Mater. Sci.*, **24** [4] 1373-79 (1989).
6. Huger, M., D. Fargeot, and C. Gault, "Ultrasonic Characterization of Oxidation Mechanism in Nicalon/C/SiC Composites," *J. Am. Ceram. Soc.*, **77**[10] 2554-60 (1994).
7. Filipuzzi, L., G. Camus, R. Naslain, and J. Thebault, "Oxidation Mechanisms and Kinetics of 1D-SiC/C/SiC Composite Materials I, An Experimental Approach," *J. Am. Ceram. Soc.*, **77**[2] 549-66 (1994).
8. Ponthieu, C., C. Marhic, M. Lancin, and N. Herbots, "SIMS, EDX, EELS, AES, XPS Study of Interphases in Nicalon Fibre-LAS Glass Matrix Composites," *J. Mater. Sci.*, **29** 4535-4544 (1994).
9. Plucknett, K.P. and M.H. Lewis, "Inhibition of Intermediate Temperature Degradation of Calcium Aluminosilicate/Nicalon by High Temperature Pretreatment," *J. Mater. Sci. Letters*, **14** 1223-26 (1995).
10. Heredia, F.E., J.C. McNulty, F.W. Zok, and A.G. Evans, "An Oxidation Embrittlement Probe for Ceramic Matrix Composites," *J. Am. Ceram. Soc.*, **78**[8] 2097-100 (1995).
11. Plucknett, K.P., S. Sutherland, A.M. Daniel, R.L. Cain, G. West, D.M.R. Taplin, and M.H. Lewis, "Environmental Ageing Effects in a Silicon Carbide Fibre-reinforced Glass-ceramic Matrix Composite," *J. Micros.*, **177**[251-63 (1995).
12. Plucknett, K.P., R.L. Cain, and M.H. Lewis, "Interface Degradation in CAS/Nicalon During Elevated Temperature Aging", pp. in Vol. 365 Ceramic

Matrix Composites-Advanced High-Temperature Structural Materials, R.A. Lowden, *et al.*, Editors. Materials Research Society, Pittsburgh, 1995.

13. Plucknett, K.P. and M.H. Lewis, "Inhibition of Intermediate Temperature Degradation of Calcium Aluminosilicate/Nicalon by High Temperature Pretreatment," *J. Mat. Sci. Lett.*, **14** 1223-6 (1995).
14. Morscher, G.N., "Tensile Stress-Rupture of SiCf/SiCm Minicomposites with C and BN Interphases at Elevated Temperatures in Air," *J. Am. Ceram. Soc.*, submitted for publication (1996).
15. Singh, R.N. and M.K. Brun, "Effect of BN Coating on Fiber-Matrix Interactions," *Adv. Ceram. Mat.*, **3** [3] 235-7 (1988).
16. Naslain, R., "Boron Nitride Interphases in Ceramic-Matrix Composites," *J. Am. Ceram. Soc.*, **74**[10] 2482-8 (1991).
17. Jessen, T.L. and B.A. Bender, "Layered BN-Coated/As Received Unidirectional CFCCs with Enhanced Mechanical Performance," *Ceram. Eng. Sci. Proc.*, **15**, 311-18 (1994).
18. Shen, L., B.J. Tan, W.S. Willis, F.S. Galasso, and S.L. Suib, "Characterization of Dip-Coated Boron Nitride on Silicon Carbide Fibers," *J. Am. Ceram. Soc.*, **77**[4] 1011-6 (1994).
19. Sheldon, B.W., E.Y. Sun, S.R. Nutt and J.J. Brennan, "Oxidation of BN-Coated SiC Fibers on Ceramic Matrix Composites," *J. Am. Ceram. Soc.*, **79** [2] 539-43 (1996).
20. Strife, J.R. and J.E. Sheehan, "Ceramic Coatings for Carbon-Carbon Composites," *Am. Ceram. Soc. Bull.*, **67**[2] 369-74 (1988).
21. Gee, S.M. and J.A. Little, "Oxidation Behavior and Protection of Carbon/Carbon Composites," *J. Mater. Sci.*, **26** 1093-1100 (1991).
22. Buchanan, F.J. and J.A. Little, "Glass Sealants for Carbon-Carbon Composites," *J. Mater. Sci.*, **28** 2324-30 (1993).
23. Goujard, S., L. Vandenbulcke, and H. Tawil, "Oxidation Behavior of 2D and 3D Carbon/Carbon Thermostructural Materials Protected by CVD Poly-layer Coatings," *Thin Solid Films*, **252** 120-30 (1994).
24. Davis, L.E., N.C. MacDonald, P.W. Palmberg, G.E. Riach, and R.E. Weber, Handbook of Auger Electron Spectroscopy, Eden Prairie, MN, Perkin-Elmer Corporation, 1978.
25. Houston, J.E., "Valence-band Structure in the Auger Spectrum of Aluminum," *J. Vac. Sci. Technol.*, **12**[1] 255-9 (1975).

26. Madden, H.H. and G.C. Nelson, "Auger-Electron Spectra from Boron Carbide," *Phys. Rev. B*, **31**[6] 3667-71 (1985).
27. Chao, S.S., J.E. Tyler, Y. Takagi, P.G. Pai, G. Jucovsky, S.Y. Lin, *et al.*, "A Study of Chemical Bonding in Suboxides of Silicon using Auger Electron Spectroscopy," *J. Vac. Sci. Technol. A.*, **4**[3] 1574-9 (1986).
28. Chen, M.Y., J.M. Battison, and T.-I. Mah, "Interface Analysis of Si-C-O Fiber/Magnesium Aluminosilicate Matrix Composites," *J. Mater. Sci.*, **24** 3213-20 (1989).
29. Steyer, T.E., K.T. Faber, and M.D. Drory, "Fracture Strength of Free-Standing Chemically Vapor-Deposited Diamond Films," *Appl. Phys. Lett.*, **66** [23] 3105-7 (1995).
30. Brennan, J.J., "Interfacial Characterization of Glass and Glass-Ceramic Matrix/Nicalon Fiber Composites", pp. 549 in Tailoring of Multiphase Ceramics. Plenum Press, New York, 1986.
31. Simon, G. and A.R. Bunsell, "Creep Behavior and Structural Characterization at High Temperatures of SiC Nicalon Fibers," *J. Mater. Sci.*, **19** 3658-70 (1984).
32. Simon, G. and A.R. Bunsell, "Mechanical and Structural Characterization of the Nicalon Silicon Carbide Fibre," *J. Mater. Sci.*, **19** 3649-57 (1984).
33. Domergue, J.-M., E. Vagaggini, and A.G. Evans, "Relationship between Hysteresis Measurements and the Constituent Properties of Ceramic Matrix Composites, II: Experimental Studies on Unidirectional Materials," *J. Am. Ceram. Soc.*, **78**[10] 2721-31 (1995).
34. Ervin, G., Jr., "Oxidation Behavior of Silicon Carbide," *J. Am. Ceram. Soc.*, **41**[347-52] (1958).
35. Kim, H.-E. and A.J. Moorhead, "Strength of Nicalon Silicon Carbide Fibers Exposed to High-Temperature Gaseous Environments," *J. Am. Ceram. Soc.*, **74**[3] 666-9 (1991).
36. Berger, M.H., N. Hochet, and A.R. Bunsell, "Microstructure and Thermo-mechanical Stability of a Low-oxygen Nicalon Fibre," *J. Micros.*, **177** 230-41 (1995).
37. Thouless, M.D., O. Sbaizero, L.S. Sigl, and A.G. Evans, "Effect of Interface Mechanical Properties on Pullout in a SiC-Fiber-Reinforced Lithium Aluminum Silicate Glass-Ceramic," *J. Am. Ceram. Soc.*, **72**[4] 525-32 (1989).
38. Huger, M., S. Souchard, and C. Gault, "Oxidation of Nicalon SiC Fibres," *J. Mat. Sci. Lett.*, **12** 414-6 (1993).

FIGURE CAPTIONS

- Fig. 1 Cross section of the composite: (a) at low magnifications, showing the fiber architecture and the porosity between the fiber bundles; backscattered images at higher magnifications, showing (b) the mixture of C and B-containing particulates surrounding a fiber bundle and (c) the interior of the fiber bundle with uniform layers of C (dark) and SiC (light).
- Fig. 2 Auger spectra obtained from the particulates.
- Fig. 3 Hysteresis loops measured at ambient temperature.
- Fig. 4 Longitudinal section through specimen tested at ambient temperature, showing cracks emanating from the SiC matrix but not penetrating into the fiber bundles. The specimen had been subjected to the loading shown in Fig. 3.
- Fig. 5 Fracture surface of specimen tested at ambient temperature: (a) longitudinal tow, showing fiber-pullout and coating fragmentation; (b) transverse tow.
- Fig. 6 Stress rupture behavior at 900°C.
- Fig. 7 Central region of a fiber bundle: (a) at low magnification, showing little pullout, and (b) at higher magnifications showing interface gaps and bonding of fibers to one another (indicated by arrows) ($\sigma = 80$ MPa, $t_f = 8.3$ h).
- Fig. 8 (a) Formation of a glass layer at the interface between the CVI SiC and the C-B mixture. (b) Complete coverage of fibers at the tow periphery by the glass. (c) Brittle (coplanar) fracture of the fibers near the tow periphery.
- Fig. 9 Auger fine structure of the fiber surface as a function of sputtering time, showing (a) silicon and (b) oxygen spectra.
- Fig. 10 Relative stress rupture behaviors of the enhanced material, a comparable Nicalon™/SiC minicomposite without the C-B additive, and the fibers alone. (The fiber data for an exposure temperature of 1000°C are essentially the same as the ones shown for 800°C.)

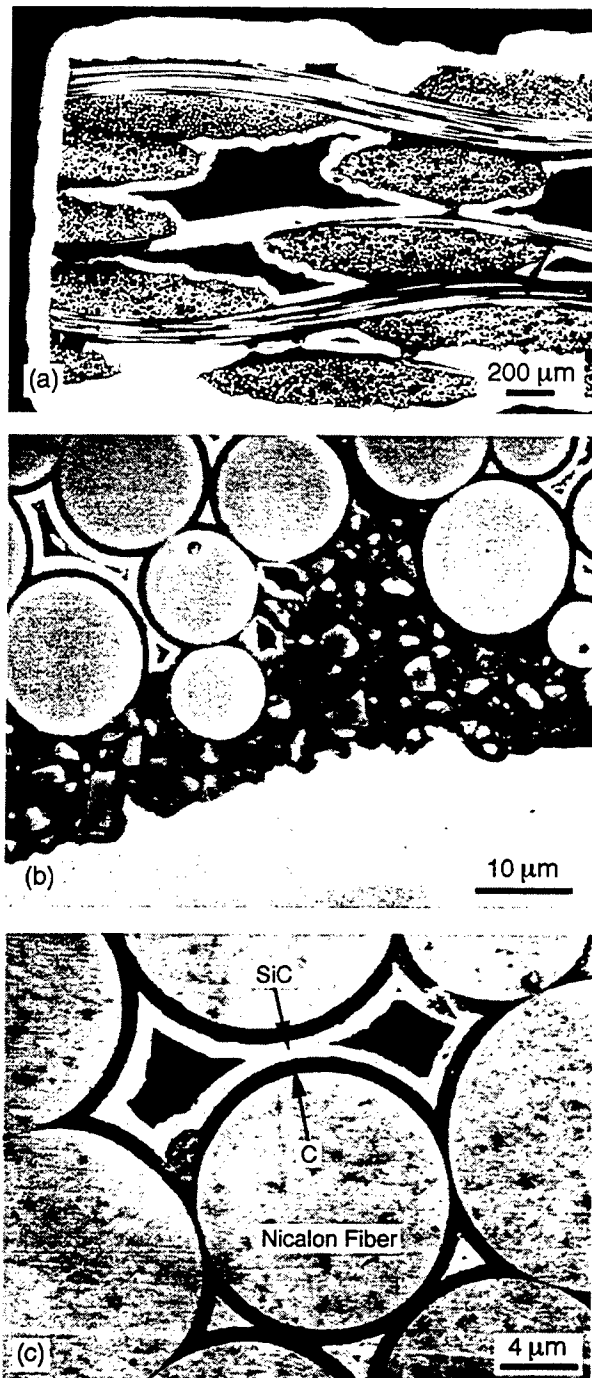


Figure 1

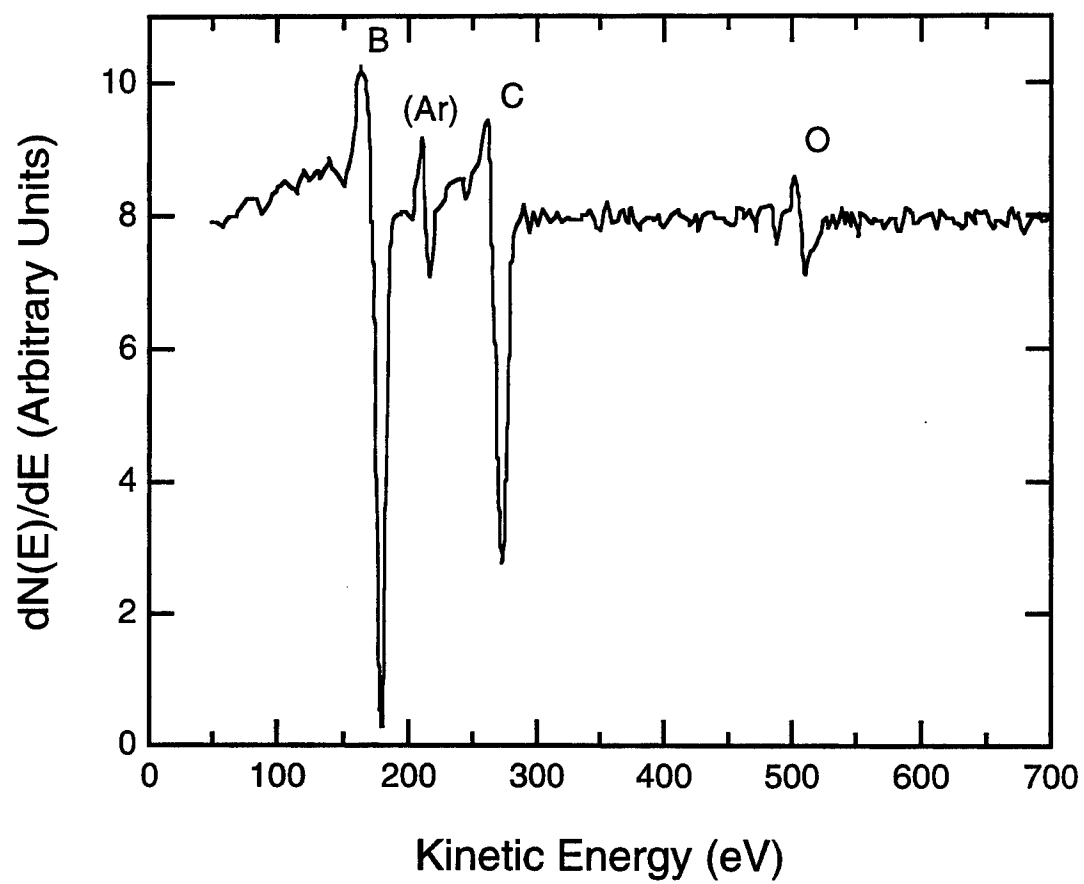


Figure 2

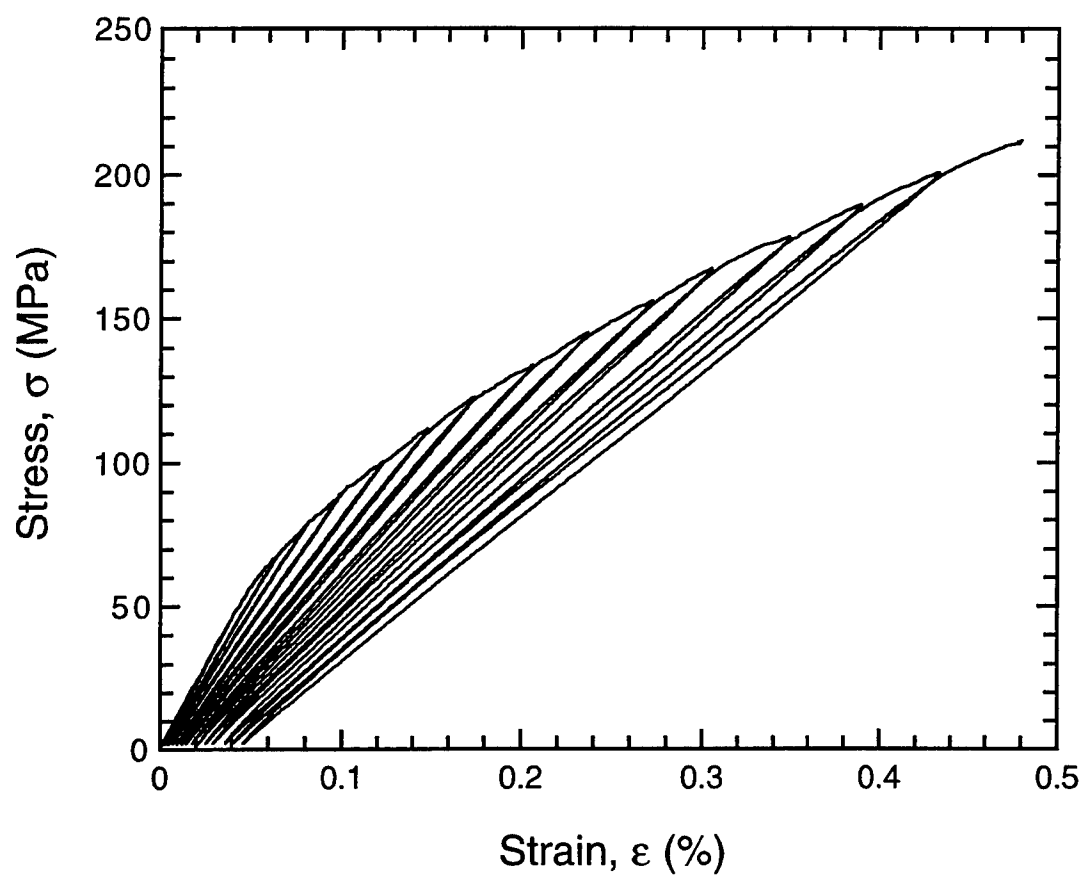


Figure 3

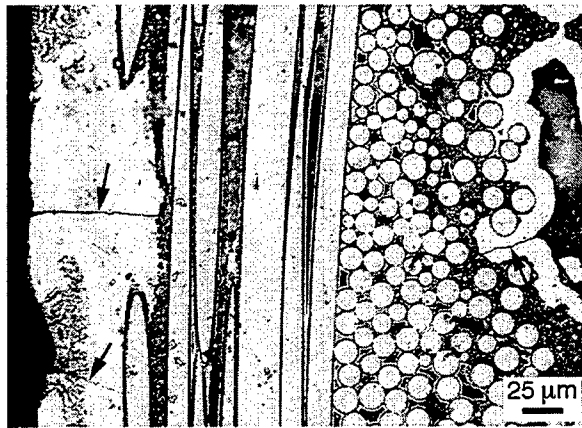


Figure 4

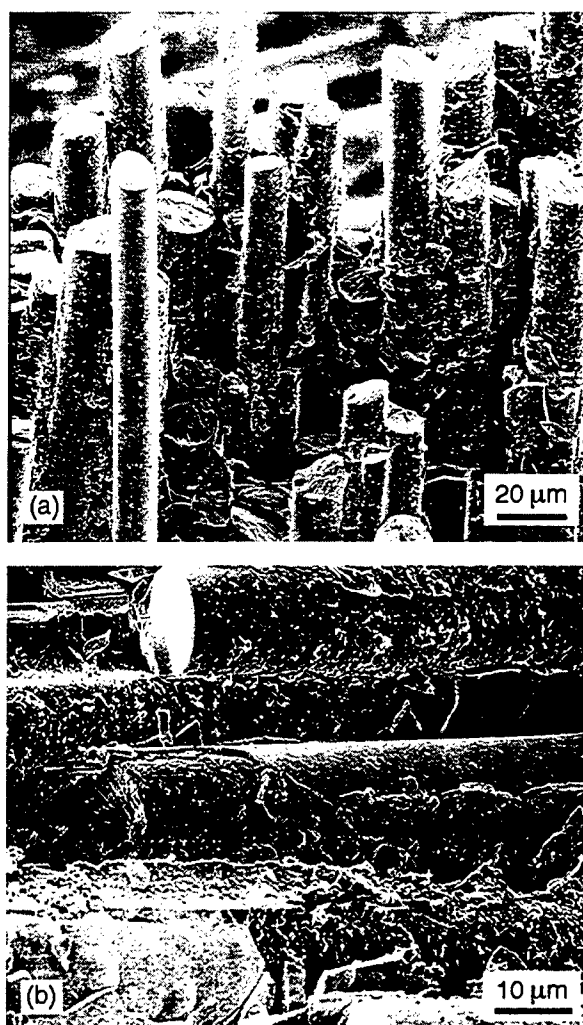


Figure 5

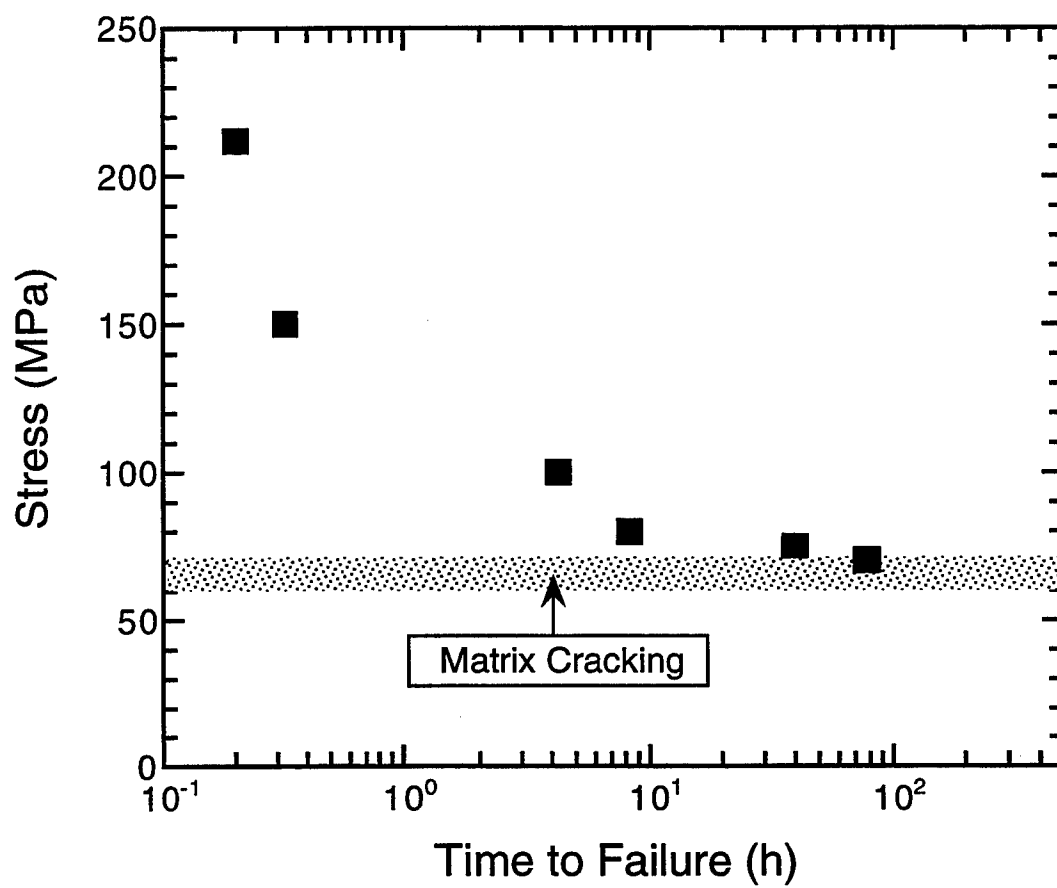


Figure 6

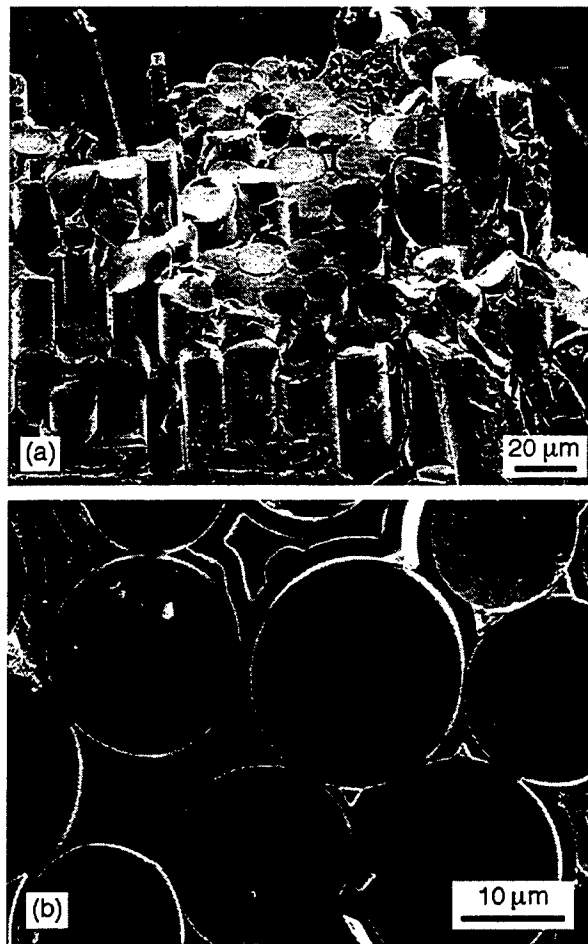


Figure 7

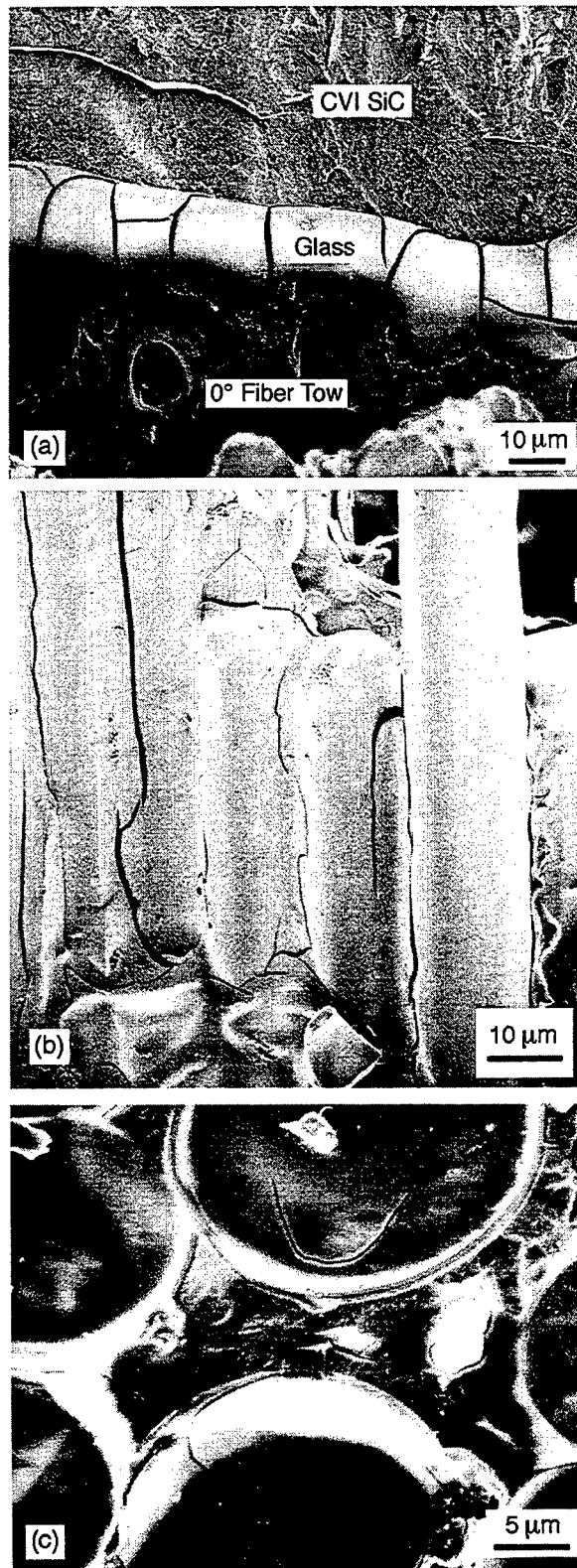


Figure 8

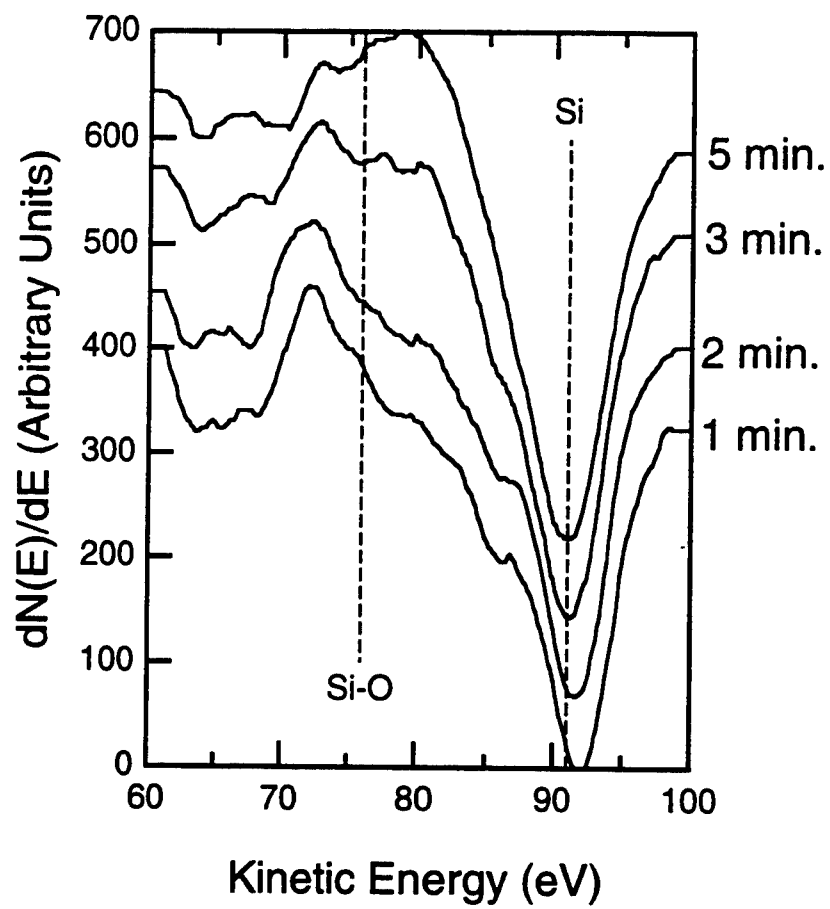


Figure 9(a)

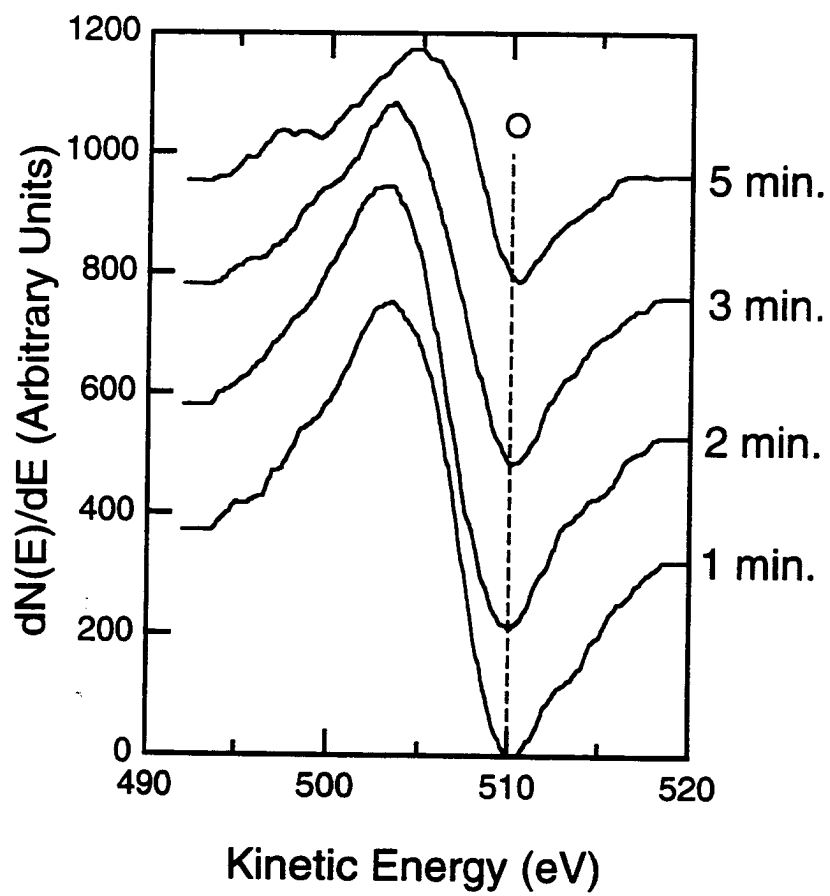


Figure 9(b)

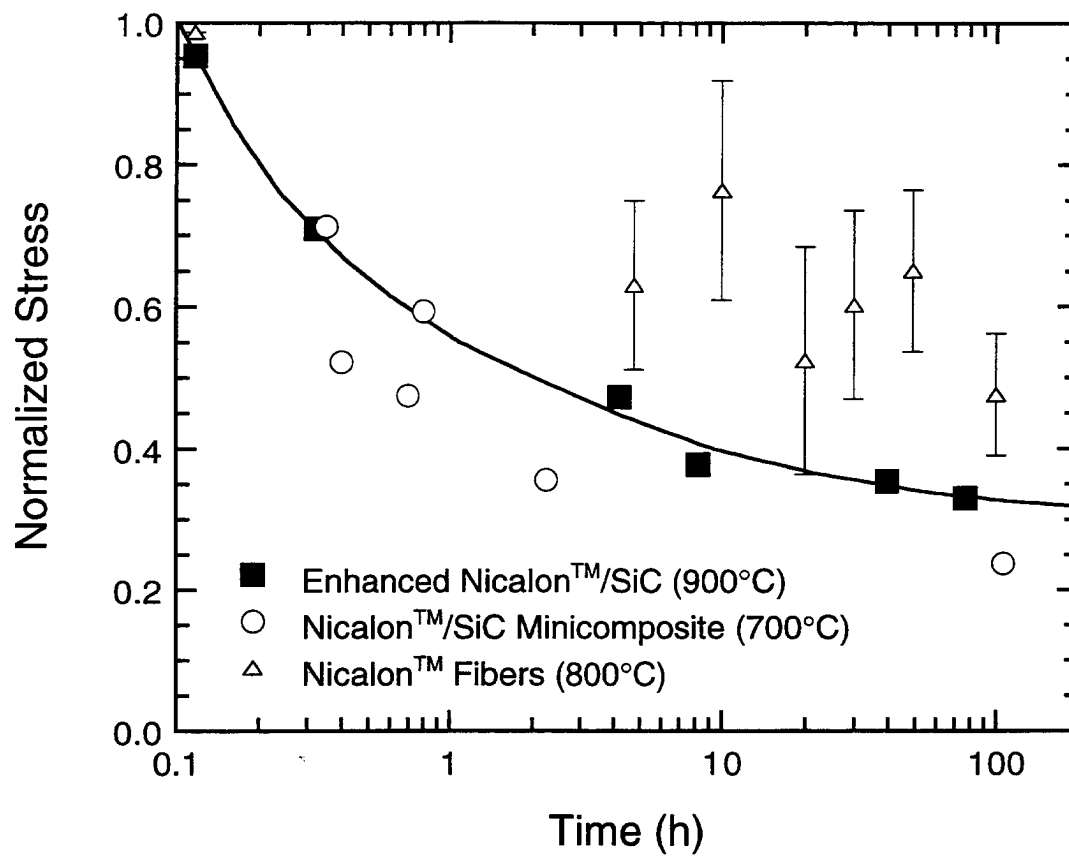


Figure 10